Experimental studies on small diameter carbon dioxide evaporators for optimal Silicon Pixel Detector cooling

Dissertation
zur
Erlangung des Doktorgrades (Dr. rer. nat.)
der
Mathematisch-Naturwissenschaftlichen Fakultät
der
Rheinischen Friedrich-Wilhelms-Universität Bonn

von
Annabell Desiree Hellenschmidt
aus
Rothenburg ob der Tauber

Bonn, Juni 2020

Angefertigt mit Genehmigung der Mathematisch-Naturwissenschaftlichen Fakultät der Rheinischen Friedrich-Wilhelms-Universität Bonn

1. Gutachter: Prof. Dr. Jochen Dingfelder
2. Gutachter: Dr. Georg Viehhauser
CERN Betreuer / CERN supervisor: Paolo Petagna

Tag der Promotion: 23.09.2020
Erscheinungsjahr: 2020

To my mother and grandmother who didn’t receive their chance
and to my parents for giving me mine.

Abstract

Since recent years the Large Hadron Collider at CERN and its experiments are the subject of upgrade programs, which are necessary to increase the foreseen collision rates and the amount of data to be gathered for the particle physics community in the future. In order to cope technologically with long operation times under high radiation levels, the LHC experiments have to upgrade or fully replace some of the most crucial detector components. To improve their resolution and read-out rate capabilities, this is especially important for the Silicon Pixel Detectors, which are installed at the very center of the large detector units at CERN. In parallel with the implementation of new and more compact detection and read-out technologies, the request for highly-effective and integrated detector cooling is getting more demanding. Due to its superior performance compared to standard refrigerants, the thermal management of many Silicon Pixel Detectors at CERN relies on boiling carbon dioxide inside compact heat exchangers of small hydraulic diameter. To allow for an optimal design of the applied cooling method and to safely operate the highly sensitive particle detectors, some of the unknowns related to carbon dioxide flow boiling in small channels must be resolved to develop new predictive methods, both for the pressure drop and heat transfer coefficient. Due to the current lack of suitable predictive models, a long-term study has been launched to create a consistent and reliable experimental data base studying the peculiarities of boiling carbon dioxide in mini- and micro-channels. By means of a new experimental setup for detector cooling R&D, various small-scale carbon dioxide evaporator layouts can be analyzed. Three dimensions of small-scale tubular evaporators in stainless steel and a multi-micro-channel cold plate embedded into silicon have been characterized for this study. By means of a parametrical characterization with high-end pressure and temperature sensors and flow visualization with a high-speed camera, results from the basic tubular single-channels can complement the findings from the multi-micro-channels and vice versa, thus creating a large and multifaceted data base. Since the thermal management of high energy physics experiments is in need for a continuous operation in the temperature range from +15°C to -30°C or even lower, the data presented focus on the influence of the saturation temperature on the two-phase pressure drop and heat transfer, whilst flow visualizations obtained for the multi-micro-channels can provide a consistent key of interpretation for the parametrical analysis. The combination of the shifting, temperature-dependent physical properties of carbon dioxide and different flow confinement conditions causes a change in the phenomenological behaviour of the flow and a transition between macro- and micro-scale flow behaviour most likely occurs within the range of test parameters. Furthermore a shift in the applicability of existing prediction methods is caused by those effects and no correlation for heat transfer and pressure drop is able to predict the experimental data and trends in the whole temperature range. A selective approach to the use of existing correlations is proposed. Thus while new comprehensive prediction models are being developed based on the data gathered for this study, at the same time some recommendations for the temperature dependent use of already existing models can be provided. This allows for an optimized design of new Silicon Pixel Detector cooling systems, today or in the very near future.

Contents

CHAPTER 1

Introduction

Located at the inner core of the highly complex detectors, which form the experiments at the Large Hadron Collider (LHC), the silicon pixel detectors consist of thousands of computer chip-sized sensors organized in compact convoluted surfaces [1, 2]. The layout of those inner detector layers is based on very strict design requirements in terms of material and position which allow for a highly accurate particle track reconstruction. However, ongoing and future upgrade programs to increase the LHC luminosity require for most experiments at the LHC a new inner pixel detector with a significantly increased pixel surface. Thus the request for mass and volume reduction of all detector components and their thermal management becomes even more demanding which requires the use of radiation resistant, lightweight materials of reduced thickness and with physical properties which allow for a maximum transparency with respect to the particles to be detected. This asks for highly effective active detector cooling which is realized in a least intrusive way. Especially in the context of recent upgrade programs performed at the LHC experiments, detector cooling gets particularly important to cope with the increased luminosity of the LHC. An effective thermal management can address the problematic of exposure to higher radiation levels and thus radiation damage and other unwanted temperature dependent effects on the active detector components can be avoided or minimized. In addition the increasing amount of heat which is generated by the new generation of read-out electronics due to higher resolution and read-out rates has to be effectively removed. One of the most promising detector cooling methods is the dissipation of heat by means of forced convective fluid flow in very small pipes or channels. The thermal management of electronics components with small channel cold plates has been attracting researchers from various scientific backgrounds since its first introduction in 1981 [3]. The benefits of minimizing the size of a heat exchanger by using small hydraulic diameter tubes or channels have been confirmed multiple times in literature for various geometries and refrigerants [3–6]. This approach provides a higher surface area to volume ratio compared to macro-channels and results in higher heat transfer rates and lower equipment size [6]. The application of compact heat exchangers is especially appealing for very confined spaces such as those typical of modern silicon detectors in high energy physics (HEP) experiments, carried out at CERN (Conseil Européen pour la Recherche Nucléaire). One of the peculiarities of the application in HEP experiments is the need for continuous operation in the full temperature range from +15°C to -30°C or even lower. The combination of compact heat exchangers with evaporative cooling has been confirmed to be highly effective for various refrigerants [7]. However, when working at low saturation temperature (T_{sat}) most of the standard refrigerants operate at very low reduced pressure and their performance in small hydraulic diameter pipes greatly deteriorates. Carbon dioxide (CO_2) is a natural refrigerant that presents very different thermo-physical properties with respect to standard refrigeration fluids and for this reason it has been recently selected as the principal choice for the thermal management of the present and next generations of Silicon Pixel Detectors [8]. Furthermore the unique characteristics of CO_2 make it particularly well suited for applications in small diameter channels. Hihara and Dang [9] were among the first to report the effect of increasing heat transfer coefficient with decreasing channel diameter for CO_2 at +15°C T_{sat}. In general, especially favourable evaporation heat transfer characteristics and much lower pressure drops have been confirmed for CO_2 in recent literature [10]. However, the available data on CO_2 boiling in channels of small hydraulic diameter (< 3 mm) are too limited, sparse and often affected by large uncertainties, to allow for the development of reliable predictive models. On the other hand, the thermal management of a silicon detector at the LHC is quite complex [11] and, in order to optimally design and safely operate such highly sensitive particle detectors, some of the unknowns related to CO_2 flow boiling in small channels must be resolved to develop new predictive methods both for the pressure drop and heat transfer coefficient. This raises the need for more accurate, systematic and reliable experimental data on boiling flows of CO_2 in small channels. To extend the existing data base, this work introduces new experimental studies on small diameter carbon dioxide evaporators for optimal silicon pixel detector cooling. For this purpose, a new dedicated experimental setup for detector cooling R&D with mini- and micro-scale CO_2 evaporators has been designed and built at CERN. Due to the immediate relevance for integrated detector cooling design layouts small-scale tubular evaporators in stainless steel and a multi-micro-channel cold plate embedded into Silicon have been characterized for this study. The parametrical results on pressure drop and heat transfer in parallel with flow visualizations will help creating new reliable prediction models, which in the future will guide the design of new small-scale CO_2 evaporators and make long iterative phases of experimental tests redundant.

In order to create a general overview, in chapter 2 the LHC and the accelerator complex at CERN, its motivation and scientific goals are shortly introduced, while in chapter 3 in particular the Silicon Pixel Detector is explained in more detail and why its efficient thermal management is so crucial to a successful experimental operation. In chapter 4 the detector cooling strategies used so far shall highlight the necessity for a highly integrated cooling solution. Chapter 5 includes a parenthesis on the basic concepts on evaporative cooling and the advantages of using CO_2 as refrigerant. The existing literature on flow boiling in small channels in general and in particular for CO_2 is reviewed in chapter 6 and focuses on the persisting limitations found so far on the subject. Based on those limitations the motivation for the new experimental setup and its description is given in chapter 7, while in chapter 8 the modalities for the flow boiling tests carried out for this study are described. In chapter 9 the new experimental data are presented, discussed and compared to existing prediction methods, with particular emphasis on the effects of the saturation temperature. Chapter 10 creates an overall framework, where the results and findings gathered for small-scale CO_2 evaporators are related to an immediate application in HEP experiments. Finally chapter 11 highlights the main conclusions driven by the present study and a short outlook on future work is given in chapter 12.

CHAPTER 2

The Large Hadron Collider and its experiments

Aiming at a deeper understanding of the structure of matter, particle physicists search for the most fundamental building blocks of the universe. The categorization of elementary particles discovered so far and the forces acting between these particles are summarized in the Standard Model of particle physics. This model describes matter in terms of quarks and leptons which interact by means of three fundamental forces: the electromagnetic, the strong and the weak force, where the fourth force which exists in nature, gravity, is not included so far. To advance our understanding of the properties of the particles and forces in the Standard Model of particle physics and to possibly find new - predicted or unpredicted - particles or phenomena, large accelerators are used to accelerate and collide particles at high center-of-mass energies. The LHC is the largest ring collider existing so far which is located at CERN near Geneva in Switzerland. The LHC is a proton-proton collider, capable of colliding proton beams with a center-of-mass energy of 14 TeV and a luminosity of $10^{34}\ \mathrm{cm}^{-2}\mathrm{s}^{-1}$. To produce beams of such high energy, the CERN accelerator complex can fall back on its own history as laboratory for particle physics where older and smaller accelerator rings are used as pre-accelerators for the main LHC collider ring. As shown in Figure 2.1, a chain of four acceleration stages is used before the protons are injected into the LHC and brought to collision. The collisions give rise to rare and highly energetic processes, which could not be accessed before. This enables scientists to experimentally study matter on its most fundamental level and its modalities before it cooled down after the Big Bang. Therefore several large and highly complex experiments have been built along the accelerator circumference in order to observe these collisions. At four main intersection points, there are four detectors installed: ATLAS[1], CMS[2], ALICE[3] and LHCb[4]. ATLAS and CMS are general purpose detectors designed to study the particle interactions according to the Standard Model and beyond. ALICE is designed to study in particular heavy ion collisions. Those are produced during the other alternative working mode of the LHC, where instead of protons lead ions are brought to collision. The LHCb detector is dedicated to the physics of heavy hadrons, in particular b-hadrons ("b physics").

---

[1] A Toroidal LHC ApparatuS

[2] Compact Muon Solenoid

[3] A Large Ion Collider Experiment

[4] Large Hadron Collider beauty

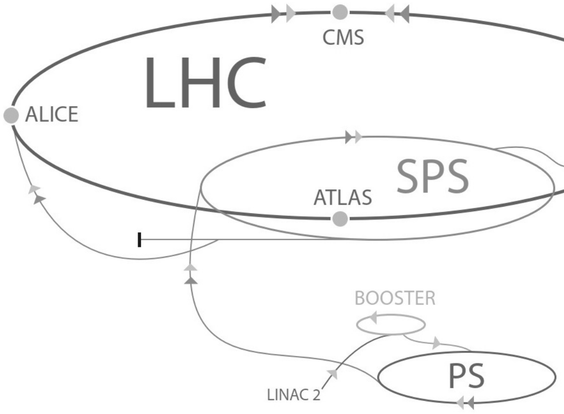

Figure 2.1: The accelerator complex at CERN.

As an example the composition and functionality of the ATLAS detector will be introduced here shortly: Figure 2.2 shows the general complex layout of the ATLAS detector [12] which is conceptualized as a shell-structure housing several specialized sub-detector systems. In order to capture as many particles as possible created by the collisions, all sub-detector systems have a cylindrical layout concentric to the beam pipe ("barrels") with additional discs at each end, so-called "end-caps", to allow for a large pseudorapidity coverage, where the pseudorapidity, η, is defined as η := -tan(Θ/2), with Θ as the angle to the beam direction. At the very center of the detector the proton beams circulating inside the LHC beam pipe are brought to collision (interaction point) and a variety of different particles with a wide range of energies are produced. In order to identify and measure the different particles the ATLAS detector is composed of four sub-detectors: the Inner Detector, the Calorimeter, the Muon Spectrometer and the Magnet System, each of which is designed to observe specific types of particles

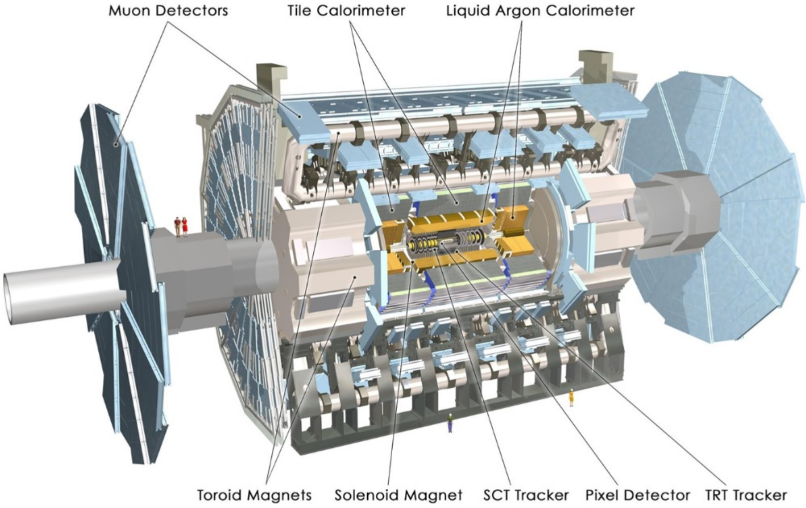

Figure 2.2: General layout of the ATLAS detector [12].

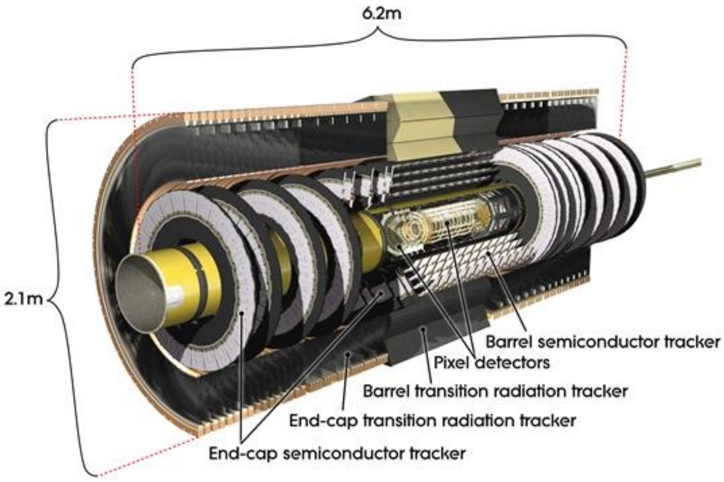

Figure 2.3: The ATLAS Inner Detector [13].

and is again made of multiple different layers. The Inner Detector measures the direction, momentum, and charge of electrically-charged particles produced in each proton-proton collision and consists of three different sensor systems which are all immersed in a magnetic field parallel to the beam axis. Moving radially outwards the main components of the Inner Detector are the Pixel Detector, the Semiconductor Tracker (SCT) and the Transition Radiation Tracker (TRT). Figure 2.3 shows the overall structure of the ATLAS Inner Detector with its three sensor systems and the different detector layouts for the barrels and end-caps, respectively [13]. Focusing on the innermost layer of the Inner Detector, in Figure 2.4 a schematic view of the initial ATLAS Pixel Detector consisting of barrel and end-cap layers is depicted [13]. The active part of the pixel system is yet again organized in three barrel layers (layer 0, so-called b-layer, layer 1 and layer 2) and two identical end-cap regions, each with three disk layers. This innermost Silicon Semiconductor Pixel Detector system will be discussed in more detail in the following chapter.

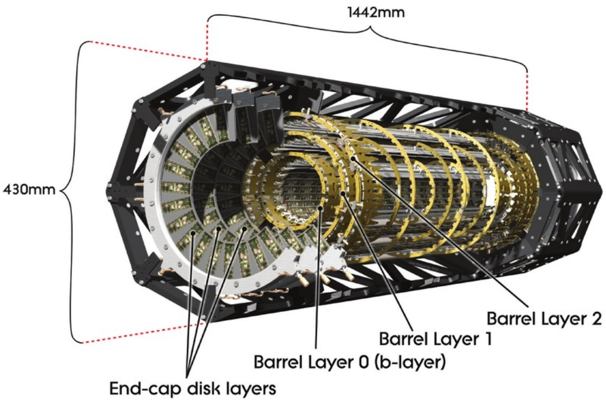

Figure 2.4: The initial ATLAS Pixel Detector [13].

The Calorimeters measure the energy a particle loses as it passes through the detector. As shown in Figure 2.2 there is the Liquid Argon Calorimeter and the Tile (Hadronic) Calorimeter, both composed of high-density material to allow for a full absorption of the particles created in a collision, forcing them to deposit all of their energy within the detector. The muon spectrometer identifies and measures the momenta of muons which usually pass through the Inner Detector and Calorimeter undetected. The magnet system bends particle tracks inside the detector systems, making it possible to measure their momenta. The main sections of the magnet system are a Central Solenoid Magnet, which produces a two Tesla magnetic field surrounding the Inner Detector and an outer toroidal magnetic field situated outside the calorimeters and within the muon system.

During the so-called LHC Run 1 which started in 2009 and successfully finished in February 2013, the experimental discovery of the Higgs boson was the major highlight for the physics community and one of the most important goals of the LHC. Afterwards, probing the Higgs mechanism remained an important part of the physics program at CERN. However despite the successful formulation of the Standard Model describing all observable matter and the forces acting on it, it fails to describe all phenomena found so far. Some - such as discrepancies in the gravitational dynamics of galaxies - are ascribed to non-observable matter, or dark matter, which is not included in the Standard Model. Several extensions of the Standard Model have been formulated and new phenomena according to the theoretical predictions could be observed in the TeV-range accessible to the LHC. The probability of the Higgs production or of new physics processes is much smaller than for well-measured Standard Model processes and a large amount of data has to be collected by the experiments to uncover new physics phenomena. This requires an increase of the LHC luminosity, runs at the LHCs final centre-of-mass energy and an improvement of the overall detector performance. Thus enlarging the probed mass range which will be beneficial for the discovery of potential new physics. In order to achieve this goal a three-staged upgrade program of the LHC was already scheduled before its first collisions were announced. To implement the three scheduled evolutionary stages of the machine performance, three long shutdown (LS) periods characterize the operation of the LHC from its first start-up until 2030 and is in general called the High Luminosity LHC Project.

Phase-0 started with a first long shutdown, taking place from February 2013 to July 2014 and was used to strengthen the magnets of the LHC, the interconnections between them and for the implementation of other various improvements. This was needed to finally run the LHC at its design energy and luminosity (7 TeV per beam, $1 \times 10^{34}\ \mathrm{cm}^{-2}\mathrm{s}^{-1}$). During Phase-0 run (run 2) about 40 fb^{-1} of data were collected.

Phase-1 started with a second long shutdown from 2018 to 2020 with the goal to further increase the LHC luminosity to 2-3 $\times\ 10^{34}\ \mathrm{cm}^{-2}\mathrm{s}^{-1}$. This is achieved with a new injector system to the Proton Synchrotron Booster (PSB) replacing the LINAC2 (see Figure 2.1) and an upgrade of the LHC collimation system can increase the future luminosity further by a reduced cross-sectional area. During the Phase-1 run (run 3) the LHC will deliver about 400 fb^{-1} of proton-proton collision data.

Phase-2 will start with a third long shutdown from 2022 on-wards and at the end of which the final luminosity of 5-7 $\times\ 10^{34}\ \mathrm{cm}^{-2}\mathrm{s}^{-1}$ is expected to be reached. The necessary changes to the LHC include the whole accelerator chain, from a renewed injector chain to new final focusing quadrupole magnets. During the Phase-2 run (run 4) the LHC is expected to deliver about 3000 fb^{-1} of proton-proton collision data.

In order to be able to cope with the increasingly higher luminosity and the foreseen long operation time under high radiation levels the major LHC experiments and the involved collaborations have to upgrade their detectors in parallel. From Phase-0 on-wards, for most experiments the inner tracking systems will be enhanced or replaced completely until about 2026 due to the end of their life-time. The upgrade of the inner tracker is fundamental to improve its resolution and readout rate capabilities which are necessary for the increased luminosity levels of the LHC. For the example of the ATLAS Pixel Detector in addition to a revision of the current Pixel Detector, a fourth Insertable B-Layer (IBL) was installed during LS1. However a complete redesign of the Pixel Detector is necessary for the Phase-2 run.

CHAPTER 3

Silicon Semiconductor Pixel Detector

The Pixel Detector is the innermost detector layer of all the experiments at CERN located very close to the proton-proton interaction point. It is used for the precision tracking of charged particles and for the reconstruction of the point in space where the proton-proton collision took place ("vertex") - hence also often called vertex detector. The Silicon Detector or Silicon Tracker is often composed of two types of technologies: Silicon Pixel Detectors and Silicon Strip Detectors, both arranged in numerous individual modules. Each Silicon Pixel Detector module contains an array of many pixel sensors of which each consists of a pn-diode. Each pixel is connected to a readout chain by means of inter-chip connection technologies (bump-bonding). The Silicon Strip Detector is an array of silicon strips read-out by a corresponding array of ASICSs in the module's periphery. Figure 3.1(a) shows an individual barrel of the ATLAS Silicon Pixel Detector, whilst Figure 3.1(b) gives an example of the highly complex organization of the Silicon Strip Detector modules within the CMS experiment (barrel without end-caps).

The Silicon Pixel Detector module provides a very precise measurement of the particle's point of impact on the module, whilst its disadvantages are larger mass, larger costs and larger power dissipation per sensitive area compared to the Silicon Strip Detector [11]. Therefore the Silicon Pixel Detector is only installed in the innermost layer of the Silicon Tracker where precision is most crucial. Thus the physical location of the Silicon Pixel Detector in the entire experiment leads to very stringent design requirements compared to all other sub-detector systems. All material used for the Pixel Detector influences the performance of the subsequent detector layers, such as - for the example of the ATLAS experiment - the Semiconductor Tracker, the Transition Radiation Tracker, the calorimeters or the muon spectrometer described above. Like those, the individual Silicon Pixel Detector modules are arranged as coaxial barrels and as end-caps to form a near-complete detector surface to be crossed by any incident particle as shown in Figure 2.4.

The design layout of tracking detectors requires sensitive and insensitive material with respect to the particles to be detected, whilst the particles ideally deposit only a small amount of their energy in both types of material. The energy transfer from the particle to the sensitive tracker material differs between different particles. Since charged particles are to be detected, the detection principle of the Pixel Detector is ionization (and excitation).

Pixel Detectors are often designed as a two-layered hybrid approach with particle detection in a first silicon semiconductor sensor layer (sensitive material) and signal processing in a second layer, the read-out chip (insensitive material). Figure 3.2 shows a schematic of the Hybrid-Pixel Detector. Due to

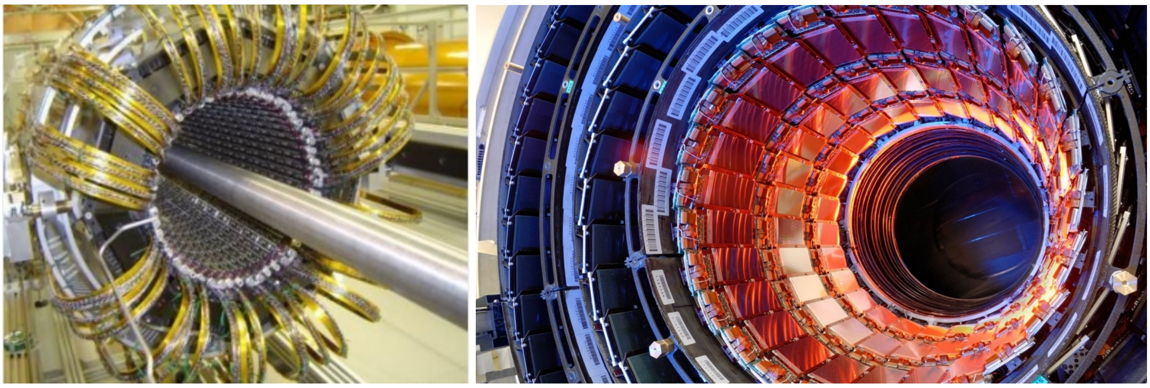
(a)

(b)

Figure 3.1: Structure of the Silicon Tracker: a) Silicon Pixel Detector barrel at ATLAS; b) Silicon Strip Detector barrel at CMS.

small segmentation and very low mass specifications, the structural integration of the Pixel Detectors is very complex. Thus there are three main components forming one Pixel Detector entity: (i) the sensor, (ii) the front-end chip and (iii) the structural integration (including services) and thermal management. The goals of any particle tracking experiment at CERN could not be achieved without a strict interlock of those three components, each fulfilling crucial tasks: (i) signal generation, (ii) signal processing, (iii) assurance of signal position in a 3D detector volume (structural integration) and assurance of signal quality (thermal management). This present work concerns mainly the thermal management of Silicon Pixel Detectors. However the signal generation and processing will be introduced here shortly to highlight the necessity for detector cooling.

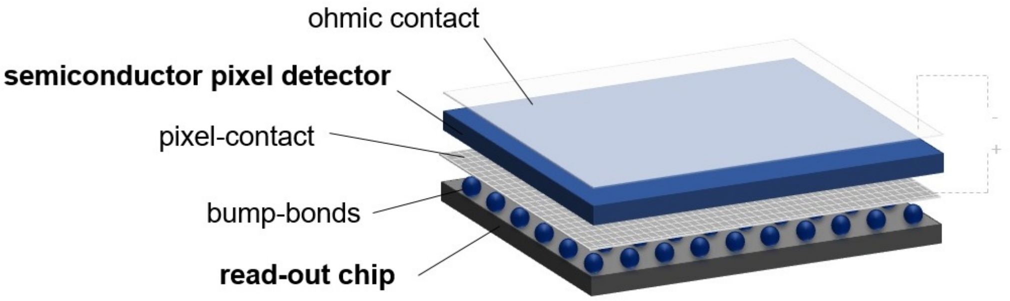

Figure 3.2: Schematic Hybrid-Pixel Detector concept.

3.1 Signal generation and processing

A traversing particle creates charges (electrons and holes) in the Silicon layer by ionization. Since the movement of these positive and negative charges in the crystal induces a signal at the pixel electrode which is used for the particle detection, the immediate recombination of the electrons and holes has to be avoided and a silicon bulk free of charge carriers is needed. This can be achieved by reversely biasing a pn-junction.

The main silicon bulk is here either slightly n- or p-doped (n-type or p-type), where the two opposite surfaces are highly doped with an n+ and p+ -implantation. In the p-doped part free holes are dominant (acceptors) and in the n-doped part electrons exist in excess (donors). Due to impurities semiconductors always contain both acceptors and donors, and their concentrations N_A and N_D are replaced with the effective doping concentration $N_{eff} = N_D$-N_A, which is positive for n-type material and negative for p-type material. Connecting the p- and n-type parts leads to a diffusion of charge carriers due to the charge carrier density gradient across the junction. Electrons move from the n-side to the p-side and vice versa and recombine. An intrinsic zone without free charge carriers is formed (depletion zone) and it grows until an equilibrium is reached. The movement of the electron-hole pair, created in this zone induces a detectable current at the pixel electrode and the electric field corresponds to the built-in potential U_{bi}. This intrinsic behaviour of the pn-diode can be actively compensated by applying an external electric field with U_{bias}. The negative bias voltage V_{bias} is applied to the p-side, whilst the n-side is kept on ground. The width of the depletion zone can thus be increased and grows to the other side allowing for more electron-hole pairs to contribute to the signal. Figure 3.3 shows the two possible configurations for n- and p-type sensors, reversely biased with growing depletion zone (a and c) and during particle detection (b and d) [14]. As shown in Figure 3.3 (b and d), the holes are

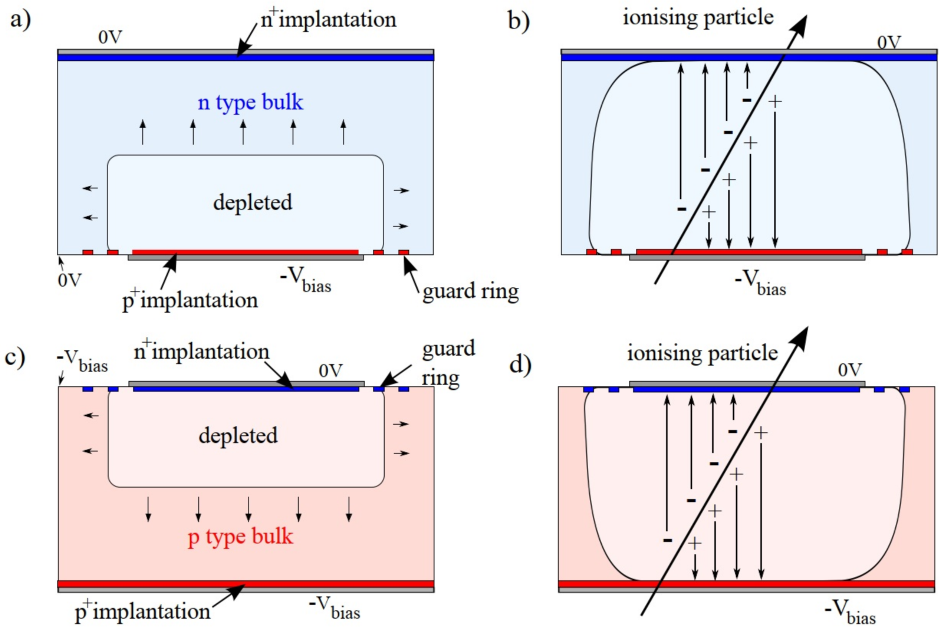

Figure 3.3: Cross section through a reversely biased silicon sensor for an n-type bulk (a and b) and a p-type bulk (c and d). Reproduced from [14].

drifting to the p-side which is on negative bias voltage, whereas the electrons are drifting to the n-side which is grounded. This way the charge carrier move through the silicon by means of drift instead of diffusion. This results in a faster signal at the electrodes. The voltage at which the sensor bulk is fully depleted is called depletion voltage V$_{dep}$ and depends mainly on the bulk thickness d and the bulk resistivity ρ. It is [15]

$$V_{dep} = \frac{d^2}{2\rho \cdot \mu_e \cdot \varepsilon_{Si} \cdot \varepsilon_0}, \tag{3.1}$$

where μ_e is the electron mobility, ε_{Si} the dielectric constant of silicon and ε_0 the permittivity constant. A charge generated inside the depleted zone will be detected, however a charge generated in the 'neutral bulk' will recombine. Thus it is necessary to operate the sensor fully-depleted of free charge carriers where the electric field reaches throughout the complete device and thus the complete sensor volume is sensitive (active). Figure 3.4 shows the characteristics of a reverse biased pn-junction in under-depletion.

The signal current is proportional to the amount of drifting charges and their velocity. This signal is processed further by the electronics in the pixel cell. The original pixel front end chips of ATLAS (FE-I3), CMS and ALICE are all fabricated in CMOS technology. Here the signal is amplified, discriminated and digitized and is then transmitted to the detector periphery.

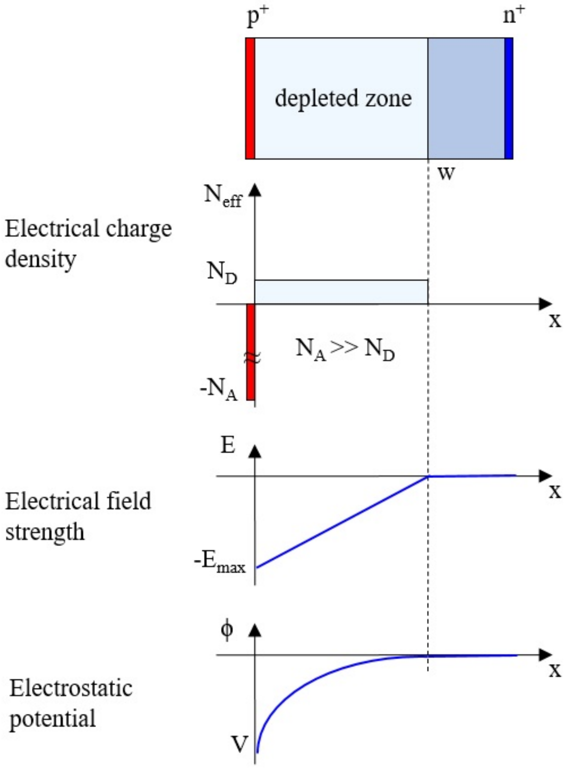

Figure 3.4: Characteristics of a reversely biased pn-junction: space charge, electric field and potential distributions.

Figure 3.5 shows a complete ATLAS Pixel Detector hybrid module with its various elements: the sensor tile; sixteen front end electronics chips (FE) connected to the sensor by means of bump-bonding; a flexible printed circuit (flex-hybrid) to route signals and power; a module control chip (MCC) situated on the flex-hybrid; another flexible foil - necessary for barrel modules - a so-called pigtail, that provides the connection to electrical services via micro-cable [13]. The thermal management tile is depicted in the cross-section view only and is not fully shown. The overall integration of multiple Pixel Detector modules into their final layout within one half-shell of the initial ATLAS Pixel Detector b-layer is shown in Figure 3.6 [16], where the fixation and integration of multiple modules parallel to the beam pipe is organized in so-called "staves".
More detailed information on the pixel module, the choice of sensor material, the involved working principles and the signal processing of the front-end electronics may be found e.g. in [13].
Note that the described Silicon Pixel sensors are planar silicon sensors and that 3D silicon sensors are also available, whilst the general working principle is very similar. Moreover for the new ATLAS insertable B-layer, both a new silicon pixel sensor [17] and a new read-out chip (FE-I4) [18] had to be developed to cope with the expected hit occupancies and radiation doses [19].

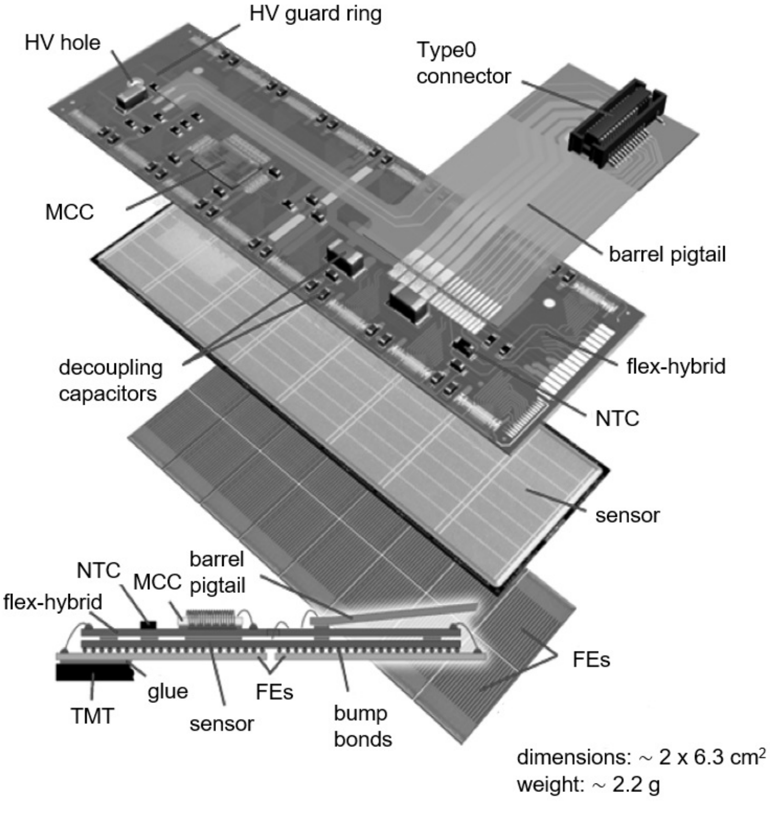

Figure 3.5: The elements of an ATLAS pixel barrel module: thermal management tile (TMT); front end electronics chips (FE); module control chip (MCC); Negative Temperature Coefficient thermistor (NTC). Adapted from [13].

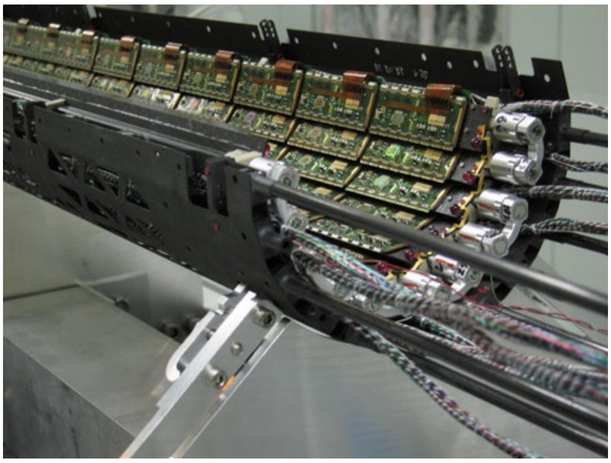

Figure 3.6: Pixel barrel modules in b-layer half-shell of the ATLAS Pixel Detector [16].

3.2 Assurance of signal quality

In the case of the Silicon Pixel Detector the signal quality may suffer from internally and externally caused processes changing the properties of sensor and read-out chip, which have to be avoided or antagonized.

3.2.1 Deterioration of the signal

Due to internal processes the sensor properties are affected by leakage current. The aforementioned depletion zone is normally free of charge carriers and acts as an insulator. In reversely biased silicon diodes, some current flows through the depletion region. This current is caused by thermally created electron-hole pairs within the silicon bulk and is proportional to the temperature dependent intrinsic density $n_i(T)$ of these charge carriers and to the bulk volume V. For a given bias voltage the leakage current is given by [20]

$$I_{leak} = \frac{e\, n_i(T)\, V}{2\tau}, \tag{3.2}$$

where τ is the life-time of the charge carriers with charge e. The density of the electrons and holes $n_i(T)$ is calculated using the Fermi-Dirac statistics estimating their occupation probability which results in the proportionality [21]

$$I_{leak} \propto T^{\frac{3}{2}} \cdot exp\left(-\frac{E_G}{2k_B T}\right), \tag{3.3}$$

where E_G is the size of the semiconductor band gap and k_B is the Boltzmann constant. Thus the effect of leakage current is highly temperature dependent and a temperature increase of the silicon bulk of 7°C doubles the leakage current. The leakage current is negligible for un-irradiated silicon sensors. However it increases for radiated sensors and causes a significant shot noise (distortion of the signal at the input of the amplifier) which needs to be avoided. Thus the most important externally imposed damage on the Silicon Pixel Detector is introduced: Radiation damage.

Both, sensor and front end chip are exposed to very high radiation levels and thus experience various damaging processes. This issue became especially important for the experiments at the LHC due to the so far unprecedented high doses received by the tracking systems of HEP experiments. Traversing high energy particles lose energy in the detector by the above described ionization processes but also by non-ionizing energy loss (NIEL) processes. Since the radiation damage differs for different particles, the damage has to be scaled to a standard irradiation in order to compare the impact of different particles. Usually the radiation damage is scaled to the damage which is caused by a fluence of 1 MeV neutrons. Thus the equivalent fluence is

$$\Phi_{eq} = \kappa \cdot \Phi_{irr}, \tag{3.4}$$

where κ is the damage factor which depends on the incident particle (type and energy) and the irradiated material. Φ_{eq} is expressed in $10^{12}\,\mathrm{cm}^{-2}$. In the case of charged particles or ions the energy transfer is mediated by the Coulomb interaction, in the case of neutrons by nuclear forces. For the sensor those processes which lead to non-reversible lattice damage in the silicon bulk have the largest impact, however there are also surface damages. Is the energy of an incident particle high enough, energy can be transferred to a silicon atom causing the displacement of this lattice atom resulting in either a point defect or more extensive cluster defects. Point defects are impurities (non-silicon atoms), vacancies in the crystal lattice (unoccupied lattice sites) or interstitial atoms (irregular lattice sites). Cluster damages are caused by recoiling atoms causing more extensive damage to the crystal lattice. Figure 3.7 shows some possible defects in a silicon crystal. The mentioned defects mainly

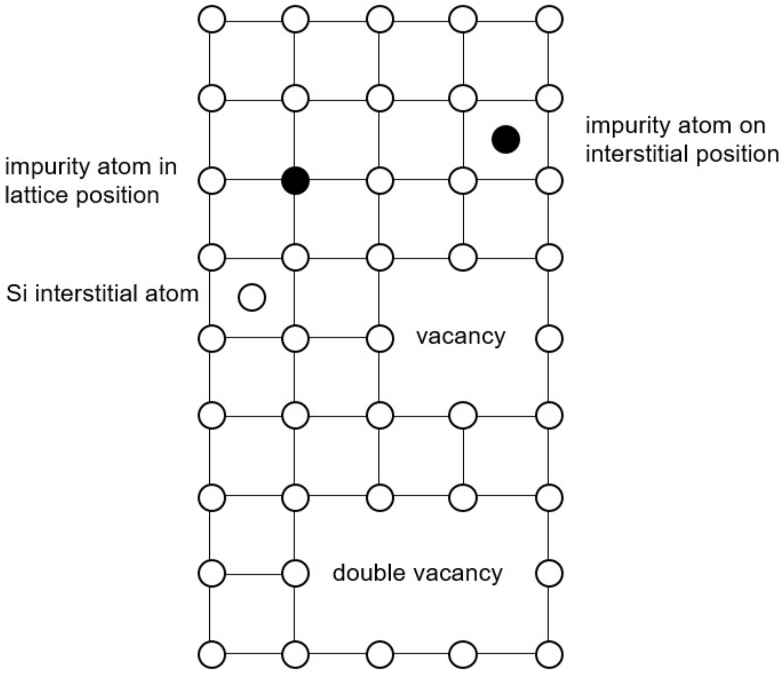

Figure 3.7: Schematic of defects in a silicon crystal lattice using a two-dimensional representation.

effect the operation of Silicon detectors in three different ways: (i) the effective doping concentration of the sensor changes which results in a change of the voltage required to operate the sensor; (ii) the creation of recombination/generation centres increases the amount of thermally generated charge carriers which increases the leakage current as described above; (iii) trapping centres may be created by the displacement of silicon atoms which trap drifting electrons. Those can no longer contribute to the signal resulting in a deterioration of the charge collection efficiency of the sensor.

The measured depletion voltage and the absolute effective doping concentration $|N_{eff}|$ as a function of the 1 MeV equivalent fluence is shown in Figure 3.8 for an initially n-type sensor [22]. The voltage needed for full depletion after large radiation doses may exceed those required for the maintenance of safety standards and it might be necessary to operate the sensor under-depleted, which results in a deterioration of the final signal. After a fluence of 2 to $5 \times 10^{12}\,\mathrm{cm}^{-2}$ for an initially n-type sensors type-inversion will occur. The change in effective doping concentration also results in a change of sensor type (n-doped type to effective p-doped type). At lower fluences N_{eff} is reduced due to the removal of donors and at the same time acceptor like states are generated leading to an inversion of the space charge from positive to negative and an increase of $|N_{eff}|$. This inversion influences the electrical behaviour of the sensor and the depletion zone now grows into the opposite direction.

The increase in leakage current after irradiation I^{irr}_{leak} is proportional to the depleted volume of the silicon bulk dA and the particle fluence Φ_{eq}. The leakage current after irradiation is [21]

$$I^{irr}_{leak} = I^{unirr}_{leak} + \alpha_{Si}\Phi_{eq}dA. \tag{3.5}$$

The proportionality constant α_{Si} was measured for silicon [22] and is in itself temperature dependent. I^{irr}_{leak} may reach several mA and in combination with bias voltages of several 100 V after irradiation causes a significant additional heat load created by the sensor. If this heat load is not dissipated

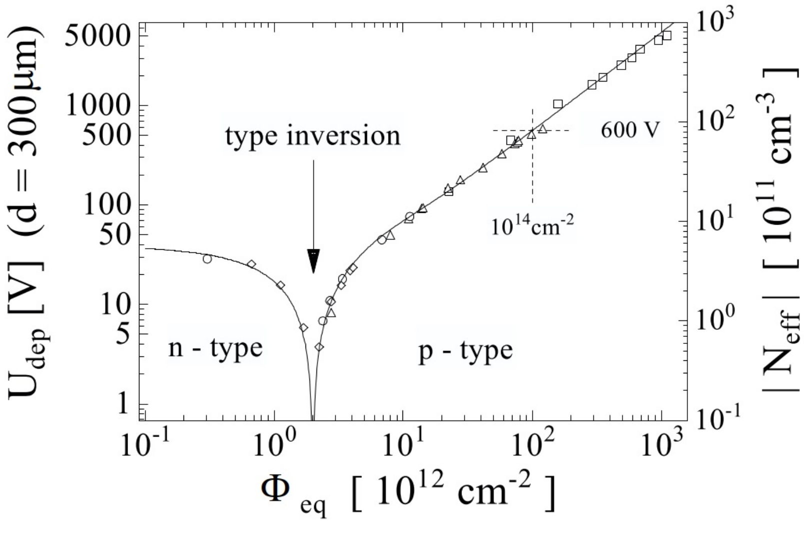

Figure 3.8: The measured depletion voltage and the effective doping concentration as a function of the 1 MeV equivalent fluence [22].

efficiently the exponential dependency of I_{leak} as given in equation 3.3 will cause an avalanche effect which is called thermal runaway: a rise in temperature induces an increase in leakage current, which again leads to a temperature increase etc. Hence efficient detector cooling must be provided to limit the impact of radiation damage.

All radiation damage caused by NIEL effects are subject to temperature dependent annealing processes. This changes the effective doping concentration, resulting in ΔN_{eff} which can be split up into three components [23]

$$\Delta N_{eff}(\Phi_{eq}, t(T_a)) = N_a(\Phi_{eq}, t(T_a)) + N_c(\Phi_{eq}) + N_y(\Phi_{eq}, t(T_a)), \tag{3.6}$$

where the term t(T_a) takes into account that the mobility of defects within the silicon bulk increases with temperature and thus the annealing time depends on the temperature. N_a is the short time annealing component which decreases with time, N_c is a stable damage which does not depend on the time but only on the fluence and N_y describes a long term annealing component. Combining the behaviour of all three contributions as a function of annealing time is reproduced in Figure 3.9 [23]. Short term annealing increases the effective doping concentration. In certain detector materials (type-inverted detectors) this leads to a lower depletion voltage and consequently better detector properties. Reverse annealing counteracts the beneficial short term annealing and leads to an increase in depletion voltage in those materials. In general interim warm-ups accelerate the beneficial annealing, however to limit the reverse annealing effects the detector should be kept as cold as possible and the warm-up periods have to be limited to the minimum in the annealing curve. The stable damage cannot be influenced with temperature control but only by the choice of detector material [24]. When using n-in-p silicon reverse annealing is not an issue and warm-ups are beneficial to the sensor properties. Since the doping densities in the active devices of the read-out chip are much higher compared to the sensor layer, the CMOS layer is much less sensitive to the described NIEL effects which change the effective doping concentration. Compared to the sensor the front end chip mainly suffers from the ionizing radiation. Here the radiation dose is the major concern not the fluence. So-called surface damage can occur close to the SiO_2-Si surface [25] and damage the analog part of the read-out chip.

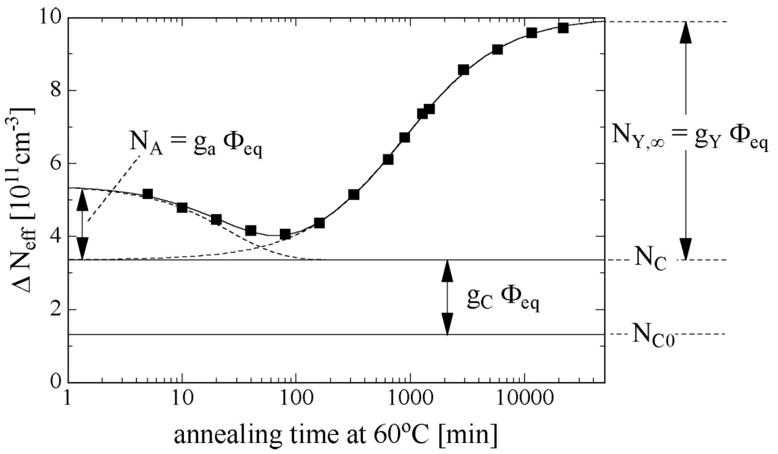

Figure 3.9: Annealing behaviour of the radiation-induced change in the effective doping concentration ΔN_{eff} at a temperature of 60°C [23].

Furthermore positive charges may be created in the SiO_2 which leads to transistor threshold shifts and changes in the transistor characteristics. The generation of leakage currents under the field oxide creates parasitic unwanted transistors. The digital parts of the front end chip also suffer from radiation. Just to name the most important, bit errors, so called "single event upsets" (SEU), have to be considered which can lead to wrong information stored or transmitted by the chip. For more information on this topic please see e.g. [23].

The above described phenomena lead to a deterioration of the signal magnitude and/or time-resolution and can be partially averted with sufficient detector cooling. Finally a deterioration of the signal position in space occurs due to multiple scattering of the particle with the sensitive and insensitive detector material prior to detection. Whilst traversing a medium a charged particle is scattered at small angles due to interactions with the Coulomb field of the materials nuclei. Each scattering center adds a small deviation to the trajectory of the incoming particle. The total random deflection of the particle trajectory reduces the accuracy of the measured track position and thus degrades the tracker resolution. The angular dispersion Θ_0 upon exiting the material may be calculated with [26, 27]

$$\Theta_0 = \frac{13.6}{\beta\, c\, p}\, z \sqrt{\frac{x}{X_0}} \left[1 + 0.038\, ln \frac{x}{X_0}\right], \tag{3.7}$$

where p, βc and z are the momentum, velocity and charge number of the particle. X_0 is the so-called radiation length and is defined as the mean distance over which the energy of a high-energy electron is reduced by 1/e due to Bremsstrahlung. X_0 may be approximated as [28]

$$X_0 = \frac{1}{\rho} \frac{716.4 \cdot A}{Z(Z+1)\, ln \frac{287}{\sqrt{Z}}}, \tag{3.8}$$

where ρ is the density, Z the the atomic number and A the mass number of the material. Thus this parameter is material dependent and the larger X_0 the lower is the disturbance imposed onto the particles. Table 3.1 compares several materials and their X_0 values [29]. x/X_0 is the thickness of the scattering medium in radiation lengths. It is used to quantify the detector mass, also referred to as material budget. For the operation of large scale Silicon Tracker detectors many different auxiliary components and their materials have to be considered. Components with high material budget are particularly susceptible to multiple scattering and may cause large errors in the track reconstruction. Figure 3.10 shows the often cited material contributions for the example of the ATLAS Inner Detector in units of X_0 traversed by a particle as a function of the pseudorapidity η [30].

Material	X_0 [cm]
Cu	1.4
Steel	1.7
Ti	3.6
Al alloy	8.9
Si	9.4
C_6F_{14} at 20°C	19.3
CO_2 at 20°C	35.8

Table 3.1: Radiation length X_0 of materials typically used in HEP detectors [29].

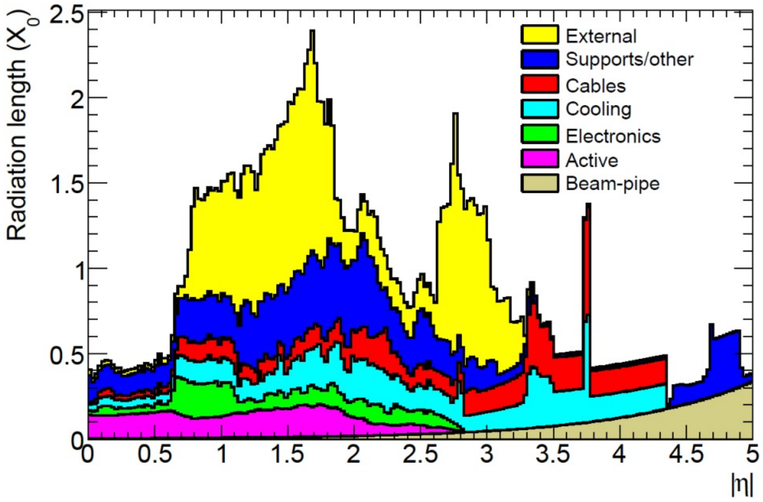

Figure 3.10: Multiple scattering material break-down for the ATLAS inner detector [30].

3.2.2 Counteraction against signal deterioration

The prevention or minimization of the above discussed influences on the signal quality can be achieved with efficient detector cooling and an optimal choice in all used materials.

Optimal materials & structural design

All material used for structural support, servicing and detector cooling is insensitive and design, layout and material have to be conceptualized in the least intrusive way to minimize the interference with the particle track to allow for a more accurate reconstruction of the latter. This translates to a material budget equivalent in terms of thickness to less than 1% of the radiation length of the material [31]. On the other hand those structures have to be very stiff and durable to guarantee a high precision position measurement. The detector and thus the support structure has to be stable within a few microns. Since the detector is installed at room temperature however operated at -30°C or even lower, materials with small coefficients of thermal expansion (CTE) are required. The mismatch of CTE between two component interfaces shall be minimized to avoid distortions and stresses within the detector. Obviously all solid and liquid materials have to be radiation hard, including glues, where necessary. In some cases the structural components also have to fulfill a secondary role as heat conduction path, where materials with high thermal conductivity are required. All those material requirements are often difficult to meet at the same time and a compromise has to be met in many cases, where maintenance and installation issues also have to be taken into account. To sum up for application in high energy physics detectors, stiff, mechanically stable (low CTE), lightweight materials with high X_0 should be used which consume as little space as possible.

Detector cooling

Detector cooling fulfills two main tasks: (I) extending the lifetime and reliability of the sensor and (II) the dissipation of heat which is produced in the front-end chip. (I) The above mentioned reverse annealing in the sensor material can be slowed down by cooling the detector below 0°C and thus limiting the needed depletion voltage of the sensor. The time constant for reverse annealing at -10°C is about 500 years, whereas only 500 days at +20°C [32]. Furthermore the leakage current can be kept low by cooling the sensor and thus avoiding thermal instability of the sensor entity and excessive noise. (II) The heat generated in the front-end electronics has to be dissipated in an efficient way. This heat load may increase for irradiated sensors due to the increasing leakage current in the sensor, which requires a higher power consumption and hence more extensive cooling. The typical surface power density of a single Pixel Detector is in the order of $1\ \mathrm{W/cm^2}$. However when all modules are considered in a 3D Pixel Detector volume this might add up to $100\ \mathrm{W/dm^3}$ [11] - similar to high power computing chip applications. For a given surface power density or quantity of heat to be removed, the temperature difference between heat source and heat sink should be minimized and a stable and uniform (cold) temperature distribution across the detector module is required at all time. Note that in parallel to the above described Hybrid-Pixel Detectors the development of monolithic Pixel Detectors for HEP experiments is evolving in the meantime. Compared to Hybrid-Pixel Detectors in monolithic Pixel Detectors the sensitive volume and the readout circuitry is combined in one piece of silicon. However this poses no difference to the general requirements for the detector cooling and the structural integration.

Resume Consequently the above-mentioned issues raise the need for very effective detector cooling realized with small material-budget components where mechanical and thermo-physical properties of all components allow for a highly-integrated solution.

CHAPTER 4

Detector cooling strategies

It has to be distinguished between off-detector cooling aspects, which investigates issues related to the cooling plant design and on-detector cooling aspects. On-detector cooling considers the actual thermal management of the detector modules, which shall be discussed in the following paragraphs. In all large scale Silicon Tracker systems the heat from the silicon detector modules is removed by a combination of conduction and forced convection [33]. First the heat from the silicon detector modules is conducted to a local heat sink. Then forced convection is used for further transport of heat to an external heat sink.

4.1 Basic heat transfer and refrigeration theory

The basic mechanisms for conduction and forced convection will be introduced now since these form the fundamentals for the heat sinks studied for detector cooling applications.

4.1.1 Conduction

Conduction is the transfer of heat from one part of a medium into another without significant movement of that substance, e.g. conduction through a solid or a stationary fluid. However, processes on the molecular scale lead to this mode of heat transfer. Higher temperatures are associated with higher molecular velocities and when neighboring molecules collide the more energetic molecules transfer energy to the less energetic molecules. If there is a temperature gradient energy transfer must occur in the direction of decreasing temperature. In solids the conductive heat transfer is due to lattice vibrations. Fourier's law describes the heat flux q_{cond} through solid materials and can be written in its one-dimensional form (perpendicular to a planar material surface) as

$$q_{cond} = -k \, \frac{\Delta T\,(x)}{\Delta x}, \tag{4.1}$$

where k is the thermal conductivity of the material, ΔT the temperature difference across the material and Δx the thickness of the wall. For several material layers (A, B and C), as shown in Figure 4.1, there is

$$q_{cond} = \frac{\Delta T\,(x)}{\frac{\Delta x_A}{k_A} + \frac{\Delta x_B}{k_B} + \frac{\Delta x_C}{k_C}}. \tag{4.2}$$

In HEP experiments the heat flux from the sensor to the local heat sink is a fixed value, with a tendency towards increasing values during the detector lifetime as described above. Whereas the temperature difference between sensor and local heat sink has to be minimized. This can be achieved by minimizing Δx and maximizing k, taking into account the material budget of the multiple material layers of the composite sensor design and its integration into the global support structure.

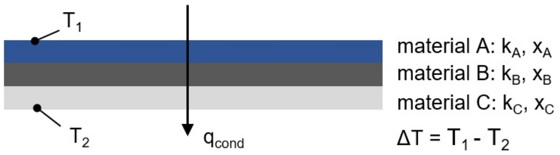

Figure 4.1: Heat conduction through a composite wall.

4.1.2 Convection

Convection describes the heat transfer in a fluid by the mixing of one part of the fluid with another. This heat transfer mode includes two mechanisms. In addition to the molecular motion described for conduction, energy is also transferred by macroscopic motions of the fluid, the bulk fluid motion. This motion can be described with the fact that at any instant large numbers of molecules are moving collectively, causing macroscopic fluid movements. If there is a temperature gradient this motion leads to heat transfer and the total heat transfer is then due to both mechanisms. Convective heat transfer can be further divided into two classes: free (or natural) and forced convection. Natural convection is a result of buoyancy forces which are due to density differences in an otherwise stagnant fluid. Forced convection is due to fluid motions caused by external means i.e. atmospheric (wind) or mechanical motions (pumps or fans). During forced convection the superposition of velocity and thermal boundary layer theory leads to heat transfer from a heated surface into the bulk fluid, while turbulent flow promotes mixing of the bulk fluid and leads to more efficient heat transfer. The heat transfer contribution due to molecular motion is more important at the heated surface where the fluid velocity is low, whilst the contribution due to bulk motion originates from a growing boundary layer with high fluid velocity, where the heat is transported downstream. To quantify the convective heat flux, following expression is known as Newton's law of cooling,

$$q_{conv} = \alpha \cdot (T_{surface} - T_{\infty}) \tag{4.3}$$

where α is the convective heat transfer coefficient and T$_{surface}$ and T $_{\infty}$ are the temperature of the surface and the bulk fluid, respectively. Two concepts of forced convection heat transfer are used for detector cooling: Convective heat transfer promoted by external flow of a gas across a local heat sink and internal flow of a liquid inside a tube brought in contact with the local heat sink. Here the outer tube wall is submitted to the heat flux from the local heat sink and conduction processes lead to a certain inner tube wall temperature T$_{w,i}$. Convection processes due to fluid mixing result in the bulk temperature T_∞ in the center of the tube. To allow for a high heat transfer coefficient the difference between $T_{surface}$ and T_∞ has to be minimized, thus natural convection is rarely relied on for detector cooling since the heat removal capacity is very limited [34]. The conductive and convective heat flux is in this case the same heat flux and will be denoted as q only henceforth. Additionally the fluid velocity influences the heat transfer coefficient. Turbulent mixing at higher velocities leads to large velocity gradients and thus large temperature gradients in the flow increasing the heat transfer coefficient. Often the mass flow rate or the mass flux are used to determine the amount of refrigerant which passes inside a tube. The mass flow rate $\dot{m}$ is the mass of a substance which passes per unit of time in $\mathrm{kg/s}$ (or g/s). The mass flux is the rate of mass flow per unit area in $\mathrm{kg/m^2s}$

$$G = \frac{\dot{m}}{A}, \tag{4.4}$$

where A is the cross-sectional area of the tube.

4.1.3 Refrigeration

The tubes harbouring the fluid flow and the pumps maintaining this fluid flow are in most cases part of a refrigeration cycle, where heat is removed from a system to lower and/or maintain its temperature - often below the ambient temperature. The use of a mechanical refrigeration cycle leads to thermo-dynamical changes in the refrigerant as it alternately absorbs and rejects heat whilst circulating through a refrigerator. In combination with the forced convection processes described above, the removal of unwanted heat may be accomplished by open or closed-loop systems where the refrigerant is either discarded into the environment after one passage at the local heat sink or is recirculated removing and discharging heat in a cyclic fashion. Both system types will be described in more detail in chapter 7 in the context of detector cooling R&D.

4.1.4 Heat transfer efficiency

To quantify the efficiency of conductive and convective heat transfer processes, a performance parameter used within the detector cooling research community is the so-called Thermal Figure of Merit (TFM), which is the inverse of the thermal impedance [34]. The smaller this number, the more efficient the applied cooling method. It is defined as

$$TFM = \frac{\Delta T_{fluid-sensor}}{surface\ power\ density}. \tag{4.5}$$

The TFM decreases with the cross-section of the heat path and materials with high thermal conductivity are mandatory where conduction processes are of importance.

4.2 Detector cooling with gases

As mentioned above, external gas or air flow without additional ducts may be used for detector cooling. Here the detector modules are ventilated by a powerful fan installed outside of the critical detector volume and the gas stream is often channeled by additional profiles to achieve a more localized application, while turbulent flow increases the heat transfer efficiency. The gas flow promotes heat transfer from the local heat sink where the front-end electronics are situated acting in addition to the overall heat conduction within the detector ladder. One of the most recent studies on air-cooling of pixel detector systems was carried out for the STAR experiment at the Relativistic Heavy Ion Collider (RHIC) at the Brookhaven National Laboratory [35]. For this application, the air-flow is channeled inside carbon fiber sector tubes, which in general form the global support structure for the sensor ladders. Figure 4.2 gives a schematic representation of the anticipated air-flow inside the detector volume. This approach is only applicable for systems with low on-detector heat loads since heat capacity and thermal conductivity of gaseous coolants are small. Various gases are, were or will be used in the future for detector cooling such as air, helium (Mu3e Silicon Pixel Tracker [36]), argon/ethane mixtures (CDF Silicon Vertex Detector [37]) or nitrogen (BELLE II pixel detector [38]). No on-detector cooling components are required which interfere with the particle track. This poses a convincing advantage for systems with less stringent thermal requirements and very high physics requirements.

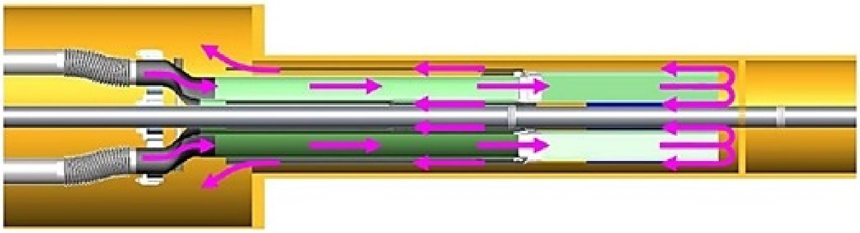

Figure 4.2: Graphical representation of the air flow (arrows in magenta) in the pixel detector cooling system of the STAR experiment [35].

4.3 Detector cooling with liquids

Detector cooling with forced convective flow of liquids is necessary for sub-detector systems with high demands on sensor life time and signal quality. The overall cooling approach is to circulate a certain refrigerant inside pipes or channels brought into close contact with the detector module itself or the provided local heat sink. Thus the on-detector material budget is > 0 and to fulfill the above mentioned strict constraints and requirements, highly efficient detector cooling requires the direct integration of the cooling method into the overall structural design of the detector. There are structural and thermo-mechanical aspects on one side and thermo-fluidic aspects on the other side which have to be taken into account for an optimal on-detector cooling design.

4.3.1 Structural and thermo-mechanical aspects

There are mainly three structural layouts for liquid cooling of silicon tracking detectors.

Metallic pipes and ledges

The first is an outdated and traditional approach using a network of metal pipes which is added rather than integrated into the global detector support structure. This cooling method was the choice for the first LHC vertex detectors due to the given independence for further design interventions

[33]. The main heat sources for power and read-out electronics which are localized in certain areas of the detector modules are brought into contact with the pipes by means of low-mass, metal and ceramic heat spreaders and thermal contacts [33]. Figure 4.3 shows a schematic of this approach for the Silicon Strip Detector (left) and the Silicon Pixel Detector (right). In the case of the Silicon Strip Detector this approach is still acceptable since the read-out electronics dissipating the most amount of heat is compactly located in the periphery of the actual module. However for the Silicon Pixel Detector where sensor and read-out are arranged directly face to face the heat is produced across the entire surface and thus the final temperature distribution across the detector module is quite inhomogeneous. This results in a steep temperature gradient across the module which may lead to thermally caused deflections. Small contact surfaces and long chains of thermal resistances lead to an average temperature difference between sink and source of about 15 to 20°C for power densities between 1 to 2 W/cm^2 [29]. This in result requires very low coolant temperatures to achieve a sufficient cooling [39]. Another disadvantage is the mismatch of CTE between the many different materials involved and the thermally caused displacements have to be considered during operation. To reduce thermal stresses between the components, elastic thermal joints can be introduced which again increase the material budget contribution. The material budget for this method was estimated to 2% X_0 per layer [29], whilst the TFM is $\sim 20\ \text{m}^2\text{K/W}$ [11]. Most commonly macroscopic metal pipes with inner diameters (ID) in the order of 1.5 to 4 mm are being used - depending on the experiment - which contribute largely to the material budget.

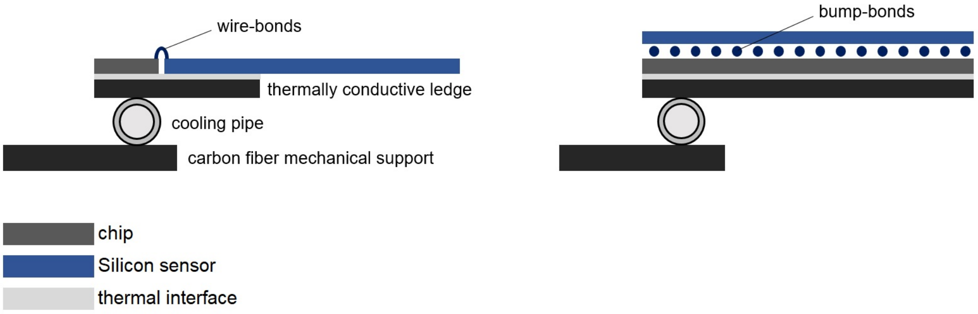

Figure 4.3: Schematic of the local thermal management for vertex detectors with metallic pipes and ledges: Silicon Strip Detector (left), Silicon Pixel Detector (right) (not to scale).

Cold plate with embedded cooling pipe

The second on-detector cooling approach was developed in the context of detector upgrade programs. Preparations for major upgrades for the period 2023-2026 are ongoing at the ATLAS and CMS experiments [40, 41], where a very important improvement will be the implementation of new, larger silicon tracking detectors. The total size of the sensor surface will be larger than 200 m^2 and with its size all other system aspects such as detector cooling become more and more demanding. To fulfill the increasing requirements a more integral thermal management solution was sought after. As a first stage towards this goal a cooling method was developed where a single pipe with a high thermal conductivity is embedded into a light weight cold plate which is directly interfaced with the backside of the detector read-out electronics. Figure 4.4 shows a schematic of this approach, which can improve the temperature difference between sink and source towards lower values compared to the traditional method described above: about 10°C for a power dissipation of 1 $\mathrm{W/cm^2}$ [42]. Furthermore the temperature can be distributed more homogeneously due to the larger contact area. Although never quite avoidable, there is still a temperature gradient across the module due to the centered location of the cooling tube, however the material budget can be reduced by 50% with respect to the old approach, while the TFM decreases to $\sim 12\ \mathrm{m^2K/W}$ [11]. In Figure 4.5 examples of advanced low-mass integrated thermal management solutions are shown: For the ATLAS IBL stave (Figure 4.5(a)) a thin-walled titanium pipe is embedded into highly conductive carbon foam. This foam also forms the core of the support structure achieving a very compact layout of the detector with very low thermal resistances. For the ALICE Inner Tracking System (ITS) upgrade (Figure 4.5(b)) polyimide pipes are wrapped into layers of carbon fleece and carbon paper integrated into an ultra-lightweight carbon fibre space frame resulting in a very good low mass performance. In general this method is pushing the traditional cooling design with macroscopic pipes to a certain limit. Thin-walled metallic and non-metallic tubes with an inner diameter in the order of 1 to 2 mm are being used (e.g. ATLAS IBL: ID 1.7 mm; ALICE ITS: 1 to 1.45 mm ID).

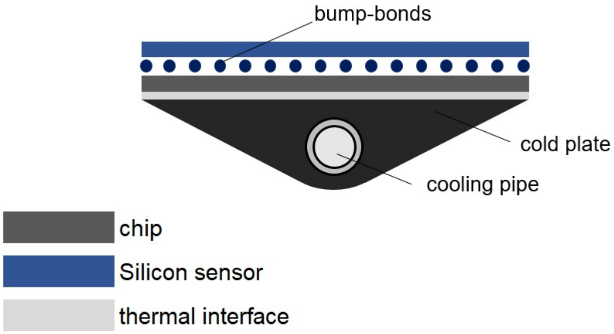

Figure 4.4: Schematic of the local thermal management for vertex detectors with embedded pipes (not to scale).

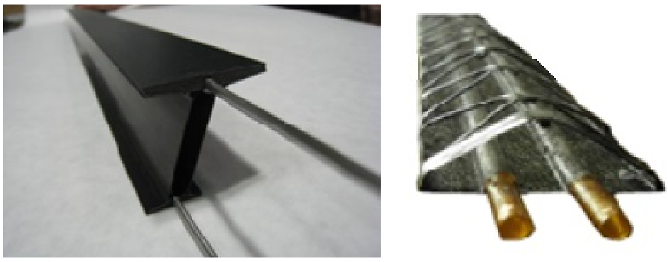

(a) (b)

Figure 4.5: Examples of low-mass integrated thermal management solutions: a) ATLAS IBL stave; b) ALICE ITS stave [33].

Micro-channel cooling

As parallel field of development to the detector cooling concept with macroscopic pipes the use of ducts and channels with a hydraulic diameter in the sub-millimeter range has been proven to be highly efficient. For this third cooling method a refrigerant is circulated within a network of micro-channels embedded into very thin silicon or polyimide substrates, however also other configurations are possible. These cold plates can be integrated into the lightweight support structures of the detectors or can be used themselves as support for the sensors and their electronics [42]. Figure 4.6 shows the schematic cross section of the most compact and efficient detector cooling approach so far developed for the application in HEP experiments. The temperature difference between sink and source can be reduced further to only 5 to 7°C. This is due to several facts: the cold plate can be brought into direct contact with the read-out chip (with only a thin layer of glue in between) and thus thermal resistances can be reduced. Since the "cooling pipes" are distributed across the whole sensor area an unprecedented homogeneous temperature distribution is achieved and the uneven power dissipation of the sensor ranging from 1 to 4 W/cm^2 distributed over the sensor surface can be removed very efficiently. The material budget is reduced to < 0.5 % X_0 per layer, with a contribution of the cooling part of lower than 0.15% X_0 when using silicon substrates [29]. The TFM was estimated to be $\sim 6.5\ \mathrm{m^2K/W}$, which is only a third of the initial value achievable with the traditional cooling approach. Micro-channel cooling was applied at CERN for the first time to thermally manage the pixel detector of the Gigatracker detector of the NA62 experiment [43]. Further upgrade solutions have been studied for the LHCb Vertex Locator (VELO) [44] and ALICE ITS [45] experiments. The micro-channel cold plate for the LHCb VELO upgrade has been manufactured by micro-structuring and bonding techniques directly derived from micro-electro-mechanical systems (MEMS) technologies and withstands internal working pressures of about 70 bar inside channels of 70 x 200 μm^2. For the ALICE ITS [46] upgrade a polyimide substrate has been developed withstanding 10 bar with a channel cross-section of 800 x 300 μm^2. Many different geometries and fluidic circuits are possible to adapt to different detector configurations and makes micro-channel cooling a rather versatile approach. Figure 4.7 depicts the examples of the LCHb (Figure 4.7(a)) and ALICE upgrades (Figure 4.7(b)).

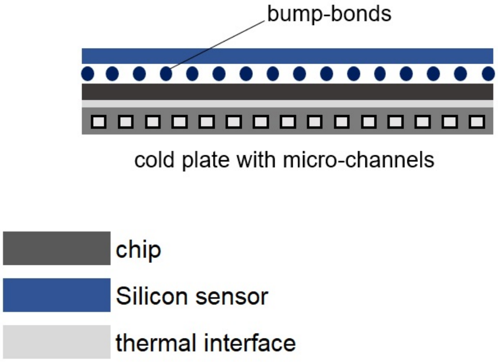

Figure 4.6: Micro-channels embedded into a substrate, e.g. silicon or polyimide (not to scale).

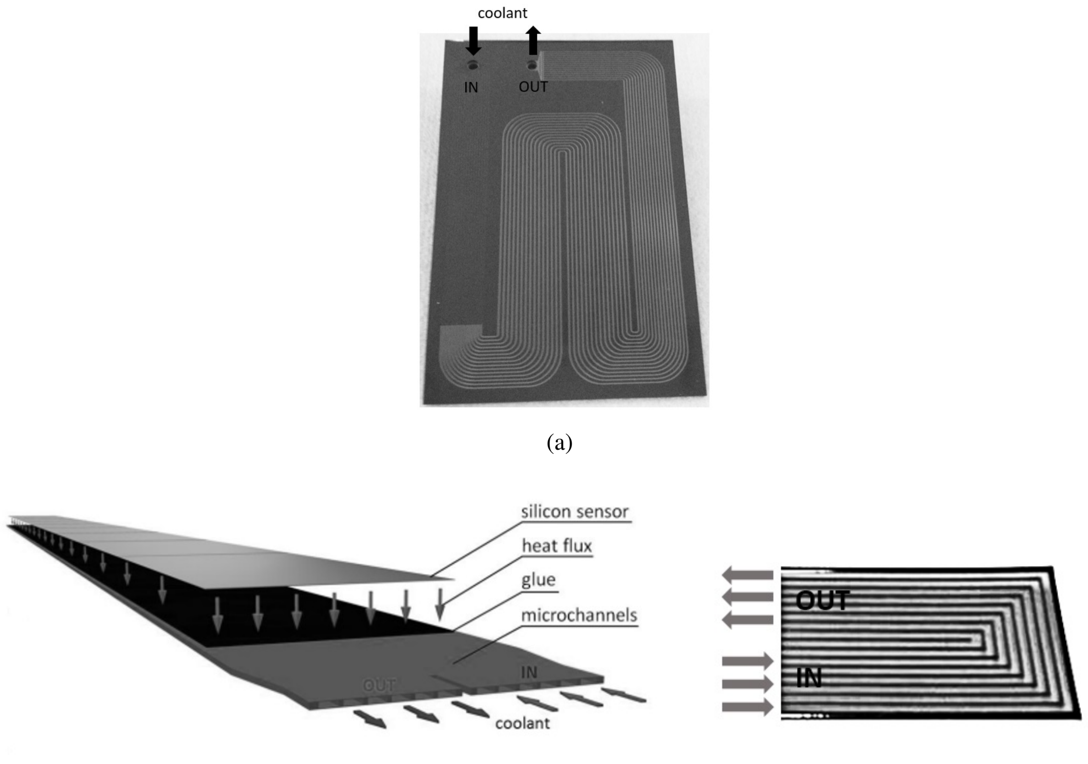

(a)

(b)

Figure 4.7: Micro-channel cooling: a) First cooling substrate prototype manufactured with silicon and Pyrex for the LHCb VELO pixel upgrade [44]; b) Schematic and detail of the fluidic circuit of the polyimide micro-channel cooling system for the upgraded ALICE inner tracker [46].

4.3.2 Thermo-fluidic aspects

The performance of the above discussed detector cooling layouts with liquids depends in addition to the general thermo-mechanical aspects on the choice of refrigerant which is circulated inside the cooling pipes or channels and if its state change is part of the refrigeration cycle or not. Here it has to be distinguished between single-phase (no state change = refrigerant in liquid state only) and two-phase cooling (with state change = refrigerant in liquid and vapour state).

Single-phase liquid cooling

The given amount of heat to be removed, the acceptable temperature gradient across the detector module and the heat capacity of the coolant defines the mass flux through the cooling pipe. Due to the low specific heat capacity of single-phase refrigerants this requires high mass fluxes in tubes with large hydraulic diameter. When applied in HEP experiments, this causes a high material budget contribution. In addition, due to the sensible heat rise in a single-phase liquid the final temperature on the detector module has to be accurately calculated with the fluid temperature at the external heat sink (refrigeration plant) and the parasitic heat leaks in possibly long transfer lines. Furthermore the temperature across the evaporator (and the detector module) is not isothermal. Single-phase refrigerants used presently or in the past for cooling purposes of HEP detectors are for example water or water/glycol mixtures and C_6F_{14} (perfluorhexan).

Evaporative cooling

Instead of single-phase heat transfer, evaporative cooling or two-phase heat transfer may be employed where possible due to its increased heat transfer efficiency. In the following chapter some general concepts and advantages of evaporative cooling will be introduced before describing selected examples where this is employed for detector cooling applications and why carbon dioxide is selected as the principal refrigerant for the thermal management of the present and next generations of Silicon Pixel Detectors at CERN [8].

CHAPTER 5

Evaporative cooling at CERN

5.1 Basics on flow boiling

There are many different modes to multi-phase or two-phase flow which find application in various different fields in science and industry (nanofluids; oil-, food- & pharma- industry). The flow of a boiling refrigerant in liquid and vapour state within an evaporator can be categorized as two-phase flow and is of relevance for this study. In this case dynamic vaporization processes which lead to the wanted cooling effect are also of importance. When a liquid and a surface are brought into contact whilst the surface is sufficiently hot - above the saturation temperature of the liquid - boiling occurs. The energy which is required to change the state from liquid to vapour at a given temperature is the so-called latent heat of vaporization. Unlike single-phase heat transfer, which relies totally on the coolant's sensible heat rise, two-phase heat transfer uses the coolant's combined sensible and latent heat. The coolant temperature is given by the saturation temperature and the corresponding pressure and does not depend directly on the absorbed heat. Far greater amounts of heat can be absorbed and thus evaporative cooling is much more efficient and the resulting heat transfer coefficients α are higher compared to the single-phase equivalent.

Compared to single-phase flows it is rather complex to describe the simultaneous motion of two phases. Two-phase boiling theory can be divided into pool boiling (no forced fluid flow) and forced convective boiling (forced flow conditions e.g. inside a tube), also called flow boiling. The flow behaviour of two phases in a channel depends on the velocity of the fluid phases, the wetting behaviour of the channel surface, the fluid properties and various forces acting between the channel walls, the liquid and the gas phase [47]. There are five forces which have to be considered:

(i) inertia force,

(ii) surface tension force,

(iii) shear force,

(iv) gravity (buoyancy) force and

(v) evaporation momentum force (only for diabatic applications).

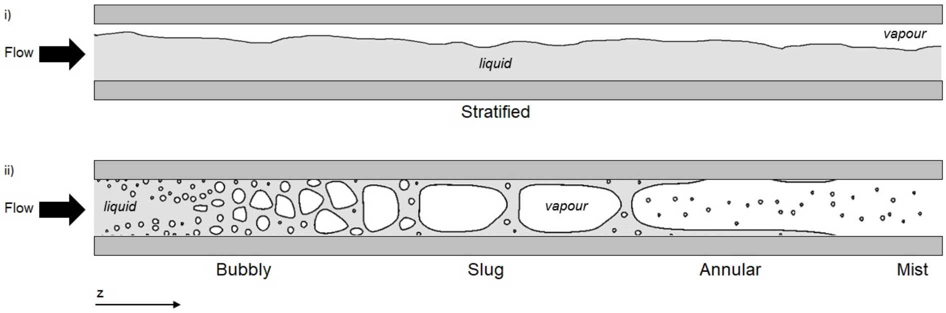

Figure 5.1: Flow patterns during flow boiling.

The interplay of these forces is responsible for the characteristic flow patterns observed during flow boiling and other two-phase applications. In general flow boiling flow phenomena can be divided into two groups where the vapour flows

i) as a continuous stream or

ii) as vapour segments separated from each other by liquid.

The first is called stratified flow, the latter may include more complex flow patterns, such as bubbly flow, slug flow, annular flow and mist flow. This most general classification is shown in Figure 5.1, while in literature more sub-classifications for ii) are defined [48]. Three important parameters for boiling flows inside tubes are introduced here now: vapour quality, void fraction and the slip ratio. In the following the two phases will be defined with subscript v and l, for the vapour and liquid phase respectively.

Vapour quality The vapour quality x is defined as the local gas mass flux divided by the local total mass flux $\dot{m}$ inside a tube [49]. Without phase change the vapour quality for the entire tube can be easily determined with following correlation,

$$x = \frac{\dot{m}_v}{\dot{m}_v + \dot{m}_l}. \tag{5.1}$$

Is the tube, channel or duct subjected to a continuous heat load, phase change conditions lead to an increase of the vapour quality downstream with (z). To determine the actual vapour quality of the liquid-vapour mixture flowing in a channel during phase change is very difficult. Instead the so-called thermodynamic equilibrium quality x_e can be calculated by assuming the two phases are at saturation condition. The saturation temperature corresponds to the pressure both phases have in common. There is

$$x_e(z) = \left.\frac{h(z) - h_l}{h_{lv}}\right|_{P=P(z)}, \tag{5.2}$$

where h_l is the enthalpy of the saturated liquid, h_{lv} is the latent heat of evaporation and h(z) is the enthalpy at a certain cross-section along the tube which can be obtained with

$$h(z) = h_{inlet} + \frac{1}{\dot{m}} \int q'(z)\, dz, \tag{5.3}$$

where q' is the power input per unit length. As depicted in Figure 5.1 with vapour quality the flow patterns in a given tube dimension changes. In the sections presenting and discussing the experimental results concerning this study the equilibrium vapour quality is used, however denoted as x only.

Void fraction The void fraction ε is the cross sectional area occupied by the gas phase. It is useful to determine the velocities of the phases and to calculate the pressure drop, flow pattern transitions and heat transfer coefficients. Figure 5.2 depicts the concept of void fraction schematically. The void fraction can be written as

$$\varepsilon = \frac{A_v}{A_v + A_l}, \tag{5.4}$$

where A_v is the area occupied by the gas phase, so-called voids, and A_l is the area occupied by the liquid.

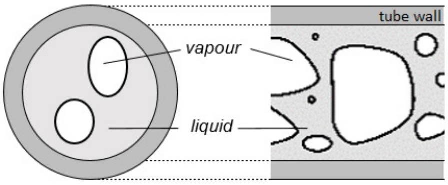

Figure 5.2: Schematic explanation of the cross-sectional void fraction within a tube.

Slip ratio According to experimental observations the velocity of the gas and liquid phase can be significantly different, depending on the flow pattern, the refrigerant and its temperature. The slip velocity ratio is the ratio of the gas velocity to the liquid velocity and can be written as [49, 50]

$$S = \frac{U_v}{U_l} = \frac{\rho_l x(1-\varepsilon)}{\rho_v (1-x)\varepsilon}, \tag{5.5}$$

where U_v and U_l are the gas and liquid velocity and ρ_v and ρ_l the gas and liquid density. Is there no slip between the two phases the slip ratio equals unity by definition and represents a very homogeneous two-phase flow, such as bubbly or mist flow where the entrained phase travels at nearly the same velocity as the continuous phase. For further reference the simple estimation of the slip ratio by Zivi [50] is used, which is

$$S_{Zivi} = \left(\frac{\rho_l}{\rho_v}\right)^{1/3}. \tag{5.6}$$

ρ_l/ρ_v is the liquid to vapour density ratio, which is used in itself as a measure for the homogeneity of the flow. Independent of flow patterns ρ_l/ρ_v approaches unity near the critical state and the flow is more homogeneous. An increase in ρ_l/ρ_v leads to an increasing separation of the flow.

Heat transfer, pressure drop and phase change phenomena during flow boiling and their prediction methods are still major research subjects, whilst in the past research was mainly conducted to study and predict the sufficient cooling of nuclear reactors. The most established findings on the heat transfer and pressure drop during flow boiling in ducts and tubes are summarized shortly in the following paragraphs and will be discussed in more detail especially for small channels in the literature review in chapter 6 and in the sections on experimental results in chapter 9. The local pressure drop and heat transfer coefficient depend on the different flow patterns mentioned above.

5.1.1 Heat transfer

Experimental findings from literature

In addition to the general convective heat transfer mechanisms described in section 4.1.2, the flow boiling heat transfer is governed by two mechanisms: nucleate boiling (connected to the formation of vapour bubbles on the tube wall surface) and convective boiling (connected to conduction and convection through a thin liquid film with evaporation at the liquid vapour interface) [51]. In the nucleate boiling region, the liquid near the heated channel wall is super-heated sufficiently to induce the nucleation and growth of vapour bubbles. Here the heat transfer coefficient depends on the heat flux and saturation pressure and is far less sensible towards mass velocity and vapour quality. This region is associated with bubbly and slug flow. The forced convection boiling region is associated with higher vapour qualities which suppresses bubble nucleation along the heated wall. Thus the heat is mainly transferred by single-phase convection through the thin film formed by annular flow patterns and is carried away by evaporation at the liquid-vapour interface. The heat transfer coefficient is dependent of mass velocity and vapour quality and is almost independent of heat flux. Figure 5.3 shows the described heat transfer processes and the typical flow patterns involved as a function of vapour quality x and position z along a homogeneously heated tube [52]. The nucleate boiling dominant heat transfer (Figure 5.3, upper) decreases monotonically as nucleation boiling is suppressed and slug and annular flow is favoured. On the other hand, as the nucleate boiling component decreases the convective boiling dominant heat transfer increases, as shown in Figure 5.3 (lower). This is due to the thinning of the annular liquid film which is beneficial for efficient heat transfer. Increasing heat flux may lead to local dry patches in annular flow and even total dry out, defining the critical heat flux location. For both heat transfer regimes the heat transfer coefficient drops for dry-out incipience. This shall be avoided during the design of cooling applications since the heat transfer efficiency is greatly reduced in this region. In summary the contributions of nucleate and convective boiling varies greatly along a homogeneously heated channel however both regimes can co-exist, whilst with increasing vapour quality convective boiling replaces nucleate boiling as dominant heat transfer mechanism. Another interesting aspect is the trend of the overall heat transfer coefficient α vs. vapour quality x as a result of the two competing flow boiling heat transfer mechanisms. This is extensively discussed in literature where the net result of the heat transfer coefficient then depends on both contributions. Figure 5.4 shows qualitatively the total trend for a generic macro-channel application.

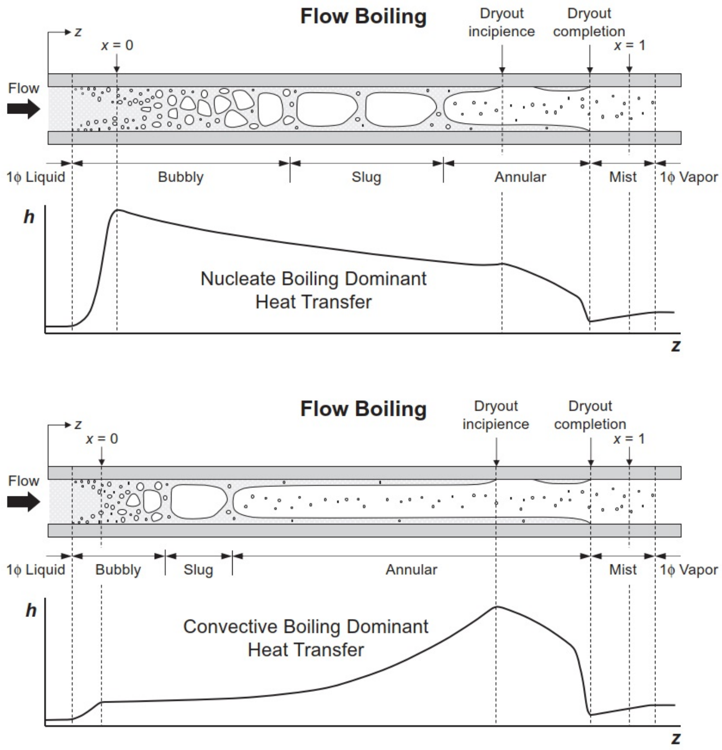

Figure 5.3: Schematic of flow regimes and variation of heat transfer coefficients (h is in this case the heat transfer coefficient). Reproduced from [52].

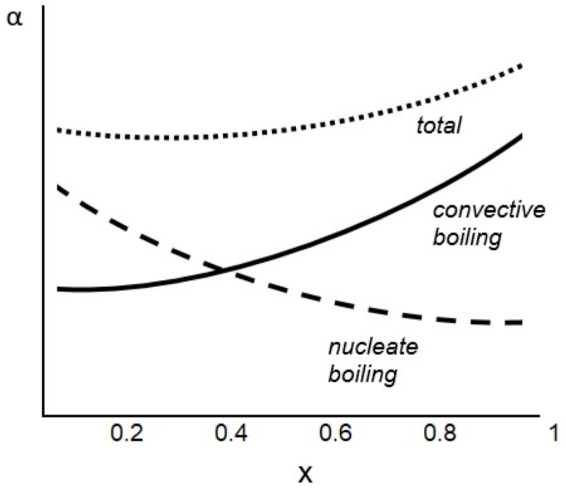

Figure 5.4: General trends of α vs. x.

Prediction methods from literature

Many empirical correlations or models have been developed to describe the heat transfer during flow boiling in ducts. Most of these correlative efforts are based on three major mathematical approaches: (1) The first approach uses correlations based on either a nucleate boiling (nb) relation or a convective boiling (cb) relation according to the assumed dominant heat transfer mechanism. The second approach (2) is to use a maximum multiplier determined for either the nucleate boiling or convective boiling component and the third approach (3) is based on super-positioning correlations for nucleate and convective boiling to account for the coexistence of both regimes under certain circumstances. However in practice defining a dominant heat transfer mechanism or using a simple superposition - or else a shear mathematical overlay - of the two boiling mechanisms is not always advisable for the prediction of the resulting heat transfer coefficient and the grade of prediction may suffer from this empirical approach. In section 9.3 this dilemma will be described in more detail in relation with the experimental data of this study. All mentioned models relate various dimensionless numbers in a certain way to predict the two-phase heat transfer coefficient empirically. Some of the most important dimensionless numbers in fluid mechanics and forced convective heat transfer shall be introduced here:

Reynolds number The Reynolds number represents the ratio of the inertial forces to the viscous forces in a fluid in motion. The most general form of the Reynolds number can be written as

$$Re = \frac{G\, D_h}{\mu}, \tag{5.7}$$

where μ is the dynamic viscosity of the fluid. D_h is the hydraulic diameter,

$$D_h = \frac{4A}{P_L}, \tag{5.8}$$

where A is the cross-sectional area of the tube and P_L is the wetted perimeter inside the duct. In the case of flow boiling the liquid Reynolds number Re_l and vapour Reynolds number Re_v can be defined for the liquid and vapour phase, respectively. There is

$$Re_l = \frac{G(1-x)D_h}{\mu_l} \tag{5.9}$$

and

$$Re_v = \frac{GxD_h}{\mu_v}. \tag{5.10}$$

Prantl number The Prantl Number is a dimensionless number approximating the ratio of momentum diffusivity, or kinematic viscosity and thermal diffusivity and can be expressed as

$$Pr = \frac{\mu c_p}{k}, \tag{5.11}$$

where k is the thermal conductivity of the fluid and c_p the specific heat of the fluid. Similar to the Reynolds number, there is the liquid and vapour Prantl number.

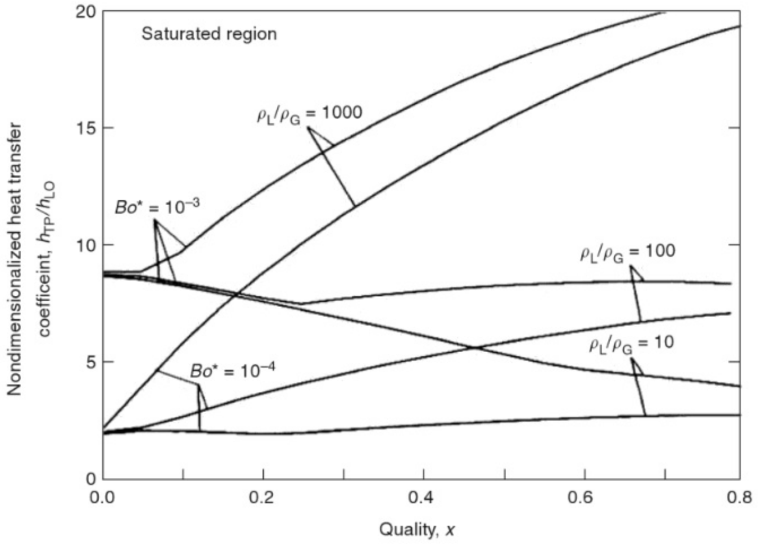

Figure 5.5: Flow boiling map for sub-cooled and saturated boiling (here the heat transfer coefficient is denoted as h). Reproduced from [53].

Nusselt number The Nusselt number combines the Reynolds number and the Prantl number and it is the ratio between convective and conductive heat transfer. In internal forced convection, the reference length is the tube diameter and the Nusselt number can be written as

$$Nu = \frac{\alpha D_h}{k}. \tag{5.12}$$

Boiling number Developed for flow boiling in particular, the Boiling number characterizes the effect of heat flux on nucleate boiling, which is defined as

$$Bo = \frac{q}{\dot{m} h_{lv}}, \tag{5.13}$$

representing the ratio of the actual heat flux to the maximum heat flux achievable by complete evaporation of the liquid. In example Figure 5.5 shows the flow boiling map developed by Kandlikar [53] for macro-channel applications defined on the Boiling number and the density ratio (ρ_l/ρ_v). Note that different values for Bo and different density ratios lead to different trends in α vs x. Thus much care has to be taken evaluating gathered data and comparing it with existing correlations. For the prediction of the heat transfer coefficient during flow boiling in conventional sized channels there are correlations by :

- Chen [54] (3)
- Shah [55] (2)
- Kandlikar [53] (2)
- Steiner and Taborek [56] (3)

- Gungor and Winterton [57] (3)
- Liu and Winterton [58] (3)
- Cooper [59] (1, nb)
- Wattelet et al. [60] (3).

where (1) again stands for the use of a correlation based either on nb or cb, (2) for the use of a maximum multiplier and (3) for a superposition of nb and cb relations. A short mathematical description of each correlation is given in Appendix A.

5.1.2 Pressure drop

Experimental findings from literature

In general four major effects on the two-phase pressure drop and resulting trends could be determined: Increasing pressure drop was found for

i) increasing mass flux,

ii) increasing heat flux,

iii) decreasing hydraulic diameter and

iv) decreasing saturation temperatures.

The first effect (i) is due to an increasing fluid speed causing higher frictional losses along the tube wall. The increasing pressure drop with increasing heat flux (ii) can be explained by higher evaporation rates, leading to a higher average vapour quality and flow speed. When all remaining test parameters are kept constant, smaller hydraulic diameters (iii) cause higher flow velocities resulting in higher wall shear stresses and thus higher frictional pressure drops. The increase in pressure drop with decreasing saturation temperature (iv) is generally explained with the changing thermo-physical properties of a refrigerant over the range of T_{sat} tested. Note that two-phase flows are very complicated and presently there is no convincing physical explanation of the observed trends of the pressure gradient. The interpretation above is reasonable but no more than intuitive and qualitative [61].

Prediction methods from literature

The pressure drop determines the pumping power required for any two-phase flow system and its accurate prediction is crucial for an optimal design and energy-efficient operation. The accurate reconstructed pressure profile along the channel is needed for the the post-processing of heat transfer data taken under evaporating flow conditions. Thus an accurate pressure drop prediction method is required and is equally important during the design phase of a heat exchanger to predict the local wall temperatures from the local saturation temperature. However the estimation of the two-phase pressure drop in ducts is also more complex compared to its single-phase counterpart. In general the pressure drop of a boiling fluid is higher compared to the single-phase equivalent caused by the additional friction between the phases. The total two-phase pressure drop ΔP is the sum of the static pressure drop ΔP_{static} (elevation head), the momentum pressure drop ΔP_{acc} (accelerational pressure drop) and the frictional pressure drop ΔP_{frict}. There is

$$\Delta P = \Delta P_{static} + \Delta P_{acc} + \Delta P_{frict}. \tag{5.14}$$

For flow in a horizontal tube ΔP_{static} is equal to zero. To formulate the momentum pressure drop ΔP_{acc} and the frictional pressure drop ΔP_{frict} there are two main prediction models,

- the homogeneous model and
- the separated flow model.

Homogeneous flow model The homogeneous model is mainly applied for very fine dispersed phases. Here the two-phase flow is represented as the flow of a "pseudo-fluid" with average properties based on a combination of those pertaining to the single-phase constituents. Considering the inlet or outlet conditions respectively, the momentum pressure drop $\Delta P_{acc,h}$ according to the homogeneous model is

$$\Delta P_{acc,h} = \left[\frac{G^2}{\rho_h}\right]_{outlet} - \left[\frac{G^2}{\rho_h}\right]_{inlet}, \tag{5.15}$$

with the homogeneous density ρ_h

$$\rho_h = \rho_l(1-\varepsilon_h) + \rho_v \varepsilon_h, \tag{5.16}$$

and the homogeneous void fraction ε_h

$$\varepsilon_h = \frac{1}{1 + \left(\frac{U_v}{U_l}\frac{(1-x)}{x}\frac{\rho_v}{\rho_l}\right)}, \tag{5.17}$$

where U_v/U_l is the above defined slip ratio S. For adiabatic flow where x = constant, $\Delta P_{acc,h}$ is equal to zero. The two-phase frictional pressure drop determined with the homogeneous model $\Delta P_{frict,h}$ can be expressed as a function of the two-phase friction factor f_{tp}, and for a steady flow in a channel with a constant cross-sectional area it is

$$\Delta P_{frict,h} = \frac{2 f_{tp} L G^2}{D_{h\rho} \rho_h}, \tag{5.18}$$

where L is the length of the channel. The friction factor may be expressed in terms of the two-phase Reynolds number considered in the Blasius equation [62]:

$$f_{tp} = \frac{0.079}{Re_{tp}^{0.25}}, \tag{5.19}$$

where Re_{tp} is the two-phase Reynolds number

$$Re_{tp} = \frac{G D_h}{\mu_{tp}}. \tag{5.20}$$

The viscosity for calculating the two-phase Reynolds number is chosen as a quality averaged viscosity μ_{tp},

$$\mu_{tp} = x\mu_v + (1-x)\mu_l. \tag{5.21}$$

In the most basic homogeneous model the two-phase viscosity μ_{tp} is considered equal to the liquid viscosity μ_l. Different improved homogeneous models have been formulated, where μ_{tp} is calculated by means of more complex relations between the vapour and liquid properties. There are e.g. the correlations by

- McAdams et al. [63],
- Beattie and Whalley [64],
- Cicchitti et al. [65],
- Dukler et al. [66],
- Akers et al. [67] and
- Lin et al. [68].

A short mathematical description of each improved homogeneous model is given in Appendix B.

Separated flow model The separated flow model is used more commonly to describe two-phase flow where the two phases are allowed to establish a slip between each other. The momentum pressure drop $\Delta P_{acc,separated}$ according to the separated flow model is

$$\Delta P_{acc,separated} = \left[\frac{G^2x^2}{\rho_v\varepsilon} + \frac{G^2(1-x)^2}{\rho_l(1-\varepsilon)}\right]_{outlet} - \left[\frac{G^2x^2}{\rho_v\varepsilon} + \frac{G^2(1-x)^2}{\rho_l(1-\varepsilon)}\right]_{inlet}. \tag{5.22}$$

The momentum pressure drop depends on the inlet and outlet vapor qualities and void fractions. The void fraction ε is determined with the correlation by Steiner [69] and can be written as follows considering the inlet or outlet conditions respectively

$$\varepsilon = \frac{x}{\rho_v}\left[(1+0.12(1-x))\left(\frac{x}{\rho_v}+\frac{1-x}{\rho_l}\right) + 1.18\frac{1-x}{G}\left(\frac{g\sigma(\rho_l-\rho_v)}{\rho_l^2}\right)^{1/4}\right]^{-1}. \tag{5.23}$$

It is difficult to predict the two-phase frictional pressure drop for separated flow $\Delta P_{frict,separated}$ as the flow pattern of a liquid-vapor mixture is very unpredictable and may occur randomly. Several correlations have been developed for macro-channel applications. They are semi-empirical prediction methods and are based on a certain experimental database. There are e.g. the correlations by

- Lockhart-Martinelli [70]
- with the approximations by Chisholm (C-method and B-method) [71, 72]
- Müller-Steinhagen and Heck [73],
- Friedel [74] and

- Grönnerud [75].

A short mathematical description of each frictional pressure drop correlation is given in Appendix B.

5.2 Evaporative cooling at HEP experiments

As detailed above evaporative cooling is attractive due to the large specific latent heat which can be absorbed during boiling and the high heat transfer coefficients involved. Two main advantages with respect to the detector design constraints result from two-phase cooling:

- Lower mass fluxes are required for a given heat load which allows for smaller tubes.
- Since there is no sensible temperature rise in the two-phase regime the evaporator can become almost isothermal, resulting in a more homogeneous temperature profile across the detector modules. Note that the pressure drop across the evaporator tube and supply lines induces a small temperature glide which has to be taken into account during the design phase of such evaporator systems.

Hence efforts were undertaken - where suitable - to implement flow boiling cooling techniques inside HEP experiments. Table 5.1 lists the refrigerants used for evaporative cooling in certain HEP experiments and the typical saturation temperatures used in this context. It has to be distinguished between low pressure and high pressure refrigerants. Using fluids which evaporate under high pressure even smaller inner diameter evaporator tubes can be used [76]. The created vapour can not expand to a large volume and the pipe volume and diameter and thus the fluid mass can be reduced. Although the high fluid pressure requires a thicker tube wall, the increase in mass of the tube wall is compensated by the diameter decrease [76]. Thus the total amount of mass (tube including fluid) is lower when using a high pressure fluid compared to a low pressure fluid. In addition the pressure drop of a fluid for a given system configuration is related to the absolute pressure inside this system and is therefore less significant for high pressure fluids. This means once more that even smaller diameter tubes can be used. It is obvious from Table 5.1, that on one hand carbon dioxide has a very high latent heat, but on the other hand the working pressures are relatively high compared to other refrigerants. Nevertheless, where very reliable and leak tight fluidic interconnections are guaranteed, the use of CO_2 can provide many benefits for the application in HEP experiments.

Fluid	T$_{sat}$ [°C]	P$_{sat}$ [bar]	Latent heat [kJ/kg]	Experiment
C_3F_8	-25	1.68	100.7	ATLAS ID [77], TOTEM [78]
C_4F_{10}	15	1.92	91.0	ALICE SPD [79]
CO_2	-25	16.83	293.3	AMS [80], CMS tracker upgrade [81], LHCb VELO [44], ATLAS phase II tracker
N_2	-180	4.68	174.9	SLD VXD3 [82], BTeV PXD [83]

Table 5.1: Refrigerants in evaporative cooling systems inside HEP experiments.

5.3 Evaporative cooling with Carbon Dioxide

The list of HEP experiments mentioned in Table 5.1 already using carbon dioxide as primary refrigerant produces evidence of an successful application. Therefore the refrigerant shall be introduced in more detail in the following paragraphs.

5.3.1 Carbon Dioxide – a natural alternative

Due to their ozone depletion and global warming potential (ODP)(GWP), the use of synthetic refrigerants categorized as HydroChloroFluoroCarbons (HCFCs) or ChloroFluoroCarbons (CFCs) is restricted, phasing-out or fully prohibited after international agreements were met accordingly by the Montreal protocol in 1987 and its subsequent amendments. First introduced in the nineteen-nineties, HydroFluoroCarbons (HFCs) or perfluorinated compounds (PFCs) were expected to be an acceptable alternative for the HCFCs and CFCs due to their zero ODP, however nowadays those are also on a list of regulated substances since they have been identified as powerful greenhouse gases in context with the Kyoto protocol. The above mentioned refrigerants C_3F_8 (R-128) and C_4F_{10} have a GWP (100-year time horizon) of 8900 and 9200 [84], respectively. Hence other alternatives are being explored to replace those refrigerants on a long term basis and for various fields of application. Alongside research on new chemicals, technologies based on ecologically-safe natural refrigerants are being investigated or are gaining renewed interest. There is for example ammonia (NH_3) which is used in large industrial refrigeration plants despite its high toxicity. Carbon Dioxide is another natural refrigerant with an ODP of zero and a GWP of 1 by definition, whilst being non-flammable and non-toxic.

5.3.2 Carbon Dioxide – a distinct refrigerant

Carbon dioxide is not considered an ideal refrigerant with respect to its critical point (73.9 bar and 31.1°C), which is the thermo-dynamical point in the pressure-enthalpy diagram of a fluid above which no additional pressure will change the vapour into a liquid. In this super-critical environment only one phase exists, a super-critical fluid. For further reference the pressure-enthalpy diagram and the critical point for CO_2 is shown in Figure 5.6. Due to its low critical temperature, the vaporization of CO_2 for standard applications takes place relatively close to the critical point and a degradation of cooling capacity may occur causing higher power consumption. Thus the use of CO_2 requires a careful design especially of the evaporator to maintain the efficiency of the system. However the low critical point of CO_2 also leads to higher reduced pressures ($P_{red} = P_{sat}/P_{crit}$) compared to standard refrigerants: at 0°C the reduced pressure of R-134a is only 0.07 while for CO_2 it is 0.47. This leads to very different thermo-physical properties with respect to standard refrigeration fluids: Table 5.2 lists some fluid properties of CO_2 in comparison with R-134a and R-404a at 0°C, where μ is the dynamic viscosity, λ the thermal conductivity and σ the surface tension. Compared for instance to R-134a at the same saturation temperature (0°C), CO_2 has a ten times lower liquid to vapour density ratio, a 2.5 times lower surface tension and a 3 times lower liquid viscosity. In comparison with traditional refrigeration fluids CO_2 exhibits in general

- higher saturation pressures P_{sat},
- higher vapour density ρ_v and thus
- lower liquid to vapour density ratio ρ_l/ρ_v,

- higher liquid thermal conductivity λ_l ,
- lower liquid viscosity μ_l and
- lower surface tension σ.

This has consequences on the general heat transfer characteristics of a CO_2 evaporator and the pressure drop along it.

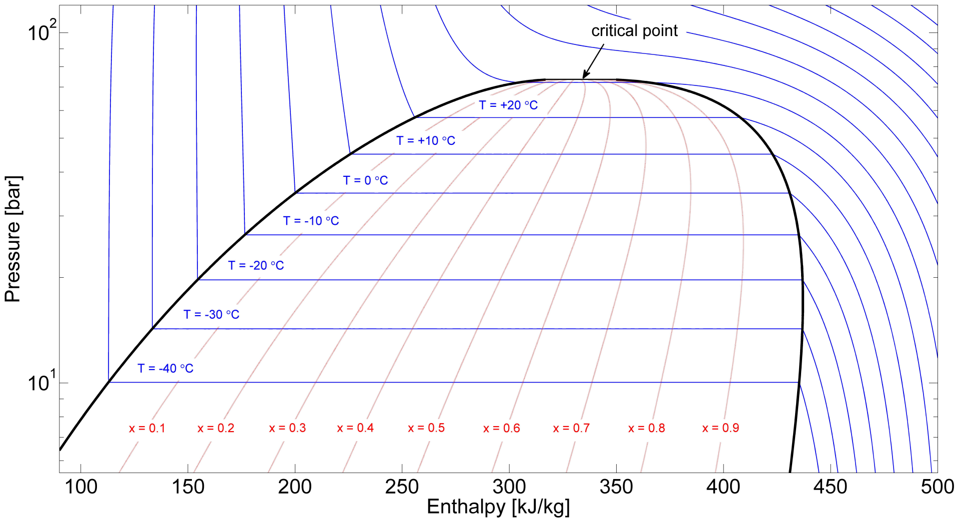

Figure 5.6: Pressure - Enthalpy (p-h) diagram of CO_2.

Fluid at 0°C	T $_{crit}$ [°C]	P $_{sat}$ [bar]	P $_{red}$ [bar]	ρ_l/ρ_v	$\mu_l \times 10^{-5}$ [Pa·s]	$\lambda_l \times 10^{-2}$ [W/m·K]	$\sigma \times 10^{-3}$ [N/m]
R-134a	101.1	2.93	0.07	89.74	26.65	9.2	11.56
R-404a	72	6.06	0.16	38.3	17.36	7.42	7.56
CO_2	31	34.85	0.47	9.5	9.94	11.04	4.54

Table 5.2: Important coolant properties by comparison.

Carbon dioxide properties: general influence on heat transfer and pressure drop

The heat transfer coefficients during CO_2 vaporization are in general higher compared to other refrigerants. It was found that the heat transfer coefficient of CO_2 is 2 to 3 times higher compared to R-134a [85]. This is often related to the dominance of nucleate boiling at low vapour qualities [86, 87]. Due to its lower surface tension compared to other refrigerants more active nucleation sites exist for a defined heat flux leading to more frequent bubble growth [86]. Furthermore, due to the low vapour velocity the so-called nucleate boiling suppression quality is delayed and extends the influence of the nucleate boiling regime towards higher vapour qualities. Thus reducing the influence of the convective boiling regime. As a consequence dry-out may occur at much lower vapour quality. Compared to other conventional refrigerants, the boiling CO_2 pressure drop across an evaporator is lower at a given saturation temperature. This is due to the lower liquid viscosity and the smaller density ratio between the liquid and the gas phase causing less additional slip between the phases. The two-phase pressure drop of CO_2 corresponds to only 60% of the pressure drop caused by R-134a under the same test conditions [85]. Additionally, the temperature glide caused by a given pressure drop is smaller for CO_2 compared to other refrigerants. At 0°C this glide is ten times higher for R-134a, compared to CO_2 at the same saturation temperature. Note that accurate pressure drop and temperature glide estimations gain importance when operating close to the relatively high freezing point of CO_2 (~ -56 °C).

Carbon dioxide properties in function of temperature

However, the physical properties of CO_2 change with saturation temperature which leads to a more complex situation when evaluating experimental data on boiling CO_2 and its heat transfer and pressure drop characteristics. This will be discussed in more detail in relation with the experimental results in chapter 9. Figure 5.7 shows the evolution of the liquid to vapour density ratio, the liquid to vapour viscosity ratio (Figure 5.7(a)), the slip ratio and the surface tension (Figure 5.7(b)) with respect to the saturation temperature.

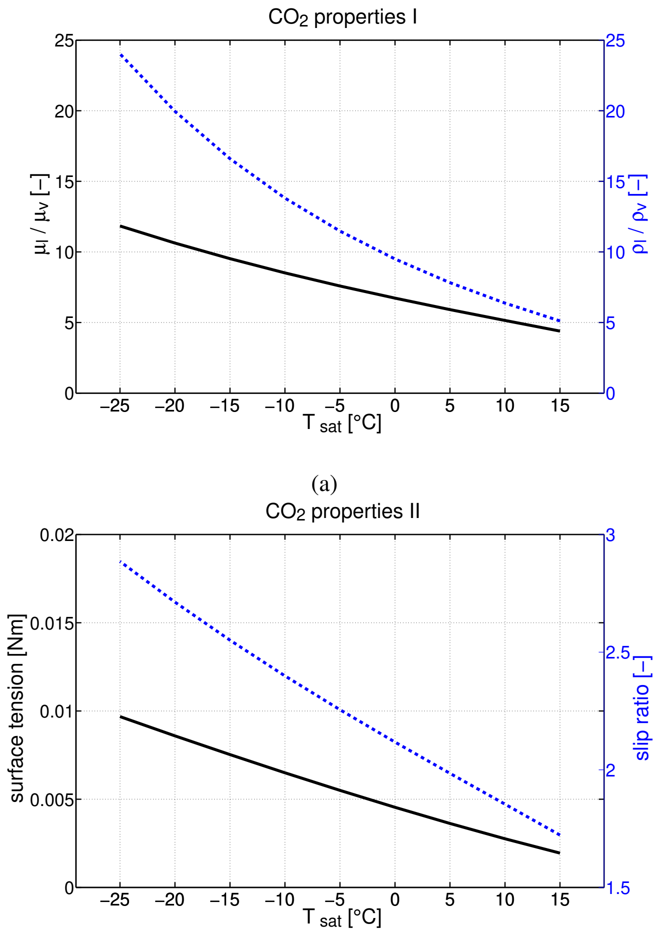

(a)

(b)

Figure 5.7: CO_2 properties as a function of T_{sat}: a) viscosity ratio μ_l/μ_v and density ratio ρ_l/ρ_v; b) surface tension and slip ratio $(\rho_l/\rho_v)^{1/3}$.

Resume Due to its beneficial thermodynamic properties compared to standard refrigerants, evaporating CO_2 can be used in smaller pipes where very high heat transfer coefficients are achievable. To summarize the reasoning given in chapter 4 and in this preceding chapter, a combination of most effective strategies is chosen for future Silicon Pixel Detectors: integrated mini- and micro-scale CO_2 evaporators for very effective detector cooling, where the effect of saturation temperature has to be considered during the design phase.

CHAPTER 6

State-of-the-art research with mini- and micro-scale carbon dioxide evaporators

Flow boiling in small channels is still a major field of investigation in heat and mass transfer research since scaling effects are not yet fully understood. After a short introduction of the general advantages and issues encountered with small-scale evaporators the focus shall be brought to mini- and micro-scale CO_2 evaporators studied so far in literature. Furthermore the prediction of pressure drop and heat transfer is crucial for the design of small-scale evaporators, however the research field is far from an established approach and this review shall further highlight this dilemma.

6.1 Basics on micro-fluidics and flow boiling in small-scale evaporators

The minimization of the heat exchanger channel size provides a larger ratio between the surface available for heat transfer and the volume available for the flow compared to macro-channels. This results in higher heat and mass transfer rates and lower equipment size [6], better axial temperature uniformity, smaller refrigerant flow rates and thus smaller pumping powers [4]. The initial concept of micro-channel cooling was introduced by Tuckerman and Pease in the 1980's where they studied a compact heat sink incorporated into an integrated circuit chip [3]. They found that for laminar flows in confined channels, the heat transfer coefficient scales inversely with the channel width, making small channel dimensions desirable. To delimit those small dimensions from macroscopic tubes, in literature it is distinguished between mini-channels and micro-channels, where a unified scale-wise differentiation between the three does not exist yet. Thus in the following explanations only the term micro-channels will be used for simplification. It also has to be distinguished between single- and multi-micro-channel configurations, where the latter is composed of multiple parallel channels often connected to a fluidic inlet and outlet plenum, where some examples were already discussed in section 4.3. Furthermore research commenced mainly with single-phase flow in micro-channels. However, already in one of the first studies on flow boiling in micro-channels subsequent to Tuckerman and Pease presented by Moriyama et al. [88] it was found that the heat transfer was 3 – 20 times higher – depending on the input parameters – compared to single-phase flow. Hence the question arises if macro-scale flow boiling design methods (typically based on experimental data covering channel sizes from about 4 mm up to about 25 mm ID) can be applied to small-scale evaporators. It was found that when extrapolated to channel sizes smaller than 2-3 mm those old-established methods were not very accurate or reliable [61]. According to an ongoing discussion in literature it is currently believed that the fundamental physical phenomena are basically the same for two-phase flows at conventional and small scales, while the flow morphology (the flow pattern) changes as the channel size is reduced leading to new flow-induced phenomena. It was found that the transition from macro to micro-scale is gradual, not abrupt or localized. As the channel size is reduced scale effects come gradually into play. The forces acting during flow boiling mentioned above which allow for developed phase behaviour during two-phase flow (inertia force, surface tension force, shear force, gravity force and evaporation momentum force) change in magnitude and importance whilst decreasing the channel size. For macro-scale channels there are different dominant flow patterns such as e.g. stratification phenomena due to the importance of gravity. With reduced channel size gravity effects become less influential and surface tension effects gain importance. Thus e.g. channel orientation is only of minor importance for micro-channels. Interfacial fluid forces acting on the fluid-fluid interfaces and on the channel walls are the most dominant forces for micro-fluidic flows. Thus additional dimensionless numbers have been developed which scale the different forces acting in small channels with respect to the surface tension force.

Bond number The Bond number describes the importance of surface tension forces related to gravity

$$Bd = \frac{gravitational\ force}{surface\ tension\ force} = \frac{(\rho_l - \rho_v) g D_h^2}{\sigma}, \tag{6.1}$$

where g is the gravitational constant and σ the surface tension. If Bo $\ll$ 1, surface tension dominates over gravitation.

Weber number The Weber number expresses the ratio between inertia to surface forces,

$$We = \frac{inertia\ force}{surface\ tension\ force} = \frac{\rho U^2 D_h}{\sigma}, \tag{6.2}$$

and is mainly expressed as the liquid Weber number We_l using the properties of the liquid phase, ρ_l, U_l and σ_l. Is We < 1, entrainment of droplets in the vapour phase is more difficult as the surface tension force at the interface becomes stronger.

Froude number The Froude number describes the ratio of inertia forces to gravitational forces. The liquid Froude number can be written as

$$Fr_L = \frac{G^2}{\rho_l^2 g D_h}. \tag{6.3}$$

Capillary number In addition multi-phase micro-flows can be characterized by the Capillary number which is the ratio of viscous to surface forces and is defined as

$$Ca = \frac{viscous\ force}{surface\ tension\ force} = \frac{\mu U}{\sigma}. \tag{6.4}$$

Figure 6.1 shows how Bd, Ca and We and their relevant forces with respect to the interfacial forces alter by changing the channel size and/or the flow velocity. Relating the different body forces, gravitational forces, viscous and inertial forces to interfacial forces it was found that in most cases the interfacial forces dominate by several orders of magnitude in micro-channels [47]. The most important issues not yet fully understood generic to all evaporating fluids during flow boiling in small channels are (i) the effect of the channel size on the flow morphology and (ii) the resulting definition of a transition criterion between macro and micro-scale flows.

(i) Size effects on the flow morphology As mentioned before stratified flows gradually disappear in small horizontal channels and more axisymmetric flow patterns are found instead. However the ultimate effect of the channel size on the flow pattern is influenced by the choice of refrigerant and its physical properties (e.g. vapour density, liquid viscosity, surface tension) and may differ for different refrigerants. In addition to the flow patterns introduced in section 5.1, a flow pattern which is peculiar to small channels is the the so called elongated bubble flow (or confined bubble flow). During growth of a vapour bubble the size of the bubble when it leaves the channel surface and gets carried away in the flow (bubble departure) depends on the evaporating fluid and its operating pressure and not on the channels size. Thus the size of bubbles does not scale with the channel size. In some cases the growing bubble may reach the size of the channel before departure and the channel limits the subsequent growth of the bubble in radial direction, thus it will grow in length as it flows downstream along the channel. Furthermore the annular flow regime is mainly laminar in small channels, whilst the counterpart in macro-channels is often turbulent and a direct comparison may not be possible. To mention another example, the channel surface roughness does not scale as the channel size is reduced and may become more important in small channels.

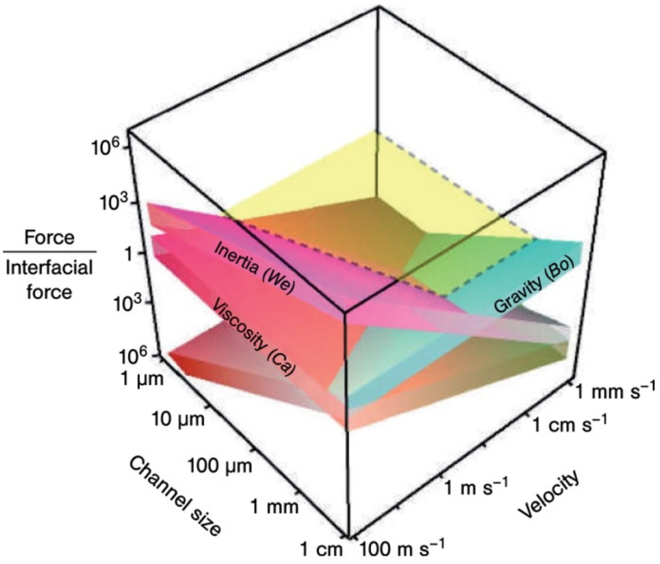

Figure 6.1: Inertial, viscous and gravitational body forces, relative to interfacial forces, as a function of the channel size and characteristic velocity in micro-fluidic multi-phase systems. Reproduced from [47].

(ii) Definition of a transition criteria in two-phase flow The scaling and tube size effects are linked to the problem of finding a scale wise definition for micro-channels. Since the beginning of micro-fluidic studies several macro-to-micro-scale transition criteria have been proposed. There are criteria to predict the lower boundary of the macro-scale and the upper boundary of the micro-scale with a transition region in between (the mini-scale or meso-scale) [61]. This transition region acknowledges the fact that the change in thermal-fluidic behaviour is gradual and not abrupt. No universally accepted transition criterion exists at the moment. As summarized by Thome and Cioncolini [61] all criteria have some physical sound justification but cannot be used solely. The distinction between micro-channels, mini-channels and conventional channels will be always dependent on the fluid, its operating pressure and temperature and the mass and heat flux. Nevertheless a transition criterion used frequently in literature shall be introduced here shortly. In order to distinguish between macro and micro-scale Kew and Cornwell [89] proposed the so-called Confinement number to be defined as follows

$$Co = \frac{1}{D_h}\sqrt{\frac{\sigma}{g(\rho_l - \rho_v)}}, \tag{6.5}$$

where the radical is the so-called Capillary length which is a length scaling factor relating gravity and surface tension forces. Kew and Cornwell [89] fixed a transition threshold at Co = 0.5, where Co > 0.5 indicated micro-scale and Co < 0.5 indicated macro-scale. This is based on the confined growth of the bubble in small channels and provides a way to determine the transition criterion from isolated to confined bubble flow. Furthermore Ullman and Brauner [90] suggested a slightly different transition point based on the Bond number, indicating as micro-channel flows those characterized by Bd < 1.6. Due to the fact that Co and Bd are linked by the relation Bd = $\text{Co}^{-0.5}$, this corresponds to a threshold for micro-channel behaviour fixed at Co = 0.79. Since the transition between macro-scale flow patterns to micro-scale flow patterns happens gradually as scaling effects come into play, Ong and Thome [91] concluded their analysis with the definition of two thresholds: one for macro-channel behaviour with Co < 0.3 - 0.4 and one for micro-channel behaviour with Co > 1.0, with a transition region in-between. Note that another channel size classification proposed by Kandlikar and Grande [92] declares that conventional channels are greater than 3 mm in diameter, whilst mini-channels cover the range between 3 mm and 200 µm and micro-channels cover the range between 200 µm and 10 µm. This rather rigid classification is still often used due to the lack of another acknowledged scheme.

There is an ongoing debate about the actual governing heat transfer mechanism for flow boiling in micro-channels. This is due to the fact that the resulting trends of α vs. x are found to be very different compared to macro-channel results but also when comparing seemingly similar experiments. Conventionally as described for macro-channels in section 5.1.1, it is also assumed that any resulting trend of α vs. x can be described with the varying contributions of the nucleate and convective boiling heat transfer. Kim and Mudawar [52] presented a summary of the possible trends of the boiling heat transfer coefficient in micro-channels depending on the mass flux, heat flux, channel diameter and saturation temperature. This summary is reproduced in Figure 6.2, where the heat transfer coefficient is denoted as h instead of α. They introduced the ratio between the nucleate boiling heat transfer and the convective boiling heat transfer ($\alpha_{nb}/\ \alpha_{cb}$) as a measure for judging the dominant heat transfer regime. Is the convective boiling the dominant regime this results in a low $\alpha_{nb}/\ \alpha_{cb}$ value and the heat transfer coefficient has a positive slope versus quality. Is the nucleate boiling the dominant regime $\alpha_{nb}/\ \alpha_{cb}$ features a high value and the slope of α versus x is negative. The contribution of convective boiling increases with mass flux and the slope of α vs. x changes from negative to

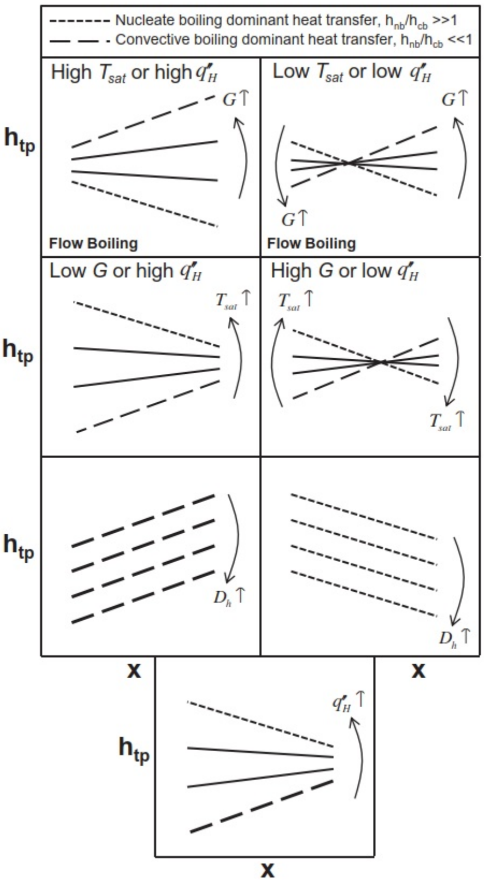

Figure 6.2: Experimental boiling heat transfer coefficient in small channels versus vapour quality for different G, T_{sat}, D_h and q. Reproduced from [52].

positive. The contribution of nucleate boiling increases with increasing T_{sat} or heat flux. For both regimes α decreases with increasing the hydraulic diameter. More confusion in the field of research was caused by findings made by Thome et al. [7]. They found that neither nucleate boiling nor turbulent convection is the dominant heat transfer mode, but transient thin film evaporation. Transient conduction/micro convection is identified here as the dominant heat transfer mechanism for elongated bubble and slug flow. In general the knowledge of the flow pattern is crucial for the interpretation of thermal and fluid phenomena in two-phase flows. As the channel size is gradually reduced the flow patterns change explaining the observed variations of two-phase flow parameters. It has to be stressed that it is impossible to find a unified trend of the heat transfer coefficient as a function of vapour quality, mass flux and heat flux. The changing fluid parameters at different saturation temperatures and the channel size, its surface roughness and geometry have to be considered. Considering all these factors simultaneously makes the interpretation of experimental trends particularly challenging [61].

A similar dilemma can be described for the pressure drop during flow boiling in small channels. In general the measured pressure gradient in micro-channels follows the same qualitative trends that are observed with macro-scale tubes and channels. Although a relatively large number of micro-channel pressure drop studies can be found in literature, especially for standard refrigerants such as R-113, R-12, R-124, R-134a and R-141b, large discrepancies among the data gathered under comparable flow conditions exist. Furthermore two-phase flows are often fluctuating and unsteady in micro-channels which complicates the acquisition of data and its prediction.

It is obvious that the prediction of experimental data in terms of heat transfer and pressure drop is very challenging. Nevertheless, many efforts were undertaken by researchers to empirically predict flow boiling in small channels and results were first compared with macro-correlations. However, due to the obvious dissimilarities between the two cooling methods, soon the correlations were empirically adapted to suit the results in micro-channels. Following methodology was used by many research teams investigating micro-channel heat sinks: They tested a certain fluid in a certain small-scale channel geometry for boiling heat transfer applications and tried to find a suitable existing correlation to describe the found heat transfer and pressure drop behaviour. If none of the existing correlations could predict the data, the researchers often developed empirically-fitted correlations tailored to their own data. This led to an innumerable amount of correlations to which again other researchers could compare their data with. Many scientific review papers were published to bring some order into the correlations published in several decades. There are for example [4, 6, 52]. To predict the pressure drop in micro-channels there are for example correlations developed by

- Mishima and Hibiki [93],
- Tran et al. [94],
- Zhang and Webb [95],
- Qu and Mudawar [96],
- Lee and Garimella [97],
- Lee and Lee [98] and
- Kim and Mudawar [99]

On the other hand to describe the heat transfer in micro-channels models have been formulated by

- Warrier et al. [100],
- Lazarek and Black [5],
- Tran et al. [101],
- Agostini and Bontemps [102],
- Li and Wu [103],
- Bertsch et al. [104],
- Yu et al. [105],
- Kandlikar and Balasubramanian [106],
- Kew and Cornwell [89],

- Oh and Son [107] and
- Kim and Mudawar [108]

A short mathematical description of each correlation is given in Appendix A.

Then the focus was shifted from the empirically found evaporation models to the actual flow patterns in the channels and their mechanistic description. By means of flow visualization researchers could use the visual data and associate it with the found heat transfer and pressure drop trends. This prediction method is non-empirical and so-called flow pattern maps have been developed. One of the most sophisticated flow pattern based prediction tool for heat transfer and pressure drop during flow boiling in small channels was developed by

- Cheng et al. [109, 110].

For a full description of this model please refer to the reference given. A higher prediction capability can be achieved when working with flow pattern based models and this approach seems to point into the correct direction for a more comprehensive research on heat transfer and pressure drop in micro-channels and in general.

6.2 Literature review on small-scale carbon dioxide evaporators

The given outline on the basics on micro-fluidics and flow boiling in small-scale evaporators also applies to carbon dioxide. However due to the different thermo-physical properties of CO_2 with respect to standard refrigerants, experimental data in literature and its prediction for both, pressure drop and heat transfer coefficient, exhibits some peculiarities so far found which will be summarized in the following paragraphs. General information on CO_2 flow boiling in macro- and micro-channels can be found in the comprehensive review by Thome and Ribatski [111].

6.2.1 Pressure drop

The amount of studies on CO_2 flow boiling in small channels is very limited and several concentrate on multi-micro-channel arrays, e.g. [85, 112, 113], whereas studies on simple single channels or tubes are even more sparse. Whilst the larger fraction of these latter studies focuses on the heat transfer performance, e.g. [114, 115], even less quantitative information is available on the pressure drop behaviour of CO_2 boiling in small diameter channels. Since the experimental and theoretical overlap between single- and multi-micro-channel observations is still a matter of research [116], Table 6.1 gives an overview of the existing literature about the pressure drop of CO_2 boiling flows, limited to single tubes of small diameter (< 3 mm) without oil effect. The limit of 3 mm is based mainly on the channel size classification proposed by Kandlikar and Grande [92], which was mentioned earlier.
The experimental studies listed are all carried out in horizontal, circular stainless steel tubes. Some important aspects often varying between different studies are also summarized in the table: (i) the adiabatic or diabatic conditions in which the published pressure drop data were gathered, (ii) the length of the test section L_{dp}, (iii) the pressure drop data reduction method, (iv) the vapour quality used for data reduction and (v) the final presentation of data. Unfortunately a generalized approach with respect to these aspects does not exist and is often not further mentioned. In some cases the

authors	ID [mm]	G [kg/m^{2}s]	q [kW/m^2]	x	T_{sat} [°C]	(i) pressure drop measurement	(ii) L_{dp} [mm]	(iii) pressure drop data reduction	(iv) vapor quality for data reduction	(v) published pressure drop data related to
Hihara and Tanaka [117]	1	360; 720; 1440	9; 18; 36		15	diabatic	not specified	not specified	not specified	mass flux
Yun and Kim [118]	0.98	1000 - 2000	20 – 40		0; 5; 10	diabatic	400	not specified	not specified	vapour quality
	2	500 - 3570	7 – 48		5; 10		1200			
Yamamoto et al. [119]	0.51; 1	300 - 1000	0	0.05 - 0.95	10 - 18.3	adiabatic	800, 400	accounting for dp_{frict} and dp_{acc}	x_{eq}	
	2	200 - 500	0	0.1-0.9	14.3		100			
Pamitran et al. [120]	1.5; 3	200 - 600	10–30		-10; -5; 10	diabatic	2000, 3000	accounting for dp_{frict} and dp_{acc}	x_{out}	mass flux
Ducoulombier et al. [121]	0.53	200 - 1400	0	0 - 1	-10; -5; 0; 5	adiabatic	191	accounting for dp_{frict} and dp_{acc}	average (x_{in}, x_{out})	vapour quality
Wu et al.[122]	1.42	300 - 600	7.5 - 29.8		-40; -35; -30; -20; -10; 0	adiabatic / diabatic	300	no reduction	calculated at the middle of the test section	vapour quality

Table 6.1: CO_2 boiling pressure drop studies in small diameter channels

measured pressure drop values are directly used as the total pressure drop, some assume this to be the frictional component of the pressure drop only, whilst other researchers explicitly distinguish between frictional and accelerational components of the pressure drop. When relating data to the vapor quality often the outlet vapor quality of an experiment is used as opposed to an arithmetic average vapor quality obtained between inlet and outlet of the tested device. The latter approach is in theory only correct when carrying out adiabatic pressure drop tests. An additional issue is caused by the fact that data are gathered for tubes of different lengths. Typically the data are then presented as a pressure gradient [pressure unit/m], which requires an upward extrapolation in the case of tubes shorter than 1 m or a downward extrapolation in the case of tubes longer than 1 m, always assuming a linear pressure drop relation. This commonly used procedure further manipulates the raw data and might cause discrepancies when comparing different data sets. Table 6.2 organizes the studies reported in the previous table in terms of inner diameter of the test section and range of saturation temperature studied, independent of the mass flux and heat flux.

The scarcity of available data and the very limited superposition between independent data sets is apparent. However, the four major general effects on the CO_2 two-phase pressure drop and resulting trends which were mentioned in section 5.1.2 could be confirmed in the listed studies: increasing pressure drop were found for (I) increasing mass flux, (II) increasing heat flux, (III) decreasing hydraulic diameter and (IV) decreasing saturation temperatures. The first effect (I) was confirmed by all studies listed in Table 6.1. In the studies based on diabatic tests, such as Hihara and Tanaka [117], Yun and Kim [118], Pamitran et al. [120] and Wu et al. [122], a direct influence of heat flux (II) is often mentioned. On the other hand, the studies based on adiabatic experiments such as Yamamoto et al. [119] and Ducoulombier et al. [121] mention no direct heat flux dependence. However also in their case the pressure drop naturally increases with the vapour quality adjusted by means of a pre-heater. Pamitran et al. [120] explicitly confirm the mentioned trend for decreasing hydraulic diameter (III). Concerning (IV), Yun and Kim [118] clearly mention that the pressure drop in mini-tubes increases with a decrease in saturation temperature, likewise this is confirmed by Pamitran et al. [120], Ducoulombier et al. [121] and Wu et al. [122]. However, from the results and discussions in the reported literature the link between pressure drop and saturation temperature appears unclear and difficult to quantify. Zhao et al. [85], Jeong et al. [123] and Jeong and Park [113] carried out CO_2 flow boiling experiments in multi-micro-channels and confirmed the generally observed increase in pressure drop for increasing mass flux and decreasing saturation temperature. In summary the most common trends reported for macro-channel applications could be qualitatively confirmed for the CO_2 two-phase pressure drop in small channels. However, the data from literature are very limited and, when compared in detail, show some inconsistencies.

The applicability analysis of existing two-phase pressure drop correlations to the studies listed in Table 6.1 may provide interesting hints towards a better understanding of the underlying physics and on the remaining open questions. The simplest historical approach to predict two-phase pressure drop in ducts and tubes is the one based on the homogeneous flow models and its amendments as described in 5.1.2. Yamamoto et al. [119] compared their data to the basic homogeneous model and found that the model predicts the data well for the 2 mm ID tube, but the prediction level drops for the smaller tube sizes of 1 mm ID and 0.5 mm ID respectively. On the other hand, Pamitran et al. [120] found that the best prediction level was achieved with the model by Dukler et al. [66], but in their case the mean deviation for their 1.5 mm ID tube is about half the value of the one for the 3 mm ID tube. Ducoulombier et al. [121], working on a much smaller tube of 0.5 mm ID, also reported a relatively good agreement of their data with the basic homogeneous model. In their work a

			T_{sat}[°C]														
authors			-40	-35	-30	-25	-20	-15	-10	-5	0	5	10	14.3	15	18.3	
Pamitran et al. [120]	ID [mm]	3							x	x			x				unique ID
Yun and Kim [118]		2										x	x				similar ID
Yamamoto et al. [119]		2												x			
Pamitran et al. [120]		1.5							x	x			x				similar ID
Wu et al. [122]		1.42	x	x	x		x		x		x						
Hihara and Tanaka [117]		1													x		similar ID
Yamamoto et al. [119]		1											x	x		x	
Yun and Kim [118]		0.98									x	x	x				
Ducoulombier et al. [121]		0.53							x	x	x	x					similar ID
Yamamoto et al. [119]		0.51											x	x		x	

x = data available

Table 6.2: Summary of CO_2 boiling pressure drop studies in small diameter channels

qualitative temperature dependence on the applicability of the homogeneous model was reported: the experimental data were in general under-predicted by the homogeneous model, with a best performance at 5°C T_{sat}, while the under-prediction increased with decreasing saturation temperature. For what concerns the conventional macro-scale correlations based on separated flow models [70–75], most studies dealing with CO_2 flows in small single channels report that they generally over-estimate the pressure drop [121]. In particular, the Lockhart-Martinelli [70] approach, using the Chisholm approximation [71] and the Chisholm parameter C (C-method), results in especially large deviations for all the studies mentioned in Table 6.1. Pamitran et al. [120] found their data over-estimated by the Chisholm correlation (B-method) [72] and the Friedel [74] correlation. The prediction slightly improved for the smaller 1.5 mm ID tube as opposed to the 3 mm ID tube, whilst the Friedel correlation [74] resulted in slightly better prediction compared to the Chisholm correlation. Ducoulombier et al. [121] found that their experimental conditions were best predicted by the Müller-Steinhagen and Heck correlation [73], but a similar prediction level was also provided by the Friedel [74] and the Chisholm B-method [72]. In addition, they found a rough temperature dependence of the applicability of some models. The best data prediction from macro-channel correlations were generally found at the lowest investigated saturation temperature of -10°C. The Müller-Steinhagen and Heck [73] correlation, for instance, over-estimated the data obtained at 5°C and 0°C, whilst for -5°C and -10°C the model under-estimated the data. Also the best prediction of the Friedel [74] correlation correlated with the lowest saturation temperature and the over-predicting behaviour increased with its increase. Well-known two-phase pressure drop correlations have been more recently modified to better fit new data gathered for different refrigerants in mini- and micro-channels [93–99]. Ducoulombier et al. [121] found that these methods mostly under-predicted their measurements, with a maximum deviation for the lowest temperature. Both Pamitran et al. [120] and Ducoulombier et al. [121] showed that with the Tran model [94] mean deviations of more than 100% were found. On the contrary, when comparing to the correlation by Zhang and Webb [95] both studies found a reasonable predictability. In the case of Pamitran et al. [120] this was mainly true for the 1.5 mm ID tube. This good fit, despite the difference in hydraulic diameter and test fluids, is in particular explained by Ducoulombier et al. [121] with the high reduced pressures of the data set used by Zhang and Webb [95] to derive their correlation ($P_{red} \approx 0.2 - 0.5$) which are close to the experimental conditions of both Ducoulombier et al. [121] and Pamitran et al. [120] with reduced pressures from ~ 0.36 to 0.54 and ~ 0.36 to 0.6, respectively. Furthermore, Ducoulombier et al. [121] implicitly explain the poor fit of the Tran et al. [94] model with the very different reduced pressures of the data set used for the formulation of this model ($P_{red} \approx 0.04 – 0.2$). As stressed in the interesting reviews by Cheng and Xia [10] and by Thome and Ribatski [111], the drastically different physical properties of CO_2 compared to those of other refrigerants may be the key cause for a poor fit between CO_2 data and models developed for conventional synthetic refrigerants. To eliminate one factor of ambiguity, the mentioned studies by

- Yamamoto et al. [119],
- Yun and Kim [118],
- Pamitran et al. [120] and
- Ducoulombier et al. [121] (with a modified homogeneous model and a modified C-method based on the approach proposed by Chisholm)

all propose new adaptations of existing correlations based on their own measurements on CO_2 flows in small diameter channels, which are described shortly in Appendix B. However, a systematic cross-validation of these correlations is still pending. The phenomenological approach proposed by Cheng et al. [109] for two-phase pressure drop of CO_2, based on a database gathered by various independent studies, improved the predictability of CO_2 flow boiling properties in larger channels. However, Ducoulombier et al. [121] reported for their case study a mean deviation of 111% from this prediction method. On the other hand, Wu et al. [122] also tested the prediction performance of this model against their data and reported a good prediction at lower to medium vapour qualities, but noted that for high vapour qualities and mist flow the model is less accurate.

The pressure drop during CO_2 flow boiling in multi-micro-channels is generally underestimated by macro-channel correlations. Cheng et al. [109] compared a data base with measurements from Pettersen [112], Zhao et al. [85, 124] and Yun and Kim [118, 125] to the classical pressure drop correlations. They found that the correlations by Friedel [74] and Müller-Steinhagen and Heck [73] correlations underestimate the experimental data. The prediction of the data base can be improved with the phenomenological model by Cheng et al. [109], which was developed for CO_2, predicting 44% of experimental data within ±30% instead of 35% when using the Friedel correlation. Nevertheless, still a high level of scatter was reported. Furthermore, Pettersen [112] also found a temperature dependence of the Friedel correlation, where the highest under-prediction of the measurements was found for the lowest saturation temperatures. The micro-channel correlations by Tran et al. [94] and Zhang and Webb [95] did not improve the overall prediction capability. The difference between single and multi-micro-channel tubes was reported by Yun and Kim [118, 125]. They argue that the pressure drop in multi-channel tubes is governed by the fluid distribution rather than the diameter which causes dissimilarities in the pressure drop behaviour. However a main factor causing those discrepancies may be the use of inlet and outlet plenums where the pressure is measured in the case of multi-micro-channels.

In summary, when comparing known prediction methods to the limited data available for CO_2 two-phase pressure drop in small channels, it surprisingly appears that the homogeneous models are relatively successful in predicting the experimental results. Furthermore, the often reported statement that old-established empirical macro-channel correlations do not apply to small diameter channel experiments could not be entirely confirmed for this specific case. The Friedel correlation [74] captures CO_2 boiling pressure drop in small channels quite successfully, in particular at low temperatures, whilst for the study conducted by Ducoulombier et al. [121] the correlation by Müller-Steinhagen and Heck [73] proved to be the best prediction method. The literature analysis suggests that the reduced pressure and thus the CO_2 saturation temperature, introduce additional factors that should be taken into account by predicting correlations. However, only Ducoulombier et al. [121] explicitly documented their findings related to the saturation temperature and amongst the four known effects on the two-phase pressure drop, the least understood and studied is definitely the effect of saturation temperature [10] – especially for CO_2.

6.2.2 Heat transfer

Table 6.3 lists the most frequently cited flow boiling studies focusing on the heat transfer coefficient of CO_2 in small diameter single-channels (ID ≤ 3 mm). Naturally some studies already mentioned in Table 6.1 for the pressure drop again appear in this context, but as explained above more independent experimental studies exist investigating the heat transfer coefficient. For the sake of completeness, the

	authors	ID [mm]	G [kg/m^{2}s]	q [kW/m^2]	x	T$_{sat}$ [°C]
ID $>$ 3 mm	Oh et al. [87]	7.75	200 - 500	10 - 40		5; 0; -5
	Yoon et al. [126]	7.53	200 - 530	12 - 20	0-0.7	-4 - 20
	Bredesen et al. [127]	7	200 - 400	3 - 9		-25 - 5
	Park & Hrnjak [128]	6.1	100 - 400	5 - 15	0.08–0.83	-30; -15
	Yun et al. [86]	6	170 - 320	10 - 20	0-0.9	5 ; 10
	Mastrullo et al. [129]	6	200-349	10 - 20.6	0.02 - 0.98	-7.8 - 5.8
	Hihara & Dang [9]	6; 4	360 - 1440	4.5-36	0-1	5; 15
ID $\leq$ 3 mm	Pamitran et al. [130]	3; 1.5	50 - 600	5-70	0-1	0-10
	Choi et al. [131] [114]	3; 1.5	200 - 600	20-40	0.01-0.87	10; 0; -5; -10
	Oh et al. [132]	3; 1.5; 0.5	50 - 600	5-40	0-1	0-15
	Yun et al. [133]	2; 0.98	500 - 3570	7-48	0-1	0; 5; 10
	Hihara & Dang [9]	2; 1	360 - 1440	4.5-36	0-1	5; 15
	Ozawa et al. [134]	3	100 - 300	5-25	0-1	10-25.4
		2	200 - 500	5-35	0-1	22.0-26.8
		1	200 - 700	10-50	0-1	5.3-26.8
	Wu et al. [122]	1.42	300 - 600	7.5 - 29.8		-40; -35; -30; -20; -10; 0
	Yamamoto et al. [119]	0.51; 1	300 - 1000	0	0.05 - 0.95	10 - 18.3
	Hihara & Tanaka [117]	1	360; 720; 1440	9; 18; 36		15
	Ducoulombier et al. [135]	0.53	200 - 1400	0	0 - 1	-10; -5; 0; 5

Table 6.3: CO$_2$ boiling flow studies in small diameter channels

table and the following paragraphs also include some studies conducted with CO_2 in macro-channels (ID > 3 mm) often cited as reference. The experimental studies listed are all again carried out in horizontal, circular stainless steel tubes. Only in the case of Park and Hrnjak [128] a copper tube was used. As pointed out above there is an ongoing debate about the actual governing heat transfer mechanism for flow boiling in mini- and micro-channels. In the specific case of CO_2 flow boiling in small diameter channels, many researchers found a constant heat transfer coefficient for low to medium vapour qualities (e.g. [9, 114, 119, 122, 129, 134]), an observation often related to a dominance of nucleate boiling [86, 87, 128] at low vapour qualities. As mentioned in section 5.3.2, due to its low surface tension more active nucleation sites exist for CO_2 leading to more frequent bubble growth [86]. Furthermore, the nucleate boiling suppression quality is delayed and extends the influence of the nucleate boiling regime towards higher vapour qualities [86], thus reducing the influence of the convective boiling regime. However, at high vapour qualities a noticeable effect of convective boiling may still occur and in this case α slightly increases. Additionally partial dry-out may occur at much lower vapour quality ($x > 0.3$) compared to standard refrigerants, causing a sudden drop in the heat transfer coefficient. This is ascribed to the general low surface tension and the low liquid viscosity of CO_2 [135]. However, the heat transfer also depends on the hydraulic diameter, the heat flux, the mass flux and the saturation temperature. The interrelation of all those effects causes complex trends of the heat transfer coefficient of boiling CO_2 versus vapour quality and sometimes contradicting results. In absence of a systematic study spanning a large range of all parameters, a clear distinction between one effect and another is in most cases very difficult. A summary of the main observations found in literature with respect to the above listed parameters is given in the following.

The most common effect presented in literature regarding the hydraulic diameter is the increase of heat transfer coefficient with the decrease of inner diameter. The basic reason for this observation is certainly the fact that whilst decreasing the tube diameter, the ratio between the surface available for heat transfer and the volume available for the flow increases. Hihara and Dang [9] were amongst the first to confirm this relation for CO_2 at $T_{sat} = 15^\circ C$. In addition, there seems to be a general agreement in literature on the dominance of nucleate boiling in small channels, in contrast to the convection-dominated heat transfer in conventional channels. An increased presence of active nucleation boiling mechanism can indeed contribute to a higher heat transfer coefficient, in particular at low to medium values of vapour quality. Results confirming this relation for the specific case of CO_2 are reported in [114, 115, 119, 130].

The other parameter having a great influence on the CO_2 boiling heat transfer in small channels is the heat flux: in general terms, the heat transfer coefficient for CO_2 increases with heat flux in the low quality region. This was confirmed by Yamamoto et al. [119], Hihara and Tanaka [117], Choi et al. [114] and is again ascribed to more active nucleation sites in the nucleate boiling regime [86]. Indeed, the critical boiling nuclei radius r_{cr} gets smaller the higher the heat flux and a smaller r_{cr} causes more possible boiling nuclei along the wall inside the tube [122]. At higher vapour qualities, where convective boiling is predominant, the effect of heat flux is much less pronounced [114]. However, an initial increase of the heat transfer coefficient might also occur due to the thinning of the liquid film along the wall, which reduces the effective thermal resistance and enhances the heat transfer [122]. The work of Yun and collaborators [86] confirmed that for qualities less than ~ 0.5 the boiling heat transfer coefficient rises with heat flux, while in the case of qualities higher than ~ 0.5 the increase of heat flux is disturbed by dry-out phenomena: actually, the higher the heat flux, the earlier the dry-out takes place [9, 122].

For what concerns the mass flux, Yun et al. [115] found that the heat transfer coefficient does not depend on this parameter for low vapour qualities. These results are confirmed by the measurements of Hihara and Tanaka [117], Yamamoto et al. [119], Wu et al. [122], Choi et al. [114], Ducoulombier et al. [135] and Pamitran et al. [130]. This is once more explained by the dominance of the nucleate boiling mechanism in this region [86]. However Choi et al. [114] found that at higher vapour qualities the mass flux becomes relevant: a higher mass flux leads to higher fluid velocity, hence higher Re, leading to an increase of heat transfer coefficient when convective boiling is predominant. Another phenomenon observed is the decrease of the dry-out quality with the increase of mass flux, as described by Hihara and Tanaka [117], Yamamoto et al. [119], Choi et al. [114]. With higher mass flux the flow pattern presents transitions to annular flow more easily and more liquid droplets get entrained into the vapour core, causing anticipated dry-out phenomena [135]. However, at very high mass fluxes and high qualities, the dry-out patches may be re-wetted and in this case the dry-out quality increases again [86]. Pamitran et al. [130] summarized their findings concerning the mass flux such that mass flux and vapour quality had an insignificant effect on the heat transfer coefficient in the low quality region. In the moderate quality region, the heat transfer coefficients increased with mass flux and vapour quality. In the high quality region, a decrease in the heat transfer coefficient occurred at a lower quality for a higher mass flux condition.

Ducoulombier et al. [135] reached the conclusion that the combined effects of vapour quality, mass flux and heat flux are much more complex and can result in a different evolution of the heat transfer coefficient. They summarized their general findings into three flow categories: (I) At low vapour qualities, α is mainly dependent on heat flux, a typical behaviour for nucleate boiling heat transfer. (II) At medium to high vapour qualities, α is strongly dependent on heat flux and moderately dependent on quality and mass flux. In this case, a combination of two mechanisms can describe the behaviour: nucleate boiling on one hand, and conduction through the thin liquid film on the other hand. (III) At high vapour qualities, α may be strongly influenced by the quality and the mass flux, while the effect of the heat flux is limited. This kind of heat transfer can be described with purely convective mechanisms occurring in annular flow.

In literature less attention has been dedicated to the direct effects of saturation temperature, although this parameter has strong effects on the properties of boiling flows. For example, the constant heat transfer coefficient and partial dry-out for low to medium vapour qualities mentioned above can mainly be confirmed for elevated saturation temperatures, whilst for decreasing T_{sat}, an increasing contribution of the convective boiling seems to be indicated by the increasing trends of α with x and no premature dry-out phenomena. The first can be explained with the higher slip ratio, the latter with the increasing surface tension and liquid viscosity of CO_2 for decreasing T_{sat}. This relation and the change in overall trend was confirmed e.g. by Wu et al. [122] and Yamamoto et a. [119]. However this means, whilst all other parameters are kept constant, that the heat transfer coefficient decreases with decreasing saturation temperature at low vapour qualities due to a reduced effect of heat transfer enhancement from nucleate boiling. It has to be noted that in this case the nucleate boiling influence is still higher than for other refrigerants [128]. However, depending on competing effects from other parameters, this shift in dominant boiling mechanism may be delayed or happens earlier with respect to vapour quality and saturation temperature. The heat transfer coefficient α may also increase again with the decreasing saturation temperature at high vapour quality, as shown in the case of Yun et al. [86] and Bredensen et al. [127]. This is explained by the higher slip ratio, the higher liquid thermal conductivity and an increasing component of convective boiling [135]. On the other hand, another phenomenon triggered by increasing saturation temperatures was observed by Ozawa et al. [134]. For saturation temperatures above 24.7°C and ID = 2 mm the heat transfer coefficient was found to decrease slightly with increasing vapour quality. This was explained with so-called intermittent dry-out, which they related to phase stratification caused by the even smaller surface tension of the fluid at this temperature, leading in general to early dry-out phenomena. This phase stratification was also apparent in the 3 mm ID tube at 18.3°C and in the 1 mm tube at 25.4°C. However when they compared those findings to the results by Yamamoto et al. [119] under similar test conditions at 18.3°C this phenomenon did not occur in the 1 mm ID tube leading to the conclusion that phase stratification and the resulting temperature difference due to the partial and temporal dry-out at the upper wall becomes significant at different pressures for different inner diameters.

The literature results reviewed above suggest that, when focusing on one specific test parameter, similar experimental results and trends between different studies may be found. But a general consensus regarding the influence of all test parameters such a mass flux, heat flux, inner diameter and saturation temperature does not exist so far. This holds for both, qualitative trends and quantitative values. In this respect, it may be useful to summarize in a single table (Table 6.4) the overall qualitative trends of the heat transfer coefficient with vapour quality as a function of the mentioned parameters, as they result from the data reported in literature. The resulting table highlights the rather complex links between all interrelating parameters and the sometimes contradicting results. First of all, due to the scarcity of experimental data gathered with small-scale CO_2 evaporators a direct comparison and cross-validation between studies is not possible since no single pair of studies could be found studying the same parameters and publishing the corresponding data as such. Furthermore, it can be interesting to notice some inconsistencies among the data summarized in Table 6.4. For instance, the study of Ozawa et al. [134] reports a constant trend of α with x for ID = 2 mm, q = 25 kW/m^2, G = 300 kg/m^{2}s and T_{sat} < 24.7°C. However, for similar parameters (ID = 2 mm; q = 18 kW/m^2; G = 360 kg/m^{2}s) but T_{sat} = 15°C Hihara and Dang [9] find an increasing trend of α with x. The discrepancy is reversed between Yamamoto et al. [119] and Hihara and Tanaka [117] for the case of a 1 mm ID tube: the first study finds and increasing trend of α with x for 23.4°C > T_{sat} > 14.2°C (q = 20 kW/m^2; G = 300 kg/m^{2}s), the latter a constant trend for T_{sat} = 15°C (q = 18 kW/m^2; G = 360 kg/m^{2}s). There are also cases where, within the same study, a small change in one parameter triggers a different trend of α with x: a change in mass flux of 200 kg/m^{2}s [135]; a change in heat flux of 9 W/m^2 [133]; or a change in T_{sat} of ~ 1.5°C [134]. However the opposite also exists, where a relatively drastic change of one parameter within the same study does not result in an overall change in trends: a change in mass flux up to 1000 kg/m^{2}s [9]; a change in heat flux of 30 kW/m^2 [133]; or a change in T_{sat} of 30°C [122]. Of course the overall parameter set has to be considered in such cases, but the discrepancies may be caused by real phenomenological differences as well as by different experimental methods and uncertainty levels between the independent studies. However, without a valid comparison between different data sets, this remains in the domain of speculation.

For the specific case of low vapour qualities, which is the focus of the present study, an extreme synthesis of the published literature on CO_2 flow boiling in small channels seems to be that the heat transfer coefficient is basically independent of x and G, however decreasing ID and increasing q have a positive effect on α, whilst a decreasing T_{sat} has a negative effect.

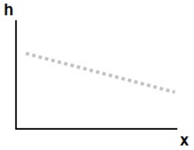

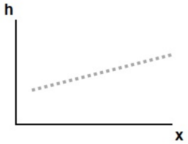

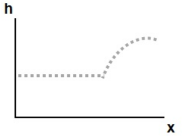

authors	ID [mm]	T_{sat} [°C]	q [kW/m^2]	G [kg/m^{2}s]	q [kW/m^2]	G [kg/m^{2}s]	q [kW/m^2]	G [kg/m^{2}s]	q [kW/m^2]	G [kg/m^{2}s]
Pamitran et al. [130]	3	10	20	300	30	300				
		3							30	450, 500, 600
		2	30	600						
		1	30	300						
Choi et al. [114]		-5							30	400, 500, 600
									40	300, 400, 500
Ozawa et al. [134]	2	> 24.7			25	300				
		< 24.7	25	300						
Hihara & Dang [9]		15	36	360, 720, 1440			18	360, 720, 1440	4.5-9	360
Yun et al. [133]		5	16-46	1000, 1500			7.2	1000, 1500		
Choi et al. [114]	~1.5	10							20	500
Pamitran et al. [130]		2							30	600
Choi et al. [114]		0							20	500
Wu et al. [122]			30	300			7.5	300		
Choi et al. [114]		-5							20	500
									30	500, 600
Wu et al. [122]		-10	30	300, 400, 500, 600			7.5	300, 400, 500, 600		
							15	400		
		-20	30	300			7.5	300		
		-30					7.5, 30	300		
		-40					7.5, 30	300		
Yamamoto et al. [119]	1	>24.7	20	300						
		< 24.7					20	300		
Hihara & Tanaka [117]		15	18, 36	360, 720, 1440					9	360, 720
Yamamoto et al. [119]	0.5	14.3	30	500, 600, 700						
		14.3	40	700, 800, 900						
Ducoulombier et al. [135]		0	10, 30	200			10, 30	400 - 1200		
		-10	10, 30	200			10, 30	400 - 1200		

Table 6.4: Overall qualitative trends of the heat transfer coefficient with vapour quality

Most studies mentioned in Table 6.3 compare their experimental data to existing correlations predicting the boiling heat transfer coefficient in ducts. There are conventional macro-channel correlations and micro-channel correlations, whilst both types are mainly based on experimental data gathered with low pressure refrigerants. The poor performance of the tested correlations was traced back by many authors working with CO_2 to the fact that the nucleate boiling component for CO_2 flow boiling in conventional channels and especially in small diameter channels is underestimated by most correlations [86, 114, 115, 117]. On the other hand, whenever correlations did provide a good prediction, this was related to the above described increasing relevance of the convective boiling component at for example higher mass fluxes or lower T_{sat}, where the suppression quality becomes smaller. In addition, it was found by Yun et al. [115] that correlations especially developed for nucleate boiling (e.g. by Cooper [59]) yield relatively good predictions of data on the two-phase CO_2 heat transfer in micro-channels. It was repeatedly stated that correlations developed for micro-channels based on low pressure refrigerants do not improve the predictability of the heat transfer coefficient [114, 130, 132]. Thome and Ribatski [111] published an overall review on boiling flows of CO_2 in conventional and small channels and they found that no available prediction method was able to predict the experimental data of CO_2 sufficiently. Therefore, in order to accommodate for the peculiarities of CO_2 boiling heat transfer in small channels, new specific correlations and models have been formulated based on data gathered with CO_2. There are correlations by

- Ducoulombier et al. [135],
- Yoon et al. [126],
- Hihara and Tanaka [117],
- Yun et al. [133],
- Choi et al. [114],
- Wang et al. [136],
- Pamitran et al. [130] and
- Oh et al. [132].

A short mathematical description of each correlation is given in Appendix A. Ducoulombier et al. [135] stated that the correlation by Hihara and Tanaka [117] in general predicted their data best (mean deviation 15%), whilst the correlation by Choi et al. [114] predicted their data with 18% mean deviation. Yamamoto et al. [119] also found a good prediction of their data by the correlation by Hihara & Tanaka [117]. In addition Cheng et al. [109, 110] proposed a phenomenological model predicting the heat transfer coefficient based on CO_2 flow boiling flow patterns which are related to the corresponding heat transfer mechanism. Some researchers who compared their data with this model found a satisfactory prediction of their data both for relatively large ID channels [129] and for small channels [122]. Ducoulombier et al. [135] found a general over-prediction of this model, which they related to both a too high contribution of the nucleate and convective boiling heat transfer, however for low vapour qualities a very good agreement between model and data was found.

It has to be mentioned that in literature often all test parameters including saturation temperature, ID and even different refrigerants are combined when comparing data to different prediction methods.

For flow boiling of CO_2 in multi-micro-channels, Yun et al. [115] confirm an increase of the heat transfer coefficient with a decrease of the hydraulic diameter (from 1.54 to 1.08 mm). The heat transfer coefficient increased with the heat flux and saturation temperature. Dry-out phenomena became more pronounced with increasing heat flux and mass flux especially at lower vapour qualities. Increasing heat transfer coefficient with increasing heat flux was also confirmed by Huai et al. [137], who carried out an experimental study of CO_2 flow boiling in a multi-port extruded aluminum tube. Furthermore they found that also a larger mass velocity led to larger heat transfer coefficients. Pettersen [138] studied a multi-channel with 25 circular channels and confirms an increasing heat transfer coefficient with heat flux at low to moderate vapour qualities. However he finds a drop in heat transfer at higher vapor qualities where the drop is more pronounced at higher temperatures and mass fluxes. Note that this study does not find an influence of the mass flux on the heat transfer coefficient over a wide range of vapour quality. Experiments with multi-micro-channels were mainly carried out at positive temperatures [135]. Thus the effect of saturation temperature on the heat transfer coefficient stays mainly unmentioned. According to the review conducted by Thome and Ribatski [111] distinct differences between small-scale single-channels and multi-channels whilst subjected to CO_2 flow boiling experiments have been found. For the latter additional complex factors, such as flow maldistribution and/or flow oscillations can influence the evaporation processes and thus the heat transfer. Furthermore it was found that in multi-channels it is more difficult to measure the local heat transfer coefficients correctly, where the individual channel walls may act as fins and the thermal efficiency of such micro-channel devices is more complex to predict. Moreover often missing information makes a comparison with prediction methods difficult.

Literature review - summary

In general it was found that

- an arbitrary definition of micro-channels is used so far and no general definition is yet given.
- channel size effects are not yet fully understood, thus
- a meaningful definition of a transition criterion between macro- and micro-channels still has to be found.
- phenomena and anomalies found for the heat transfer during flow boiling in small channels are often still explained with the known heat transfer mechanisms, regardless of possible new processes occurring.

The heat transfer coefficients during forced convective boiling is so far typically measured with an experimental uncertainty in the order of 10-20%. Any fine structure and second-order effects are thus lost in the data [61]. Thus many publications on micro-channel cooling seem to contradict each other. The found discrepancies among the experimental data gathered by independent research teams may be caused by a high channel dimension uncertainty, incorrect data reduction methods and improper design of the test facility. As long as not all uncertainty sources in the experimental data can be eliminated, no attempted correlation or flow pattern based model can claim to predict data in an accurate way [6] and the main error sources can be summarized as:

- most models are based on limited test conditions, such as small range of saturation temperatures, mass fluxes, heat fluxes, channel shape and diameter whilst working with a single test fluid.

- many correlations on fluid flow and heat transfer in micro-channels are found empirically on those limited parametric conditions and thus cannot predict very well a different data set. This has the disadvantage of non-generality and defeats the purpose of prediction.
- non-empirical models, although confirmed to be more accurate in predicting flow boiling phenomena, are still rare and some physical behaviours in the channels are still subject of speculation.

The main shortcomings of the experimental research with evaporative CO_2 in small channels are:

- no systematic research was carried out on a larger scale so far thus the existing data is very limited and inconsistent.
- the available correlations for CO_2 flow boiling in small channels are scarce and suffer from the general limitations mentioned above, whilst too little data is available for a cross-validation.
- the literature analysis suggests that the reduced pressure and thus the CO_2 saturation temperature, introduce additional factors that should be taken into account by predicting correlations.

Resume Before adding more flow boiling prediction models to the already extensive list without sound knowledge of the underlying processes, more basic and systematic experimental research is needed. It is necessary to extend the existing database on CO_2 two-phase pressure drop and heat transfer in small channels towards a larger range of saturation temperatures, mass fluxes, heat fluxes, channel shapes and hydraulic diameters, whilst improving the accuracy level compared to exiting experimental studies. Uncharacteristic to other CO_2 flow boiling applications, the range in saturation temperature explored for detector cooling in HEP experiments is very wide and more attention should be given to the effects of saturation temperature on the CO_2 flow boiling behaviour with respect to pressure drop and heat transfer.

CHAPTER 7

Experimental setup for detector cooling R&D with mini- and micro-scale carbon dioxide evaporators at CERN

Due to the reasoning given in the literature review this study is a purely experimental and investigative operation to extend the existing data in a consistent and reliable way and thus to improve predictive methods in the future.

7.1 Mini- and micro-scale CO_2 evaporators investigated for this study

For the implementation into low-mass integrated thermal management solutions for detector cooling in HEP experiments following heat exchanger layouts have been investigated further whilst being submitted to evaporative CO_2 flows:

1. small scale metallic tubular evaporators in single-channel configuration and
2. silicon-substrate-based small-scale heat exchangers in multi-channel configuration.

The first is implemented into detector cooling strategies as described in 4.3.1, the latter is needed for the detector cooling strategies as described in 4.3.1. Results from the more basic single-channels can complement the rather multifaceted findings from the multi-micro-channels and vice versa. Thus it is possible to address the need of a deeper understanding of CO_2 boiling properties at mini- and micro-scales at all temperatures of interest and on various levels.

7.1.1 Tubular evaporators

Very basic and accurate data gathered on single-channels are of immense value for the directly involved research community working in general with two-phase micro-channel cooling and evaporative CO_2 as refrigerant in particular. Simple small-diameter tubular evaporators are directly used for detector cooling at CERN and thus a reliable forecast can be generated which will enhance the design optimization process of future mini- and micro-channel evaporators in the context of HEP experiments.

Channel dimensions

Following tables summarize the various dimensions and materials of single channels which were obtained for long-term experimental studies. It has to be differentiated between circular and rectangular single channel cross-sections. Table 7.1 lists the test channels with circular cross-section with their inner and outer diameter (OD) and an example for the corresponding metallic and glass tubes is depicted in Figure 7.1(a) and Figure 7.1(b). Table 7.2 lists the test channels with rectangular cross-section depicted in Figure 7.1(c). The standard length of all tubes is 200 mm, which can be reduced for interconnection purposes. Please note that only a few of the shown and listed dimensions were tested and characterized for this thesis. The motivation for the procurement of this wide variety of channel dimensions and materials is based on the intention of creating a large 'experimental map' where cross-comparison is possible between the different channel dimensions and materials. The research proposal is to compare the test results of different channel geometries at various refrigerant mass fluxes, heat fluxes and saturation temperatures: To study (i) tube size transition effects, investigations may be carried out on the same tube material e.g. stainless steel but different diameters; (ii) surface roughness effects can be studied with investigations on the same inner diameter e.g. 0.5 mm but different channel materials; (iii) interesting geometry effects may result from investigations on approximately the same cross-section but comparing between circular and squared channel cross-sections.

Stainless steel (nominal)	
ID [mm]	OD [mm]
0.13	1.58
0.25	1.58
0.5	1.58
0.75	1.58
1	1.58
1.5	3.175
2.15	3.175

(a)

Titanium (nominal)	
ID [mm]	OD [mm]
0.3	1.58
0.5	1.58
0.8	1.58

(b)

Glass (Borosilicate) (nominal)	
ID [mm]	OD [mm]
0.13	0.99
0.25	1
0.3	1
0.5	1.6
0.8	2.65
1	4
1.5	5
2.2	9

(c)

Table 7.1: Procured single channels with circular cross-section.

Glass (Borosilicate) (nominal)	
inner cross-section [mm]	wall thickness [mm]
0.1 x 0.1	0.05
0.2 x 0.2	0.1
0.3 x 0.3	0.15
0.5 x 0.5	0.1
0.7 x 0.7	0.14
0.8 x 0.8	0.16
0.9 x 0.9	0.2

Table 7.2: Procured single channels with rectangular cross-section.

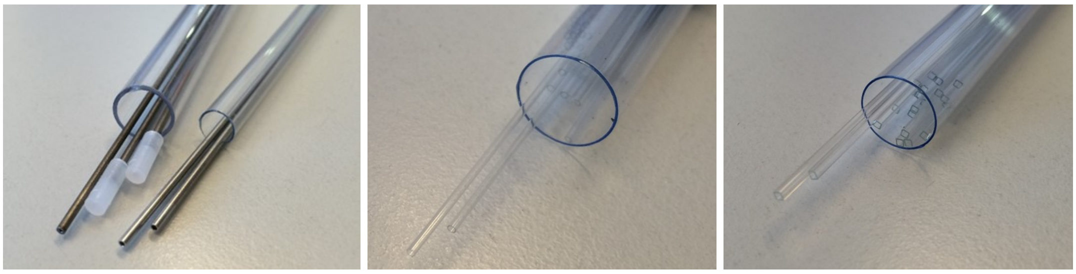

(a) (b) (c)

Figure 7.1: Single-channels with circular hydraulic diameter: a) left: titanium, right: stainless steel; b) borosilicate glass; Single-channels with rectangular hydraulic diameter: c) borosilicate glass.

The glass channels in addition allow for direct flow visualization which is a very crucial part of any recent study on flow boiling in small channels. In order to supply a heat load to the glass tubes it is possible to deposit Indium Tin Oxide (ITO) onto the channel surface, which is a transparent conducting oxide and does not interfere with the tubes transparent properties. Another possibility is considered where the test tube is divided into one half metal and one half glass. Here only the metal part is heated whilst the glass part can be used for diabatic flow visualization. However, this has not been applied for this thesis, but should be kept in mind for future experiments.
As mentioned above only a few single-channel dimensions from the discussed research plan were tested and characterized for this thesis. Stainless steel tubes with

- 2.15 mm,
- 1 mm and
- 0.5 mm

inner diameter have been studied and tube size transition effects (i) can be evaluated.

7.1.2 Multi-micro-channels

Multi-micro-channels have been tested with evaporative CO_2 due to the immediate need for effective detector cooling in HEP experiments and a more thorough understanding of their thermal-fluidic behaviour.

Channel design & dimensions

The layout of the studied multi-micro-channel devices was agreed upon by a collaboration between the Laboratoire de Physique Nucléaire et de Hautes Énergies (LPNHE) in Paris and the EP Detector technology department at CERN. Multiple micro-channel evaporator layouts were etched into a six inch Ø silicon wafer (0.5 mm thickness) by Deep Reactive-Ion Etching (DRIE) and the micro-fluidic layout is then closed by a flat wafer to produce circulating devices. Under normal circumstances and for the final application of the evaporator, the silicon wafer with the micro-channel patterns is bonded to a second silicon wafer. However for this R&D project the channel wafer was anodically bonded to a glass wafer (Borofloat, 2 mm thickness) for the visual characterization of the flow inside the channels. This leads to valuable new insights concerning evaporative CO_2 flowing in small channels. Figure 7.2 shows an example of such compound wafer. Three wafer of this kind were produced and shipped to CERN for further processing and testing. Five different micro-channel layouts can be seen on the unprocessed wafer. There are three 20 mm x 40 mm devices and one 20 mm x 100 mm. Each featuring 13 channels with special inlet restrictions and outlet manifolds. There is one 20 mm x 80 mm device with 11 channels. The device shown at the bottom was designed for a future interconnection of these channels. In addition there is a circular micro-channel layout along the edge of the wafer with only three individual channels, which can be more closely compared to single channels. The mentioned individual devices had to be removed and cut from the common substrate before testing. Since also a circular cut was involved to retrieve the annulus with the circular channel-layout, this proved to be non-trivial and non-standardized cutting (dicing) methods had to be chosen. For more information on the faced difficulties during the preparation of these devices until testing please refer to Appendix C. Again not all devices could be tested within the scope of this thesis. Tests were carried with the device shown in Figure 7.3(a). This silicon evaporator shall simulate a possible multi-micro-channel configuration for the thermal management of a pixel module. Figure 7.3(b) shows the micro-fluidic footprint of this device. Sub-cooled liquid CO_2 enters the device through a circular inlet on the silicon side and is immediately distributed to 13 rectangular channels, 0.2 mm in width and 0.12 mm in height (D_h = 0.15 mm), via 13 inlet restriction. The inlet restrictions are very narrow channels and cause a larger pressure drop than the one that pure liquid flow would experience in the main channels. The restrictions are 0.06 mm in width and 0.1 mm in height and have the same length of 6.0 mm. By entering the inlet restrictions in sub-cooled conditions it is possible to ensure that liquid CO_2 is evenly distributed among the channels. The restrictions induce the same effect as capillaries which are installed before the evaporator line of standard refrigeration configurations. By inducing a sensible pressure drop in the incoming liquid flow the restrictions

- ensure a uniform flow distribution among the evaporator channels;
- bring the sub-cooled liquid to saturation conditions;
- block possible local back-flow in the channels created by large bubbles, thus preventing known instability phenomena often observed in multi-micro-channels [139]

The main evaporator channels are in turn designed to have all a very similar length (67.5 mm ± 18%). Before reaching the outlet of the evaporator the two-phase fluid is collected in a manifold. The "pillars" etched into this area reduce the size of the free surface exposed to the high CO_2 pressure while minimizing the two-phase pressure drop at the outlet.

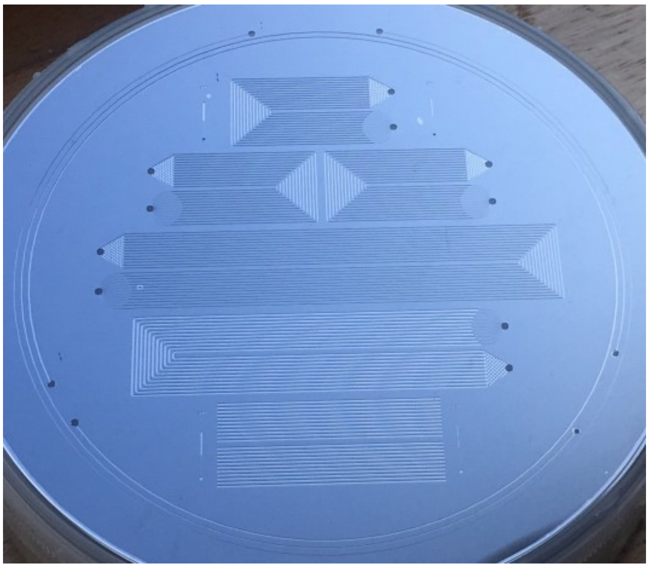

Figure 7.2: Compound wafer with multiple multi-micro-channel layouts.

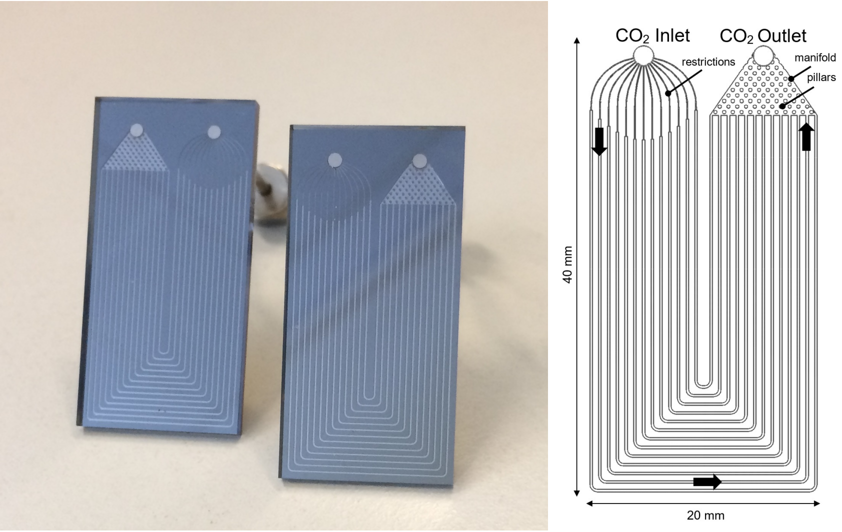

(a) (b)

Figure 7.3: Multi-micro-channel device tested for this study: a) real life; b) schematic.

7.2 Preliminary experimental setup

To study the envisioned small-scale CO_2 evaporators they have to be submitted to experimental flow boiling tests and thus an experimental setup providing boiling CO_2 flows was required. To facilitate the needed experiments there was an already existing experimental setup. As a first approach it was used for the proposed experiments and will be explained in more detail in the following paragraphs. However, the system exhibited some limitations with respect to the suggested research plan and reasons will be given on why it was used as a preliminary setup only. The main goal of the experiments carried out with this setup was to obtain data on evaporative CO_2 pressure drops and heat transfer coefficients in single mini- and micro-channels. The preliminary setup can be divided into two main parts. There is (i) a refrigeration unit which supplies subcooled liquid CO_2 to the (ii) experimental section.

7.2.1 Refrigeration unit

The CO_2 cooling system which was available for initial tests was a manual carbon dioxide cooling blow system which was developed for research purposes at the Dutch National Institute for Subatomic Physics (NIKHEF) in Amsterdam. This carbon dioxide cooling system has been already used for cooling tests of detector units which were developed for the upgrade of the ATLAS Inner Detector [140]. It is an open loop system which means that the cooling medium, carbon dioxide, is blown into the atmosphere after cooling the mock-up detector unit, hence the name blow system. The blow system can be described as the evaporator section of a common refrigerator cycle. Compressing and condensing the CO_2 back to liquid is replaced by just venting it to the atmospheric surroundings. The CO_2 is provided by a CO_2 gas bottle instead of a condenser which is normally implemented into a closed-loop refrigeration cycle. An open loop CO_2 blow system has the following advantages towards the more complex closed loop system:

- no pump is needed,
- the system is easy to build and to use,
- the start-up time is short and
- the setup is relatively cheap.

Therefore several of such blow systems were distributed to various research facilities in Europe which were involved in studies concerning detector cooling R&D. Amongst these institutes is the Physics Institute of the University of Manchester where some initial tests for this present study were carried out. Figure 7.4 shows a schematic of the fluidic circuit within the CO_2 blow system (without experimental section).

In the following please consider the numbered points given in the schematic. Liquid CO_2 enters the system from a gas bottle at room temperature. The CO_2 flows through a filter and into the heat exchanger (1). In the heat exchanger the CO_2 is sub-cooled further with CO_2 from the experimental return line. Before the CO_2 enters the experiment, the pressure drops to a set value which can be adjusted with a relief valve (6). This isothermal expansion can provide coolant temperatures down to -35°C. When the coolant enters the experiment, heat from the detector mock-up is absorbed and initiates boiling. The needle valve between (2) and (3) is used to regulate the mass flow. After experimental cooling the CO_2 passes the first (return-line) heat exchanger before it is heated to about

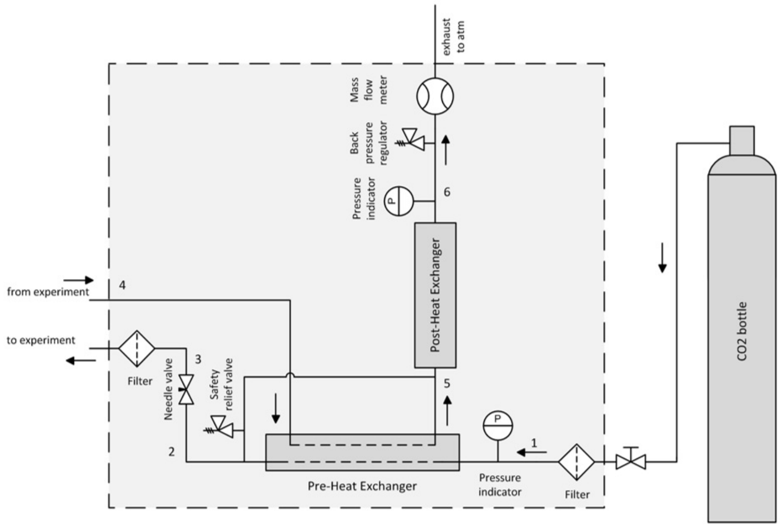

Figure 7.4: Schematic of the CO_2 blow system.

20°C in a second heat exchanger to prevent freezing at the exhaust. This spiral heat exchanger is situated in an open water reservoir with a set water temperature of 40°C. After passing through a Coriolis flow meter, the CO_2 finally is blown into the atmosphere. Figure 7.5 shows the blow system as it is provided by NIKHEF and the altered blow station which was available at the University of Manchester (gas bottle not shown). Figure 7.6 displays the thermodynamic cycle of the CO_2 blow system in the pressure-enthalpy diagram. It has to be distinguished between the continuous line which is the blow system cycle and the dashed line which is the imagined abandoned vapour-compression cycle. Generally, the vapour compression refrigeration system consists of an expansion valve, an evaporator, a compressor and a condenser. Instead of the compressor inlet, in the blow-system the overheated vapour is now heated further to room temperature, expanded to atmospheric pressure and vented to the surroundings. Before the adiabatic expansion the liquid is sub-cooled to minimize the vapour quality at the evaporator inlet. For more information on this refrigeration unit, please refer to [140].

(a) (b)

Figure 7.5: CO_2 blow system in two different configurations: a) initial version by NIKHEF; b) altered version at the University of Manchester.

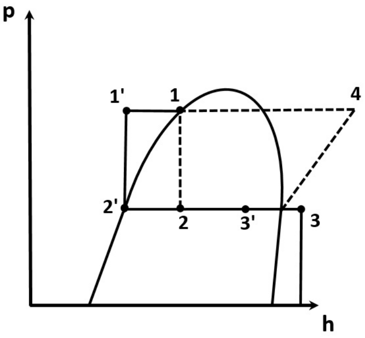

1 - 1’ liquid from the bottle is sub-cooled
1’- 2’ adiabatic expansion
2’- 2 heat from the detector experiment is absorbed and part of the CO_2 changes from liquid to vapour.
2 - 3’ pre-cooling of the liquid from the bottle
3’- 3 external heating of the CO_2 to about 20°C to prevent freezing
3 - Expansion of CO_2 to atmospheric pressure

Figure 7.6: Thermodynamic cycle of the CO_2 blow system in the pressure-enthalpy diagram.

7.2.2 Experimental section

The fluid delivered by the refrigeration unit is driven through a simple experiment as shown in Figure 7.7. The main components of the rather straightforward experiment are two absolute pressure sensors (UNIK 5000, General Electric) and two in-flow temperature sensors (PT100, $4-$ wire configuration, Rodax) installed at the in- and outlet of an experimental stainless-steel tube, 200 mm in length. Accordingly both ports for temperature and pressure are installed by means of a fluid-mechanical cross. Six thermocouples (K-Type) are fixed on the outer tube wall by means of a steel-reinforced epoxy putty. The distance between each thermocouple is of about 30 mm. The stainless steel test tubes are heated via Joule heat to simulate an experimental heat load. Before re-entering the circuit of the blow system an additional needle valve was installed to regulate the sub-cooling level of the liquid whilst leaving the upstream needle valve (see Figure 7.4) fully open. Thus in theory it is possible to run calibration tests with liquid single-phase CO_2 for the validation of the experimental setup. All components of the experimental section are insulated by two insulation sheets pressed together. The flowmeter (mini CORI-FLOW, Bronkhorst) of the blow system was used to evaluate the flow rate applied to the test channel. All sensors are read out via National Instruments hardware and LabView software. This includes the pressure and temperature sensors, the thermocouples, the flowmeter and some of the parameters measured within the blow system.

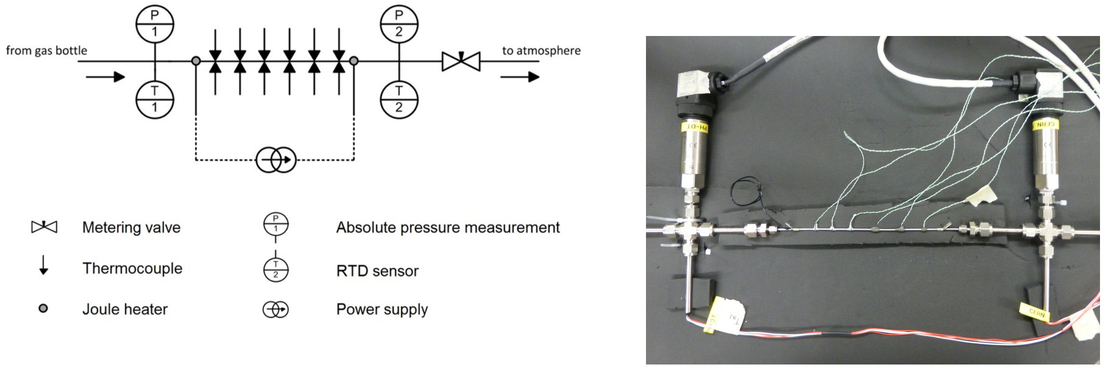

(a) (b)

Figure 7.7: Experimental test section at the University of Manchester in combination with the CO_2 blow system: a) schematic; b) real-life.

7.2.3 Preliminary results and findings

The test matrix - as given in 7.1.1 - with inner tube diameters ranging between 2 mm and 0.13 mm was prepared prior to the experimental tests. Whilst mass fluxes between 100 and 1400 $\mathrm{kg/m^2s}$ were anticipated, different heat loads shall be applied. However it was soon discovered that the initial test matrix could not be realized with the given setup. The most disturbing finding was that no stable flow could be achieved with the system. So steady-state data could not be obtained for most of the tested cases. Figure 7.8 shows the evolution of the flow rate during one day of measurements. It is obvious that stable flow cannot be assumed at any point. Furthermore the gathered data showed uncharacteristic behaviour and contradicted the initially given input parameters. It showed gas-phase at the inlet and liquid-phase at the outlet of the test section which was not possible under the given circumstances. The data had to be discarded and the error was interpreted as a sensing mistake. This error was not compensable with applying off-sets in the data processing procedure without losing valuable information on the actual measurement. With the existing blow cooling system the needed experimental data cannot be provided reliably. At best both parts of the preliminary setup (refrigeration unit and experimental section) which were described above have to be altered in order to optimize the quality of the gathered data. The disadvantages of the refrigeration unit can be summarized as follows:

- unstable flow and thus no steady state conditions possible,
- no recirculation of CO_2 possible,
- limited in saturation pressure and temperature close to ambient temperatures and

- pump-less refrigeration unit is more susceptible to high pressure drops in the experiment causing large instabilities of system parameters.

Note that the inner tube diameter for the experimental cooling R&D of the ATLAS Inner Detector [140] - for which this refrigeration unit was conceptualized - was > 1 mm where the overall pressure drop was less pronounced and the flow could reach steady-state conditions more easily. The disadvantages of the experimental section on the other hand are:

- insufficient insulation causing extensive heat leaks to the surrounding,
- and less accurate temperature and heat transfer measurements.
- absolute pressure sensors are less accurate to measure pressure drop and
- the in-flow temperature sensors as used in this setup cause various sensing errors.

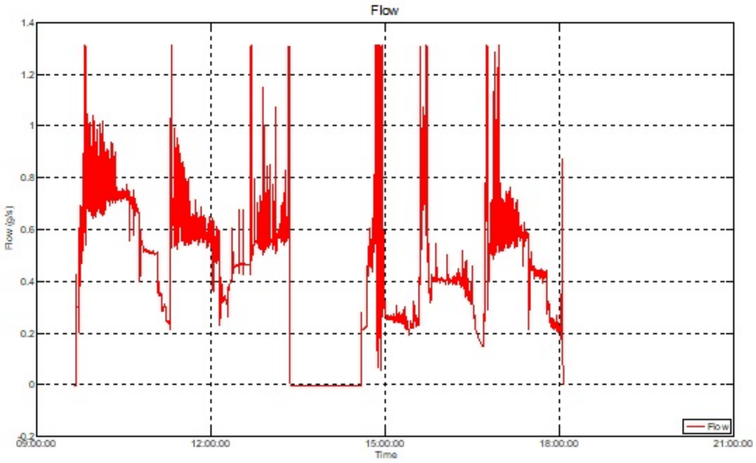

Figure 7.8: Flow rate signal during measurements with blow system.

Resume Due to the limitations of the blow system with respect to the suggested research plan it was discarded for further experimental tests. A new and purpose build experimental setup for evaporative cooling with CO_2 was needed to provide reliable data on pressure drop and heat transfer within small-scale evaporators.

7.3 New experimental setup

The setup optimization process was assessed by means of the immediate shortcomings found whilst carrying out the measurements on the first setup but also by means of limitations encountered with similar test rigs described in literature. In general

- higher accuracy levels,
- more consistent and reliable data sets and a

- generally larger data base
- including a more extensive range of fluid temperatures

were needed to study CO_2 pressure drops, heat transfer coefficients and flow patterns in mini- and micro-channels. An entirely new test setup was initiated at CERN to address those issues. The final version of the new experimental setup can again be divided into two main parts. There is (i) a new transportable refrigeration unit which supplies sub-cooled or saturated liquid CO_2 to a (ii) newly designed experimental unit. The blow system was discarded completely as refrigeration unit whilst the experimental section was extended and enhanced drastically compared to the first version.

7.3.1 Refrigeration unit

The new refrigeration unit is a Transportable Refrigeration Apparatus for CO_2 Investigation (TRACI) which was recently developed at CERN for experimental studies on detector cooling for high energy physics experiments at the LHC and other research facilities [141]. Like all existing CO_2 cooling systems at CERN, TRACI is also operated using the so-called 2PACL concept (2-Phase Accumulator Controlled Loop) [142]. Here the cooling plant is connected to an experimental setup and both together form a pumped 2-phase feedback loop, whilst the saturation temperature of the fluid is solely controlled by an accumulator filled with liquid and vapour. Figure 7.9 gives a schematic of the general 2PACL system. There is a liquid pump, an internal heat exchanger, a restrictor (capillary or calibrated orifice), an evaporator (experiment), a condenser and a two-phase accumulator. For the following description of the operational mode, please refer to the numbers given in the schematic: The pump compresses the subcooled liquid from the condenser (1-2). Then the liquid is heated by an internal heat exchanger (2-3) where it exchanges heat with the return flow from the evaporator (5-6). The pressure of the liquid decrease to the pressure in the accumulator passing through the restrictor (3-4). Liquid expansion takes place ending with saturated liquid at the entrance of the experiment. The evaporation of CO_2 takes place due to an experimental heat load (4-5) and the liquid vapour mixture from the evaporator passes through the above mentioned heat exchanger (5-6), before it is condensed and subcooled again in the condenser of the cooling plant (6-1). The subcooled liquid is then recirculated to the experiment again undertaking the same steps as described. The temperature of the two-phase CO_2 in the evaporator is the main parameter which has to be controlled in a 2PACL loop. This is achieved by the accumulator (P7) in the cooling plant. In the accumulator vessel there

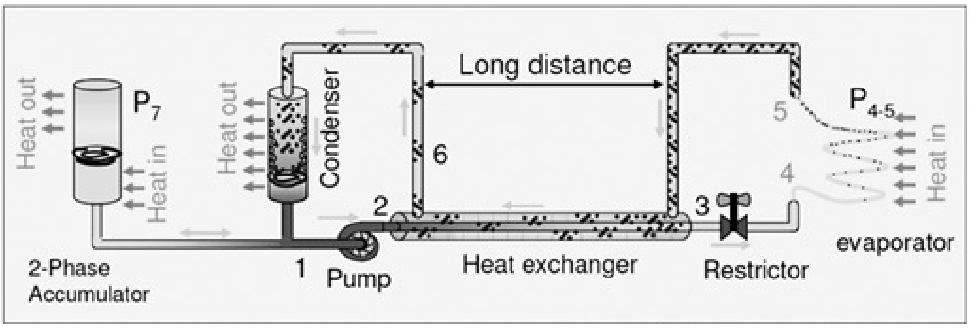

Figure 7.9: Schematic of the two-phase cooling principle used at CERN [142].

is always a liquid/vapour pool, whilst its pressure is controlled by heating or cooling. The fluidic distance between the evaporator and the accumulator is relatively small such that the pressure drop in the connecting line is very small. Thus the pressure in the evaporator is directly linked to the pressure in the accumulator giving only a little offset. In this way the pressure in the evaporator can be controlled accurately by controlling the pressure in the accumulator. Furthermore the pressure in the return line defines the saturation temperature of the two-phase flow. Therefore this system is controlled by the accumulator only and is consequently called 2-Phase Accumulator Controlled Loop. The transfer line from the cooling plant to the evaporator runs concentrically inside the return line from the evaporator. In this way, the inlet liquid temperature is basically the same of the outlet two-phase temperature, and the CO_2 before the inlet of any experiment is always in slightly subcooled liquid state, due to the fact that it has a slightly higher pressure.

The TRACI system – in addition - is called I-2PACL (Integrated 2-Phase Accumulator Controlled Loop) which is a compact version of the 2PACL concept for laboratory applications where piping and control are minimized, whilst the range of operation is maximized and flexibility is sustained.

In the TRACI I-2PACL the accumulator is cooled by liquid CO_2 circulating in the system. All the subcooled cold liquid is pumped through a heat exchanger in the accumulator which is therefore directly cooled by the liquid CO_2 circulating in the system, while a heater regulates it to the desired saturation temperature. This method differs from the 2PACL concept where the cooling action in the accumulator is obtained through a separately controlled heat exchanger connected to the primary chiller. The approach used for the TRACI units is energetically less efficient, but it makes the system regulation much easier, while allowing for a wider range of temperatures. In Figure 7.10 a schematic of the TRACI I-2PACL concept is shown. The transfer line between the cooling plant and the experiment is realized via a flexible concentric hose which is approximately 3 m long. A local box on the other

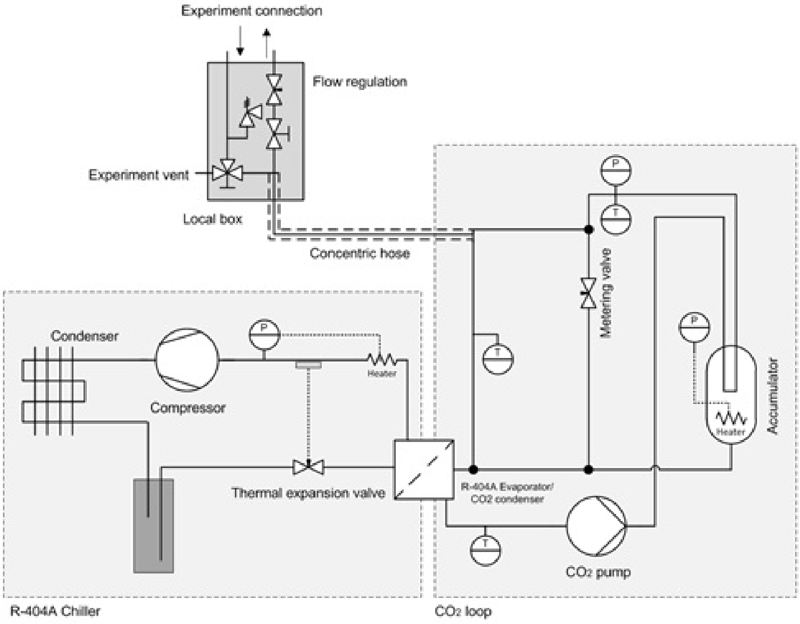

Figure 7.10: Schematic representation of the TRACI I-2PACL concept. Adapted from [76].

side of the concentric tube allows for a robust connection to the experiment and has some additional flow regulating features. Due to an efficient heater controller a very stable temperature control is achievable with the I-2PACL unit. An operational range of -25°C to +20°C in saturation temperature is possible with this cooling plant. The flow rate which can be delivered by the plant lies between 1.8 and 4.0 g/s. Therefore by-passing of some of the delivered liquid is essential for the proposed experiments with small inner diameter tubes and micro-channels. In Figure 7.11 the TRACI cooling plant is shown with one side panel taken off to show the internal components and the concentric flexible hose. Figure 7.12 displays the thermodynamic cycle of the I-2PACL in the pressure-enthalpy diagram explaining the major thermodynamical steps of the two-phase cooling cycle. It is obvious that the cycle does not show much resemblance with the normally used vapour-compression cycle and the vapour quality at the evaporator inlet is per design very close to 0 or minimally sub-cooled.

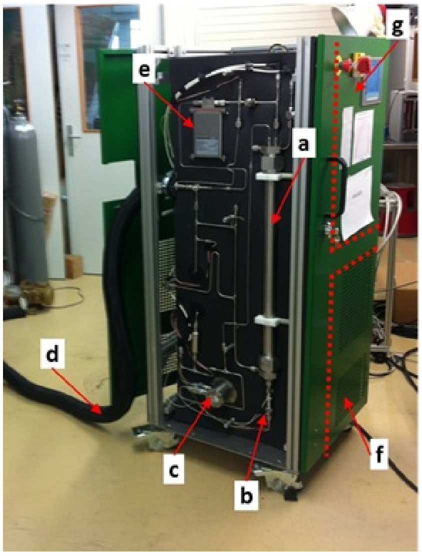

Figure 7.11: TRACI CO_2 cooling plant (one panel removed): a: accumulator; b: accumulator heater; c: pump head; d: transfer line; e: mass flow meter; f: primary chiller housing (inside); g: monitor, control and user interface area (inside).

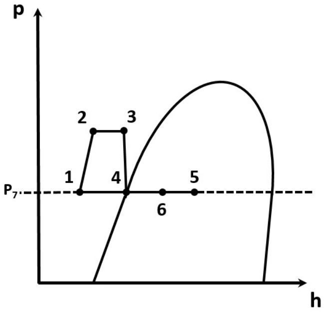

1-2 Sub-cooled liquid is compressed by the pump. This results in increasing pressure and temperature.

2-3 Liquid CO_2 passes through the spiral heat exchanger inside the accumulator exchanging heat with saturated liquid inside.

3-4 The pressure of the liquid decrease to the pressure in the accumulator.

4-5 CO_2 liquid evaporates in the experiment due to heating.

5-6 Two-phase CO_2 in the return line exchanges heat with CO_2 liquid.

6-1 Two-phase CO_2 passes through the chiller (air cooled R-404A).

Figure 7.12: Thermodynamic cycle of the I-2PACL in the pressure-enthalpy diagram.

7.3.2 Experimental unit

The fluid delivered by the cooling plant is pumped through a circuit as shown in Figure 7.13, where the experiment inside the orange dashed box is essentially the experimental section with a single tube shown for the preliminary experimental setup in Figure 7.7. However the increased complexity of the entire new experimental unit compared to the preliminary one will become obvious with its description below. For simplicity, in the following the full control and measurement unit is referred to by the term experimental unit, whilst the term experiment only refers to the mini- or micro-channel device under test. Figure 7.14 shows the experiment for the case of multi-micro-channels under test schematically.

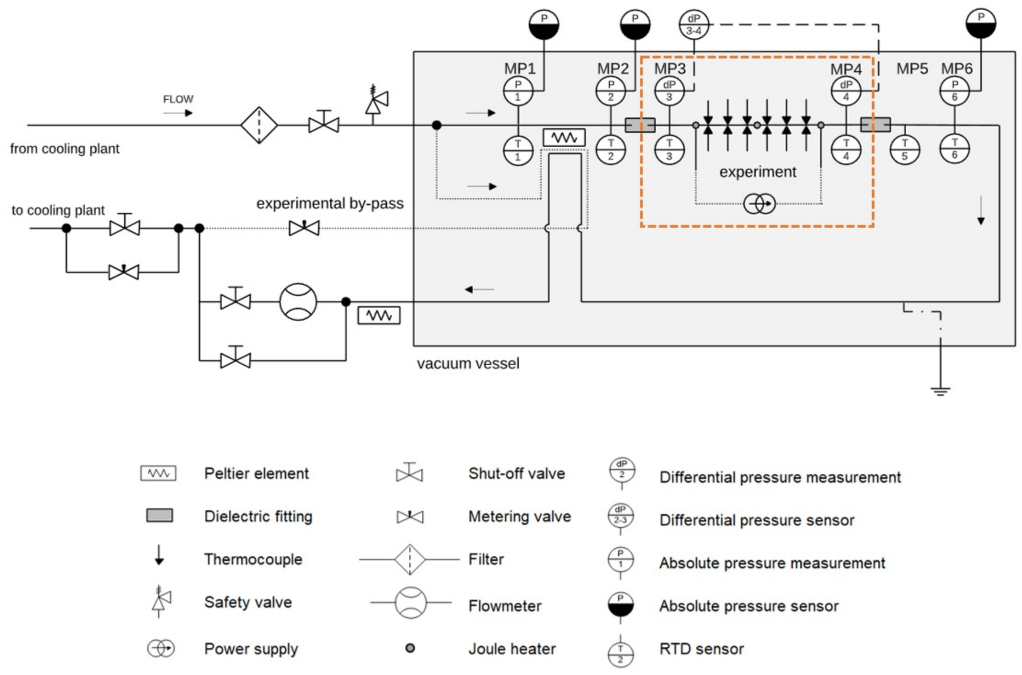

Figure 7.13: Schematic of the fluidic system with a simple straight micro-pipe mounted as test section.

Fluidic system and measurement points

The subcooled liquid from the refrigeration plant arrives at the experimental unit via aforementioned local box. Here the experimentalist has the first possibility to regulate the influx of liquid into the experiment by means of a regulating valve, where the flow can be by-passed partially back to the cooling plant. The inlet and the outlet of the experimental unit are connected to the local box via two short flexible lines. The fluid then enters a system of 6 mm OD (4 mm ID) stainless steel tubing tracing a course as described in the following. The incoming fluid passes various passive components before any measurements are carried out: a filter (inline-filter, 25 µm, type F-MI2, HNP Mikrosysteme GmbH), a shut-off valve (ball valve, SS-43GES6MM, Swagelok) and a safety valve (HPRV Series Proportional Relief Valve, HPRVSM6A-KZ-K3-1305, PARKER HANNIFIN EUROPE SARL). The CO_2 then enters a stainless steel vacuum vessel where the actual evaporator experiment

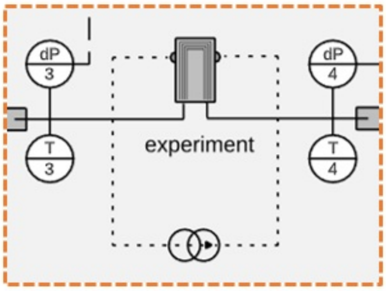

Figure 7.14: Detail: Schematic of experiment with multi-micro-channels.

is taking place and all the measurements relevant to the proposed experiments are carried out. The vacuum vessel is installed to achieve adiabatic test conditions for more accurate temperature and heat transfer measurements. The vessel was manufactured at the Centre de Recherches du Cyclotron in Louvain-la-Neuve, Belgium, whilst only one of the main vessel flanges was altered at CERN to suit the experiment's proposal. The alterations where mainly done to implement the feed through of fluid-mechanical and electrical components. Figure 7.15 shows the open vacuum vessel with the modified flange with vacuum feed throughs on the left side (early stage of the project, March 2017). To determine the fluid saturation temperature at various locations in the experiment the circuit is equipped with six local fluid pressure and temperature measurement points (MP), realized by means of stainless steel cross fittings (Swagelok SS-6M0-4 series), installed vertically. Custom-made resistance temperature detectors (RTD, PT100, 4- wire configuration) are inserted into the bottom outlet of the crosses obtaining T$_{MP}$ where the small sensing elements are directly submerged in the flow and thus no major flow disturbance has to be expected. These temperature sensors were calibrated by means

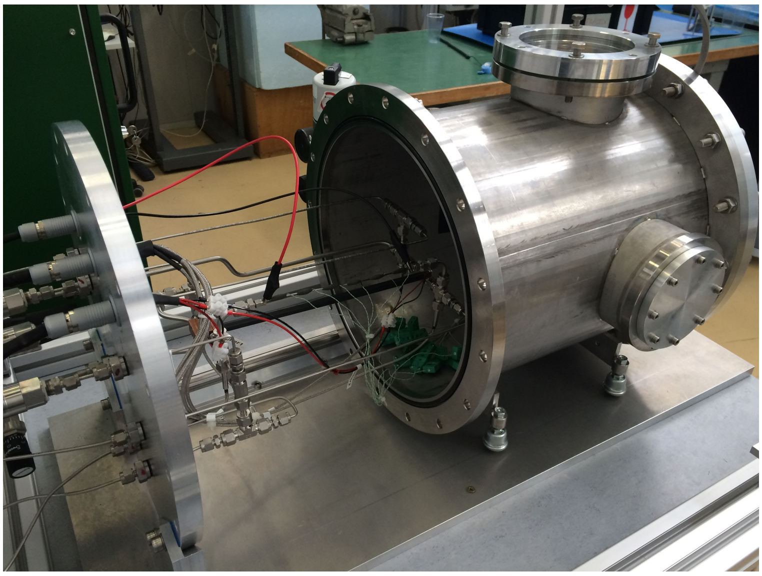

Figure 7.15: Vacuum vessel at early stage of the project (March 2017).

of a secondary standard reference thermometer (Fluke, HART 5626-12). For the absolute pressure P_{abs} measurements, 1.6 mm ID stainless steel pressure lines connected to the top outlet of the cross fittings are fed through the main flange of the vessel, whilst the actual sensor (General Electrics, UNIK 5000) is installed outside the vacuum vessel. Figure 7.16 shows a schematic of such measurement point. After entering the vacuum vessel, the fluid passes the first measurement point (MP1) where temperature and absolute pressure are acquired mainly validating the set parameters of the cooling plant. Subsequently a Peltier element is installed in the circuit to function as a pre-heater or cooler to bring the fluid to a desired temperature and thus to control the inlet vapour quality of the experiment, if desired. The Peltier element is fixed between small copper blocks mounted onto the 6 mm OD tubing of the main circuit whilst one side of the Peltier is brought in contact with the return line in order to provide a heat sink for the correct functionality of the Peltier effect in vacuum. The Peltier is connected to a power supply and a relay outside of the vacuum vessel, so the user can switch between its heating and cooling properties. After this heating/cooling section the fluid passes through a second measurement point (MP2) monitoring the effectiveness of the heating/cooling process with the Peltier element. A dielectric fitting separates this measurement point from a third measurement point (MP3) which acts as the inlet of any test section, where a differential pressure port is installed. Dielectric fittings were installed on either side of the experiment to isolate it from any stray currents caused by the connected electronics and to act as thermal separators between the test section and the remaining circuit. The setup is designed to test horizontal single mini- and micro-channels of 200 mm length - or shorter - (e.g. stainless steel, titanium), glass tubes of equivalent size but also multi-micro-channel devices. For this study (i) stainless steel tubes of 200 mm length and various inner diameters and (ii) a silicon multi-micro-channel device has been tested. The fluid-mechanical integration of the experiment into the experimental unit, the application of a dummy heat load and the temperature measurements on the test device differs for both approaches and will be explained in more detail in chapter 8 after this generic description of the experimental unit. After the experiment the fluid passes the fourth measurement point (MP4), where differential pressure and temperature are acquired as the outlet parameters of the experiment. The pressure drop ΔP between the inlet and the outlet of the

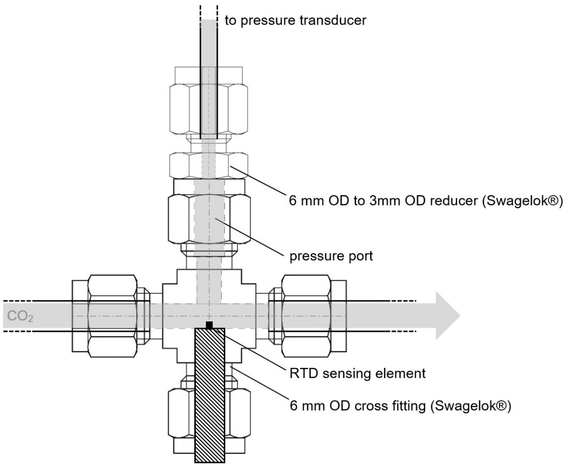

Figure 7.16: Measurement point.

device under test is measured with a differential pressure transducer (Endress+Hauser, DeltabarM). The two following measurement points are installed for monitoring reasons and possible upgrades in the future (MP5: temperature, MP6: temperature and absolute pressure). After passing MP6 the fluid exits the vacuum vessel again. Two different flow meters cover two different mass flow test ranges. For flow rates from 4 g/s to 0.13 g/s a first Coriolis mass flow meter (Rheonik, RHM015) with an accuracy of 0.2 % of reading is used, whilst for flow rates from 0.17 g/s down to 0.003 g/s a second Coriolis mass flow meter (Bronkhorst, mini CORI-FLOW M13) with an accuracy of 0.2 % of reading $+1.4 \cdot 10^{-4}$ g/s is used in fully vaporized conditions after operating the dedicated by-pass valves. For very small flow rates which are desired in micro-channel applications, there is a second possibility to split the fluid coming from the cooling plant by using a second by-pass. This by-pass is installed in such way that the fluid flow coming from the cooling plant and the local box can be reduced further. Just after entering the vessel the flow is split in two. Whilst the ‘main flow’ follows the fluidic path just described above, the by-pass flow is guided past the Peltier element and then outside the vessel where a valve is installed for flow control. Opening this valve reduces the fraction of the flow going through the actual experimental device. This by-pass fulfils a second purpose. By guiding the by-pass past the first Peltier element, the Peltier element can thus draw its energy from the by-passed flow whereas it would be otherwise left without energy source/sink during vacuum operation. At the very end of the experimental unit, just before the fluid enters back into the local box and to the cooling plant a regulating valve was installed. This acts as a variable pressure drop. By adding this pressure drop at the outlet of the experiment the cooling plant will deliver single-phase flow when desired. As mentioned above the pressure in the outline is regulated by the accumulator of the TRACI cooling plant. By creating a sensitive pressure drop there all the upstream flow (including the experiment) will be in subcooled liquid. Tests with single-phase liquid are needed to validate the experimental setup. To be able to go back to the initial conditions (without pressure drop) this is yet again designed in such way that the valve can be by-passed. From this point in the setup the fluid flows back to the cooling plant passing a second flexible hose and the local box. The system was built to handle pressures up to 90 bar (safety valve), which is far above the highest working pressure. All mentioned fluidic lines outside the vacuum vessel are insulated with Armaflex insulation foam. Figure 7.17 depicts an overall impression of the experimental unit with TRACI in the background. Figure 7.18 shows the inside of the vacuum vessel at a later stage of the project with the experiment highlighted in orange: In Figure 7.18(a) a single stainless steel tube is installed, whilst in Figure 7.18(b) the silicon multi-micro-channel device is being tested.

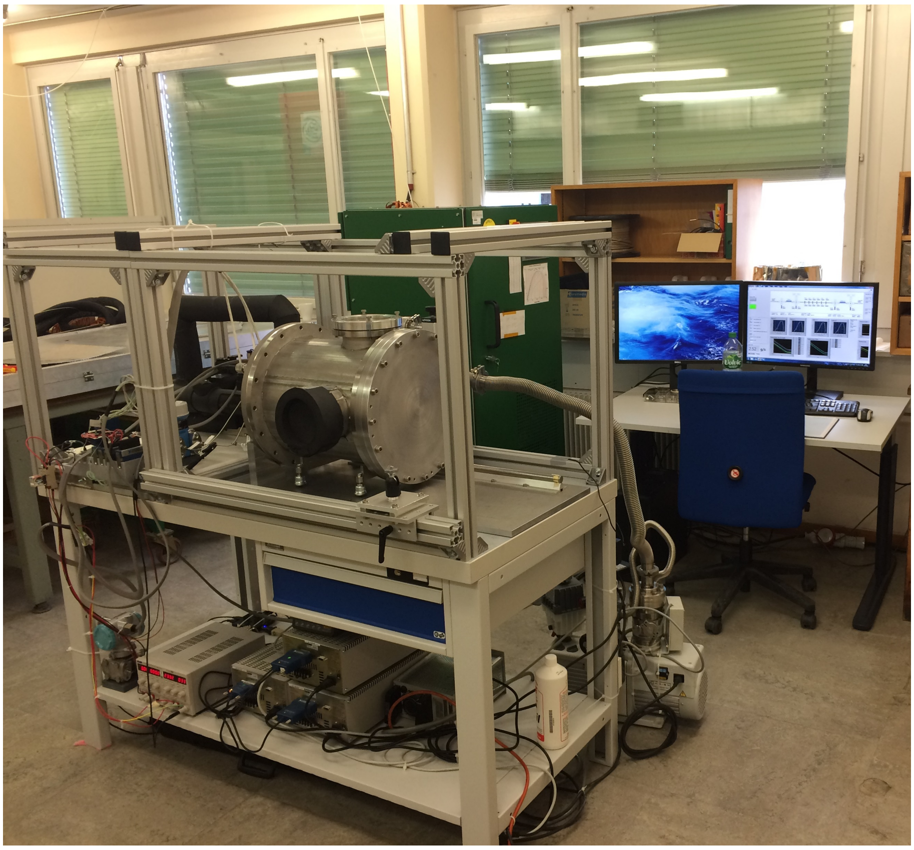

Figure 7.17: New test facility for evaporative CO_2 flow measurements in mini- and micro-channels (June 2018).

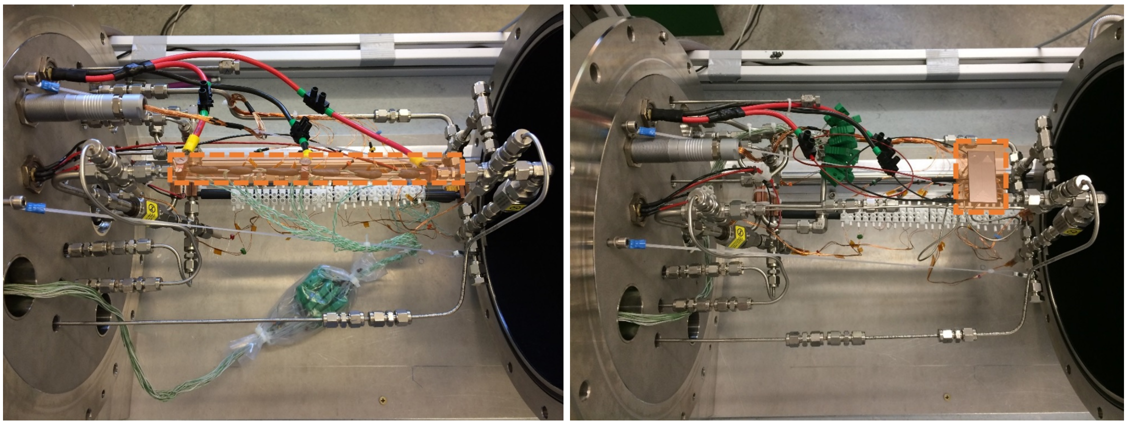

(a)

(b)

Figure 7.18: Experiment within the vacuum vessel: a) single-tube; b) multi-micro-channels.

Vacuum installations

The vacuum vessel is described in more detail in Figure 7.19: The main vessel housing (1) is installed on a guiding rail (2) and gliding carriage (3) for an easy access. The main vessel flange (4) is fixed onto a support board (5), whilst the whole experiment inside the vessel is only attached to this flange and supported at the feed through location of any fluidic and electrical components. To avoid heat leaks and to maximize the use of vacuum insulation, further contact of the components with the vessel wall had to be avoided and a self supporting design of the experiment had to be chosen. The vacuum vessel can be closed by sliding the vessel towards the main flange. The back flange (6) can be removed for possible extensions of the vessel. Two ports (7 and 8) allow for the installation of sight windows. The vacuum pump in operation (RV12, Edwards) is connected to a stainless steel hose which is attached to the vacuum port of the vessel (9). The pump is operated manually and an adjoined turbo molecular pump (TPU 062, Pfeiffer vacuum) can promote the final pumping power. Vacuum levels of the order of 10^{-5} mbar can be achieved with this vacuum pump/vacuum vessel assembly, read out by a vacuum gauge (TPG 362, Pfeiffer vacuum). For the thermocouples a special SPECTITE feed through for 12 thermocouples type K was acquired, whilst for the coolant pipes (inlet and outlet) special thermally insulated fluid feed throughs are installed. In this way all crucial fluidic tubing is disconnected from the vessels's thermal inertia limiting the heat leaks into the experiment. In order to install these feed throughs multiple KF flanges had to be welded onto the main vessel flange. The feed through of any electrical component (RTDs, Joule heater, Peltier element) is realized by means of vacuum-tight commercial electrical connectors (4- and 24-pin configuration, 105 series, Fischer connectors). The feed through of the 3 mm OD pressure lines is done with Swagelok of-the-shelf face seal fittings (SS-4-VCR-6-6M0, Swagelok).

Further thermal considerations

Due to the near-adiabatic test conditions inside the vacuum vessel convective heat transfer losses can be neglected. Radiative heat gain was also considered and neglected after experiments carried out with an aluminized multi-layer insulation (MLI) material inside the vacuum vessel did not influence the experiments at hand. The main externally caused influence on the experiments was assumed to be caused by conductive heat losses through the pressure lines and electrical components, which were estimated with single-phase tests and considered during data processing. However to limit this effect where possible cables inside the vacuum vessel were wound around the "cool" outline downstream of the experiment. Furthermore the pressure lines inside the vacuum vessel were fitted with small PEEK intersections which act as thermal buffer and electrical insulation. In addition the setup is installed in an air-conditioned laboratory with a constant temperature of $\sim 19^\circ$C to ensure more accurate temperature measurements.

Read-out hardware and software

The read-out of all temperature and pressure measurements is done with National Instruments hardware and LabView software. The RTDs are connected to an AI RTD 100 Ohm module (NI 9217), the thermocouples to a 16-channel 24-Bit Thermocouple Input module (NI 9214) and both types of pressure transducers (absolute and differential) are connected to an AI +/- 20mA module (NI 9203). All modules are plugged into a National Instruments compact data acquisition chassis (NI cDAQ-9178) which is connected to a standard PC. Logging of all signals is performed at 1 Hz default

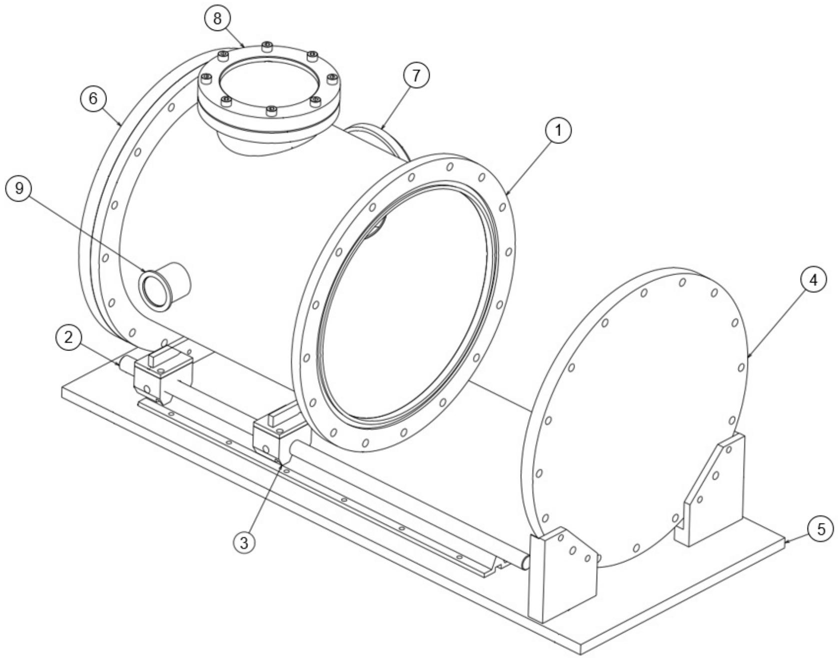

Figure 7.19: Main components of the vacuum vessel: (1) main vessel housing; (2) guiding rail; (3) gliding carriage; (4) main flange; (5) support board; (6) back flange; (7, 8) ports for sight windows; (9) vacuum port.

acquisition frequency if not specified differently and all raw data are saved for further analysis. Various measurements from other setup components are acquired through the component itself however the data acquisition is also managed via LabView. This includes e.g. the experimental flow meter and the vacuum gauge. Since the TRACI cooling plant is connected to an internet platform, some parameters measured by internal sensors within the cooling plant can be read out via internet connection and are live-fed into the same LabView program used for the other components. This for example can be achieved for the sub-cooling level and the CO_2 temperature before the experiment. The power supplies for the Joule heater and the Peltier elements (incl. relay) are also connected to the PC via GPIB-USB cable and their power output can be controlled accordingly via LabView. In summary this enables the user to have a complete depiction of the running experiment on one table-top screen whilst controlling it at the same time. The measured data of pressure and temperature is evaluated on-line by means of the REFPROP database (Reference Fluid Thermodynamic and Transport Properties) by NIST. Predefined points from the database for CO_2 are fed into the same LabView program which allows for a live evaluation of state points on the p-h-diagram. Table 7.3 lists the parameters read out or calculated by the LabView program for further evaluation.

Since frequently reoccurring oscillations in the measured pressure signal can be an indication for a special flow phenomenon, the pressure signals are analysed in such way that the sample rate can be increased according to a suspected frequency in the signal (1 kHz max.). To find embedded frequencies in a noisy pressure signal the pressure signal can be additionally processed with a power spectral density function. In this way phenomena such as e.g. vibrations, pulsations, vortex shedding

Parameter	unit
fluid temperature	°C
outer tube wall temperature	°C
silicon temperature	°C
room temperature	°C
saturation temperature	°C
absolute pressure	bar
differential pressure	bar
vacuum pressure	mbar
mass flow	g/s
mass flux	$\mathrm{kg/m^2s}$
power Peltier element	W
power Joule heat	W
power leak	W
heat flux Peltier	$\mathrm{W/m^2}$
heat flux Joule heat	$\mathrm{W/m^2}$
enthalpy	kJ/kg
vapour quality	-

Table 7.3: Experimental readout parameters.

or bubble nucleation can be traced more easily.

Cameras

The setup is installed on a work bench surrounded by a cubic test rig made of aluminium profiles for a more flexible three dimensional access to the setup components (see Figure 7.17). This primarily allows for a rigid installation of two cameras. The first camera is a high-speed camera to visualize details on bubble dynamics, whilst the second camera is an infrared camera for heat transfer visualization. These cameras can be aligned with two windows installed in the vessel housing (see Figure 7.19). The sight glasses within the window ports are interchangeable, however one window is intended for visual access with the high-speed camera and thus the window is a borosilicate glass window (MAXOS, DIN 7080). The second window is intended for the use with the infrared camera. Due to that the window is made of AMTIR-1 (amorphous material transmitting infrared radiation, $Ge_{33}As_{12}Se_{55}$, transmission at 0.7–12.0 µm). The mentioned high-speed camera is a FASTCAM Mini AX (Model 100) by Photron with a frame rate performance up to 100 000 fps. The infrared camera is from the FLIR A600-Series. The inside of the vessel is covered with an adhesive coated foil (Metal Velvet) which has extremely black diffusive appearance and a very low reflectance. This is applied for more accurate results from the infrared camera and to minimize the reflectance of the vessel walls which therefore limits the heat load into the vessel and any ongoing experiment. Figure 7.20 shows the inside of the vacuum vessel with the special adhesive coating. The vessel's back flange was removed for the application of the foil.

In the paragraphs above the experimental unit is described in its final layout. However many alterations had to be made over time and the cause of those is described in more detail in Appendix D.

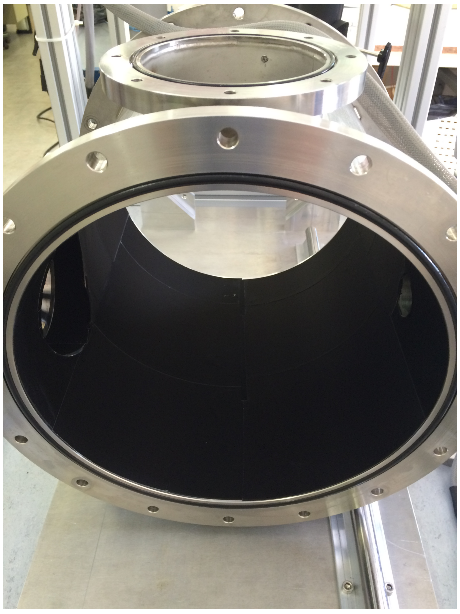

Figure 7.20: Inner wall of the vacuum vessel fitted with black diffusive foil.

7.3.3 Advantages of the new experimental setup

The main advantages of using the refrigeration unit TRACI for the proposed experiments are:

- very stably controlled temperatures and
- very stably controlled flow are possible.
- thus steady-state test conditions are much easier to achieve.
- a large range of saturation temperature and pressures can be explored and
- devices with smaller hydraulic diameters can be tested since the pumped loop maintains certain flow properties more easily whilst
- CO_2 is re-circulated inside closed loop.

The advantages of the experimental unit may be summarized as:

- near-adiabatic test conditions in vacuum vessel leads to
- more accurate temperature and heat transfer measurements.
- differential pressure sensor achieves higher accuracy levels to measure pressure drop and
- custom made in-flow temperature sensors eliminate all initially observed sensing errors with off-the-shelf sensors.

Resume The needed improvements mentioned at the beginning of this chapter and in the literature review could be addressed with the new experimental setup to reliably test small-scale CO_2 evaporators with a wide range of saturation temperatures and other test parameters.

CHAPTER 8

Flow boiling tests for detector cooling R&D with mini- and micro-scale carbon dioxide evaporators at CERN

8.1 Tubular evaporators

As a reminder three different stainless steel single tubes of 200 mm length were characterized for this study with inner diameters of 2.15 mm, 1 mm and 0.5 mm.

8.1.1 Fluid-mechanical integration

For the integration of the single tubes into the experimental unit a fluid-dynamical adapter is installed accordingly to reduce the external tubing diameter of the remaining experimental unit from 6 mm OD to the outer diameter of the test tube. Figure 8.1 shows the steps in internal diameter at the inlet junction of the test section schematically. The outlet junction mirrors the shown configuration for the inlet. Although only a minor influence has to be expected the geometry of the connector and especially L_3 and ID_3 - as shown in Figure 8.1 - are taken into account during data analysis.

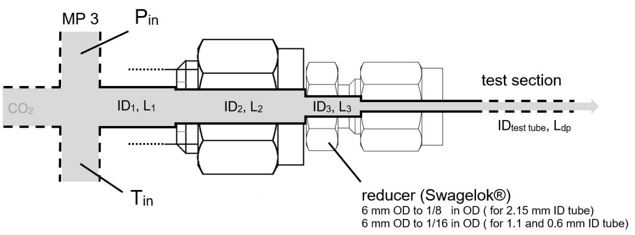

$ID_{test\ tube}$		2.15	1.1 ; 0.5
L_{dp}		200	200
ID_1	approx. in mm	4.8	4.8
ID_2		4	4
ID_3		2.3	1.3
L_1		11.7	11.7
L_2		16.3	14
L_3		7.1	6.4

Figure 8.1: Schematic of the junction between MP3 and the test section (with dimensions).

8.1.2 Application of experimental heat load

Direct Joule effect is used to apply a desired heat flux to the metallic tubes. Hence, three copper electrodes are clamped and screwed onto the tubes. For this setup the configuration of two anodes attached to the left and right side of the tube and one cathode in the middle was chosen for security and accuracy reasons to avoid stray currents beyond the test tube. The effective heated length L_q is 180 mm for the 1 mm ID tube and the 0.5 mm ID tube and 170 mm for the 2.15 mm ID tube and has been considered for the calculation of q. Outside of the vacuum vessel a power supply delivers the required current.

8.1.3 Tube wall temperature measurements

To measure the local outer wall temperature $T_{w,o}$, K-Type thermocouples are fixed onto the tubes by means of a steel-reinforced epoxy putty. The sensing tip of the thermocouple itself is covered by a thin layer of insulating rubber paste, which acts as an electric insulator whilst maintaining a good thermal contact with the outer tube wall. The thermocouples are fixed along the top and bottom generatrix lines of the tube resulting in six pairs within a distance of 30 mm and they were calibrated with a secondary standard reference thermometer (Fluke, HART 5626-12). The used data acquisition module by National Instruments (NI 9214) has a build-in cold-junction compensation (cjc) feature to avoid temperature drift caused by the surrounding. Figure 8.2 shows the flow boiling experiment with tubular single tubes schematically and in real life (dismounted from experimental unit).

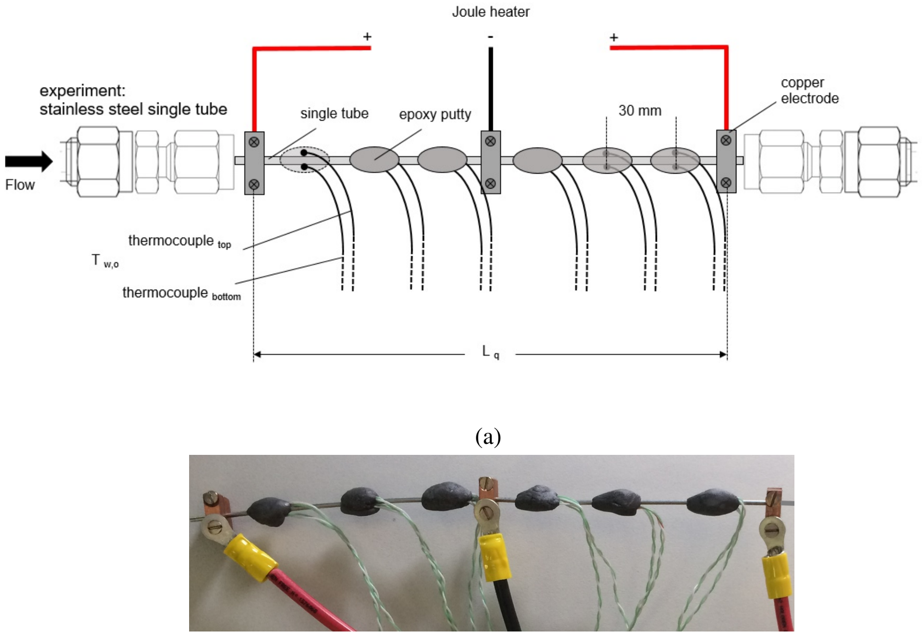

(a)

(b)

Figure 8.2: Flow boiling experiment with tubular single tube: a) schematic; b) real life.

8.1.4 Further considerations

For further calculations the exact tube dimensions had to be determined. The inner tube diameters were measured with an optical microscope (Zeiss O-Inspect 863) at the central CERN Metrology Lab as depicted in Figure 8.3 and the exact values are listed in Table 8.3 at the end of this section. However, for the sake of clearness the three tube dimensions are otherwise denoted by their nominal inner diameter throughout this entire work. The internal arithmetic average surface roughness R_a of the test tubes was measured with an uncertainty of 30 nm using a profiling system (VEECO - NT 3300). The surface roughness of the 2.15 mm ID tube, the 1 mm ID tube and the 0.5 mm ID tube was measured to be 0.32 μm, 0.61 μm and 3.3 μm respectively. To carry out these destructive measurements, tubes from the same batch as the ones used for the flow boiling tests were cut open and measured.

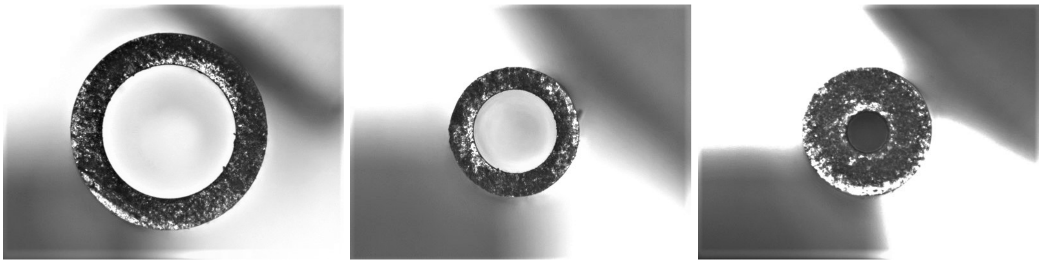

(a) (b) (c)

Figure 8.3: Tube ID and OD measurement with optical microscope: a) 2.15 mm ID tube; b) 1 mm ID tube; c) 0.5 mm ID tube.

8.1.5 Flow boiling tests with tubular evaporators

After the installation of the single tube into the experimental unit all interconnections are firmly tightened and any remaining humidity is removed from the fluidic circuit by pumping a minor vacuum within the test circuit. Under such slight under-pressure the test circuit is flushed with CO_2 from TRACI thus creating the closed test circuit ready for experimental testing. After a short start-up cycle TRACI delivers a certain flow rate at a set saturation temperature according to the principle described in section 7.3.1. For all flow boiling tests minimally subcooled liquid CO_2 was delivered to the experiment and boiling was initiated by increasing the heat flux q along the tubes. There is no working pressure and working temperature per se for this setup since it was designed to span a wide range of saturation temperatures and pressures.

Test parameters

The mass fluxes, heat fluxes and saturation temperatures applied for flow boiling experiments with tubular evaporators are listed in Table 8.1 and Table 8.2. An upper limit to the mass flux attainable with the 2.15 mm ID tube (800 $\mathrm{kg/m^2s}$) was set by the maximum RPM regime advised for safe stable operation for the pump installed inside TRACI. On the other hand, a lower limit to the mass flux for the 0.5 mm ID tube was set by the presence of flow instabilities observed below 1000 $\mathrm{kg/m^2s}$, since no flow restriction (orifice) was installed upstream of the test section for this first series of tests.

mass flux G [$\mathrm{kg/m^2s}$]		
2.15 mm ID	1 mm ID	0.5 mm ID
-	-	1800
-	-	1400
-	1200	1200
-	1000	1000
800	800	-
600	600	-
500	500	-
400	400	-
200	200	-
150	150	-
100	100	-

Table 8.1: Mass flux during flow boiling experiments.

heat flux q [$\mathrm{W/m^2}$]		
2.15 mm ID	1 mm ID	0.5 mm ID
5000		
10000		
20000		
30000		
35000		

(a)

saturation temperature T_{sat} [°C]		
2.15 mm ID	1 mm ID	0.5 mm ID
15		
10		
5		
0		
-5		
-10		
-15		
-20		
-25		

(b)

Table 8.2: Test parameters during flow boiling experiments: a) heat flux; b) saturation temperature.

The data points potentially affected by flow instabilities were identified by means of a combined analysis of different signals: A first on-line indicator of the mentioned instabilities was a highly unstable and fluctuating mass flow rate, which then affected the pressure drop signal accordingly. Additionally in some cases the temperature signal from the thermocouples fixed along the test tube picked up those irregularities in the flow, which in return affected the heat transfer. Thus steady-state conditions did not exist for these test parameters and after several unsuccessful attempts to achieve steady-state conditions those data points have been discarded and are not taken into account in the following discussion. It is worth mentioning that, similarly to other critical applications, CO_2 evaporators for HEP silicon pixel detectors are dimensioned to operate with low exit vapour qualities (never higher than ~ 0.4) in order to guarantee a safe operation of the detectors in the whole temperature range of interest. For this reason, in all two-phase experiments carried out for this first study the entrance vapour quality is set to $x \approx 0$ (saturated liquid conditions) resulting in vapour qualities at the evaporator outlet between 0 and ~ 0.4 for the single tubes depending on the mass flux G and heat flux q. All data points were obtained at steady-state conditions. Steady-state conditions were assumed to exist when the time average of all relevant state-variables (temperature, pressure, mass flux, heat flux) were constant and the fluctuations in the differential pressure and temperature signals did not exceed a value of ~ 0.1 bar and ~ 0.02°C, respectively. All signals were logged continuously at 1 Hz, also during change of parameters. After establishing steady-state conditions, the most important signals were additionally stored at an elevated acquisition rate according to the maximum read-out rate given by the hardware and read-out chain. This is 1000 Hz for the differential pressure transducer, 400 Hz for the RTDs and 60 Hz for the thermocouples. Table 8.3 summarizes the working conditions for each tube dimension and the related uncertainties, which already include the estimated errors induced by the different NI acquisition modules and power supplies used. The corresponding error analysis carried out for this study can be found in Appendix E. In result the CO_2 flow boiling pressure drop ΔP and heat transfer coefficient α are being studied with an unprecedented level of accuracy.

			Range	Uncertainty	
				Span	Typical
	L_{dp}	[mm]	200		0.5
	T_{sat}	[°C, °K]	15; 10; 5; 0; -5; -10; -15; -20; -25	0.0447; 0.0479; 0.0516; 0.0558; 0.0607; 0.0663; 0.0729; 0.0806; 0.0898	
	dp	[bar]	0 - 1	0.0007 - 0.001	
	P_{abs}	[bar]	15 - 60	0.048 - 0.056	
	T_{MP}	[°C]			0.015
	α	[$\mathrm{kW/m^2K}$]			5-10%
	$T_{w,o}$	[°C]			0.1
diabatic test conditions	**Tube 1**				
	ID	[mm]	2.179 (nominal: 2.15)		0.0073
	G	[$\mathrm{kg/m^2s}$]	800; 600; 500; 400; 200; 150; 100	0.63 %[a]	
	q	[$\mathrm{kW/m^2}$]	5; 10; 20; 30; 35[b]	0.01	
	L_q	[mm]	180		1
	Ra	[μm]	0.32		0.03
	Tube 2				
	ID	[mm]	1.023 (nominal: 1)		0.0066
	G	[$\mathrm{kg/m^2s}$]	1200; 1000; 800; 600; 500; 400; 200; 150; 100	1.32 % (1200 - 600); 1.39 % (500 & 400); 1.33 % (200 - 100)[a]	
	q	[$\mathrm{kW/m^2}$]	5; 10; 20; 30; 35[b]	0.7 %	
	L_q	[mm]	170		1
	Ra	[μm]	0.61		0.03
	Tube 3				
	ID	[mm]	0.492 (nominal: 0.5)		0.0064
	G	[$\mathrm{kg/m^2s}$]	1800; 1400; 1200; 1000	2.65 %[a]	
	q	[$\mathrm{kW/m^2}$]	5; 10; 20; 30; 35[b]	1.3 %	
	L_q	[mm]	180		1
	Ra	[μm]	3.3		0.03

[a] according to the two flow meters used

[b] value given in text, in reality it was 33 $\mathrm{kW/m^2}$ for the 2.15 mm and 1 mm ID tube and 37 $\mathrm{kW/m^2}$ for the 0.5 mm ID tube

Table 8.3: Working conditions and corresponding uncertainties.

Data Reduction

The mass flux G [kg/m^{2}s] through the experiment is calculated by means of the measured values of mass flow rate $\dot{m}$ [kg/s] and inner cross-sectional area of the test tubes [m^2]. The heating power Q [W] provided by resistive Joule heat is obtained by means of the measured voltage and current level at the corresponding power supply. Accordingly the applied heat flux q [W/m^2] is calculated with the heating power and the inner cylindrical area of the heated tube section [m^2]. The data presented in the following are in all cases the total measured pressure drop ΔP. No further calculation is therefore needed for the evaluation of dp. For the evaluation of the heat transfer coefficient α, the following assumptions are made:

- the test tube is homogeneous and isotropic in material composition, such that the generated heat inside the tube due to the Joule effect can be considered uniform;
- no electric leakage occurs from the test tube to the remaining part of the loop, since dielectric fittings are installed at the inlet and outlet of the test tube;
- the effect of axial heat conduction is neglected;
- the heat flux at the inner wall of the test tube is uniform;
- the heating power is completely transferred to the fluid and convective heat transfer to the test tube can be neglected, due to the vacuum surroundings;
- radiative heat gain of the test section is negligible.

The local heat transfer coefficient is determined classically by the Newton equation:

$$\alpha = \frac{q}{T_{w,i} - T_{sat}} = \frac{q}{T_{w,o} - (\Delta T_w) - T_{sat}}. \tag{8.1}$$

The inner wall temperature T$_{w,i}$ at each thermocouple position is calculated from the measured outside wall temperature T$_{w,o}$, where the one-dimensional, radial, steady-state heat conduction equation for a hollow cylinder with a uniform heat flux is used:

$$\Delta T_w = \left[\frac{q \cdot D_i}{4\lambda_{SS316}}\right]\left[\frac{\psi(1 - ln\psi) - 1}{1 - \psi}\right], \tag{8.2}$$

with

$$\psi = (D_o/D_i)^2. \tag{8.3}$$

Thus for each thermocouple position two heat transfer coefficients, α_{top} and α_{bottom} are obtained, resulting in twelve local heat transfer coefficient measurements. All results given in the following denoted as α will be the arithmetic mean of α_{top} and α_{bottom}. The pressures along the experimental tubes may be estimated in two ways:

1. Following a linear interpolation between the measured pressure value at the inlet and outlet of the test tubes, resulting in P(z) at any thermocouple position z along the tube:

$$P(z) = P_{in} - \Delta P_{exp} \frac{z}{L_{dp}} \tag{8.4}$$

where P_{in} is the pressure at the tube inlet, ΔP_{exp} is the experimentally determined pressure drop across the entire test tube and L_{dp} is the length of the entire test tube. This approach does not take into account a possibly more realistic evolution of the pressure, e.g. a pressure gradient with changing vapour quality. However the final total pressure drop ΔP_{exp} represents the real measured value.

2. Following the forecast of a certain pressure drop correlation found in literature. In this case to obtain P(z) the length of the tube may be discretized into several sections in accordance with the thermocouple positions and the vapour quality at each position can be estimated based on a linear fit between the derived value at the inlet and outlet. The pressure P(z) at any thermocouple position z along the tube is then obtained by step-wise integration of different correlations along the tube length. This approach does take into account a more realistic evolution of the pressure however the predicted total pressure drop ΔP_{pred} does not represent the real measured value.

In the most optimal case at a given saturation temperature the calculation of the local heat transfer coefficient should be based on the best fitting pressure drop correlation. However, since a very wide range of T_{sat} has been studied, the first approach of a linear pressure drop estimation has been used to avoid confusion and thus the same methodology is applied for all data. A comparison of this simple linear assumption with the Friedel correlation [74] for example does not show a larger deviation than 5% on the heat transfer coefficient, for 100% of the data points gathered for the 2.15 mm ID tube and the 1 mm ID tube. Whilst the deviation is not larger than 10% for 85% of the data gathered for the 0.5 mm ID tube. The saturation temperature, the enthalpy and vapour quality along the experimental tube – where no direct measurement is carried out – are calculated from the mentioned estimation of the pressure at each thermocouple position along the tube.

The thermodynamic equilibrium quality x_e(z) is acquired from the fluid's specific enthalpy h(z), the saturated liquid enthalpy h_l and the latent heat of vaporization h_{lv}

$$x_e(z) = \left.\frac{h(z) - h_l}{h_{lv}}\right|_{P=P(z)}. \tag{8.5}$$

h(z) is calculated with an energy balance for any location along the test tube,

$$h(z) = h_{in} + \frac{Q_{leak} + q\pi D_h z}{\dot{m}} \tag{8.6}$$

where h_{in} is the enthalpy of the liquid CO_2 at the inlet, acquired from the pressure and temperature measurements at this position. Q_{leak} is the heat gain from the environment to the test section due to conductive heat leaks through the pressure lines and electrical components, which was estimated with single-phase tests. All CO_2 properties were calculated with the REFPROP 8.0 software by NIST.

In order to show the effect of saturation temperature on the CO_2 boiling heat transfer coefficient in a more compact way, the twelve local heat transfer coefficients have been in many cases averaged to one single value. This is justified by the fact that only low to medium vapour qualities are investigated for this study, which very often results in an almost constant heat transfer coefficient versus vapour quality. Thus a representative value α_{ave} is created for each data set (one T_{sat}, one q and one G), which then can be related in various ways with the remaining test parameters:

$$\alpha_{ave} = \frac{\alpha_{1,bottom} + \alpha_{1,top} + \ldots + \alpha_{6,bottom} + \alpha_{6,top}}{12}. \tag{8.7}$$

In a few cases a slight trend can be found for the heat transfer coefficient with vapour quality. Whilst acknowledging that in these cases the averaged value is not representative of the evolutive heat transfer coefficient along the tube, the same averaging procedure has been applied.

Single-phase validation test

To validate the experimental procedure and the two-phase measurements, single-phase tests were carried out for some selected test parameters. The experimental Darcy friction factor,

$$f = \frac{\Delta P \cdot D_i \cdot \rho_l}{2 \cdot L_{dp} \cdot G^2} \tag{8.8}$$

was compared to the widely adopted theoretical friction factor given by Blasius [62] (see equation 5.19 using the single-phase Reynolds number instead). As an example, Figure 8.4 depicts the adiabatic experimental single-phase friction factor deduced for the 1 mm ID and 2.15 mm ID tube at 10°C fluid temperature as compared to the correlation by Blasius [62]. An acceptable Mean Absolute Error (MAE) of ~ 8% between data and prediction witnesses of the reliable quality of the pressure drop measurements. Note that for all the observed configurations the CO_2 liquid-phase Reynolds number lies always in the turbulent regime, in spite of the small diameter of the tubes. Unfortunately, for the 0.5 mm ID tube it was not possible to obtain stable single-phase flows for a significant number of points. Indeed, the CO_2 refrigerating and circulating unit is designed to bring the fluid very close to saturation conditions at the entrance of the test section. In addition the pressure drop in the smallest pipe quickly becomes relatively high. Therefore, even when using the pre-cooling Peltier stage, in most cases it was impossible to provide sufficient sub-cooling to the liquid CO_2 at the tube inlet. Thus the onset of boiling could not be avoided before the outlet.

Furthermore, conductive heat losses through the pressure lines and electrical components were estimated with adiabatic single-phase tests and were further considered during data reduction. A linear dependence of the heat leak was found in function of the temperature difference between the liquid CO_2 and the room temperature. The total heat gain to the test section was found to be 0.007 W/K for the 2.15 mm ID tube and 0.02 W/K for the 1 mm ID tube. Since no single-phase tests could be carried out with the 0.5 mm ID tube the same relation as for the 1 mm ID tube has been used.

To validate the two-phase heat transfer measurements, diabatic experiments were carried out in single-phase. Due to the design of the cooling plant again those tests had to be limited to low heat flux values (1000 W/m^2) and high T_{sat} (15°C) and could be carried out for the 2.15 mm ID tube only. An example is given in Figure 8.5 and a deviation of the single-phase Nusselt number of ~ 11.9% and ~ 10.8% from the well-known correlations by Dittus-Boelter [143] and Gnielinski [144] have been found respectively. In order to calculate the theoretical Nusselt number there is

$$Nu_{Dittus-Boelter} = 0.023 Re^{0.8} Pr^{0.4} \tag{8.9}$$

and

$$Nu_{Gnielinski} = \frac{(f/8) \cdot (Re - 1000) \cdot Pr}{1 + 12.7 \cdot (f/8)^{0.5} \cdot (Pr^{2/3} - 1)}. \tag{8.10}$$

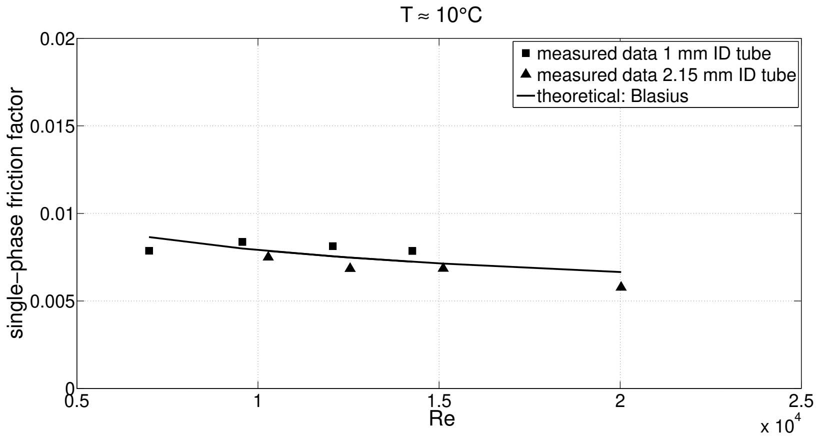

Figure 8.4: Adiabatic single-phase validation of the friction factor with the Blasius [62] correlation for the 2.15 mm and 1 mm ID tube at 10°C fluid temperature.

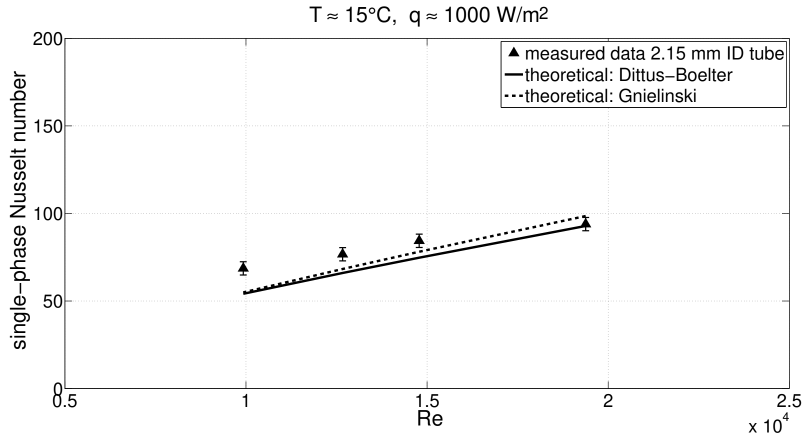

Figure 8.5: Diabatic single-phase validation of the Nusselt number with the Dittus-Boelter [143] and Gnielinski [144] correlations for the 2.15 mm tube at 15°C fluid temperature.

8.2 Multi-micro-channels

In addition to the simple tubes described above, a more complex evaporator based on multi-micro-channels embedded into silicon and covered with glass have been characterized for this study.

8.2.1 Fluid-mechanical integration

Around the inlet and outlet opening of the multi-micro-channels (silicon side) metal pads were deposited. Thus a connection between the silicon device and standard tubes (1/16” OD) can be achieved by soldering the tubes to the metal patches. This connection method was developed in-house (G. Romagnoli) and is shown in Figure 8.6(a). Equipped with the relevant connectors and further tubing a fluidic link to the experimental unit can be created as shown in Figure 8.6(b). To connect the channels to the setup without inducing additional mechanical stresses on the in- and outlet of the silicon device the additional tubing was bend in spirals (not shown in Figure 8.6). The multi-micro-channels were installed horizontally and in alignment with the glass window at the top of the vacuum vessel. The additional standard tubing has to be taken into account when evaluating the pressure drop within the channels.

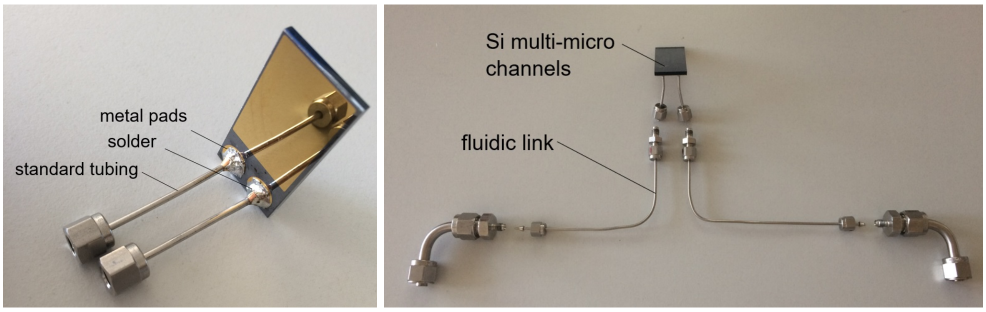

(a) (b)

Figure 8.6: Fluidic connections of the silicon multi-micro-channels: a) connection to the silicon device; b) connection to the experimental unit.

8.2.2 Application of experimental heat load

The experimental heat load is introduced by a silicon heater (0.1 mm in thickness). The area of the heater is 20 x 20 mm^2 which simulates the footprint of e.g. an ATLAS FEI4 chip [18]. As shown in Figure 8.7, one side of the heater was metalized and electrical contacts were soldered along the two opposite heater edges in order to produce a uniform power dissipation. The heater was then glued onto the silicon side of the multi-micro-channel evaporator by means of a 0.03 mm thick double sided tape and is powered with a power supply situated outside of the vacuum vessel.

8.2.3 Silicon temperature measurements

In order to monitor the surface temperature of the heater and therefore to evaluate the thermal performance of the evaporator, one thermocouple was glued onto the outside-facing surface of the heater in a position preliminarily evaluated as the hottest spot. The difference between the temperature measured at the hot spot and the saturation temperature of the CO_2 flow is then used to calculate the Thermal Figure of Merit.

8.2.4 Flow boiling tests with multi-micro-channels

Table 8.4 summarizes the parameters applied for the flow boiling tests with the multi-micro-channel device. The surface power density dissipated by the heater is expressed in $\mathrm{W/cm^2}$ for a direct comparison with the usual values given for the surface power density produced by standard computing chips. However, for comparison with heat and mass transfer measurements reported in literature, the usual corresponding parameters of heat flux $[\,\mathrm{kW/m^2}]$ through the micro-channel walls and mass flux $[\,\mathrm{kg/m^2s}]$ inside the micro-channels are also provided.

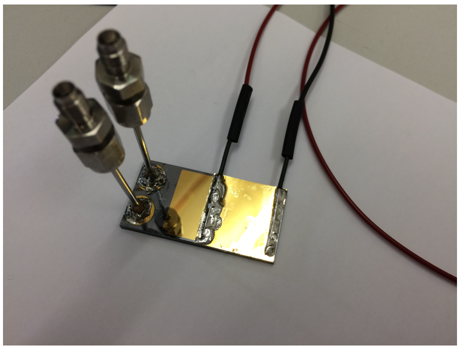

Figure 8.7: Silicon heater with electrodes glued onto the multi-micro-channels (silicon side).

T_{sat} [°C]
15
10
5
0
-5
-10
-15
-20
-25

(a)

mass flow rate [g/s]
0.1
0.3

(b)

mass flux [kg/m^{2}s]
320
960

(c)

power density [W/cm^2]
1
2
3
4
5

(d)

channel heat flux [kW/m^2]
15.9
31.8
47.7
63.6
79.5

(e)

power density [W/cm^2]	$\dot{m} \approx 0.3$ g/s $T_{sat} \approx$ -25 to +15°C	$\dot{m} \approx 0.1$ g/s $T_{sat} \approx$ -25 to +15°C
1	x = 0.05 - 0.08	x = 0.14 - 0.23
2	x = 0.09 - 0.15	x = 0.27 - 0.45
3	x = 0.14 - 0.23	x = 0.41 - 0.67
4	x = 0.18 - 0.3	x = 0.54 - 0.9
5	x = 0.23 - 0.37	x = 0.7 - 1

(f)

Table 8.4: Test parameters for flow boiling tests with multi-micro-channels a) to e) and nominal outlet vapour quality f).

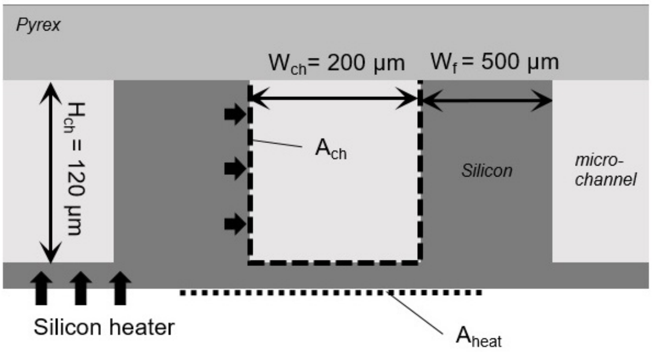

Figure 8.8: Schematic of the heat flux inside the multi-micro-channels (2D only).

To estimate the heat flux per channel q_{ch} consider Figure 8.8. The channel surface is determined as

$$A_{ch} = (H_{ch} + W_{ch} + H_{ch}) \cdot L, \tag{8.11}$$

where L is the channel length and W$_{ch}$ and H$_{ch}$ are the width and the height of the channels, respectively. The Pyrex wall can be considered thermally neutral. The heated surface is

$$A_{heat} = (0.5W_f + W_{ch} + 0.5W_f) \cdot L, \tag{8.12}$$

where W$_f$ is the width of the wall. The channel heat flux is then

$$q_{ch} = \frac{Q}{A_{ch}} = \frac{PA_{heat}}{A_{ch}}, \tag{8.13}$$

where P is the initial power density in $\mathrm{W/cm^2}$. The resulting nominal outlet vapour qualities are listed in Table 8.4(f).

Due to the geometry of the multi-micro-channels, where the inlet restrictions very reliably trigger flow boiling, single-phase tests were not carried out in this setup configuration. The pressure drop, the Thermal Figure of Merit and the bubble dynamics in the channels have been studied.

The bubble dynamics within the multi-micro-channels were studied by means of the aforementioned Photron FASTCAM Mini AX-100 high-speed camera. The experimental setup was adapted accordingly and the camera was fixed onto the test rig to be aligned with the top glass window of the vacuum vessel, which allowed for direct visual access onto the multi-micro-channels. The camera was connected to an additional portable PC and can be controlled by the native Photron software. The main camera parameters to be adjusted were frame rate and shutter speed. Additional light was provided by two cold LED spots as shown in Figure 8.9. Special care was taken to minimize the lighting time of the LED spots in order to avoid radiation heat uptake by the CO_2 flow.

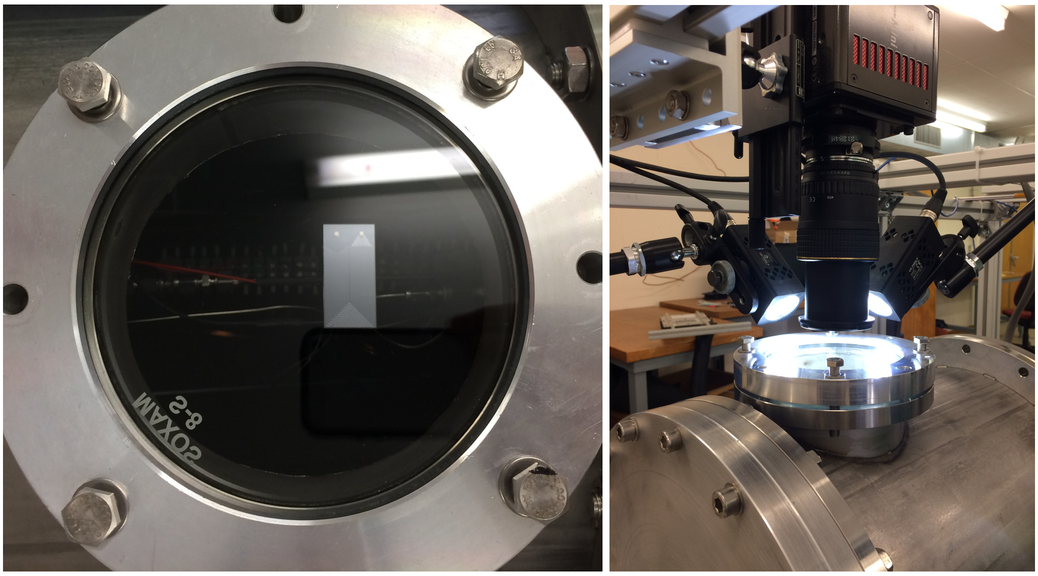

(a) (b)

Figure 8.9: Details of the experimental setup during flow visualization: a) multi-micro-channel position inside the vacuum vessel; b) Arrangement of high-speed camera and LED-spots.

CHAPTER 9

Experimental results and analysis

9.1 Visual results

The high-speed camera visualizations of the CO_2 boiling pattern and bubble dynamics provide a very useful key of interpretation for the pressure and temperature measurements executed on both the multi-micro-channel device and the tubular evaporators. They are therefore discussed first. High-speed camera recordings were carried out in the areas labelled as “position 1” to “position 5” in Figure 9.1 at all saturation temperatures, power densities and mass flow rates reported in Table 8.4. The visual examples discussed below are recorded at a nominal power density of 3.0 $\mathrm{W/cm^2}$ and a flow rate of 0.3 g/s, which corresponds to a nominal value of the vapour quality x at the exit of the channels ranging from 0.14 at T_{sat} = -25°C to 0.23 at T_{sat} = +15°C. One of the most interesting direct findings is that the bubble size for boiling CO_2 indeed is increasing whilst decreasing T_{sat}. This is due to the drastically changing surface tension of CO_2, which increases five times over the tested temperature range. At a constant theoretical Laplace pressure, an increasing surface tension leads to a larger bubble radius. The Laplace pressure $\Delta P_{Laplace}$ is the pressure difference between a gas and a liquid or between the inside and the outside of a curved surface which in this case forms the bubble. In the case of a bubble $\Delta P_{Laplace}$ can be defined as

$$\Delta P_{Laplace} = P_{in} - P_{out} = \sigma \frac{2}{R_b}, \tag{9.1}$$

where R_b is the bubble radius and σ is the fluids surface tension. Under the assumption that for decreasing T_{sat} the overall Laplace pressure between gas and fluid remains the same, the bubble radius increases due to the increase in surface tension. Furthermore, during flow boiling the bubble departure is influenced by surface tension, buoyancy and drag forces. Thus at a fixed mass flux increasing, surface tension leads to an increasing bubble departure diameter and a lower bubble frequency [145]. The liquid/vapour density ratio also increases with a factor 5 while the saturation temperature passes from +15° C to -25°C and contributes as well to this phenomenon. Figure 9.2 shows this effect in a series of still-images extracted from high-speed camera recordings at Position 1 for different T_{sat}. Whilst all other system parameters are kept constant, at +15°C the bubble departure size is in the order of microns, at +5°C the bubble departure size is in the order of a few tens of microns or less, whilst at -25°C the bubble departure size is in the order of the channel size. Therefore, while decreasing T_{sat} the boiling pattern becomes more and more confined by the channel walls. The trend towards an

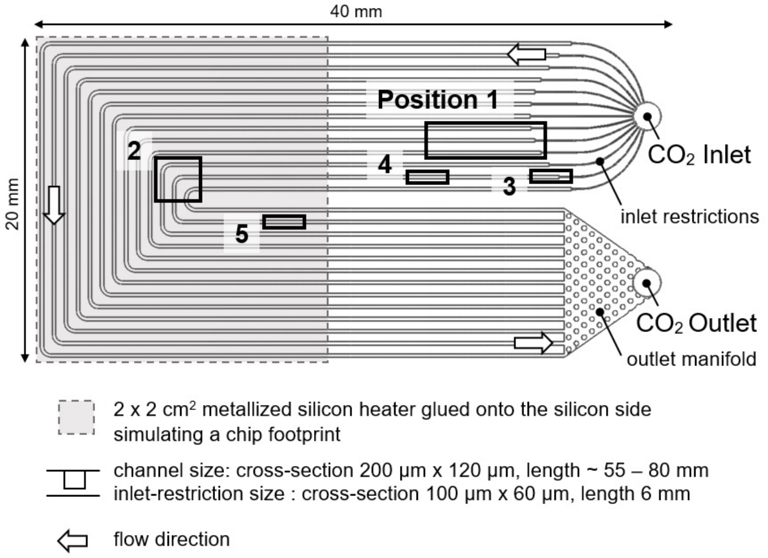

Figure 9.1: Layout of the multi-micro-channel device. The positions used for high-speed camera recordings are indicated by the labelled rectangles.

increasing confinement of the flow is also obvious in Figure 9.3 recorded at Position 2. At +15°C an uninterrupted flow of small bubbles can be found further along the channels, at +5°C flow of bubbles with intermittent vapour slugs is the dominant flow pattern, whilst for -25 °C vapour slugs and liquid film along the walls are predominant. However, it was observed that, due to the very small channel dimensions, with further heat uptake along the channel the bubbles soon occupy the whole channel cross-section for all studied T_{sat}. Other interesting phenomena were studied within the channels. The very efficient boiling enhancement by expansion ("flash boiling") produced by the backward-facing step after the restriction at the inlet of each channel, was confirmed for the whole test range. Figure 9.4 gives an example of such behaviour at Position 3 at +5°C. Furthermore, different fluid films were observed in the channels. Figure 9.5 compares two different fluid film occurrences. At +10°C a homogeneous and smooth film was found at Position 4, whilst in Position 5 the film appeared very in-homogeneous and wavy. This is due to the progress of the evaporation moving downstream along the channel. In general the bends seemed to trigger a change in flow behaviour. Incoming bubbles colliding with the bend wall can form a spontaneous gaseous film after the bend. In addition very small secondary bubbles are created at the starting location of the bend, thus enhancing heat transfer within the channels.

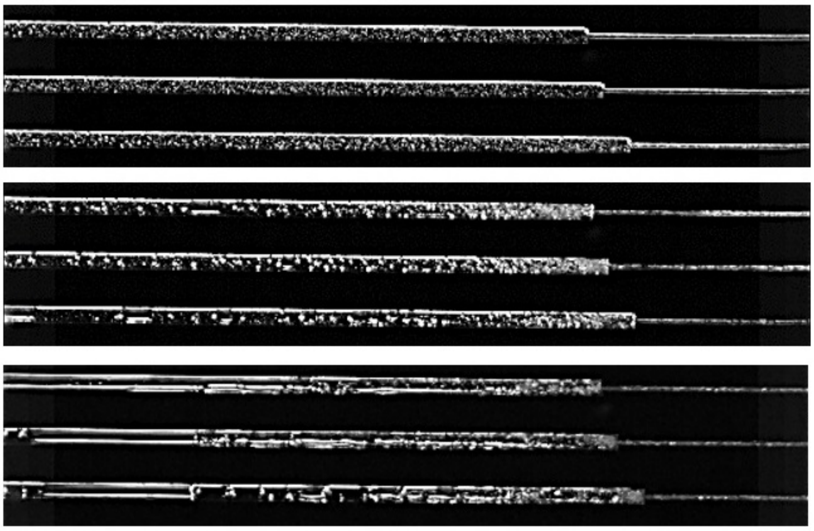

Figure 9.2: Flow boiling of CO_2 in multi-micro-channels recorded at Position 1: T_{sat} variation upper to lower: 15°C, 5°C, -25°C.

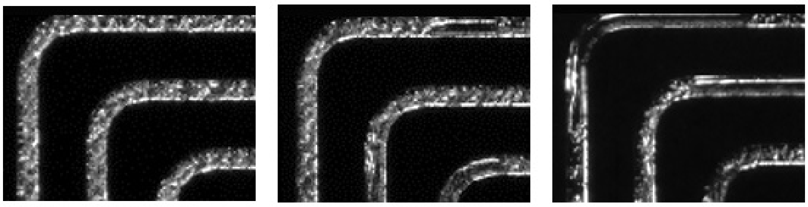

Figure 9.3: Flow boiling of CO_2 in multi-micro-channels recorded at Position 2, T_{sat} variation left to right: 15°C, 5 °C, -25°C.

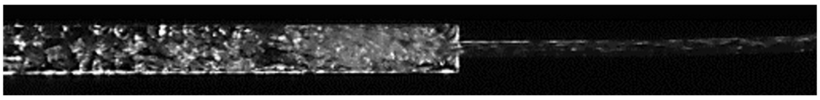

Figure 9.4: Flow boiling of CO_2 in multi-micro-channels at 5 °C: boiling enhancement at inlet restrictions recorded at Position 3.

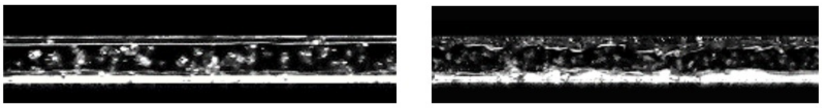

Figure 9.5: Flow boiling of CO_2 in multi-micro-channels at 10 °C: fluid film behaviour in the channels: homogeneous and smooth (left) recorded at Position 4, in-homogeneous and wavy (right) recorded at Position 5.

9.2 Parametrical results

9.2.1 Multi-micro channels

The multi-micro-channel device was further characterized by means of pressure drop and temperature measurements. The CO_2 boiling pressure drop across the device at a constant chip power density of $3\,\mathrm{W/cm^2}$ and various T_{sat} is shown for the two flow rates in Figure 9.6. As expected, the pressure drop increases with increasing mass flow rate and with decreasing saturation temperature. However, the found behaviour is definitely more extreme than what would be foreseen by using pure liquid flow assumptions: at both flow rates the pressure drop increases with a factor ~2.5 passing from +15°C to -25°C, while in both cases the CO_2 density and viscosity variations due to temperature would lead to an increase in the liquid pressure drop of a factor ~1.6. Similarly, at all temperatures the increase of pressure drop for pure liquid flow in a channel scales linearly with the mass flow rate in the laminar regime (which is the case for the configuration tested). Therefore, an increase of a factor 3 would be expected under pure liquid flow assumptions when passing from a mass flow rate of 0.1 g/s to 0.3 g/s, whereas the measured increase of a factor ~7 is visible in Figure 9.6. These observations provide immediate acquaintance to the sensitivity of the pressure drop in boiling flows to changes in saturation temperature and mass flow rate. However, it is interesting to notice that the effect of saturation temperature is the same for both flow rates considered. This is particularly surprising, as the nominal value of the exit vapour quality is 3 times larger at the lower flow rate than at the higher one and appears to be in contrast with some of the observations made on the tubular evaporators, which will be discussed in the next section. In anticipation to results presented in section 9.2.2, the pressure drop increase for the smallest diameter tubular evaporator (ID = 0.5 mm) caused by the same change in saturation temperature is also found to be much more extreme compared to the other tube dimensions and which is comparable to the case of the multi-micro-channels discussed here. Finally, while flow instabilities where observed in the 0.5 mm ID tubular evaporator for mass fluxes $< 1000\ \mathrm{kg/m^2s}$, no flow instabilities were recorded for the multi-micro-channel device, featuring a much smaller hydraulic diameter of the channels. This is true even at a mass flux as low as G = 320 $\mathrm{kg/m^2s}$. Although further investigations are required it is possible that the main explanation for this phenomenon relies on the special geometry of the multi-micro-channel device, i.e. on the relatively long restrictions before the channel stabilizing the flow; on the backward-facing step at the inlet of each channel triggering intense nucleation boiling; and on the presence of the bends introducing a very similar level of flow perturbation at all flow rates and temperatures.

The TFM based on the temperature measured on the external surface of the heater was found to be constant for the whole test range of the multi-micro-channel device. This implies that the average heat transfer coefficient along the channel is almost constant in the whole range of parameters explored. The intense nucleation boiling triggered at the channel inlets and the very high level of flow confinement in the multi-micro-channels may explain those findings. It has been mentioned above that, with further heat uptake along the channel, the bubbles rapidly occupy the whole channel cross-section for all T_{sat} considered in the study. As a consequence, the flow pattern, and thus the dominant heat transfer mechanism, although very different at the incipience of boiling directly after the channel inlet, becomes very similar along the channel for all T_{sat}. Figure 9.7 displays the result of this behaviour at a constant flow rate of 0.3 g/s and various T_{sat}. The TFM obtained with the multi-micro-channel device is ~3 $\mathrm{m^2K/W}$ for all power densities and saturation temperatures considered. A comparison of this value with typical values featured by standard thermal management techniques so far adopted for pixel detectors demonstrates the unparalleled cooling effectiveness of micro-structured silicon cold plates. As already reported above and in [11], conventional detector cooling with thermal ledges exhibits typically a TFM of ~20 $\mathrm{m^2K/W}$, while highly optimized pipe-structure integrated designs may reach a TFM of ~12 $\mathrm{m^2K/W}$. Thus, with multi-micro-channel silicon cold plates a TFM can be achieved which is a factor 4 better than the best performing, conventional grand-scale detector cooling method applied so far. In addition, if properly designed, an almost constant TFM over a large range of saturation temperatures and dissipated power densities makes the dimensioning and subsequent operation of those cold plates extremely easy throughout the entire life-cycle of a detector, from commissioning to end-of-life operation, where very different values may be required for these parameters.

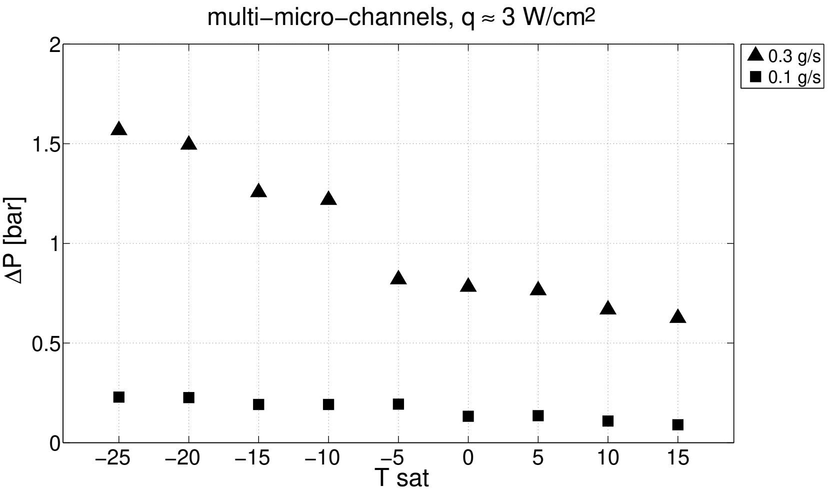

Figure 9.6: Effect of T_{sat} on ΔP for boiling CO_2 in multi-micro-channels at constant $q \approx 3\ \mathrm{W/cm^2}$.

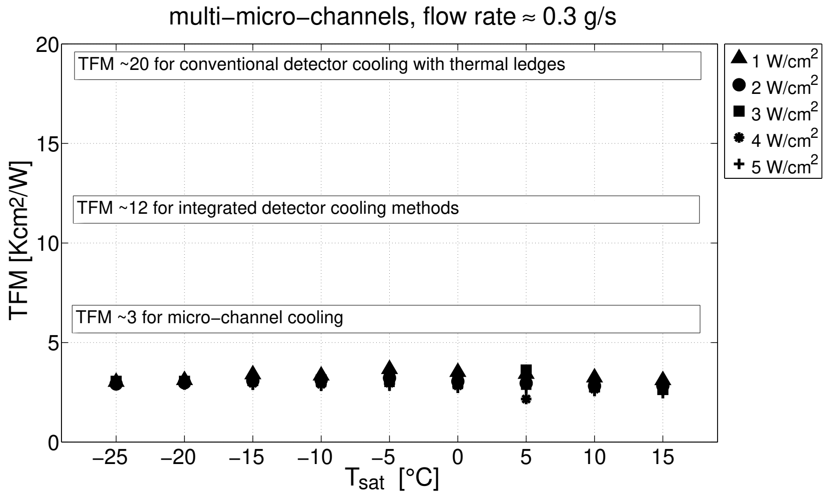

Figure 9.7: Effect of T_{sat} on the TFM for boiling CO_2 in multi-micro-channels at constant flow rate ≈ 0.3 g/s.

9.2.2 Tubular evaporators

Pressure drop

The data presented in the following are in all cases the total measured pressure drop ΔP. They are obtained from the elevated acquisition rate samples (1000 Hz for pressure values) averaged over 60 second steady-state time slots. Concerning the effect of mass flux, heat flux and inner diameter on the CO_2 two-phase pressure drop, the data gathered for this study confirm the trends reported in literature. As an example, Figure 9.8(a) shows the pressure drop as a function of the mass flux for the 2.15 mm ID tube and the 1 mm ID tube at $T_{sat} \approx 15^{\circ}C$ and $q \approx 10$, 20 and 30 kW/m^2, whilst Figure 9.8(b) shows the data gathered for the 0.5 mm ID tube under the same conditions. It is interesting that the effects linked to both G and q gain in relevance with decreasing ID. Very similar trends are observed for all T_{sat} investigated. An important focus of the present study lies on the effect of saturation temperature, globally presented in Figure 9.9 for the data corresponding to a heat flux of $q \approx 35\,kW/m^2$. Again very similar trends are observed for all other heat fluxes investigated. The highest heat flux has been selected to show the general trends, as it enhances some characteristic features. The saturation temperature is represented by the reduced pressure P_{red} to underline its generally high values compared to standard refrigerants at the same temperature. For a temperature range of +15°C to -25°C the reduced pressure corresponds to ~ 0.7 to 0.2 (R134a: ~ 0.12 – 0.026; R404a: ~ 0.26 – 0.06). Figure 9.9(a) depicts the two-phase pressure drop dependence on the reduced pressure and the mass flux for the 2.15 mm ID tube, Figure 9.9(b) for the 1 mm ID tube and Figure 9.9(c) for the 0.5 mm ID tube. For all three diameters, the highest pressure drop is observed at the lowest P_{red} (T_{sat}) and the highest mass flux, but a shift in the overall behaviour for decreasing P_{red} (T_{sat}) takes place when varying the inner diameter. Indeed, for the 2.15 mm ID data set the dominant effect appears to be the increase in mass flux, while the increase in pressure drop passing from +15°C to -25°C is limited and is essentially constant at all mass fluxes observed. This trend changes dramatically for the 1 mm ID tube. Here the pressure drop increase due to a decrease of P_{red} (T_{sat}) is larger and becomes more and more apparent when the mass flux is increased, causing a characteristic “fan-out” alignment of the data on the plot. This behaviour may suggest a transition of the flow pattern. The trend drastically changes again for the 0.5 mm ID tube, where the dominant effect on the pressure drop increase is clearly linked to the decrease of P_{red} (T_{sat}). This is true until $P_{red} \approx 0.4$ (-10°C), where at $P_{red} < 0.4$ the pressure drop effect due to the increase of G appears nearly negligible with respect to the one caused by the decrease of T_{sat}. To visualize the discussed trends a predefined polynomial fit (n = 2) was applied to the data. This fit covers in good agreement the data for the 2.15 mm and the 1 mm ID tubes. However for the 0.5 mm ID tube this fit is less accurate and a higher order polynomial fit (not shown) has to be used to cover the shown trends. This is mainly due to the sudden shift in the overall pressure drop behaviour below -10°C which leads to a reduced dependence from the mass flux. Figure 9.10 compares the data sets of the 1 mm ID and the 0.5 mm ID tube for a fixed mass flux ($G \approx 1200\ kg/m^2s$), where the ratio between the pressure drop measured at a certain temperature (ΔP) and the pressure drop measured at +15°C (ΔP_{+15C}) is related to the reduced pressure. The difference in pressure drop for the 1 mm ID tube across the tested temperature range stands in stark contrast with the very drastic pressure drop increase for the 0.5 mm ID tube. The ratio ΔP_{-25C} / ΔP_{+15C} is twice as large for the 0.5 mm ID compared to the 1 mm ID tube. The mentioned trends in Figure 9.9 can be quantified when comparing the pressure drop dependence on the mass flux and heat flux at +15°C and -25°C. The slopes of the data sets provide an indicator for the qualitative trends described above.

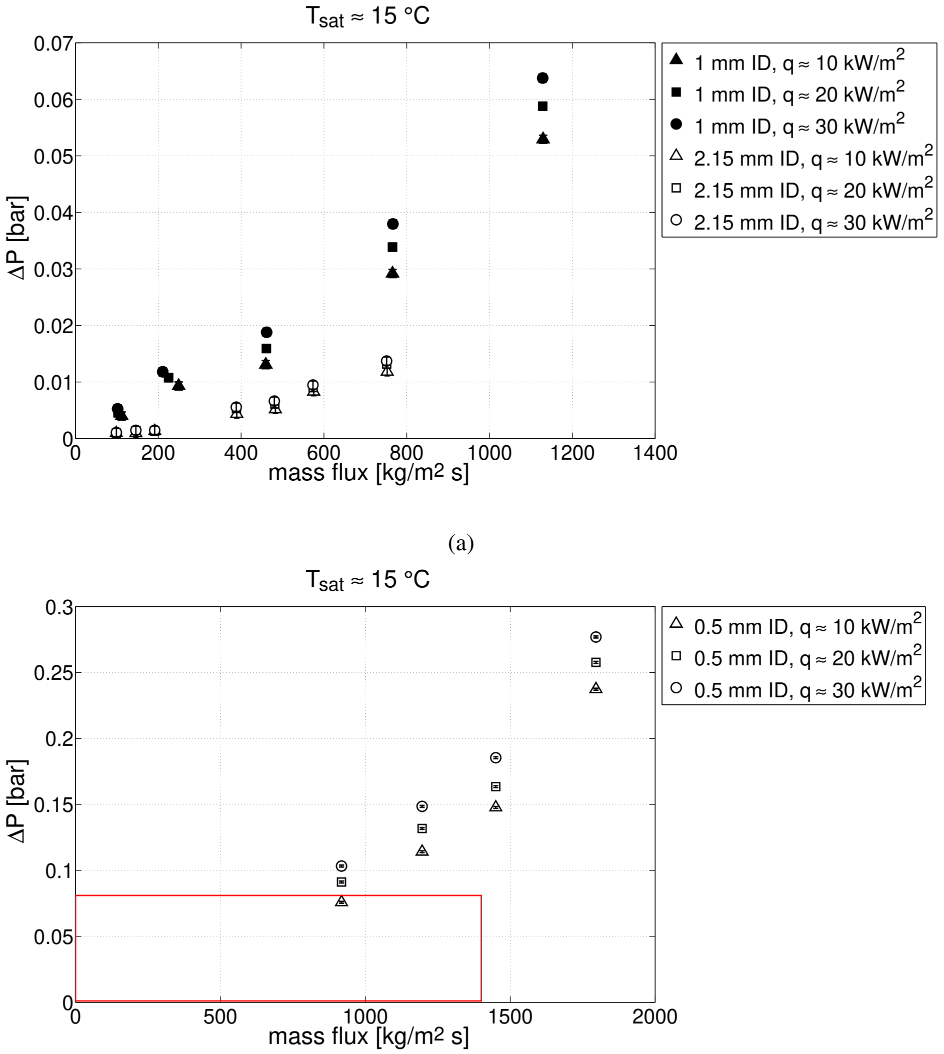

(a)

(b)

Figure 9.8: Effect of mass flux, heat flux and inner tube diameter on the CO_2 two-phase pressure drop at 15°C T_{sat} : a) 2.15 mm ID tube and 1 mm ID tube; b) 0.5 mm ID tube (dashed inset shows the parameter range of Figure a)).

In Figure 9.11(a) the slope of all data sets is roughly the same, demonstrating the parallel pressure drop trend found for different mass fluxes inside the 2.15 mm ID tube. The offset of $\sim$ 0.004 bar at q $\approx$ 35 kW/m^2 indicates the slight increase in ΔP with decreasing T_{sat}. The pressure drop value at G $\approx$ 800 kg/m^2s is about 30% higher at -25°C compared to the +15°C value. In Figure 9.11(b) the same comparison is carried out for the 1 mm ID tube. Here the slopes for the two data sets differ, indicating a diverging pressure drop trend towards lower saturation temperatures and higher mass fluxes, resulting in the fan-shaped trend described above. At G $\approx$ 800 kg/m^2s the pressure drop value at -25°C is already more than twice the +15°C value with an increasing tendency towards higher mass fluxes. Figure 9.11(c) shows the same comparison for the 0.5 mm ID tube and the large offset of about

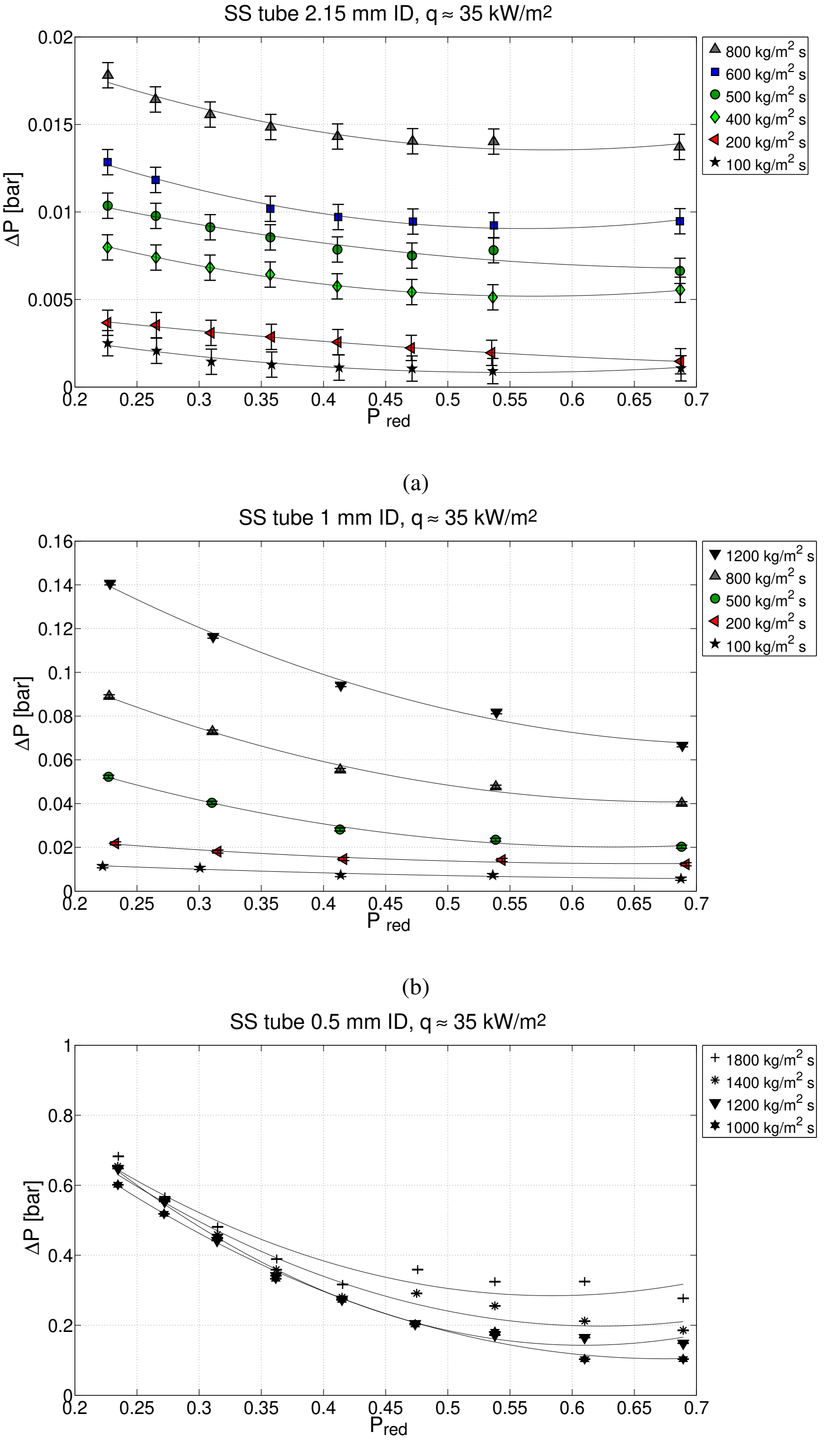

SS tube 2.15 mm ID, q ≈ 35 kW/m2

(a)

SS tube 1 mm ID, q ≈ 35 kW/m2

(b)

SS tube 0.5 mm ID, q ≈ 35 kW/m2

(c)

Figure 9.9: Effect of reduced pressure and mass flux on the two-phase pressure drop at 35 kW/m^2: a) 2.15 mm ID tube; b) 1 mm ID tube; c) 0.5 mm ID tube.

0.5 bar between the two different data sets is obvious, whereas the slopes are in this case very similar again. At G ≈ 1000 kg/m^2s the pressure drop is about 5 times higher at -25°C compared to the +15°C value. In general an influence of the heat flux on the two-phase pressure drop is obvious for all three tubes, where at +15°C the difference in ΔP due to an increase of heat flux from q ≈ 10 kW/m^2 and q ≈ 35 kW/m^2 is smaller compared to -25°C. The influence of the heat flux increases with increasing mass flux. Both findings are strongest for the 1 mm ID tube.

In summary it is anticipated that two independent phenomenological effects superimposed onto each other influence the final parametrical results and trends. The first effect is based on the known change in physical properties of CO_2 for different T_{sat}. The second effect appears to be linked to an increasing level of confinement for decreasing ID. The radical change of all properties of interest across the test range is discussed in section 5.3.2. The density ratio ρ_l/ρ_g is five times higher at -25°C than at +15°C, whilst the viscosity ratio μ_l/μ_g is 2.5 times higher at -25°C compared to the value at +15°C. In general with decreasing T_{sat} the difference between the vapour and liquid properties increases. Thus the slip ratio, in this case estimated as $(\rho_l/\rho_g)^{1/3}$ with the simple relation proposed by Zivi [50], also increases. As a consequence of these changes, the two-phase frictional pressure drop logically increases with decreasing T_{sat}. However, the change of CO_2 properties as a function of temperature also influences the flow patterns, for instance through the effects of the surface tension. As reasoned above an increasing surface tension leads to a larger bubble radius, an increasing bubble departure diameter and a lower bubble frequency [145]. This was confirmed with the high-speed camera visualizations discussed above, where the images showed the mentioned variation of bubble size with T_{sat}. Pettersen [138] also conducted visualization of CO_2 vaporization in a 0.98 mm ID tube at T_{sat} +20°C and 0°C aiming at the effects of T_{sat}: at vapour qualities in the order of 0.4, smaller bubbles could be observed for +20°C T_{sat} with respect to visualizations obtained in similar conditions at 0°C T_{sat}. Concerning the effect of confinement, several criteria have been proposed in literature to quantify the confinement of the flow. The present study does not produce sufficient evidence to

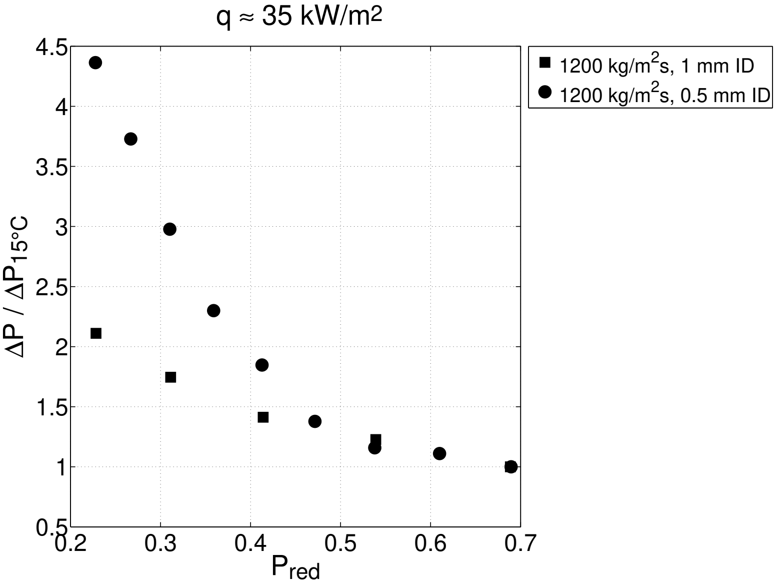

Figure 9.10: Effect of reduced pressure and inner diameter on ΔP / ΔP_{15C} at q ≈ 35 kW/m^2.

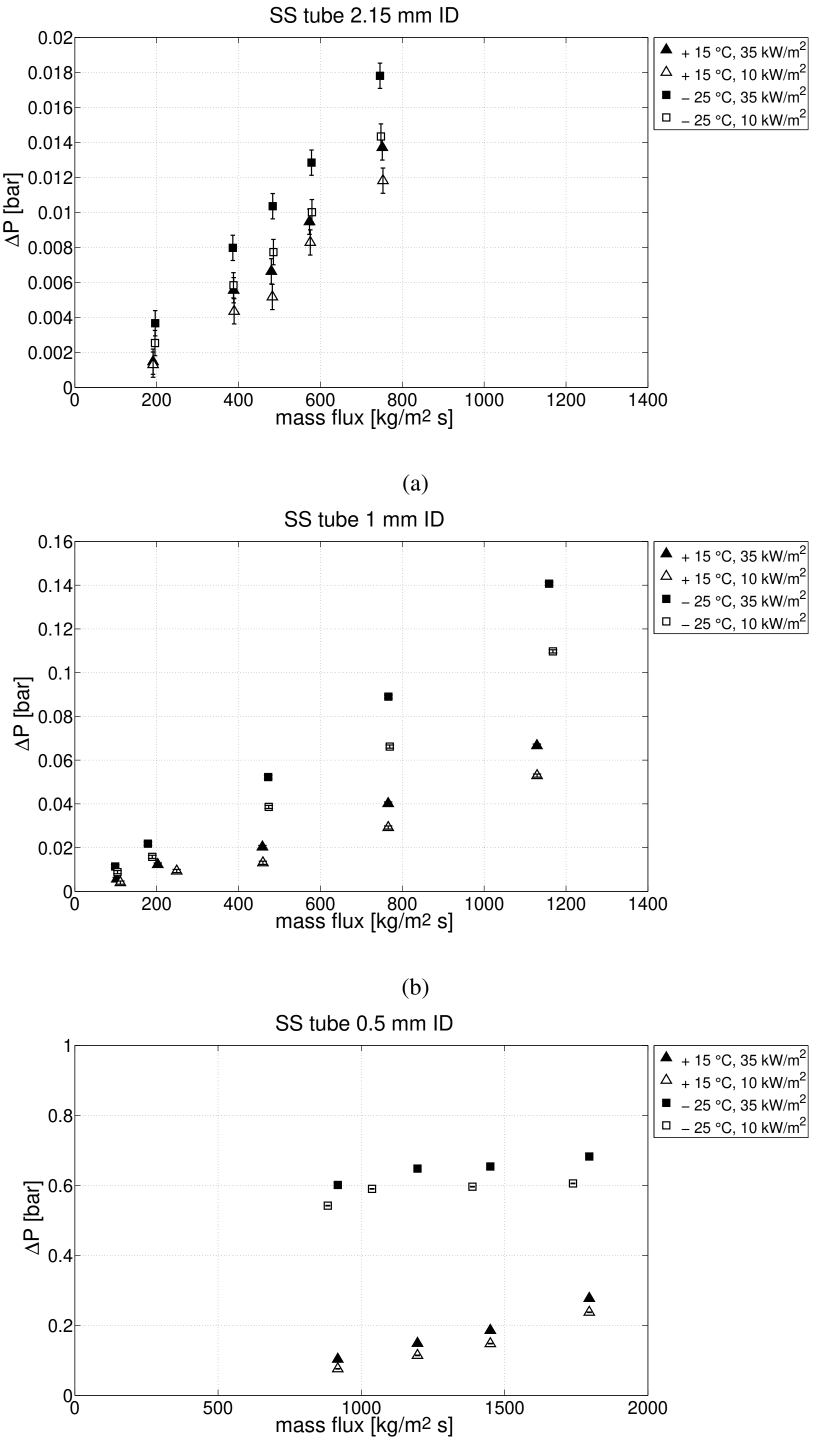

(a)

(b)

(c)

Figure 9.11: Effect of mass flux and heat flux on the two-phase pressure drop at T$_{sat}$ ≈ 15°C and -25°C: a) 2.15 mm ID tube; b) 1 mm ID tube; c) 0.5 mm ID tube.

define a quantitative relation between any macro-to-micro-scale transition criterion and the actual phenomenological flow behaviour within the tubes. However, the simple transition criteria based on the Confinement number, which were shortly introduced in section 6.1, appear to be consistent with the observations made with the tubular evaporators. As a reminder following thresholds were proposed by

- Kew and Cornwell [89]: Co > 0.5 = micro-scale and Co < 0.5 = macro-scale
- Ullmann and Brauner [90]: Co > 0.79 = micro-scale and Co < 0.79 = macro-scale
- Ong and Thome [91]: Co > 1.0 = micro-scale and Co < 0.3 - 0.4 = macro-scale, with a transition region in-between.

Figure 9.12 shows the evolution of the confinement number for the test parameters of this study, adding the indication of the threshold values defined above. For all tube diameters Co increases with decreasing T_{sat} since the surface tension of CO_2 increases more than the difference between liquid and gas densities. According to all criteria shown the tests in the 2.15 mm ID tube would be characterized by macro-scale behaviour for the whole test range, whereas all tests carried out with the 0.5 mm ID tube would basically fall into the micro-scale regime. On the other hand, with the variation of T_{sat} the conditions in the 1 mm ID tube cross both thresholds of Co = 0.5 and Co = 0.79 and fall into the transition region as proposed in [91]. It has been suggested [4, 146, 147] that the dependence on the sole confinement number is not enough to formulate a macro-to-micro-scale transition criterion and flow characteristics should also be taken into account. It is nevertheless interesting to notice that simple criteria based only on Co seem to agree – at least qualitatively – with the experimental observations, suggesting a transitional behaviour of the flow inside the 1 mm ID tube across the observed temperature range. A more advanced criterion for the transition from

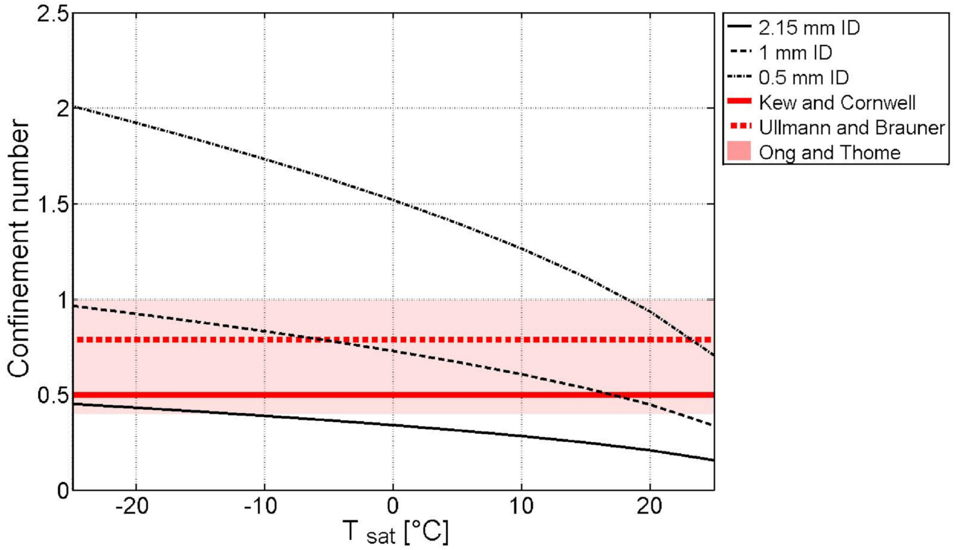

Figure 9.12: Confinement number and confinement criteria for CO_2 between +25°C and -25°C inside three tube dimensions (2.15 mm ID, 1 mm ID and 0.5 mm ID).

macro- to micro-channel behaviour combining the Bond number and the liquid Reynolds number was proposed by Harirchian and Garimella [146] based on their observations on FC72 boiling flows. A comparison of the present data set with this criterion did not provide a consistent interpretation of the experimental measurements. From the above considerations, it seems correct to assume that for the 2.15 mm ID tube the channel cross-sectional area is still large enough to allow for individual bubbles and unconfined flow in the whole range of T_{sat}. The parallel trends described in Figure 9.9(a) and the very slight increase in pressure drop between +15°C and -25°C found in this case seem to reflect a macro-scale flow behaviour and fully unconfined flow. For the 1 mm ID tube confinement effects gain importance for decreasing T_{sat}. This is especially true when the surface tension is higher and thus the bubble size larger compared to the relatively small cross-sectional area, causing the diverging trends for decreasing T_{sat} found in Figure 9.9(b). The 0.5 mm ID tube is finally assumed to be in the fully confined flow regime.

It is worth noticing that this statement also appears consistent with the visualizations of CO_2 flow patterns made by Ozawa et al. [134] which were carried out in small diameter tubes of 3 mm, 2 mm and 1 mm ID and at 14.3°C and 25.4°C T_{sat}. When comparing the observed flow patterns in the 2 mm and the 1 mm tube, for the higher T_{sat} they observed in both cases flow patterns typical for macro-channels (stratification), while at lower T_{sat} the 1 mm ID tube started to show axisymmetric flow patterns (slug flow), typical of confined flow.

Further insights regarding the changing physical behaviour linked to the change in saturation temperature and regarding its differing relevance for flows in tubes of different diameter, can be offered by the analysis of the time signatures of the differential pressure signals acquired at 1 kHz. As an example, in Figure 9.13 the visual appearance and the mean amplitude (RMS and peak-to-peak) of the different signals gathered for the two smaller tubes are compared for different T_{sat} (+15°C, -5°C and -25°C). The time signature for the 1 mm ID tube (Figure 9.13(a)) and the 0.5 mm ID tube (Figure 9.13(b)) show the most obvious transformations for the three selected temperatures. Whereas, in agreement with the observations made above, no obvious quantitative and qualitative change in the signal composition could be found for the 2.15 mm ID tube and therefore it is not further discussed here. The signal composition and peak-to-peak amplitude for the 1 mm ID tube is changing for the different temperatures. Whilst the mean pressure is only increasing from 0.07 to 0.1 bar, the periodical signal structure is changing strongly and the peak-to-peak amplitude is increasing from 0.03 to 0.1. However for the same temperature range the signal composition for the 0.5 mm ID tube is only changing slightly from a clearer signal to a slightly noisier signal, whilst the peak-to-peak amplitude is about 0.1 in all shown cases. As discussed earlier the mean pressure though increases sharply from 0.15 to 0.7 bar. Those findings are in line with the description given before: as argued, the flow within the 1 mm ID tube undergoes a transition between macro and micro-scale, whereas the 0.5 mm ID tube is harbouring confined flow for the whole test range. Since the peak-to-peak amplitude found for the 1 mm ID tube is converging to 0.1, which is typically found for the 0.5 mm ID tube this can be interpreted as another indication for an increasingly confined flow within the 1 mm ID tube. It is interesting to mention that numerical simulations of the flow boiling pressure drop in mini- and micro-channels [134, 148] confirm the highly periodical pressure drop signal found for the present study.

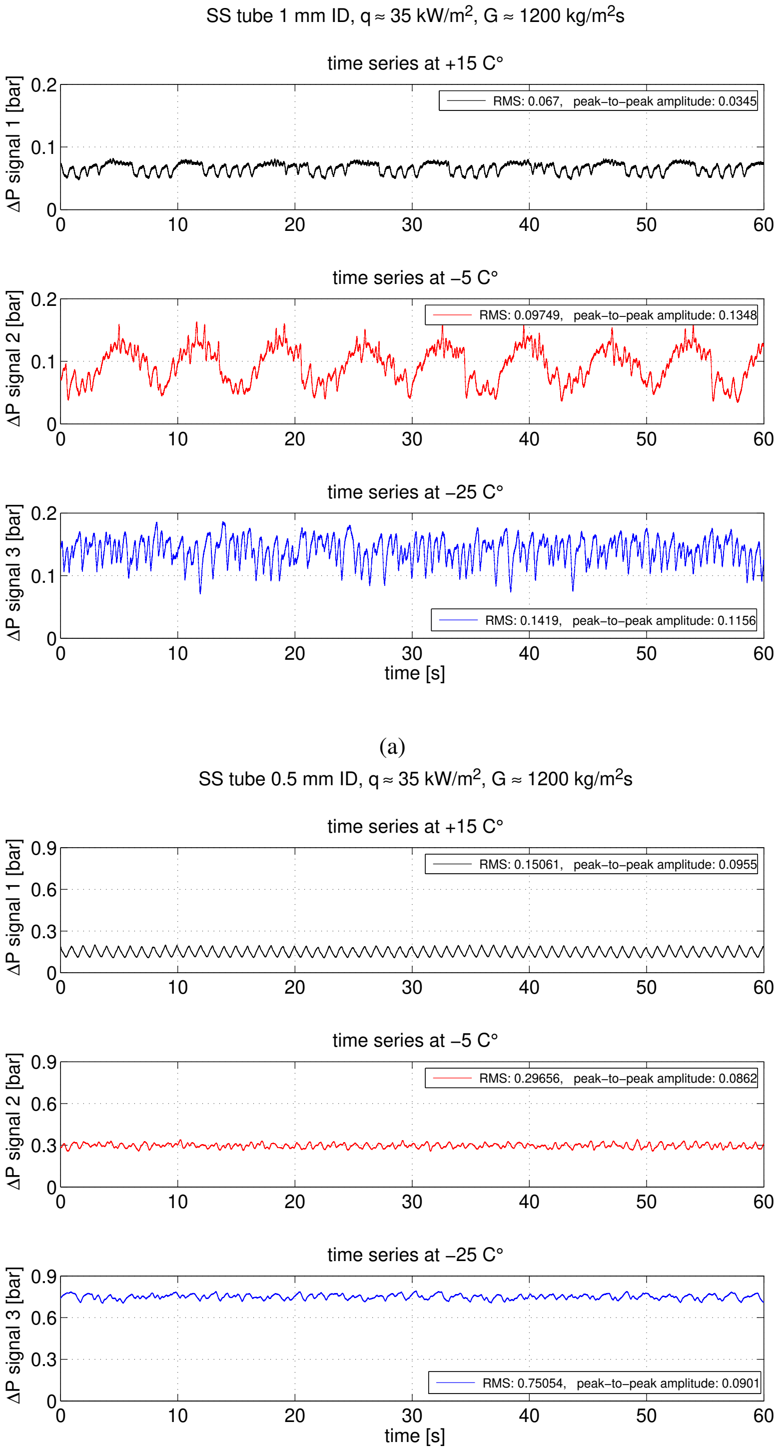

(a)

(b)

Figure 9.13: ΔP time signals at $T_{sat} \approx 15^{\circ}$C, -5°C and -25°C: a) 1 mm ID tube; b) 0.5 mm ID tube.

Heat Transfer

Evaluating the experimental heat transfer coefficient obtained for the three different tubular evaporators, the most general trends reported in the literature review above concerning the inner diameter, the heat flux, the mass flux and the saturation temperature can be confirmed. Figure 9.14 shows the influence of the inner diameter on the heat transfer coefficient at two different saturation temperatures. Figure 9.15 depicts the influence of the heat flux for all three tube diameters, while Figure 9.16 shows the influence of the mass flux.

A general tendency of the heat transfer coefficient to increase with a decrease of the inner diameter of the tube can be verified. However, when comparing the data gathered for the 0.5 mm ID tube and the 1 mm ID tube, the difference in the magnitude of α is more distinct for low q, at both, high and low T_{sat} and for high q at low T_{sat}, whilst at high q and high T_{sat} the values of the heat transfer coefficient are more similar. On the contrary in this case of high q and high T_{sat}, the comparison between the 1 mm tube and the 2.15 mm tube, shows the only real increase in heat transfer coefficient with decreasing inner diameter. The trend that, in the low vapour quality range, the heat transfer coefficient increases for increasing heat flux can be confirmed for all three diameters and across the whole range of tested parameters. However, this effect appears to be more pronounced at e.g. +15°C compared to negative T_{sat} and in particular for the 1 mm ID tube. A near-complete mass flux independence can be confirmed for most studied cases. The same is true for the dependence on the vapour quality, especially for the 2.15 mm ID tube and the 0.5 mm ID tube. The independence of the heat transfer coefficient from the mass flux is generally interpreted in terms of nucleate boiling as dominant heat transfer mode. However, for the 1 mm ID tube, the heat transfer coefficient exhibits a shift after the initial increase in vapour quality and the higher the mass flux the earlier this shift appears. This is more pronounced for elevated T_{sat} around 15°C.

The given examples show that, although the main trends of the heat transfer coefficient as a function of the inner diameter, the heat flux and the mass flux as found in literature can be confirmed, in all cases a superposed effect of the saturation temperature further influences those findings. Thus, the following discussion on the evolution of the heat transfer coefficient will again focus in more detail on the effects of saturation temperature. Figure 9.17 depicts examples of the decreasing heat transfer with decreasing saturation temperature for all tested tubes. This trend is very clear and progressive for the 2.15 mm ID tube and even more apparent for the 1 mm ID tube. For the 0.5 mm ID tube, after an initial sensible variation passing from +15°C to +5°C, the heat transfer coefficient is much less effected by T_{sat} below +5°C.

To further highlight the effect of T_{sat} on the heat transfer coefficient the evolution of the above introduced α_{ave} can be discussed. Figure 9.18 reports the general decreasing trend of the average heat transfer coefficient for decreasing T_{sat}. The variation of α_{ave} across the test range is the largest for the 1 mm ID tube. This effect is particularly apparent due to the very high values of α found for this tube at elevated T_{sat}. For the shown case of high heat flux, the average heat transfer coefficient of the 1 mm ID tube is roughly reduced by a factor five when comparing the results at +15°C and -25°C. For the 2.15 mm ID tube the same reduction in T_{sat} leads to only two times lower heat transfer coefficient values. For the 0.5 mm ID tube the average heat transfer coefficient shows an initial reduction in the order of 25% down to T_{sat} around -5°C, and then remains more or less constant across the remainder of the explored range. This latter observation is in line with findings by Ducoulombier et al. [135] gathered for a test tube with the same nominal ID (0.5 mm) and experiments carried out with highly confined flow of boiling CO_2 in multi-micro-channels [149] described in section 9.2.1 and Figure 9.7.

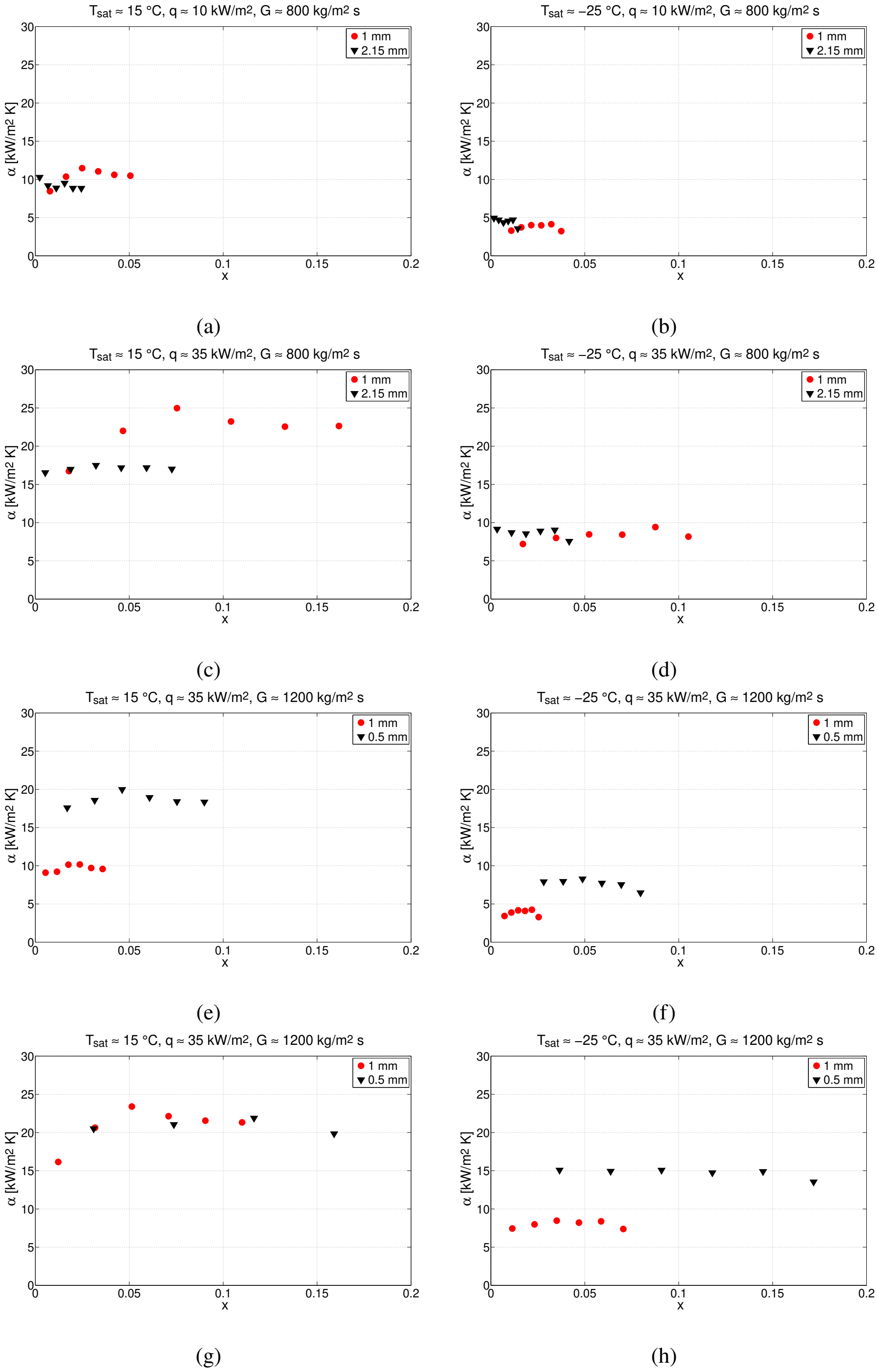

(a) (b) (c) (d) (e) (f) (g) (h)

Figure 9.14: Influence of ID and T_{sat} on the heat transfer coefficient: a) to d) comparison between the 1 mm ID tube and the 2.15 mm ID tube; e) to h) comparison between the 1 mm ID tube and the 0.5 mm ID tube.

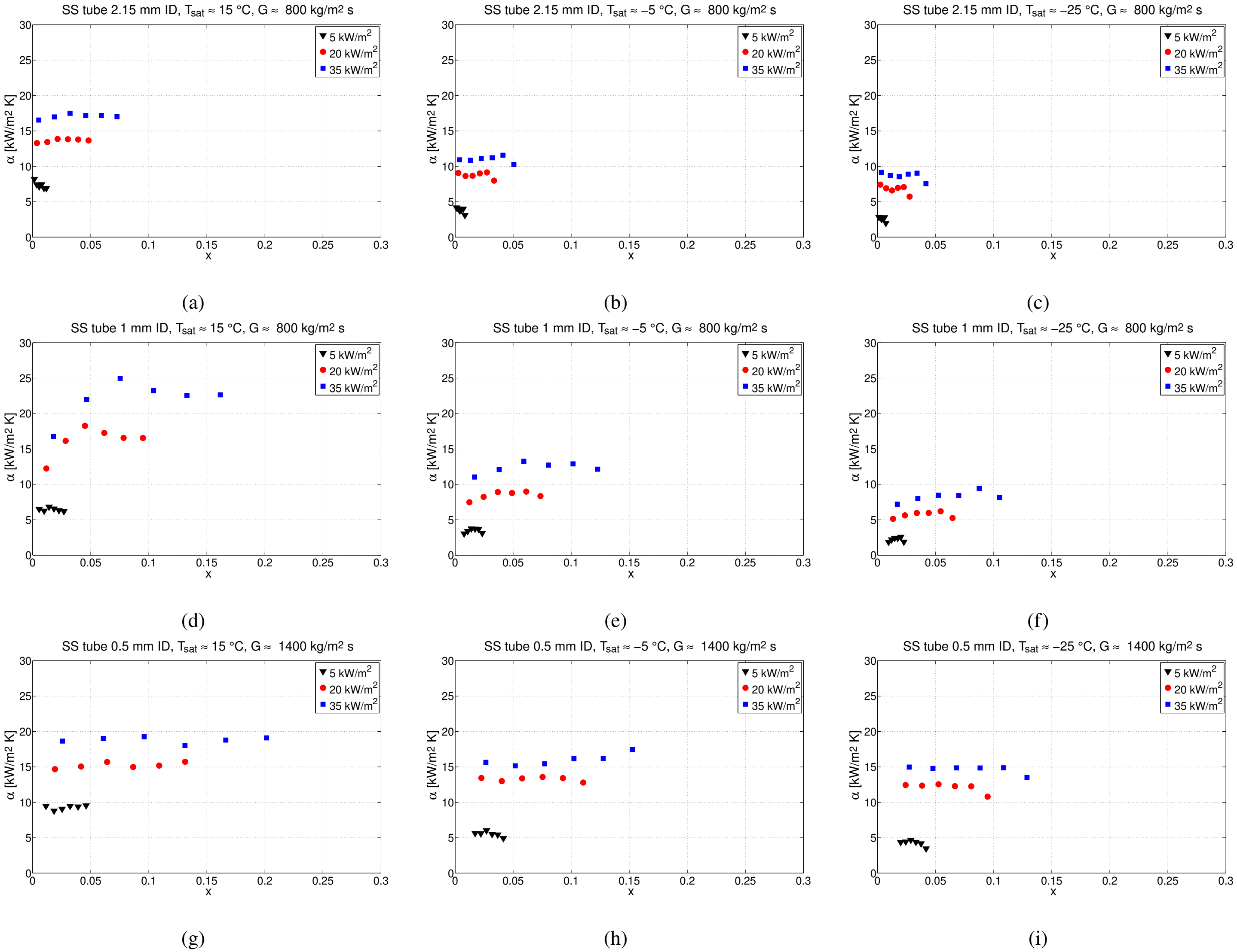

(a) (b) (c)

(d) (e) (f)

(g) (h) (i)

Figure 9.15: Influence of q and T_{sat} on the heat transfer coefficient: a) to c) 2.15 mm ID tube; d) to f) 1 mm ID tube; g) to i) 0.5 mm ID tube.

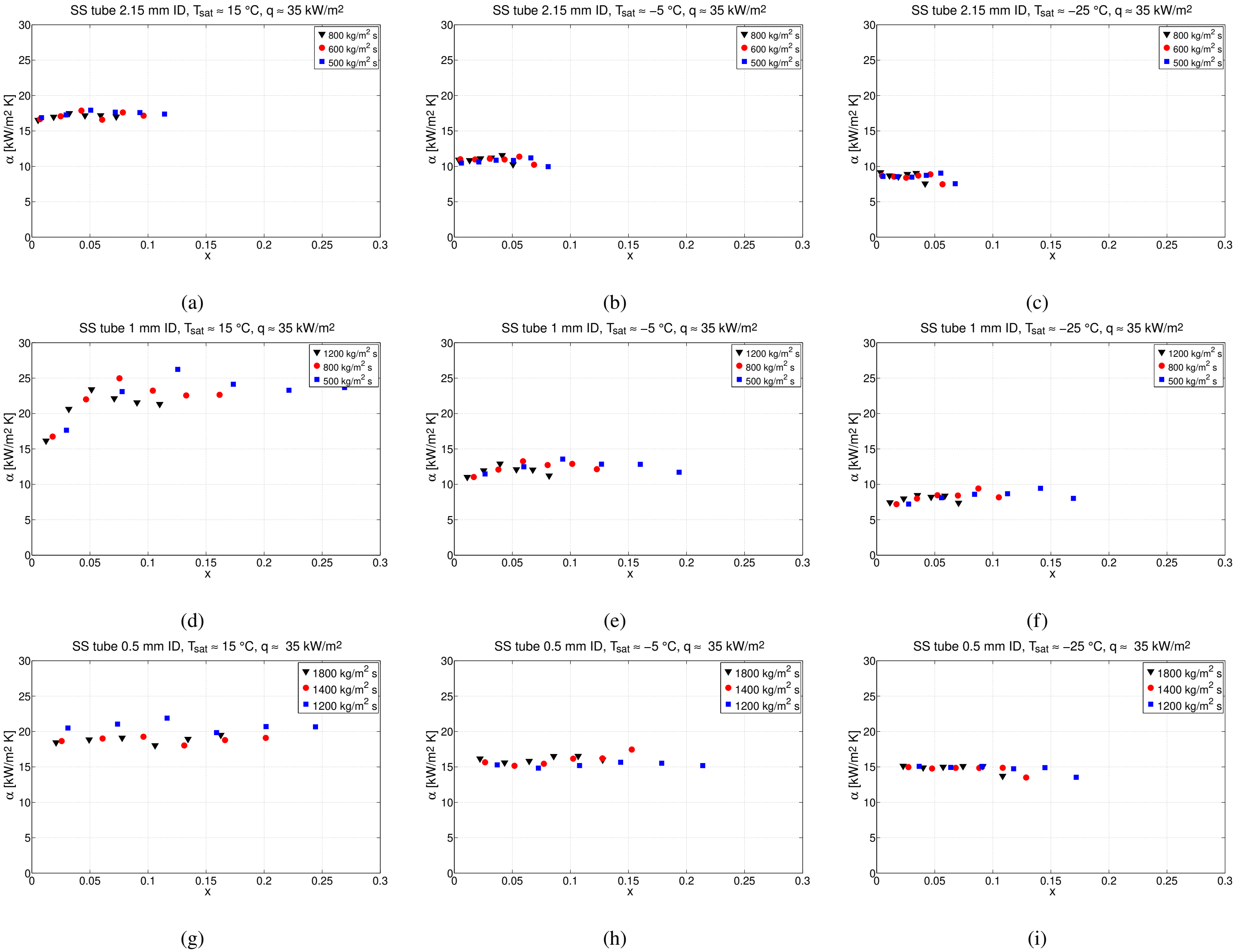

(a) (b) (c)

(d) (e) (f)

(g) (h) (i)

Figure 9.16: Influence of G and T_{sat} on the heat transfer coefficient: a) to c) 2.15 mm ID tube; d) to f) 1 mm ID tube; g) to i) 0.5 mm ID tube.

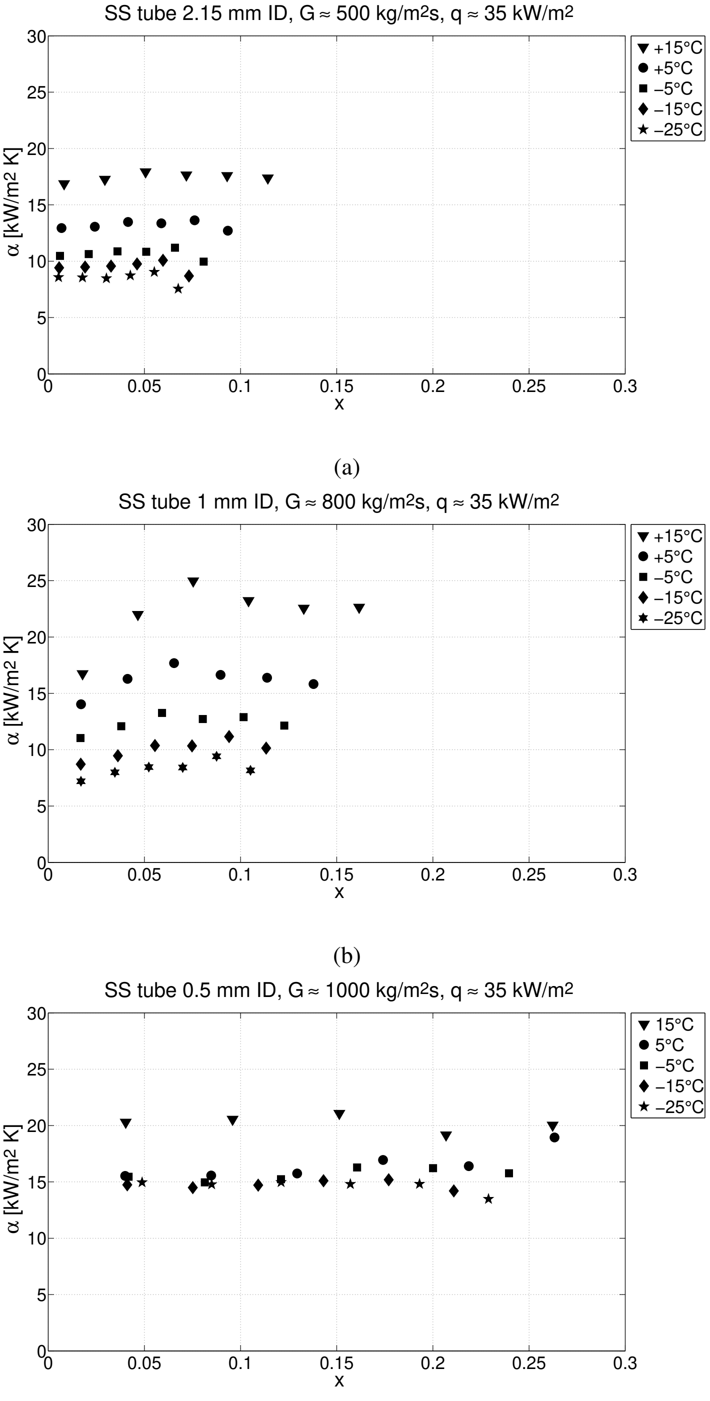

(a)

(b)

(c)

Figure 9.17: Examples of decreasing heat transfer coefficient with decreasing T$_{sat}$: a) 2.15 mm ID tube; b) 1 mm ID tube; c) 0.5 mm ID tube.

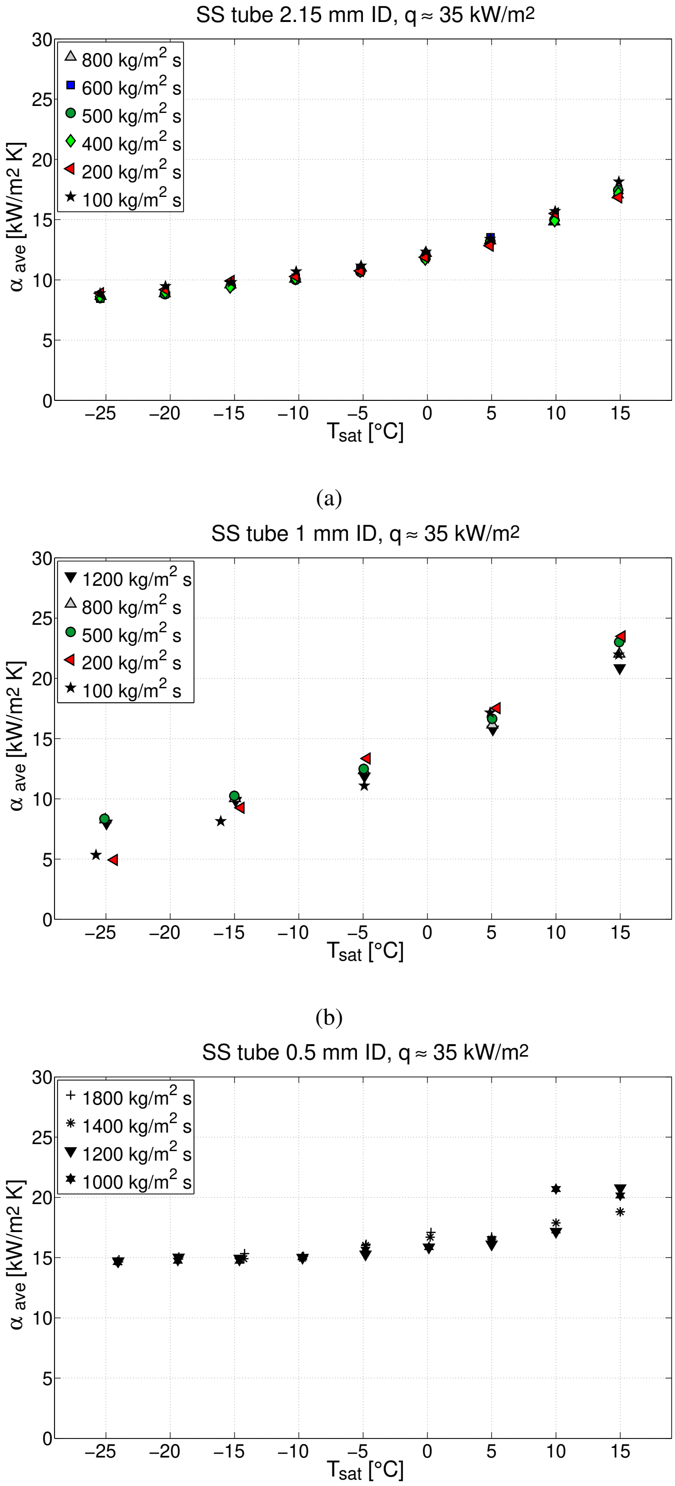

(a)

(b)

(c)

Figure 9.18: Trend of decreasing heat transfer coefficient for decreasing T$_{sat}$: a) 2.15 mm ID tube; b) 1 mm ID tube; c) 0.5 mm ID tube.

The large variation of the average heat transfer coefficient observed for the 1 mm ID tube at different temperatures, combined with rather different trends of α as a function of x, when varying the different parameters, may indicate the presence of different flow patterns due to different flow confinement levels. This point was already stressed and substantiated in 9.2.2, based on findings on the pressure drop across the same 1 mm ID tube. It was in particular shown for this tube size that the pressure drop is strongly influenced by the changing physical properties of CO_2 across the tested temperature range and thus by radically different confinement levels of the flow. In this section the presence of different boiling regimes over the range of observed temperatures shall be discussed in addition, where the historic differentiation between nucleate and convective boiling shall be retained as a first basic approach, however especially due to the mentioned inconsistency in acquired data found in literature no true evidence has been found that a simple subdivision or otherwise superposition of nucleate boiling and convective boiling is a valid approach to provide a complete interpretation of flow boiling in ducts. For the 2.15 mm ID tube, the increasing α_{ave} as a function of T_{sat} is coupled to a constant trend of α as a function of x at low vapour quality, which was already observed by Yun et al. [115] and Hihara and Dang [9]. This combination of effects may be ascribed to a fully unconfined flow, with nucleate boiling as possible dominant heat transfer mode at low vapour quality, including the lowest observed temperature. The largely temperature independent heat transfer coefficient found for the 0.5 mm ID tube is consistent with the hypothesis of a fully confined flow behaviour inside this tube across the entire tested temperature range, which was already argued in 9.2.1. However since in this case axisymmetric flow patterns are known to be more dominant the previously shown constant trend of α as a function of x can not be explained anymore with a sole dominance of nucleate boiling and the possibility of multiple or different mechanisms has to be considered.

In this respect it needs to be stressed that the confinement level may be decoupled from the heat transfer effectiveness and thus different confinement levels may produce similar quantitative heat transfer coefficient values. Furthermore similar heat transfer coefficient values may be caused by different prevalent heat transfer mechanisms due to the different channel sizes. As an example, according to Figure 9.14 and Figure 9.18 the heat transfer coefficient is dissimilar for the 1 mm ID tube and the 2.15 mm ID tube at high T_{sat}, however similar for the 1 mm and the 0.5 mm ID tubes. On the other hand, the heat transfer coefficient is similar for the 1 mm ID tube and the 2.15 mm ID tube at low T_{sat}, however dissimilar for the 1 mm and the 0.5 mm ID tubes below $T_{sat} \approx -5°C$. This underlines the remark given above on the possibility of a more complex nature of heat transfer processes during flow boiling in small channels - especially for CO_2 - and which must allow for more than two basic boiling mechanism: e.g. in the case of the 0.5 mm tube a novel phenomenon may occur at low $T_{sat} < -5°C$, which accounts for the stabilisation of α at a constant value, whilst for the 1 mm ID tube, although similar to the 0.5 mm ID tube data at high T_{sat}, there is still a discernible drop in α to be found.

Furthermore temporal homogeneous heat transfer properties can be maintained independent of the transitional effects happening in the flow. To provide evidence of this conclusion analogous to the results given in section 9.2.2, the time signal of the temperature sensors can be analysed. There are the thermocouples on the outer tube wall (60 Hz acquisition rate) and the in-flow RTD temperature sensor at the tube outlet (400 Hz acquisition rate). In Figure 9.19 the temperature signal of an example thermocouple (TC 4) is shown for the 1 mm ID tube and the 0.5 mm ID tube. As opposed to the pressure drop signal, significant variations of the outer tube wall temperature in time could not be found for the shown cases. Focusing on the flow behaviour whilst using the same set of test parameters, in Figure 9.20 the temperature signals from the in-flow temperature sensor at the tube outlet are compared for the 1 mm ID tube and the 0.5 mm ID tube. In this case the temperature of the

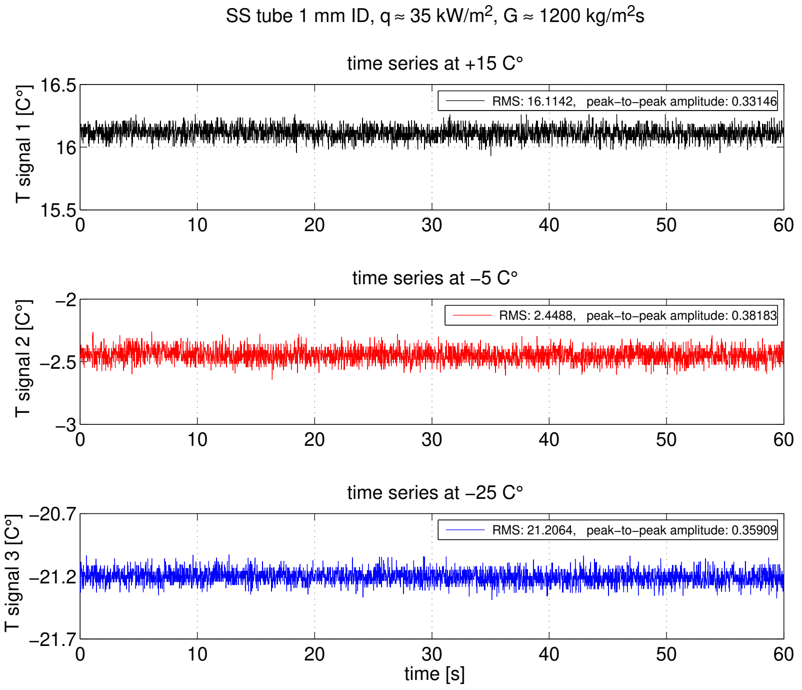

(a)

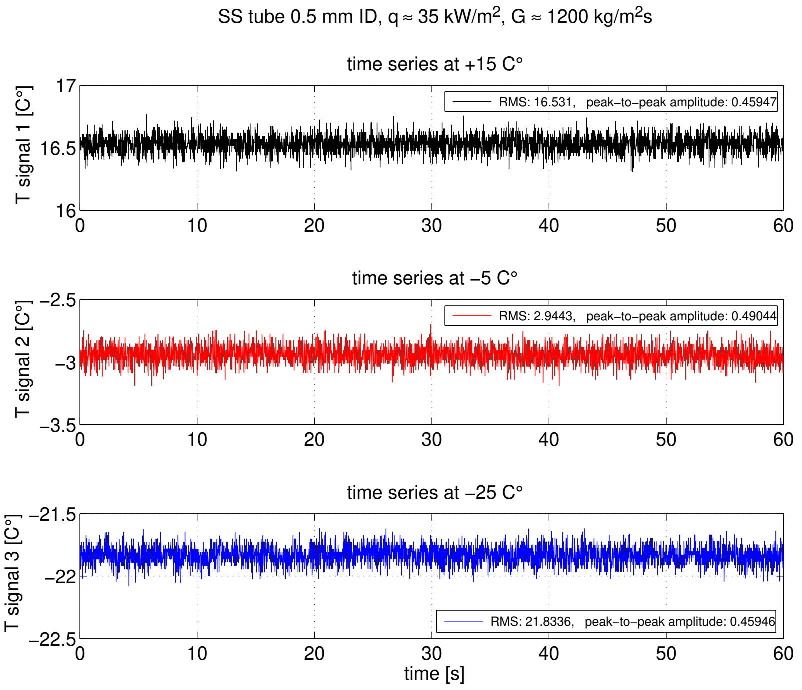

(b)

Figure 9.19: Thermocouple time signals at $T_{sat} \approx 15^{\circ}$C, -5°C and -25°C: a) 1 mm ID tube; b) 0.5 mm ID tube.

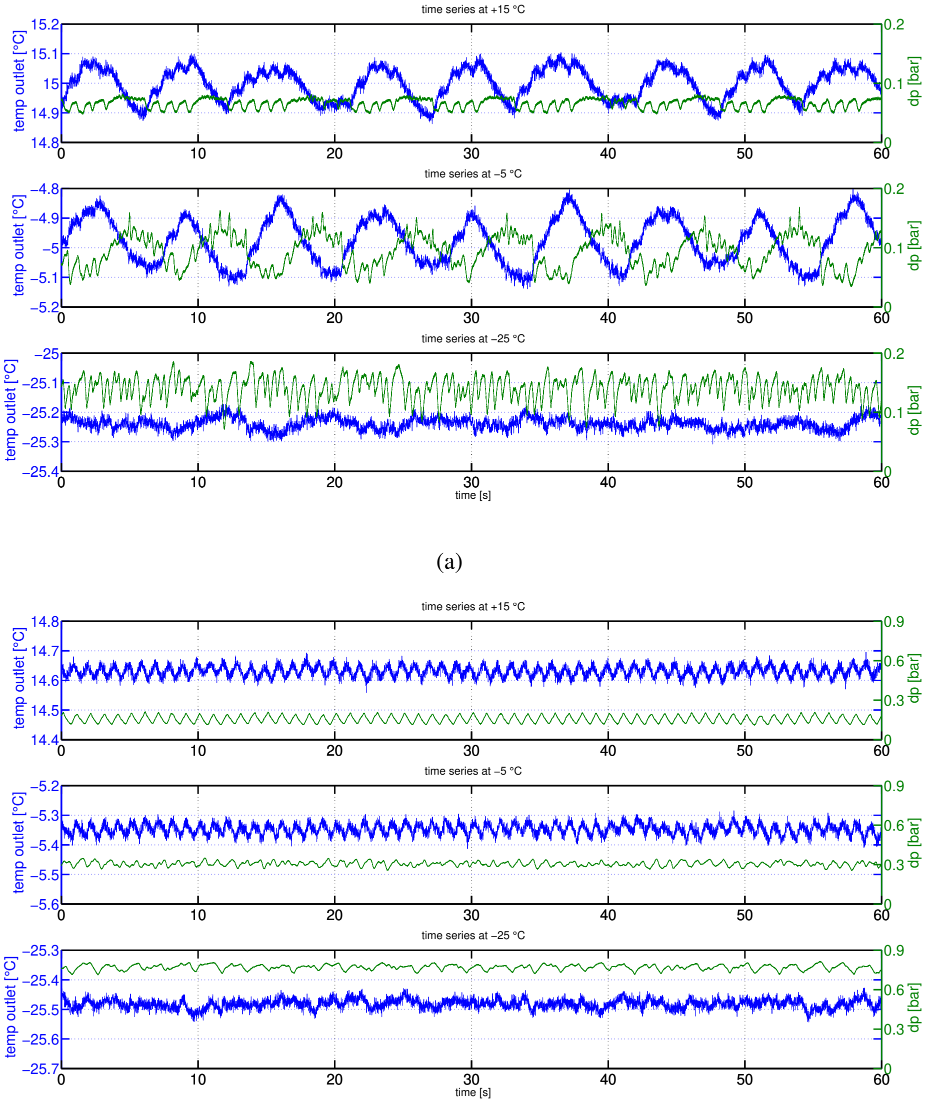

(a)

(b)

Figure 9.20: dp and RTD$_{outlet}$ time signals at T$_{sat}$ ≈ 15°C, -5°C and -25°C: a) 1 mm ID tube; b) 0.5 mm ID tube.

fluid at the outlet of the 1 mm ID tube is subjected to higher fluctuations at +15°C and -5°C compared to -25°C. This is consistent with the results found for the pressure drop, which are added to Figure 9.20 for comparison. The period length of the dp and fluid temperature fluctuation is in both cases about 5s, however slightly out of phase. The peak-to-peak amplitude of the signal gathered for the 1 mm ID tube is again more similar to the signal gathered for the 0.5 mm ID tube at low T_{sat}. Here the peak-to-peak amplitude for the 1 mm ID tube is about 0.1 °C, whereas this is the amplitude for the whole test range for the 0.5 mm ID tube. This re-occurrence of a higher level of similarity of the flow inside the two different tubes at low T_{sat} hints once more towards similar flow behaviour and confinement levels. The mass flux was acquired at 1 Hz acquisition rate only, however no meaningful oscillation could be found in parallel to the above described phenomena. Since the found oscillations in pressure and temperature described above do not cause a temporal degradation of the heat transfer, they are denoted as fluctuations and not as instabilities.

It is known that two-phase flow under certain circumstances may be subjected to various flow behaviour induced phenomena causing flow instabilities and fluctuations of test parameters [150, 151]. This occurrence has been discussed for narrow channels [139] and additional phenomena compared to conventional channels occur [136, 152]. The onset of full bubble confinement leads to an over-pressure in the channel caused by a vapour blockage and as the flow transforms into elongated slug flow the pressure decreases again. The fluctuations due to flow pattern transition are long-period (more than 1s) or short-period (less than 0.1 s) oscillations depending on the different alternating flow patterns. For the present study no parallel visualization exists to the parametrical analysis. However the fact that relatively long period fluctuations of pressure and fluid temperature are especially occurring inside the 1 mm ID tube may be caused by similar phenomena as described for the flow pattern instability and the transitional nature of the flow inside the 1 mm ID tube can be described with this context. However during this study data were also affected by obvious flow instabilities and they have been identified by means of a combined analysis of different signals as described in section 8.1.5. Please note that no orifice or any other flow regulation device is installed upstream of the test section and so far unrestricted flow is being studied. Figure 9.21 gives an example where obvious instabilities occurred within the 1 mm ID tube at low mass flux (100 kg/m^2s). Compared to the other fluctuations described above, in the case of instabilities the tube wall temperatures and thus the heat transfer coefficient are heavily affected. Table 9.1 shall summarize in short the instabilities found for this study to guide the future design of small-scale CO_2 evaporators. At low mass fluxes (< 200 kg/m^2s) the flow in the 1 mm tube indeed starts to be subjected to flow instabilities however only at T_{sat} < -5°C. This is yet a further indication for the transformation of the flow inside the 1 mm ID tube due to a decrease in T_{sat} and which explains the slight anomaly of the data points taken at 200 and 100 kg/m^2s and at $T_{sat} \leq$ -15°C shown in Figure 9.18(b) which have not been excluded for presentation in this case. Figure 9.22 shows the increasing effect of such instabilities on the outer tube wall temperature for decreasing fluid temperature. At -5°C the instabilities are still minor (0.2°C), whilst at -15°C and -25°C they gain in magnitude, (~ 1.5 to 3°C, respectively). However with the installation of a flow restriction (e.g. orifice) in the upstream direction of the test section those instabilities can be avoided in the future. The restrictive sections implemented into the multi-micro-channel design, discussed in 7.1.2, confirm the flow stabilizing effect of this method.

Furthermore the quantitative findings for the 1 mm ID tube, especially at elevated T_{sat} where the trend in α results in a peak, can be once more explained with the bubble dynamics within the tube. Yin and Jia [153] also found a maximum in the heat transfer coefficient at low vapour quality. In this case flow boiling was studied with deionized water along a rectangular micro-channel with 0.5 mm x

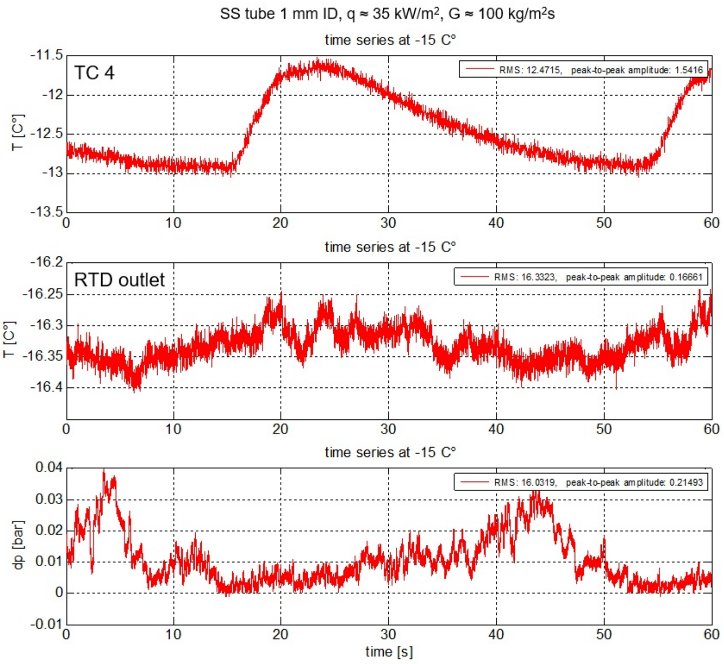

Figure 9.21: Instability of system parameters: tube wall temperature, tube outlet fluid temperature and pressure drop.

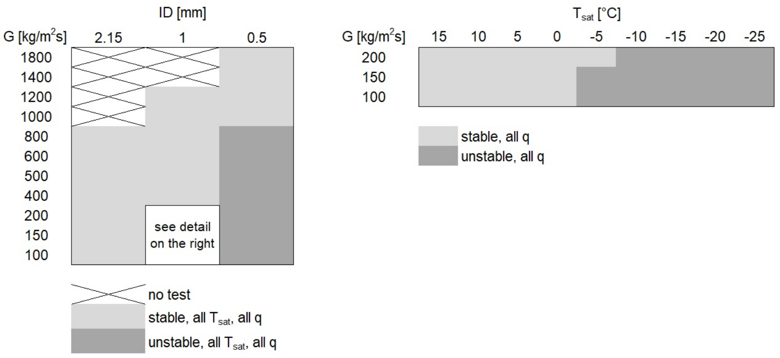

G [kg/m^2s] \ ID [mm]	2.15	1	0.5
1800	☒	☒	░
1400	☒	☒	░
1200	☒	░	░
1000	☒	░	░
800	░	░	▓
600	░	░	▓
500	░	░	▓
400	░	░	▓
200	░	see detail on the right	▓
150	░		▓
100	░		▓

☒ no test
░ stable, all T_{sat}, all q
▓ unstable, all T_{sat}, all q

G [kg/m^2s] \ T_{sat} [°C]	15	10	5	0	-5	-10	-15	-20	-25
200	░	░	░	░	░	▓	▓	▓	▓
150	░	░	░	░	▓	▓	▓	▓	▓
100	░	░	░	░	▓	▓	▓	▓	▓

░ stable, all q
▓ unstable, all q

Table 9.1: Instability matrix found for this study.

1 mm cross-section. The properties of water are of course very different to CO_2 however the bubble growth dynamics in confined channels as described in the study by Yin and Jia [153] may apply to any liquid and could be linked to the trend in α found for the 1 mm ID tube. At the channel inlet with very low vapour quality dispersed bubble flow was dominant, as the vapour quality increased along the channel due to the applied heat flux the flow showed confined bubble flow and elongated bubble flow. The local heat transfer coefficient could be coupled to the flow pattern. The initial bubbly flow causes a rapid increase of the heat transfer coefficient. After this the confined bubble growth enhances the

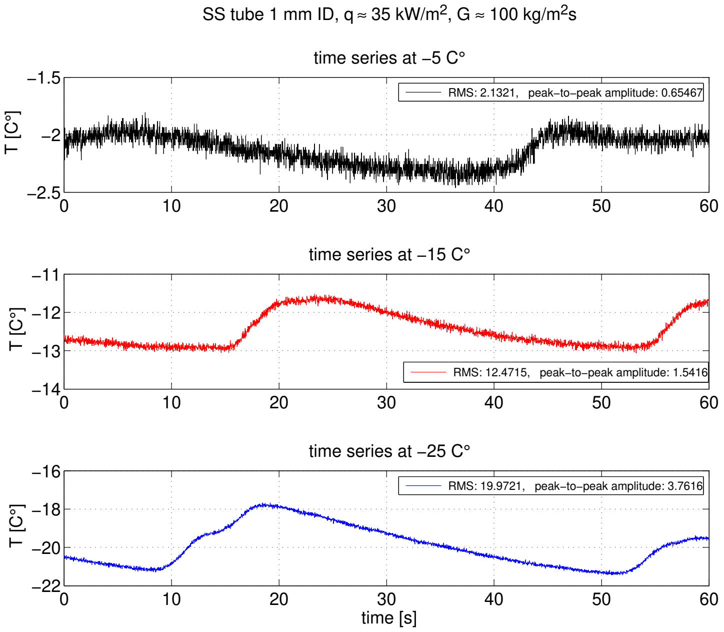

Figure 9.22: Effect of T_{sat} on instability: tube wall temperature.

heat transfer until a maximum is reached. The following drop in α is explained with the continuous thinning of the liquid film along the wall as the flow pattern goes over into annular flow which favours convective heat transfer. For the present study the maximum of α at elevated T_{sat} is possibly due to similar flow behaviour as described by Yin and Jia [153]. Nevertheless, with decreasing T_{sat} this maximum in α diminishes for the 1 mm ID tube. This can be explained with the increase of the surface tension of CO_2 which favours a larger bubble size. As motioned already in 9.2.2, during flow boiling the bubble departure is influenced by surface tension, buoyancy and drag forces. Thus at a fixed mass flux increasing surface tension at low T_{sat} leads to an increasing bubble departure diameter and a lower bubble frequency. Due to the increased size of the bubbles at departure they may already be classified as confined or even elongated and the described shift between the two flow patterns is less pronounced, which leads in this case to the constant heat transfer coefficient versus vapour quality, but also to the decay of the fluctuations in the pressure and fluid temperature. Additionally the above mentioned higher heat flux dependence of α in the 1 mm ID tube at +15°C compared to lower T_{sat} may be due to the fact that smaller bubbles and nucleate boiling are more dominant at elevated T_{sat} compared to low T_{sat}. At low T_{sat} the confined bubbles in the 1 mm ID tube may lead to more convective flow boiling which is in general heat flux independent.

Even without direct flow visualization on the tubular evaporators, which is important for a final evaluation of the results, many other investigative methods were proposed successfully to analyse the phenomenological transition of the flow within the three tube dimensions and across the tested temperature range (parametrical and direct signal analysis, comparison to transition criteria, comparison to external findings). Note that visualization methods on tubular CO_2 evaporators have been investigated during this study. However, due to the high fluid pressures a reliable and safe interconnection between the remaining stainless steel tubing of the setup and a high-pressure glass tube still had to be found, while taking into account fluid-dynamical aspects: Due to the high internal pressures the wall-thickness of the glass tube in some cases had to be multiple times the one of the adjoining stainless steel tubes whilst the inner diameter had to be very similar. This requires a custom-made interconnection without fluid-mechanical step between the two different tubes to allow for a continuous, undisturbed flow.

9.3 Comparison to existing correlations

The comparison of the experimental data set with existing correlations modeling the two-phase pressure drops and heat transfer brings additional information on the physical phenomena involved and puts into evidence the limits of the two-phase flow models developed until now. In general it was found that the prediction capability for the heat transfer coefficient of already existing correlations is better than for the pressure drop.

9.3.1 Pressure drop

As the experimental data set is formed by measured values of the total pressure drop ΔP_{exp}, the comparison must be made with the prediction of the total pressure drop ΔP_{pred}. In this case, the frictional component $\Delta P_{pred,frict}$ is calculated based on various correlations available in literature - introduced in 5.1.2 and 6.1 - while the accelerational component $\Delta P_{pred,acc}$ is calculated based on the homogeneous or separated phase formulation considering the fluid properties at the inlet and outlet of the test section - also explained in section 5.1.2. However, when comparing diabatic pressure drop results to existing correlations it is important to acknowledge the contribution of the increasing vapour quality along the tube. Thus for the correlative analysis of this study the length of the tube was discretized into several sections and the vapour quality within each section was calculated based on a linear fit between the derived value at the inlet and outlet. The assumption of a linear increase of the vapour quality during evaporation tests is consistent with the uniformly distributed heat load during the experiment. Different predictions of the frictional component are therefore obtained by step-wise integration of different correlations along the tube length. The result is then added to the accelerational component and this quantity is compared to the measured value of the pressure drop. Table 9.2 shows the prediction performance of an extensive group of correlations as compared to the complete data set of this study consolidated per value of the tube ID and indicating the average deviation $\bar{\xi}$, the mean deviation $|\bar{\xi}|$ and the fraction of the data predicted within ±20%, ξ_{20}. It has to be mentioned that when using the homogeneous models the outcome is strongly influenced by the surface roughness of the tube and trends might differ from other studies. The correlation proposed by Pamitran et al. [120] is not listed in the table due to the extremely large deviations produced at low mass fluxes, in line with the findings by Ducoulombier et al. [121]. As frequently presented in literature, Figure 9.23 compares in a global way the outcome of some correlations (ΔP_{pred}) with the experimental data (ΔP_{exp}) of each tube diameter. For this comparison the best suitable correlation of each class listed in Table 9.2 has been selected, defined as the one providing the largest fraction of data predicted within an error of ±20% from the measured value (ξ_{20}).

Some general observation can be made on the basis of the plots reported in Figure 9.23: the case of the 2.15 mm ID tube (Figure 9.23(a)) is relatively well predicted by at least one correlation in each class, including the basic homogeneous model, with the largest discrepancies between measurement and prediction clustering in the region $\Delta P < 5$ mbar. Here the experimental uncertainties have

	Deviation [%]								
	2.15 mm ID tube			1 mm ID tube			0.5 mm ID tube		
correlation (class)	average $\bar{\xi}$	mean $\lvert\bar{\xi}\rvert$	ξ_{20}	average $\bar{\xi}$	mean $\lvert\bar{\xi}\rvert$	ξ_{20}	average $\bar{\xi}$	mean $\lvert\bar{\xi}\rvert$	ξ_{20}
homogeneous model	-11.26	17.78	67.74	-20.68	20.78	47.30	4.60	37.82	25.00
McAdams et al. [63]	-13.70	17.17	66.67	-24.75	24.75	41.89	0.41	37.30	24.44
Beattie and Whalley [64]	-32.09	32.78	30.11	-42.89	42.89	2.70	-13.03	35.27	25.56
Cicchitti et al. [65]	-11.49	17.64	67.74	-21.44	21.50	45.95	3.84	37.38	25.00
Dukler et al. [66]	-15.03	17.77	64.87	-26.10	26.10	39.19	-0.79	37.60	22.22
Akers et al. [67]	-11.74	17.10	68.82	-22.45	22.48	45.95	2.84	37.43	24.44
Lin et al. [68]	-11.91	16.98	69.18	-22.39	22.43	45.95	2.73	37.45	24.44
macro-channel correlations									
Müller-Steinhagen/Heck [73]	-8.06	16.53	72.40	-21.07	21.21	45.95	-11.32	31.54	31.11
Grönnerud [75]	-11.86	18.90	63.08	-24.98	25.23	40.54	-15.19	32.24	31.67
Friedel [74]	13.99	22.50	48.03	-4.00	12.77	83.78	4.38	33.17	31.67
Lockhart-Martinelli :									
C-method [70, 71]	67.20	73.30	28.32	63.67	70.35	16.22	111.71	120.68	15.56
B-method [72]	129.18	130.04	22.58	9.51	22.26	58.11	-1.13	29.79	35.56
micro-channel correlations									
Mishima and Hibiki [93]	-29.40	29.64	33.69	-41.23	41.23	10.81	-39.43	40.74	38.33
Tran et al. [94]	6.39	21.91	53.05	17.77	24.27	44.59	111.59	113.16	8.33
Zhang and Webb [95]	-7.25	16.17	72.76	-19.52	19.52	56.76	-11.91	28.39	35.00
Qu and Mudawar [96]	-29.36	29.60	34.05	-41.14	41.14	10.81	-39.29	40.63	38.33
Lee and Garimella [97]	-28.41	28.68	36.92	-40.82	40.82	10.81	-39.24	40.58	38.33
Lee and Lee [98]	18.06	25.49	45.52	7.37	23.17	50.00	18.71	49.79	19.44
Kim and Mudawar [99]	31.61	35.72	25.81	5.72	16.67	66.22	11.33	39.68	26.67
CO_2 correlations									
Yamamoto et al. [119]	1.75	17.89	65.23	-8.73	19.37	52.70	0.70	38.24	25.00
Yun and Kim [118]	-25.62	26.62	42.65	-37.68	37.68	20.27	-33.84	37.57	38.33
Ducoulombier et al. [121]:									
homogeneous model	5.75	22.98	50.18	-15.65	18.38	72.97	13.08	31.00	33.89
C-method	23.14	31.94	49.82	6.20	19.96	78.38	11.80	27.11	42.22
phenomenological model									
Cheng et al. [109] :									
annular	9.68	33.30	44.44	-16.81	35.59	28.38	-4.15	46.33	22.78
slug - intermittent	5.94	32.78	48.75	-24.45	30.96	32.43	-12.66	38.89	27.78
stratified - wavy	23.17	39.28	39.07	-4.21	37.42	28.38	10.59	52.75	20.00
slug-stratified wavy	14.27	36.89	48.75	-18.49	30.29	33.78	-4.31	41.20	25.00
stratified	-16.09	23.86	46.95	-35.96	36.37	22.97	-30.88	40.06	28.33

Table 9.2: Average deviation $\bar{\xi}$, mean deviation $|\bar{\xi}|$ and fraction of the data predicted within ±20% ξ_{20} calculated for different pressure drop prediction methods.

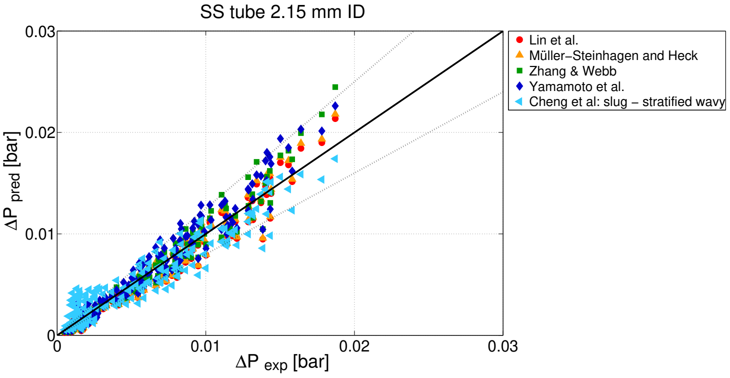

(a)

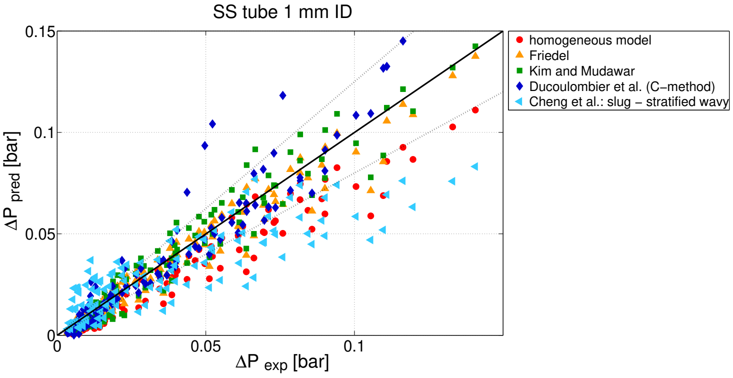

(b)

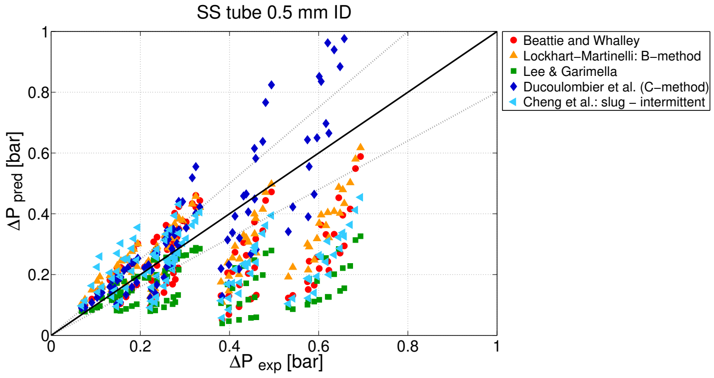

(c)

Figure 9.23: Experimental data ΔP_{exp} versus predicted pressure drop ΔP_{pred}: a) 2.15 mm ID tube; b) 1 mm ID tube; c) 0.5 mm ID tube.

the maximum impact on the measurements. The global performance of all correlations examined, including those expressly based on micro-channel and/or CO_2 databases, deteriorates passing to the smaller diameters. According to Figure 9.23(b), at 1 mm ID the homogeneous model starts to systematically under-predict the measurements, while the correlations specifically derived for micro-channels show a tendency to over-prediction. It is interesting to observe that the correlation that shows the best performance in this case is the one elaborated by Friedel [74], initially based on data gathered on air-water and oil-water mixtures and R12 in tubes with ID > 4 mm. At 0.5 mm ID (Figure 9.23(c)), all correlations provide a very poor performance. Whilst the model elaborated by Ducoulombier at al. [121] for a very similar case shows however a balanced behaviour between under-prediction and over-prediction.

Representations such as given in Table 9.2 and Figure 9.23 are in any case too general to allow for any substantial guidance when no differentiation between different T_{sat} is given. It was indeed observed that the saturation temperature introduces effects which lead to a transformation of the flow due to the combined effects of the changing properties of CO_2 and confinement effects. Thus, the real applicability of correlations cannot be appreciated through a global approach, as it changes with changing T_{sat} for each ID individually. In this respect, Charnay et al. [154] presented an interesting discussion about the validity of prediction tools for the two-phase flow pressure drop of R-245fa in a horizontal 3 mm ID tube. They explicitly compared the applicability of different correlations at different saturation temperatures and found inconsistencies in the correlations under assessment. This can also be studied for the experimental data at hand and some interesting trends with respect to T_{sat} can be discussed for chosen examples at $q \approx 35\ \mathrm{kW/m^2}$. For this exercise, in addition to the "best suitable correlations" defined above according to Table 9.2, the correlations proposed by Friedel [74], Ducoulombier et al. [121] and Müller-Steinhagen and Heck [73] have been included and special attention is also given to the basic homogeneous model. Figure 9.24 relates the experimental and predicted pressure drop to the mass flux and compares the outcome for the minimum and the maximum T_{sat} observed (15°C; -25°C). Figure 9.25 relates the experimental and predicted pressure drop to T_{sat} and compares the outcome for each tube diameter at a fixed mass flux. Finally, Figure 9.26 reports the effect of T_{sat} on the applicability of the prediction methods, represented as average deviation ($\bar{\xi}$) from the experimental value and representing all data gathered at different mass fluxes and heat fluxes.

It is apparent from this sequence of figures that, when used at different saturation temperatures, no correlation can predict the data in a consistent way. According to Table 9.2 and Figure 9.24 - except for the extreme case of the smallest ID at the lowest temperature - the general applicability of the Friedel correlation [74] is quite acceptable when applied to the present data set, which is surprising, when thinking about the reference database used for its development. Based on an extensive comparison between various published correlations, Whalley [155] established some recommendations on the application of prediction methods to the design of heat exchangers. For $\mu_l/\mu_g < 1000$ and mass fluxes < $2000\ \mathrm{kg/m^2s}$ he recommended to use the Friedel correlation [74]. Since the highest μ_l/μ_g value of the present test range is about 12 and mass fluxes below $2000\ \mathrm{kg/m^2s}$ are being studied, the relatively good average performance appears compatible with the given guideline. On the other hand, Figure 9.26(a) illustrates well the prediction capability of the Friedel correlation with T_{sat}. For the 2.15 mm ID tube the Friedel correlation over-predicts the present data set, with a tendency to lesser over-prediction towards lower T_{sat}. This might be explained with the fact that with decreasing T_{sat}, the differences between CO_2 vapour and liquid properties increase and the flow resembles more

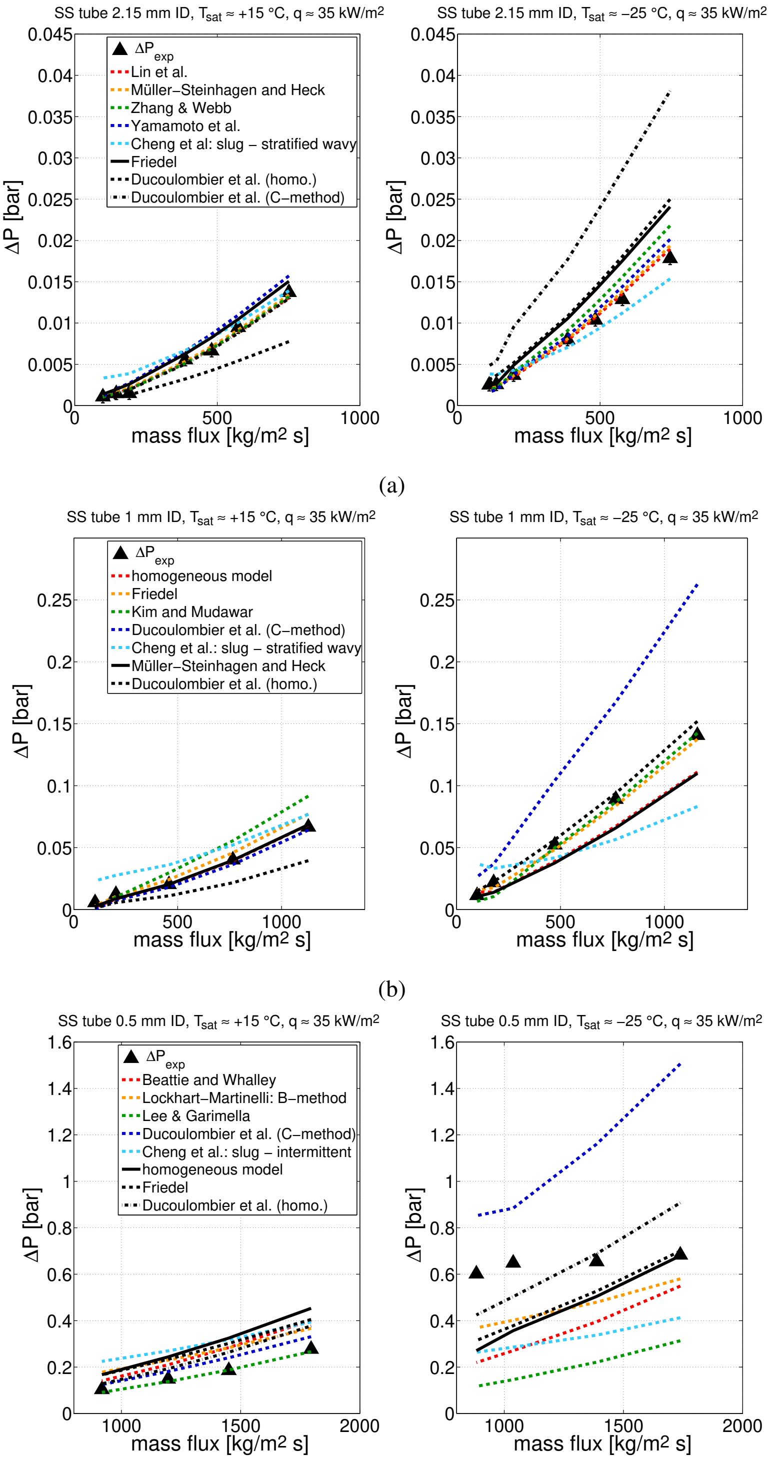

(a)

(b)

(c)

Figure 9.24: Effect of T$_{sat}$ and mass flux on the applicability of different pressure drop correlations at T$_{sat}$ ≈ 15°C and -25°C: a) 2.15 mm ID tube; b) 1 mm ID tube; c) 0.5 mm ID tube.

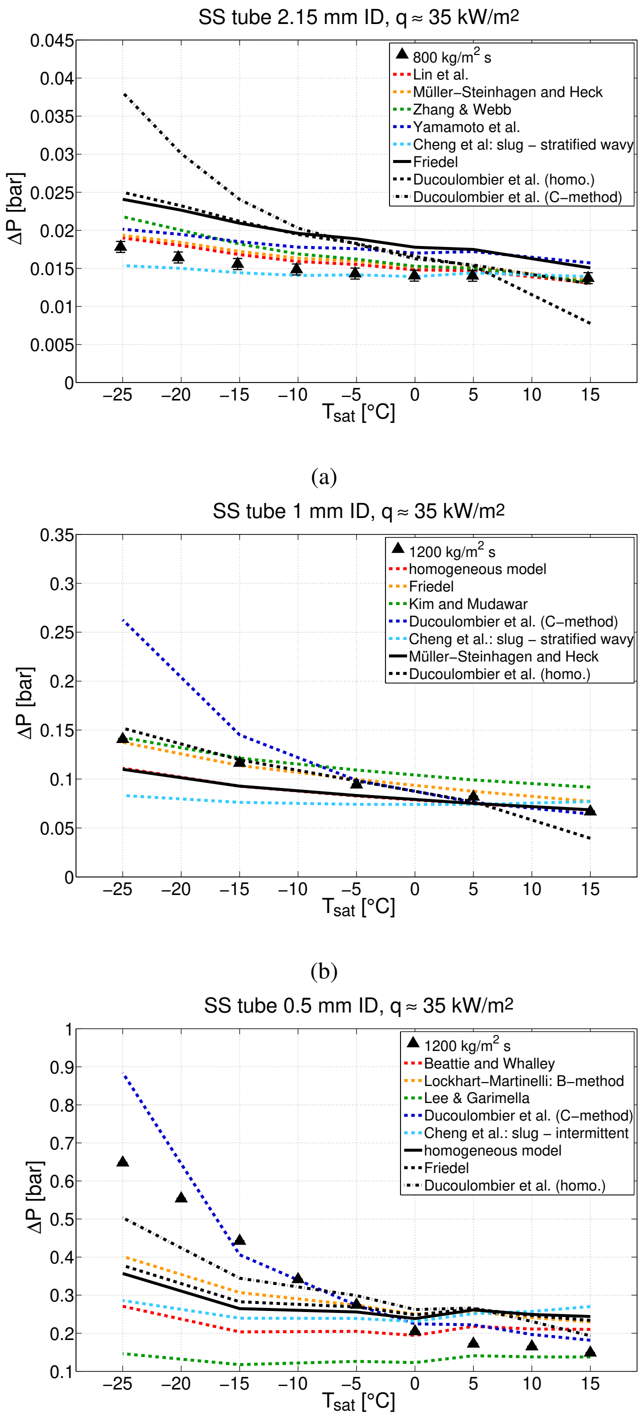

(a)

(b)

(c)

Figure 9.25: Effect of T_{sat} on the applicability of different pressure drop correlations at ≈ 35 kW/m^2: a) 2.15 mm ID tube; b) 1 mm ID tube; c) 0.5 mm ID tube.

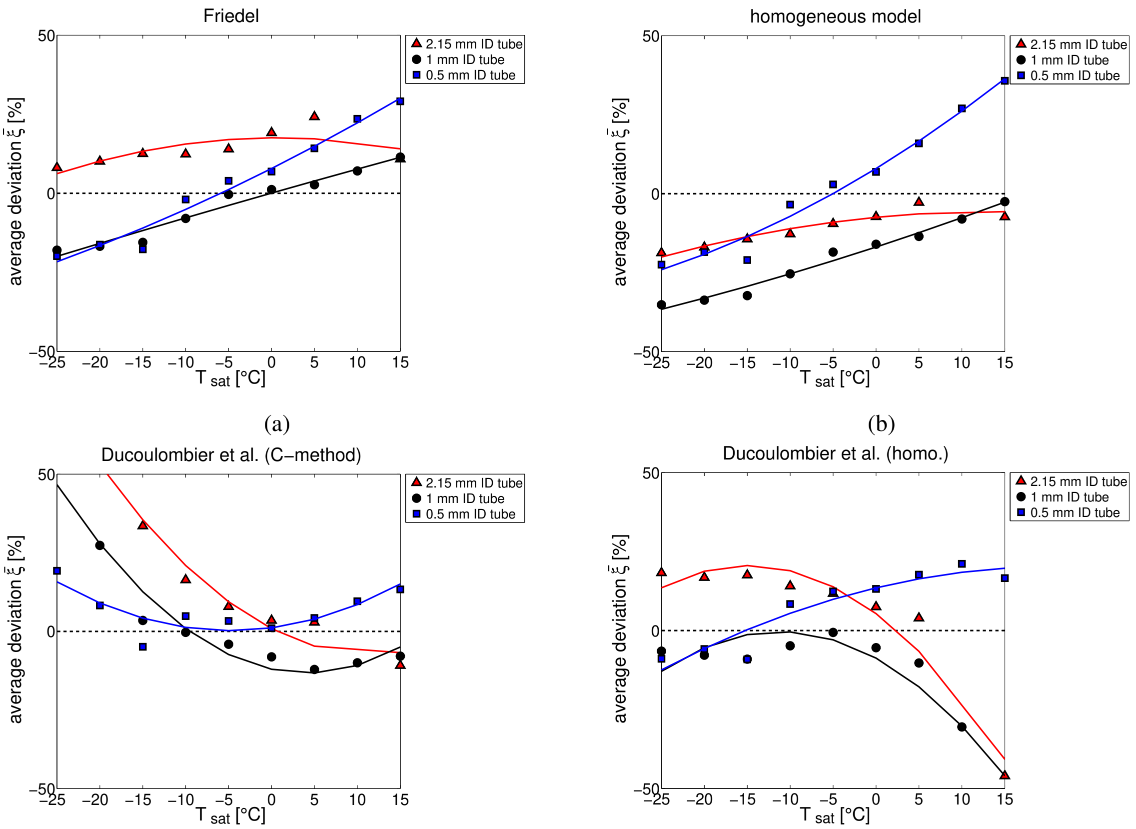

(a)

(b)

(c)

(d)

Figure 9.26: Average deviation $\bar{\xi}$ of experimental values from selected pressure drop prediction methods: a) Friedel correlation [74]; b) homogeneous model; c) Ducoulombier et al. [121]: C-method; d) Ducoulombier et al. [121]: homogeneous model.

the separated-phase flow on which the Friedel model is mainly based on. The best fit of the Friedel correlation for the 2.15 mm ID tube is achieved around -25°C. For the 1 mm and 0.5 mm ID tube the Friedel model changes overall applicability: a shift between over- and under-prediction is taking place in both cases at T_{sat} around -5°C. Note that at +15°C the prediction level for the 1 mm ID is very similar to the prediction level for the 2.15 mm ID tube, while below -15°C the prediction level is very close to the one for the 0.5 mm ID tube. This can be regarded as an indirect confirmation of the increasing similarity of the flow phenomena inside the 1 mm and 0.5 mm ID tube at low temperature due to confinement effects. It might be worth noticing that Ducoulombier et al. [121] mention that the Friedel correlation predicts their data best at -10°C, which is also the case for the 0.5 mm ID data of the present study.

For what concerns the homogeneous model, Figures 9.24 and 9.25 show that for the 2.15 mm and the 1 mm ID tubes the best fit with the homogeneous model can be achieved at +15°C. This can be explained by the consideration that the slip ratio is at its smallest value and the vapour and liquid phases are here flowing more uniformly. Thus another practical recommendation made by Whalley [155], which is to use the homogeneous model for high reduced pressures can be confirmed. Indeed, when consulting Figure 9.26(b) the homogeneous model increasingly under-predicts the data for the 2.15 mm and the 1 mm ID tubes when decreasing T_{sat}, which is again explained by an increasing separated two-phase flow. For the 0.5 mm ID tube the best prediction by the homogeneous model is achieved around -5°C, with over-prediction above -5°C and under-prediction below. This shift was also observed by Ducoulombier et al. [121] and is most likely caused by a change in phenomenological behaviour of the flow due to increasing confinement effects. The overall results for the Müller-Steinhagen and Heck correlation [73] are very similar to the ones described for the homogeneous model and are not explicitly shown here. Instead one example shall be shortly discussed for the micro-channel correlations (Kim and Mudawar [99]), the CO_2 correlations (Ducoulombier et al. [121]) and the phenomenological models (Cheng et al. [109]). According to Figure 9.25(b) the correlation by Kim and Mudawar [99] predicts the data set for the 1 mm ID tube reasonably well at +15°C. This is most likely due to the extensive data base this correlation is based on: 2378 data points related to IDs between 3 mm and 0.3 mm , 25% of which with CO_2. This encourages using an as large as possible database when developing new models. The most relevant observation about the correlations by Ducoulombier et al. [121] comes from Figure 9.26(c) and 9.26(d): a good prediction level of the two correlations (homogeneous and C-method) can be found within the parameter range of their own database (-10 to 5°C), whilst above 5°C a reasonable prediction level can be maintained by their modified C-method and below -10°C by their modified homogeneous model – especially for the smaller ID tubes. Opposite to the correlation by Kim and Mudawar [99] the database is in this case quite limited and the good fit of the correlation can only be guaranteed within that range of test parameters (including fluid properties and tube dimensions). A final mention should be reserved to the performance of the phenomenological models developed by Cheng et al. [109] as shown in Figure 9.24. Although the predictions provided by these models are never the most accurate from a quantitative point of view, their slug-stratified wavy model reproduces the peculiar shape and slope of ΔP vs. G for the 2.15 mm and the 1 mm ID tubes at +15°C. In addition their slug-intermittent model is reproducing well the same trend for the 0.5 mm ID tube at both temperatures considered in the figure. The database used to develop these models, focusing on CO_2, was largely dominated by data from a single channel of 6 mm ID, clustered with some available data on multi-micro-channel devices and the formulations do not explicitly contain a corrective factor for the reduced pressure. Therefore, the quantitative discrepancy with the present data is not surprising. But the fact that two of their sub-models specific to two distinct flow patterns capture correctly the trend of ΔP vs. G for the described cases, where experimental observations suggest the presence of those flow patterns, seems to be encouraging towards a further development of this approach.

Possible guidelines & recommendations The findings described above and the additional results depicted in Appendix F result in a set of guidelines which might be applied during the future design phase of CO_2 evaporators used in the context of detector cooling. The estimation of the total pressure drop across a certain CO_2 evaporator is achieved with the step-wise calculation and integration of the frictional and accelerational pressure drop component, whilst taking into account the evolution of the vapour quality - as described in 5.1.2 and 9.3.1. For a vertical or non-horizontal installation of the evaporator line the static pressure drop is non-zero and in this case is not negligible. An engineer who is facing the implementation of a CO_2 evaporator tube of ~ 2 mm ID, which will be submitted to mass fluxes between 800 and 100 kg/m^2s and to heat fluxes between 5 and 35 kW/m^2, may consult Table 9.3 for the selection of suitable prediction methods of the frictional two-phase pressure drop emphasizing on the effect of saturation temperature. The table lists the most promising correlations (average deviation $\bar{\xi}$ < 20 %) obtained with a comparison to data from this specific study and grouped in temperature ranges of 15°C to 10°C, 5°C to 0°C, -5°C to -10°C and -15°C to -25°C. This results in a tabular temperature dependent guide for the application of two-phase pressure drop correlations - as opposed to Table 9.2 where no temperatures were taken into account. The corresponding information for the 1 mm ID tube and the 0.5 mm ID tube are given in Table 9.4 and 9.5. Note that individual heat and mass fluxes are not considered. Additional plots are given in Appendix F for possible guidance.

2.15 mm ID: T$_{sat}$ +15 to +10°C	$\bar{\xi}$ [%]	+5 to 0°C	$\bar{\xi}$ [%]
Cheng et al. [109]: stratified	1	Müller-Steinhagen & Heck [73]	-1
Müller-Steinhagen & Heck [73]	-4	Grönnerud [75]	-3
Grönnerud [75]	-4	Ducoulombier et al. [121] (C-method)	3
homogeneous model	-6	Zhang & Webb [95]	-4
Tran et al. [94]	7	Cheng et al. [109]: stratified	-4
Zhang & Webb [95]	-7	homogeneous model	-5
Ducoulombier et al. [121] (C-method)	-7	Ducoulombier et al. [121] (homo.)	6
Friedel [74]	14	Tran et al. [94]	12
Yun & Kim [118]	-15	Yamamoto et al. [119]	13
Yamamoto et al. [119]	15	Yun & Kim [118]	-17

(a)

2.15 mm ID: T$_{sat}$ -5 to -10°C	$\bar{\xi}$ [%]	-15 to -25°C	$\bar{\xi}$ [%]
Yamamoto et al. [119]	1	Tran et al. [94]	4
Cheng et al. [109]: slug - intermittent	4	Lee & Lee [98]	5
Cheng et al. [109]: annular	5	Cheng et al. [109]: slug - strat.-wavy	-6
Tran et al. [94]	6	Cheng et al. [109]: strat.-wavy	-7
Müller-Steinhagen & Heck [73]	-8	Zhang & Webb [95]	-8
Zhang & Webb [95]	-9	Yamamoto et al. [119]	-9
homogeneous model	-11	Friedel [74]	10
Cheng et al. [109]: slug - strat.-wavy	12	Cheng et al. [109]: slug - intermittent	-12
Ducoulombier et al. [121] (C-method)	12	Müller-Steinhagen & Heck [73]	-13
Ducoulombier et al. [121] (homo.)	13	Cheng et al. [109]: annular	-15
Grönnerud [75]	-13	homogeneous model	-16
Friedel [74]	13	Ducoulombier et al. [121] (homo.)	17
Lee & Lee [98]	16	Grönnerud [75]	-19
Cheng et al. [109]: stratified	-17		
Cheng et al. [109]: strat.-wavy	17		

(b)

Table 9.3: Average deviation $\bar{\xi}$ <20% for different pressure drop prediction methods across the 2.15 mm ID tube and for varying temperature regimes: a) +15°C to 0°C; b) -5°C to -25°C.

1 mm ID: T$_{sat}$ +15 to +10°C	$\bar{\xi}$ [%]	+5 to 0°C	$\bar{\xi}$ [%]
Cheng et al. [109]: slug - intermittent	4	Yamamoto et al. [119]	1
homogeneous model	-5	Friedel [74]	2
Müller-Steinhagen & Heck [73]	-5	Cheng et al. [109]: annular	-6
Grönnerud [75]	-7	Cheng et al. [109]: strat.-wavy	8
Ducoulombier et al. [121] (C-method)	-9	Ducoulombier et al. [121] (homo.)	-8
Zhang & Webb [95]	-8	Cheng et al. [109]: slug - strat.-wavy	-9
Friedel [74]	9	Ducoulombier et al. [121] (C-method)	-10
Cheng et al. [109]: stratified	-10	Kim & Mudawar [99]	14
Cheng et al. [109]: strat.-wavy	13	Müller-Steinhagen & Heck [73]	-14
Yamamoto et al.[119]	16	homogeneous model	-14
Yun & Kim [118]	-18	Lockhart-Martinelli (B-method) [72]	15
		Cheng et al. [109]: slug - intermittent	-15
		Zhang & Webb [95]	-16
		Grönnerud [75]	-18
		Tran et al. [94]	19
		Lee & Lee [98]	19

(a)

1 mm ID: T$_{sat}$ -5 to -10°C	$\bar{\xi}$ [%]	-15 to -25°C	$\bar{\xi}$ [%]
Ducoulombier et al. [121] (C-method)	-2	Lockhart-Martinelli [72] (B-method)	-3
Ducoulombier et al. [121] (homo.)	-3	Ducoulombier et al. [121] (homo.)	-8
Friedel [74]	-4	Kim & Mudawar [99]	-12
Lee & Lee [98]	5	Tran et al. [94]	13
Kim & Mudawar [99]	5	Friedel [74]	-17
Lockhart-Martinelli [72] (B-method)	10	Lee & Lee [98]	-19
Yamamoto et al. [119]	-11		
Cheng et al. [109]: strat.-wavy	-17		
Tran et al. [94]	19		

(b)

Table 9.4: Average deviation $\bar{\xi}$ <20% for different pressure drop prediction methods across the 1 mm ID tube and for varying temperature regimes: a) +15°C to 0°C; b) -5°C to -25°C.

0.5 mm ID: T$_{sat}$ +15 to +10°C	$\bar{\xi}$ [%]	+5 to 0°C	$\bar{\xi}$ [%]
Lee & Garimella [97]	-2	Cheng et al. [109]: slug-intermittent	1
Qu & Mudawar [96]	-2	Müller-Steinhaagen & Heck [73]	1
Mishima & Hibiki [93]	-2	Zhang & Webb [95]	-1
Yun & Kim [118]	4	Grönnerud [75]	-1
Cheng et al. [109]: stratified	11	Ducoulombier et al. [121] (C-method)	3
Ducoulombier et al. [121] (C-method)	11	Cheng et al. [109]: annular	6
Zhang & Webb [95]	13	Cheng et al. [109]: slug - strat.-wavy	6
Grönnerud [75]	15	Lockhart-Martinelli [72] (B-method)	6
Müller-Steinhaagen & Heck [73]	17	Yamamoto et al. [119]	10
Ducoulombier et al. [121] (homo.)	19	Cheng et al. [109]: stratified	-10
		Friedel [74]	10
		homogenous model	11
		Yun & Kim [118]	-12
		Cheng et al. [109]: strat.-wavy	15
		Ducoulombier et al. [121] (homo.)	15
		Lee & Garimella [97]	-15
		Qu & Mudawar [96]	-15
		Mishima & Hibiki [93]	-15
		Kim & Mudawar [99]	15

(a)

0.5 mm ID: T$_{sat}$ -5 to -10°C	$\bar{\xi}$ [%]	-15 to -25°C	$\bar{\xi}$ [%]
homogeneous model	-1	Ducoulombier et al. [121] (C-method)	7
Friedel [74]	1	Ducoulombier et al. [121] (homo.)	-8
Yamamoto et al. [119]	-3	Lockhart-Martinelli [71] (C-method)	12
Lockhart-Martinelli [72] (B-method)	-3	Kim & Mudawar [99]	-18
Kim & Mudawar [99]	4	Friedel [74]	-18
Ducoulombier et al. [121] (C-method)	4	Lockhart-Martinelli [72] (B-method)	-19
Lee & Lee [98]	5		
Cheng et al. [109]: strat.-wavy	-6		
Müller-Steinhaagen & Heck [73]	-8		
Zhang & Webb [95]	-8		
Cheng et al. [109]: slug - strat.-wavy	-9		
Grönnerud [75]	-10		
Ducoulombier et al. [121] (homo.)	10		
Cheng et al. [109]: annular	-12		
Cheng et al. [109]: slug-intermittent	-13		

(b)

Table 9.5: Average deviation $\bar{\xi}$ <20% for different pressure drop prediction methods across the 0.5 mm ID tube and for varying temperature regimes: a) +15°C to 0°C; b) -5°C to -25°C.

In particular in context with the phenomenological explanation given above it is recommended to use primarily the Cheng et al. [109] phenomenological model, the homogeneous model and the Friedel correlation [74] for the prediction of the frictional pressure drop along a 2 mm ID tube. The Cheng et al. [109] sub-model for stratified flow may be used for T_{sat} from about +15°C to 0°C. In parallel the basic homogeneous model may be applied for T_{sat} from about +15°C to -10°C, while below -10°C the Friedel [74] correlation may result in a good prediction, at least until the lower limit of -25°C according to the measurements presented. The observations conducted suggest that for larger diameters the temperature separating the validity of the two latter models would likely shift progressively to lower values, where the separation of the flow is more pronounced. For the equivalent temperature range instead of the homogeneous model also the correlation by Müller-Steinhagen and Heck [73] may result in a similar prediction level. If only one correlation is sought after which supplies a constant medium fit, the micro-channel correlations by Tran et al. [94] and Zhang and Webb [95] and the CO_2 correlation by Yamamoto et al. [119] may predict the two-phase pressure drop inside a 2 mm ID tube in a consistent way.

During the design phase of a CO_2 evaporator tube of ~ 1 mm ID, which will be submitted to mass fluxes between 1200 and 200 kg/m^2s and to heat fluxes between 5 and 35 kW/m^2, according to the findings of this study it is advisable to use primarily the homogeneous model, the Friedel correlation [74] and the modified homogeneous model by Ducoulombier et al. [121] for the prediction of the frictional pressure drop along the tube. The homogeneous model results in a good prediction between 15°C and 10°C; from 5°C to -10°C the Friedel [74] correlation provides an acceptable prediction level; finally from 0°C to -25°C the modified homogeneous model of Ducoulombier et al. [121] shows good results. Again similar results to the homogeneous model may be achieved with the correlations by Müller-Steinhagen and Heck [73] or Grönnerud [75]. Whilst using only one correlation a constant medium prediction level can be achieved with the correlation by Tran et al. [94] for the whole temperature range between +15°C to -25°C T_{sat}.

When investigating the pressure drop along a ~ 0.5 mm ID which is submitted to mass fluxes between 1800 and 1000 kg/m^2s and to heat fluxes between 5 and 35 kW/m^2, both models of Ducoulombier et al. [121] may result in a good prediction, with the modified C-method model showing better results above -5°C and the modified homogeneous model below -5°C. Other standard correlation may fit for very specific T_{sat}, since in most cases a cross-over between over- and under-prediction was found within the range of tested T_{sat}. Please refer to Table 9.5 and to the additional plots given in Appendix F for additional guidance.

All observations confirm that any empirical two-phase pressure drop correlation is only valuable as far as the underlying data base and as long as its range of test parameters presents strong similarities with the configurations being analysed. Despite the quantitatively less accurate results obtained for some studied parameters, the Cheng et al. [109] phenomenological model can be found repeatedly amongst the correlations listed in Tables 9.3, 9.4 and 9.5 and in some cases it captures the pressure drop trends in a way the empirical models are not able to. This encourages the further development of phenomenological models based on the actual physical flow behaviour.

9.3.2 Heat transfer

Concerning the heat transfer coefficient, Table 9.6 shows the prediction performance of an extensive group of correlations as compared to the complete data set of this present study associated to each tube ID, whilst indicating the average deviation $\bar{\xi}$, the mean deviation $|\bar{\xi}|$ and the fraction of the data predicted within ±20%, ξ_{20}. Figure 9.27 compares in a global way the outcome of some heat transfer correlations (α_{pred}) with the experimental data (α_{exp}) gathered for each tube diameter. For this comparison the best suitable correlation of each class listed in Table 9.6 has been selected, defined as the one providing the largest fraction of data predicted within an error of ±20% from the measured value (ξ_{20}). The overall prediction capability of the shown correlations is in all cases about 50% ξ_{20} or better. The best prediction level of the macro-channel correlations is degrading and the overall scatter increases with decreasing inner diameter. For the micro-channel correlations, Lazarek & Black [5] and Kew and Cornwell [89], whose correlations are very similar, can provide a consistent general good fit. Amongst the CO_2 correlations the Yun et al. [115] correlation provides a good fit for the two larger tube dimensions, whilst this correlation is indeed based on data gathered on 2 mm and 0.98 mm ID tubes. Whereas the correlation by Ducoulombier et al. [135], being based on data gathered with a 0.5 mm ID tube, achieves the best fit for the corresponding data of this present study. As expected, also other studies in literature point out that correlations may fit better when certain experimental test parameters are in line with the ones the used correlation is based on [86, 114]. Thus again representations such as given in Table 9.6 and Figure 9.27 are too general to allow for a fundamental guidance whilst no distinction between different T_{sat} or other test parameters is given. Due to the combined influence of the changing properties of CO_2 and flow confinement effects, it was indeed observed that the saturation temperature introduces effects which lead to a transformation of the flow. Since the applicability of heat transfer prediction methods changes with changing T_{sat} and for each ID individually, again some interesting observations with respect to both parameters can be discussed for chosen examples from this study.

For the following graphical illustrations, in addition to the "best suitable correlations" defined above according to Table 9.6 and Figure 9.27, the scheme of correlations proposed by Ducoulombier et al. [135] has been included for comparison. For their first regime (Duc. I) discussed before, the term for nucleate boiling defined by Cheng et al. [109, 110] is used, for type II (Duc. II) the prediction method is equal to the correlation by Hihara and Tanaka [117] and for type III (Duc. III) they proposed a new correlation with a convective intensification factor depending on the Lockhart–Martinelli variable X_{tt}. Between type II and III the Boiling number is used as a selector (if $Bo > 1.1 \times 10^{-4}$ type II is chosen, otherwise type III). Finally the maximum value between type I (nucleate boiling) and II/III (convective boiling) is used for the calculation of the final local heat transfer coefficient. The outcome of the complete scheme and the three sub-models are also presented in Table 9.6. Similar to the examples given in section 9.3.1, Figure 9.28 relates the experimental and predicted heat transfer coefficient to the heat flux and compares the outcome for the minimum and the maximum T_{sat} observed (15°C; -25°C). In the same way Figure 9.29 shows the influence of the mass flux for the smallest and largest tube. Figure 9.30 relates the experimental and predicted heat transfer coefficient to T_{sat} and compares the outcome for each tube diameter at a fixed mass flux.

It is apparent from these examples that, at different saturation temperatures, a good fit can be found however no single correlation can predict the data in a fully consistent way. In Figure 9.28, 9.29 and 9.30 the effect of T_{sat} on the effectiveness of prediction methods is obvious. It may be sensible indeed to distinguish between different correlations for different T_{sat} and thus different heat transfer regimes,

	Deviation [%]								
	2.15 mm ID tube			1 mm ID tube			0.5 mm ID tube		
correlation (class)	average $\bar{\xi}$	mean $\lvert\bar{\xi}\rvert$	ξ_{20}	average $\bar{\xi}$	mean $\lvert\bar{\xi}\rvert$	ξ_{20}	average $\bar{\xi}$	mean $\lvert\bar{\xi}\rvert$	ξ_{20}
macro-channel correlations									
Chen [54]	-65.43	66.59	4.18	-23.45	43.95	21.78	-4.51	31.66	39.07
Shah [55]	-18.16	24.78	48.04	25.31	35.60	41.11	25.51	27.94	52.50
Kandlikar [53]	-14.82	18.47	56.30	21.04	28.76	47.78	25.75	27.41	40.83
Steiner & Taborek [56]	109.48	109.48	0.00	187.22	187.22	0.00	208.02	208.02	0.00
Liu & Winterton [58]	1.32	9.52	90.53	27.61	33.42	51.33	30.39	33.09	52.69
Gungor & Winterton [57]	52.51	52.59	7.56	105.58	105.58	2.00	101.55	101.55	0.46
Cooper [59]	12.40	14.61	68.20	8.69	11.13	82.89	-13.48	20.51	43.15
Wattelet et al. [60]	18.14	19.23	56.46	38.69	39.56	36.00	40.19	41.29	34.54
micro-channel correlations									
Warrier et al. [100]	25.09	66.58	22.17	160.16	165.88	14.44	164.53	165.34	6.57
Lazarek & Black [5]	-8.16	15.24	70.90	11.86	21.14	52.89	6.49	15.86	70.09
Tran et al. [101]	-16.40	22.33	46.93	-35.42	35.59	9.56	-58.46	58.46	1.76
Agostini & Bontemps [102]	-22.59	26.00	43.97	-39.82	40.87	19.78	-63.43	63.43	0.00
Li & Wu [103]	50.18	51.32	28.62	40.23	49.03	29.78	-9.28	21.25	48.15
Bertsch et al. [104]	-12.78	25.98	42.75	4.30	26.61	48.89	-15.54	25.17	41.20
Yu et al. [105]	49.88	49.88	6.72	19.96	20.22	56.89	-24.11	26.73	28.98
Kandlikar & Balasub. [106]	-22.79	28.00	50.90	14.29	27.01	48.00	11.91	19.75	63.15
Kew & Cornwell [89]	-7.28	14.87	72.01	12.64	21.46	53.11	7.84	16.74	66.76
Oh & Son [107]	-90.35	90.35	0.00	-75.41	75.41	0.22	-56.23	56.65	5.28
Kim & Mudawar [108]	11.57	16.65	66.24	38.99	39.00	10.67	41.17	41.57	25.09
CO_2 correlations									
Ducoulombier et al. [135]	26.01	26.06	27.04	28.99	30.04	43.33	22.47	29.10	55.09
Yoon et al. [126]	37.14	37.47	27.99	113.86	114.03	11.11	133.87	133.87	0.56
Hihara & Tanaka [117] : Duc II	-15.74	24.94	44.13	-16.40	21.89	51.56	-15.79	22.60	49.44
Yun et al. [133]	3.39	14.36	70.00	-1.99	9.59	90.22	-19.30	24.82	36.30
Choi et al. [114]	16.94	20.10	61.38	36.05	38.02	40.22	35.22	36.33	38.52
Wang et al. [136]	105.50	105.50	0.11	68.64	68.64	5.33	-2.23	28.02	40.00
Pamitran et al. [130]	-69.96	71.05	3.92	-32.68	50.81	16.22	-27.04	44.14	16.85
Oh et al. [132]	-1.58	25.67	45.87	37.87	46.76	37.33	26.61	32.28	52.59
Cheng et al. [110] : Duc I	24.59	24.63	30.32	22.43	23.49	46.00	-6.19	13.45	77.41
Duc III [135]	-63.29	64.83	5.24	-15.85	43.98	22.67	4.77	33.43	40.74
phenomenological model									
Cheng et al. [110] :									
annular, intermittent & bubbly	24.63	24.67	31.53	33.39	34.52	35.33	27.10	29.71	52.13
fully stratified	17.87	18.10	64.71	25.32	27.88	48.22	17.20	22.51	66.67
stratified - wavy	21.74	21.79	47.46	27.10	29.51	45.33	15.28	21.32	71.67
others									
Fang et al. [156]	-2.89	4.28	100.00	0.16	3.95	80.00	16.97	17.06	70.83

Table 9.6: Average deviation $\bar{\xi}$, mean deviation $|\bar{\xi}|$ and fraction of the data predicted within ±20% ξ_{20} calculated for different heat transfer coefficient prediction methods.

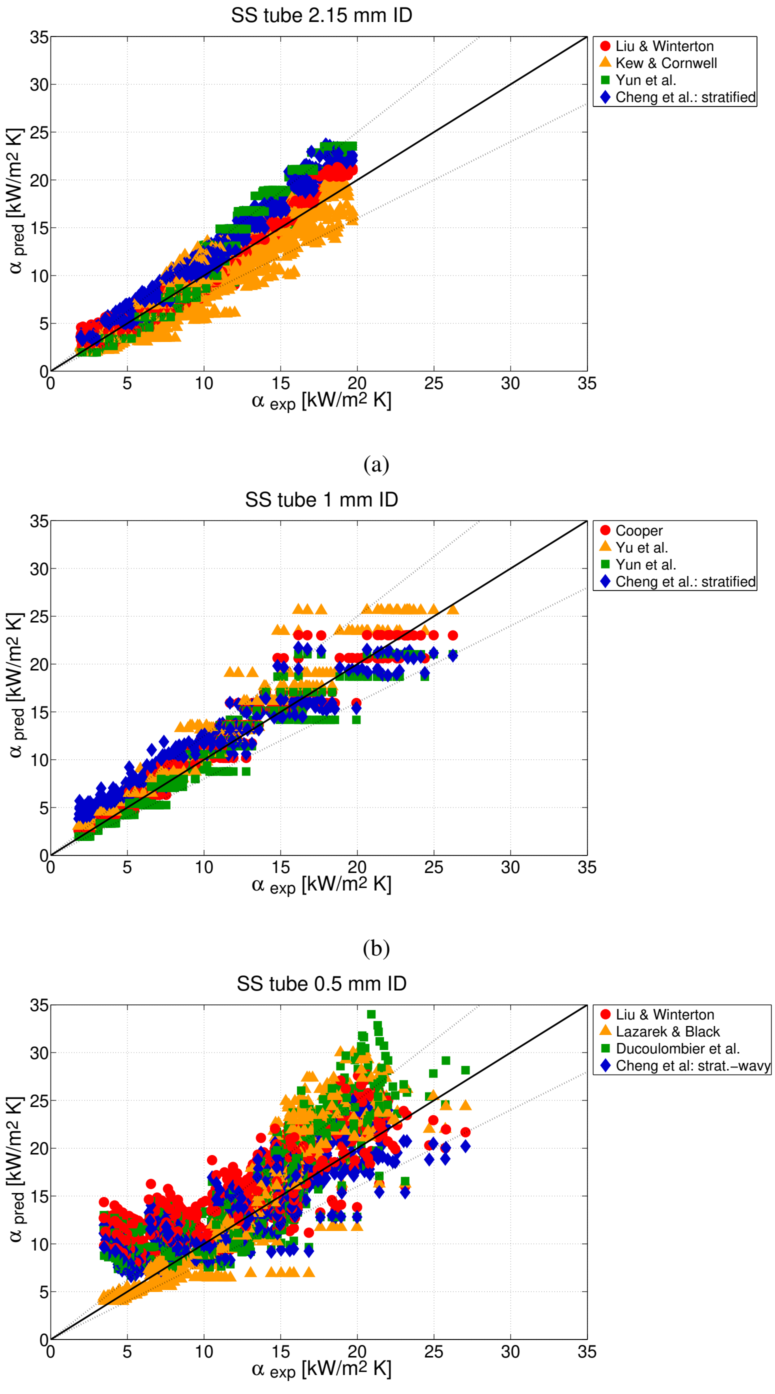

(a)

(b)

(c)

Figure 9.27: Experimental data α_{exp} versus predicted heat transfer coefficient α_{pred}: a) 2.15 mm ID tube; b) 1 mm ID tube; c) 0.5 mm ID tube.

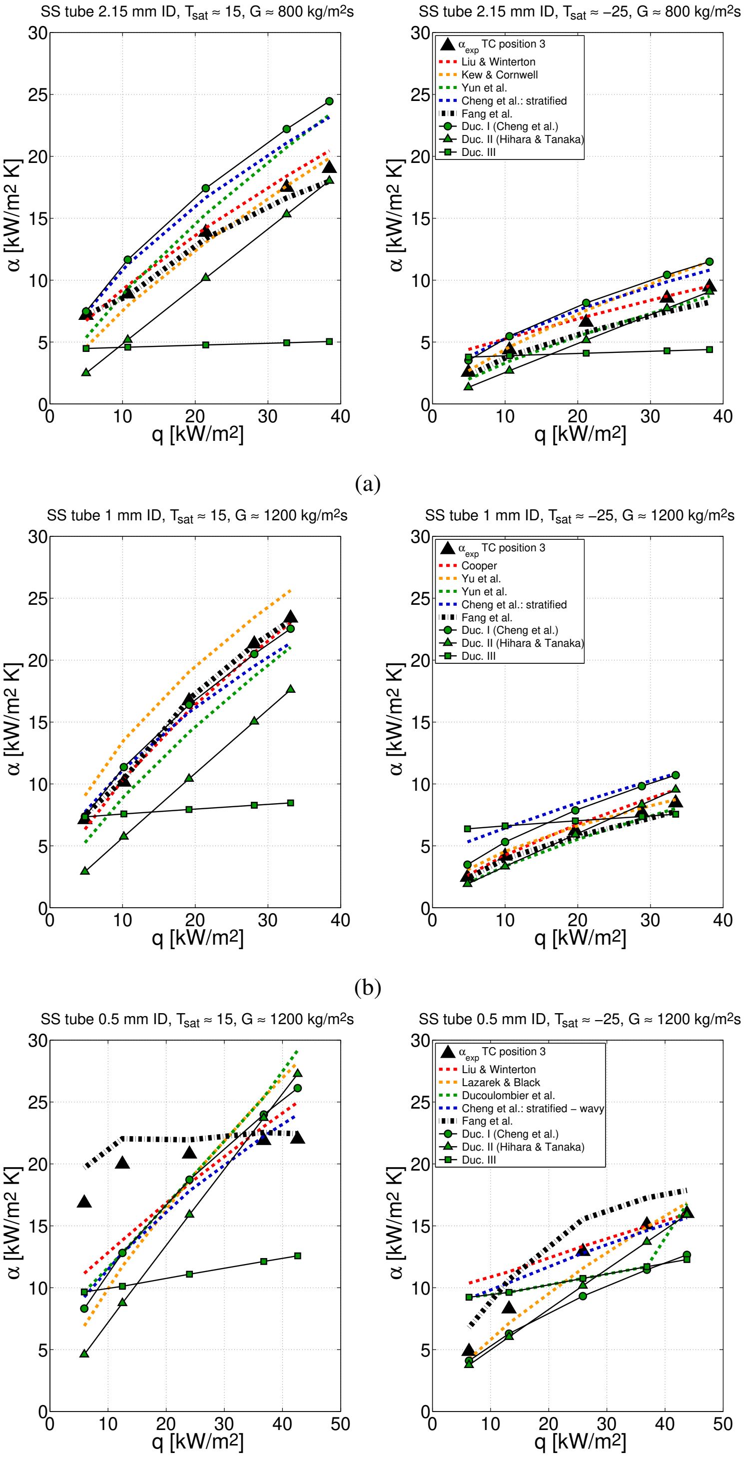

(a)

(b)

(c)

Figure 9.28: Effect of T$_{sat}$ and heat flux on the applicability of different heat transfer coefficient correlations at T$_{sat}$ ≈ 15°C and -25°C: a) 2.15 mm ID tube; b) 1 mm ID tube; c) 0.5 mm ID tube.

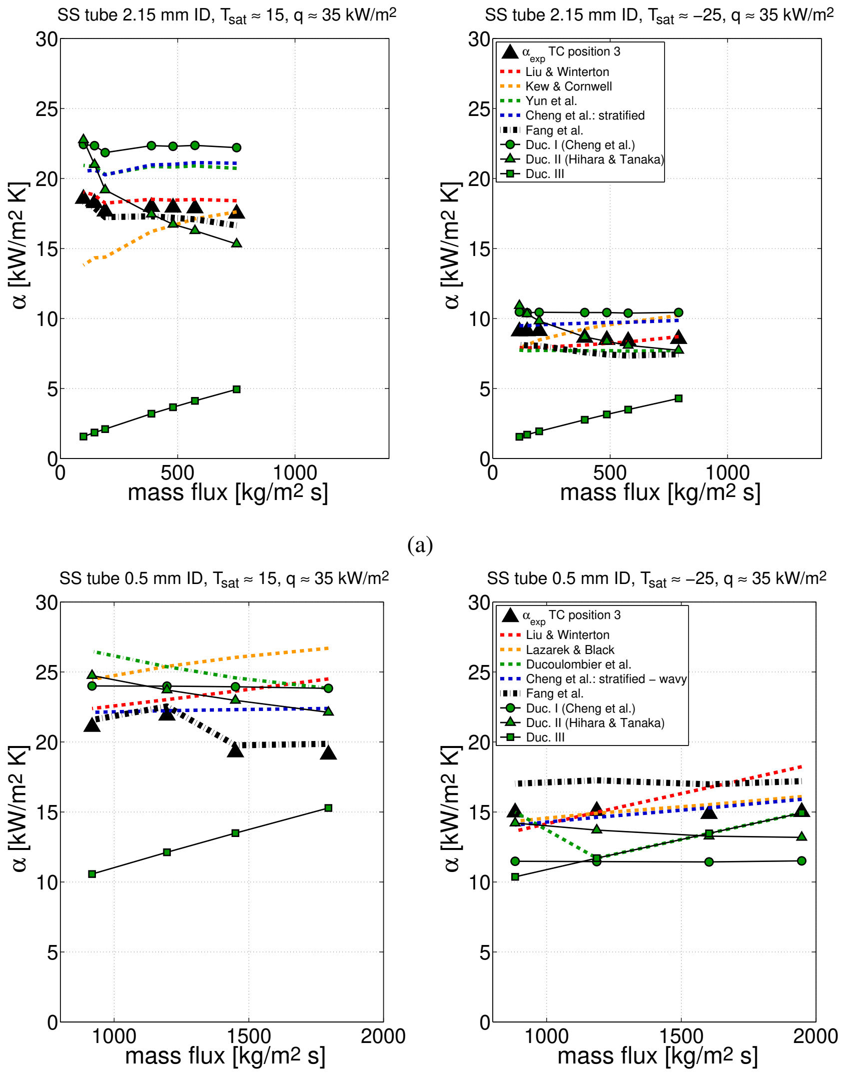

(a)

(b)

Figure 9.29: Effect of T_{sat} and mass flux on the applicability of different heat transfer coefficient correlations at $T_{sat} \approx 15^{\circ}$C and -25°C: a) 2.15 mm ID tube; b) 0.5 mm ID tube.

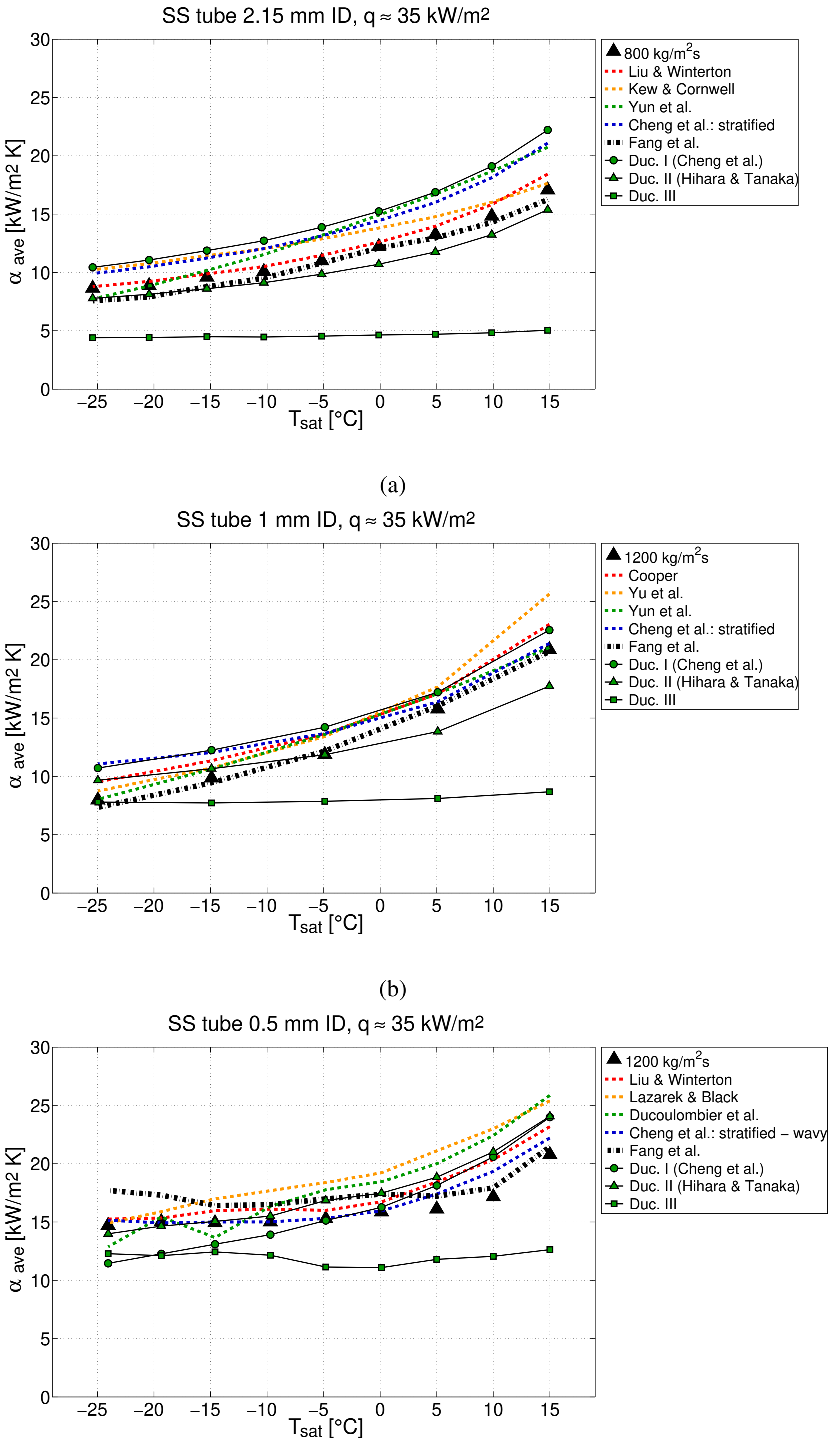

(a)

(b)

(c)

Figure 9.30: Effect of T_{sat} on the applicability of prediction methods for the heat transfer coefficient at ≈ 35 kW/m^2: a) 2.15 mm ID tube; b) 1 mm ID tube; c) 0.5 mm ID tube.

where certain parameters may have more or less influence on the heat transfer coefficient. A similar approach was also adopted by Ducoulombier et al. [135], when defining their three thermal regimes mentioned above. It is interesting to note that the defined selector according to the Boiling number is not always correct for the present study. This may be due to the fact that they based their three different thermal regimes on the vapour quality and the Boiling number and not explicitly on T$_{sat}$.
According to Table 9.6 - except for the correlation by Fang et al. which will be discussed at a later point - the best overall prediction of the present data set is achieved mainly by correlations based on nucleate boiling: Cooper [59] (pool boiling), Lazarek and Black [5], Kew and Cornwell [89], Yun et al. [115], Yu et al. [105] and the first sub-model defined by Ducoulombier et al. [135]. This is in line with the often proposed dominant nucleate boiling regime for evaporative flow of CO_2 in small channels. However when put into relation with the saturation temperature a more comprehensive picture may be created. For this purpose Figure 9.31 reports the effect of T$_{sat}$ on the applicability of selected prediction methods, represented as average deviation ($\bar{\xi}$) from the experimental values which include all data gathered at different mass fluxes and heat fluxes. The selected correlations shown in Figure 9.31(a) to 9.31(d) were chosen on the following demonstration: The procedure chosen by Ducoulombier et al. [135] described above, is similar to a proposal made by Cornwell and Kew [157], who also defined three thermal regimes which they linked to three different flow patterns and developed a recommended scheme for the formulation of prediction methods for each case: isolated bubble (IB) regime, confined bubble (CoB) regime and annular slug flow (ASF), which may be formulated as

$$(I)\, Nu_{IB} = C_1\, Bo^{0.7}\, Nu_{lo}, \tag{9.2}$$

$$(II)\, Nu_{CoB} = C_2\, Bo^{m} Co^{n}\, Nu_{lo} and \tag{9.3}$$

$$(III)\, Nu_{ASF} = C_3\, F\, Nu_{lo}, \tag{9.4}$$

where Nu$_{lo}$ is the liquid-only Nusselt number, F the Chen convective boiling enhancement factor and C$_{1-3}$, m and n are empirical factors and exponents.
As argued above, within the range of studied parameters the flow inside the 2.15 mm ID tube may be characterized as unconfined. Individual unconfined bubbles or isolated bubbles (IB) can exist and may be predominant for the entire temperature range. The flow inside the 1 mm ID tube is showing transitional effects, where at high T$_{sat}$ isolated bubbles still may be predominant, however for decreasing T$_{sat}$ the regime may transit from confined bubble (CoB) flow to annular-slug flow (ASF) as dominant flow regime. Finally the flow inside the 0.5 mm ID tube is assumed to be fully confined and mainly axisymmetric. Based on this reasoning the three regimes defined by Cornwell and Kew [157] are now discussed in view of the data gathered for this study where instead of the vapour quality the overall saturation temperature and the confinement level shall be used as delimiter of the three regimes:

(I) Isolated bubble regime According to the recommendations by Cornwell and Kew [157] the heat transfer in the isolated bubble regime is governed by the Boiling number and thus by nucleate boiling. Similar to this recommendation the correlations of Lazarek and Black [5] and Kew and Cornwell [89] have been formulated. Figure 9.31(a) shows the good applicability of the latter for the 2.15 mm ID tube at medium to low T$_{sat}$ with an decreasing under-prediction towards lower T$_{sat}$ (results for

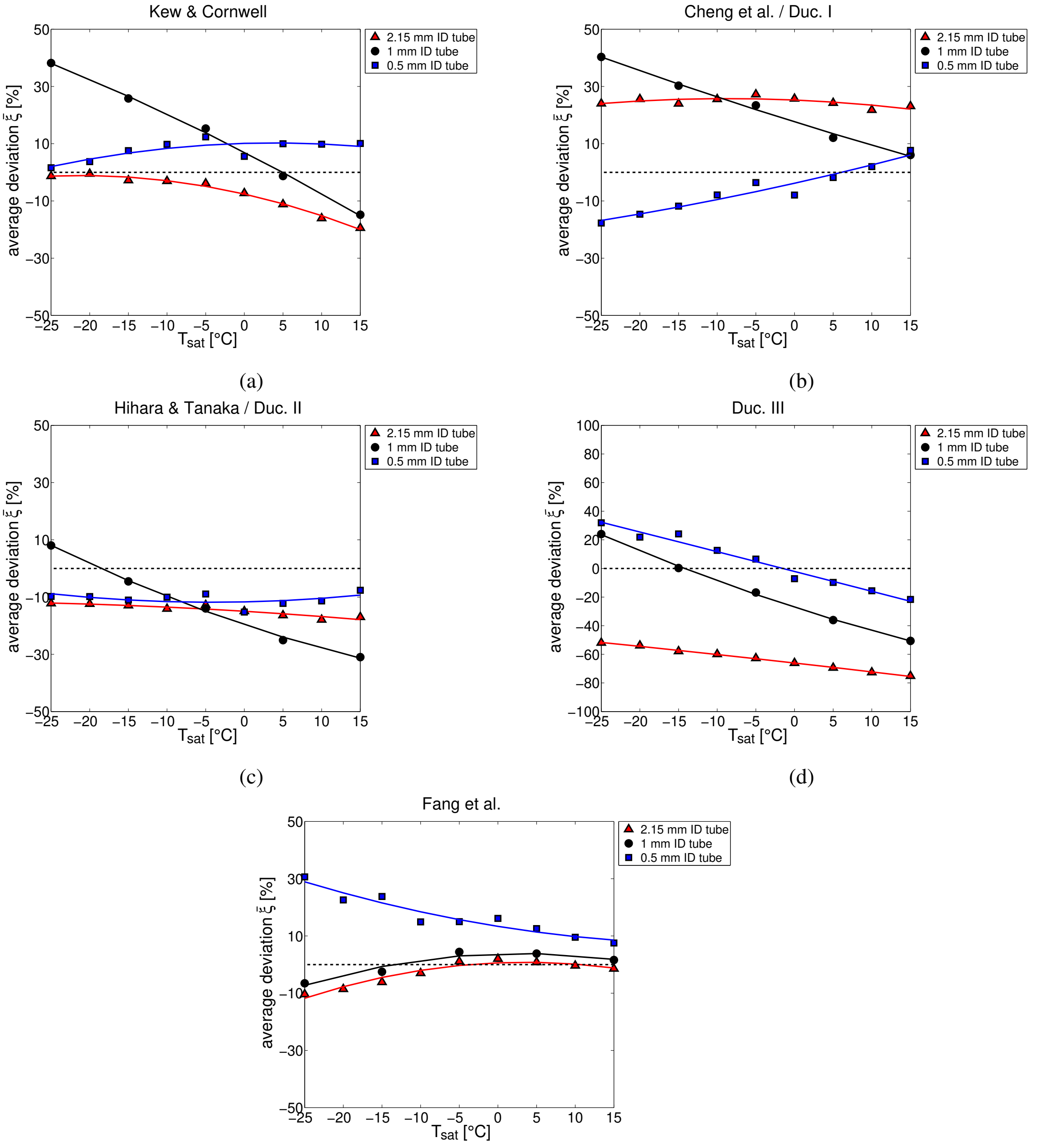

(a)

(b)

(c)

(d)

(e)

Figure 9.31: Average deviation $\bar{\xi}$ of experimental values from selected prediction methods for the heat transfer coefficient: a) Kew & Cornwell [89]; b) Cheng et al. [109, 110]; c) Hihara & Tanaka [117]; d) Ducoulombier et al. [135]; e) Fang et al. [156].

Lazarek & Black [5] very similar, not shown). Those findings confirm the assumption of isolated bubbles and nucleate boiling in the 2.15 mm ID tube even at low T_{sat}, which is however more effective at high T_{sat} and is thus under-estimated by the model which in turn is due to the different physical properties of CO_2 at high T_{sat} compared to standard refrigerants. For the 1 mm ID tube the data is equally under-estimated at high T_{sat} and the best fit can be found around +5°C, however for lower T_{sat} the data is over-predicted, confirming the transition from nucleate boiling to a more convective boiling dominant heat transfer. The 0.5 mm ID tube is predicted well by Kew and Cornwell [89] with a constant over-prediction across the whole test range, thus attesting the possibility of a reduced influence of nucleate boiling for this tube dimension across the whole temperature range.

When comparing data with different models which are based seemingly on the same dominant boiling mechanism discrepancies in the prediction level are most likely caused by the different weighting of parameters used by the models. For example the correlation by Cooper [59] is one of the oldest methods to predict nucleate boiling. However in this case it is based on the reduced pressure, the molar mass and the heat flux and not the Boiling number. Similar to the Cooper model a formulation adapted to CO_2 is used in the Cheng et al. [109, 110] model, which is the method applied by Ducoulombier et al. [135] for their first thermal regime (Duc. I). As presented in Figure 9.31(b) the data gathered for the 2.15 mm ID tube is in this case constantly over-estimated by this method. Furthermore when comparing the 1 mm and the 0.5 mm ID tube data with the correlation this results in a similar good fit at high T_{sat}, with an increasing over-prediction for the 1 mm ID tube and an increasing under-prediction for the 0.5 mm ID tube for low T_{sat}, confirming the dominance of isolated bubble flow at high T_{sat} and the increasingly different heat transfer processes for the two smaller tubes at low T_{sat}. Using the same nominal tube ID as [135] this method indeed predicts the data gathered for the 0.5 mm ID tube reasonably well at elevated T_{sat}.

(II) Confined bubble regime To predict the heat transfer in the confined bubble regime Cornwell and Kew [157] recommended to implement the Boiling number and the Confinement number. Accordingly Hihara and Tanaka [117] proposed a modification of the Schrock-Grossman [158] expression for data gathered with CO_2:

$$\frac{\alpha}{\alpha_{lo}} = K_1\,Bo + K_2\left(\frac{1}{X_{tt}}\right)^{2/3}. \tag{9.5}$$

Here the empirical factors K_1 and K_2 are intensifying the impact of the Boiling number or the Lockhart–Martinelli variable X_{tt}, respectively. According to Chen [54], X_{tt} is the governing quantity in the convective boiling heat transfer, whilst the Boiling number represents the nucleate boiling contribution. Thus in the confined bubble regime boiling may be a mixture of thin film and nucleation effects. For this present study all three tube dimensions are predicted relatively well with this method. Figure 9.31(c) shows that, for the 0.5 mm and 2.15 mm tube an almost constant, however slightly under-predicted prediction value can be provided across the range of T_{sat}, thus achieving a reasonable temperature dependent weighting of the two mentioned factors. In the case of the 2.15 mm ID tube the weighting on Bo, and thus on nucleate boiling may be under-estimated, whilst for the 0.5 mm ID tube weighting on X_{tt} and thus on the convective boiling may be under-estimated. However the prediction capability for the 1 mm ID tube is submitted to a shift between under- and over-prediction at about -15°C, where the heat transfer is under-predicted at higher T_{sat} and slightly over-predicted at low T_{sat}, witnessing the transitional character of the flow inside the 1 mm ID tube with changing T_{sat}. At high T_{sat} the flow is less confined favouring nucleate boiling which is under-estimated by Hihara

and Tanaka [117] and the weighting on Bo may be too less. At lower T_{sat} where the flow becomes increasingly confined convection plays a more dominant role which is then captured more correctly by the correlation. With modifications to the two factors K_1 and K_2 the relevance of X_{tt} and Bo can be traced down further for the case of the 1 mm ID tube for different T_{sat}. According to Table 9.7 based on the values for K_1 and K_2 defined by Hihara and Tanaka [117], the prediction level at +15°C could be improved drastically by increasing the nucleate boiling factor K_1 by 50%, whilst a 50% higher K_2 factor barely changed the fit. At -25°C the outcome is reversed: an appropriate adaptation of the K_2 factor can provide a better prediction at low T_{sat} putting more relevance on the convection. Whilst being a mathematical exercise only it once more highlights the fact that the saturation temperature and the changing physical properties may require a more dynamic application of prediction models.
Overall those findings confirm the statement given by Ducoulombier et al. [135] that the CO_2 boiling heat transfer in small tubes is driven more by convective phenomena at low T_{sat} than commonly assumed.

					+15 °C	-25° C
	K_1		K_2		av. deviation %	
Hihara & Tanaka [117]	14700.00		0.93		-30.98	8.05
	22050.00	K_1 + 50%	0.93		-0.35	49.80
	14700.00		1.40	K_2+ 50%	-27.05	20.46
	11760.00	K_1 - 20%	0.93		-43.23	-8.65
	14700.00		0.74	K_2 - 20%	-32.57	3.04

Table 9.7: Modifications of factors K_1 and K_2.

(III) Annular-slug flow Cornwell and Kew [157] linked the pure convective boiling regime in restricted passages to the annular-slug flow regime. In terms of model formulation they propose the implementation of the convective boiling enhancement factor F developed by Chen [54]. Accordingly Ducoulombier et al. [135] developed a simple relation implementing $1/X_{tt}$ and F based on their experimental data gathered with CO_2 which is then used for their type III thermal regime (Duc. III). Figure 9.31(d) presents the outcome of this correlation for all three diameters. Using this relation, the heat transfer coefficient in the 2.15 mm ID tube is highly under-estimated for all T_{sat}, which confirms that pure convection may play only a small role in the heat transfer across the biggest tube. The prediction improves for the smaller tubes and thus for increasingly confined flow. The proposed model is most relevant for the 1 mm ID tube at about -15°C and for the 0.5 mm ID tube at 0°C. This confirms that with decreasing ID the influence of convective heat transfer gains importance at higher T_{sat}. The over-estimation for the two smaller tubes at low T_{sat} may be explained with a thicker liquid film since the surface tension increases and thus reducing the overall heat transfer. The relative high over-prediction for the 0.5 mm ID tube at low T_{sat} may also be due to the fact that this correlation is based on data gathered at -10°C, -5°C and 0°C only, which is also in line with its best prediction found for this study between -5°C and 0°C.

It has to be stressed that neither the scheme of correlations by Cornwell and Kew [157] nor in this context the other mentioned correlations providing a good fit are based on the very frequently used summation-model type mentioned earlier. In this case - based on empirical findings - a nucleate boiling and a convective boiling component are superposed mathematically, whilst in one way or the other more relevance is given to the first or the latter in order to predict the heat transfer coefficient during flow boiling. For completeness sake it has to be mentioned that some of the worst predictions listed in Table 9.6 are due to a comparison to these Chen-type summation models [54, 56, 57, 130, 136]. Thus whilst this approach is the historically most commonly used, an application seems not advisable and a prediction based on the actual phenomenological behaviour of the flow should be encouraged.

However, aside from the fully empirical summation models and the rather complex formulation of phenomenological models, Fang et al. [156] developed an entirely mathematical prediction method. The procedure is based on the similarity principle, rather than empirical superposition and can provide a slightly more realistic fit by using a multiplicative formulation instead of a shear summation. For the development of this correlation a large data base was used (17,778 data points from 101 sources and 13 different fluids, including CO_2). All non-dimensional parameters which proofed to be of relevance during flow boiling in the past were submitted to a purely numerical optimization process, targeting the minimal mean absolute deviation (MAD) and mean relative deviation of the predicted heat transfer coefficient over the whole database. In result based on the Buckingham theorem a set of 7 non-dimensional groups (and one additional fluid-dependent factor) have been selected and related with each other in a multiplicative way. This resulting correlation then was tested with a completely independent second data base (664 data points from 60 sources and 18 different fluids, including CO_2) and a MAD of 4.4% could be reported, with 69.0% and 93.5% of the data predicted within ±5% and ±10%. Figure 9.28, 9.29, 9.30 and in particular Figure 9.31(e) confirms the good prediction capability of the correlation by Fang et al. [156] with respect to the data from this present study. Across the whole temperature range and especially for the larger tube dimensions the specific trends of the heat transfer coefficient are often reproduced very accurately. Some limitations can be found for the prediction of the data gathered on the 0.5 mm ID tube, which is due to the general scarcity of CO_2 flow boiling data in this sector and furthermore highlights the possibly fundamentally different flow behaviour of CO_2 in small channels compared to standard refrigerants or inside large channels.

Possible guidelines & recommendations The findings described above may again result in a set of basic guidelines concerning the evolution of the heat transfer inside small-scale CO_2 evaporators. Emphasizing on the found temperature dependence on the applicability of prediction methods, an engineer who is facing the implementation of small-scale CO_2 evaporator tubes of $\sim$ 2 mm, 1 mm and 0.5 mm ID, which will be submitted to mass fluxes as mentioned in 8.1.5, may consult Table 9.8 (2 mm), Table 9.9 (1 mm) and Table 9.10 (0.5 mm) for the selection of suitable prediction methods of the two-phase heat transfer coefficient. Those tables list the most promising correlations (average deviations $\bar{\xi} < 20$ %) obtained with a comparison to data from this study and grouped in temperature ranges of 15°C to 10°C, 5°C to 0°C, -5°C to -10°C and -15°C to -25°C. This results in a tabular temperature dependent reference for the application of two-phase heat transfer correlations - as opposed to Table 9.6 where no temperatures were taken into account. Note that individual heat and mass fluxes are not considered in this case and additional information may be found in Appendix F.

Based on the phenomenological explanation given above, for the estimation of the heat transfer coefficient across a CO_2 evaporator tube of ~ 2 mm ID it is recommended to apply the correlations by Yun et al. [133] and Kew and Cornwell [89]. Above +5°C the nucleate boiling correlation by Yun et al. [133] provides a good fit, since it is based on a very similar ID and CO_2 as working fluid. The nucleate boiling correlation by Kew and Cornwell [89] may be used for T_{sat} from about +5°C to -25°C.
Similar recommendations stand for a tube of ~ 1 mm ID, whilst at +15 and +10°C the nucleate boiling correlations proposed by Cheng et al. [109, 110] (Duc. I) result in a good prediction level. At lower temperatures around +5°C, the correlation by Kew and Cornwell [89] seems appropriate, whilst for T_{sat} < 0°C, the correlation by Hihara and Tanaka [117] (Duc. II) and by Ducoulombier et al. [135] (Duc. III) may capture the flow boiling heat transfer coefficient sufficiently.
Special attention should be given to the correlation by Fang et al. [156] which provides a very good overall fit for the entire temperature range investigated, especially for the two larger tube dimensions. This correlation is still relatively new (published in 2017) at the time of this investigation and more experience is needed to confirm a recommended application. Nevertheless, from the point of view of this study its cautious application shall be encouraged in the future.
The heat transfer coefficient during CO_2 flow boiling inside a ~ 0.5 mm ID tube may be predicted with the scheme of correlations by Ducoulombier et al. [135]: The first type (Duc. I) may be applied between +15°C and +5°C T_{sat}, the third type (Duc. III) between 0°C and -5°C T_{sat} and the second type (Duc. II) for T_{sat} < -10°C. Note the order of recommended application of the three regime related correlations whilst in [135] the vapour quality and not - like in this study - T_{sat} is used as a delimiter.

2.15 mm ID: T$_{sat}$ +15 to +10°C	$\bar{\xi}$ [%]	+5 to 0°C	$\bar{\xi}$ [%]
Liu & Winterton [58]	-1	Fang et al. [156]	1
Fang et al. [156]	-1	Liu & Winterton [58]	1
Bertsch et al. [104]	2	Oh et al. [132]	-3
Yun et al. [133]	8	Tran et al. [101]	-8
Warrier et al. [100]	-8	Kew & Cornwell [89]	-9
Oh et al. [132]	-10	Lazarek and Black [5]	-10
Tran et al. [101]	12	Bertsch et al. [104]	-10
Cheng et al.: stratified [110]	16	Warrier et al. [100]	12
Li and Wu [103]	17	Yun et al. [133]	13
Cooper [59]	18	Cooper [59]	16
Kew & Cornwell [89]	-18	Kim and Mudawar [108]	16
Choi et al. [114]	18	Hihara & Tanaka [117]	-17
Hihara & Tanaka [117]	-18	Choi et al. [114]	17
Cheng et al. [110]: stratified - wavy	19	Cheng et al. [110]: stratified	18
Kim and Mudawar [108]	19	Wattelet et al. [60]	19
Lazarek and Black [5]	-19		

(a)

2.15 mm ID: T$_{sat}$ -5 to -10°C	$\bar{\xi}$ [%]	-15 to -25°C	$\bar{\xi}$ [%]
Fang et al. [156]	-1	Kew & Cornwell [89]	-2
Liu & Winterton [58]	2	Liu & Winterton [58]	2
Oh et al. [132]	2	Agostini and Bontemps [102]	-2
Kew & Cornwell [89]	-3	Lazarek and Black [5]	-2
Lazarek and Black [5]	-4	Oh et al. [132]	3
Yun et al. [133]	8	Kim and Mudawar [108]	3
Kandlikar [53]	-12	Cooper [59]	6
Cooper [59]	13	Kandlikar [53]	-7
Hihara & Tanaka [117]	-15	Gungor and Winterton [57]	8
Shah [55]	-15	Shah [55]	-8
Choi et al. [114]	17	Fang et al. [156]	-8
Bertsch et al. [104]	-17	Yun et al. [133]	-9
Agostini and Bontemps [102]	-17	Hihara & Tanaka [117]	-14
Gungor and Winterton [57]	18	Choi et al. [114]	15
Wattelet et al. [60]	19	Wattelet et al. [60]	15
Cheng et al. [110]: stratified	19	Cheng et al. [110]: stratified	18

(b)

Table 9.8: Average deviation $\bar{\xi}$ <20% for different heat transfer prediction methods across the 2.15 mm ID tube and for varying temperature regimes: a) +15°C to 0°C; b) -5°C to -25°C.

1 mm ID: T$_{sat}$ +15 to +10°C	$\bar{\xi}$ [%]	+5 to 0°C	$\bar{\xi}$ [%]
Liu & Winterton [58]	-1	Bertsch et al. [104]	-1
Cooper [59]	2	Yun et al. [133]	1
Bertsch et al. [104]	2	Lazarek and Black [5]	2
Fang et al. [156]	2	Kew & Cornwell [89]	3
Li and Wu [103]	-3	Kandlikar & Balasubramanian [106]	4
Gungor and Winterton [57]	3	Fang et al. [156]	4
Cheng et al. [110]: stratified	4	Cooper [59]	5
Cheng et al. [110]: stratified - wavy	4	Kandlikar [53]	6
Oh et al. [132]	7	Shah [55]	10
Shah [55]	-7	Gungor and Winterton [57]	11
Kandlikar & Balasubramanian [106]	-8	Liu & Winterton [58]	12
Ducoulombier et al. [135] (I)	8	Cheng et al. [110]: stratified	13
Ducoulombier et al. [135]	8	Cheng et al. [110]: stratified - wavy	14
Yun et al. [133]	-8	Ducoulombier et al. [135] (I)	15
Kandlikar [53]	-9	Ducoulombier et al. [135]	17
Choi et al. [114]	9	Hihara & Tanaka [117]	-18
Cheng et al. [110]: annular	9	Li and Wu [103]	19
Kew & Cornwell [89]	-11	Yu et al. [105]	19
Lazarek and Black [5]	-12	Cheng et al. [110]: annular	19
Wattelet et al. [60]	14		

(a)

1 mm ID: T$_{sat}$ -5 to -10°C	$\bar{\xi}$ [%]	-15 to -25°C	$\bar{\xi}$ [%]
Bertsch et al. [104]	2	Chen [54]	2
Fang et al. [156]	3	Yun et al. [133]	-2
Yun et al. [133]	5	Fang et al. [156]	-4
Hihara & Tanaka [117]	-6	Hihara & Tanaka [117]	7
Cooper [59]	11	Bertsch et al. [104]	9
Ducoulombier et al. [135] (III)	-12	Ducoulombier et al. [135] (III)	12
Lazarek and Black [5]	17	Pamitran [130]	-12
Kew & Cornwell [89]	18	Cooper [59]	14
Kandlikar & Balasubramanian [106]	19	Agostini and Bontemps [102]	-18
Yu et al. [105]	19	Yu et al. [105]	18

(b)

Table 9.9: Average deviation $\bar{\xi}$ <20% for different heat transfer prediction methods across the 1 mm ID tube and for varying temperature regimes: a) +15°C to 0°C; b) -5°C to -25°C.

0.5 mm ID: T_{sat} +15 to +10°C	$\bar{\xi}$ [%]	+5 to 0°C	$\bar{\xi}$ [%]
Cooper [59]	3	Cheng et al. [110]: stratified - wavy	3
Yu et al. [105]	-3	Cheng et al. [110]: stratified	4
Hihara & Tanaka [117]	-3	Ducoulombier et al. [135] (I)	-5
Cheng et al. [110]: stratified - wavy	4	Lazarek and Black [5]	6
Ducoulombier et al. [135] (I)	5	Kew & Cornwell [89]	8
Bertsch et al. [104]	5	Kandlikar & Balasubramanian [106]	8
Yun et al. [133]	-5	Ducoulombier et al. [135] (III)	-8
Cheng et al. [110]: stratified	7	Hihara & Tanaka [117]	-9
Lazarek and Black [5]	8	Cooper [59]	-10
Fang et al. [156]	9	Wang et al. [136]	-10
Kew & Cornwell [89]	10	Yun et al. [133]	-11
Wang et al. [136]	-11	Cheng et al. [110]: annular	12
Cheng et al. [110]: annular	13	Ducoulombier et al. [135]	13
Kandlikar & Balasubramanian [106]	13	Fang et al. [156]	14
Ducoulombier et al. [135]	15	Bertsch et al. [104]	-14
Liu & Winterton [58]	16	Li and Wu [103]	-15
Shah [55]	18	Chen [54]	-17
Ducoulombier et al. [135] (III)	-19	Liu & Winterton [58]	18
Li and Wu [103]	-19	Shah [55]	19
		Kandlikar [53]	19

(a)

0.5 mm ID: T_{sat} -5 to -10°C	$\bar{\xi}$ [%]	-15 to -25°C	$\bar{\xi}$ [%]
Chen [54]	-1	Li and Wu [103]	-2
Wang et al. [136]	-1	Lazarek and Black [5]	3
Li and Wu [103]	-4	Kew & Cornwell [89]	4
Hihara & Tanaka [117]	-5	Hihara & Tanaka [117]	-5
Ducoulombier et al. [135] (I)	-6	Wang et al. [136]	8
Ducoulombier et al. [135] (III)	10	Kandlikar & Balasubramanian [106]	12
Lazarek and Black [5]	10	Ducoulombier et al. [135] (I)	-15
Kew & Cornwell [89]	11	Chen [54]	15
Kandlikar & Balasubramanian [106]	13	Pamitran et al. [130]	-16
Cooper [59]	-14		
Fang et al. [156]	15		
Cheng et al. [110]: stratified - wavy	15		
Cheng et al.: stratified [110]	16		
Yun et al. [133]	-17		
Bertsch et al. [104]	-19		

(b)

Table 9.10: Average deviation $\bar{\xi}$ <20% for different heat transfer prediction methods across the 0.5 mm ID tube and for varying temperature regimes: a) +15°C to 0°C; b) -5°C to -25°C.

In summary the prediction capability of the CO_2 boiling heat transfer coefficient according to already existing correlations is in general better compared to the pressure drop. This is due to the fact that more efforts were undertaken in the past to understand the heat transfer coefficient for boiling CO_2 and other refrigerants, whilst the understanding for pressure drop is less crucial for many applications. Often a slight over-dimensioned pump is enough as a buffer. Nevertheless the pressure drop signal may be enhanced and distorted by multiple additional and second order effects, whilst propagating at the speed of sound. Due to the high accuracy levels achievable with the installed differential pressure sensors some insights into the complex behaviour of the boiling CO_2 pressure drop in small-scale evaporators could be gathered with this study. For the heat transfer on the other hand, conduction and convection effects may also include more complex phenomena, however here the involved solid materials of the evaporator tubes or channels are damping the overall signal at the outer evaporator surface which is in most cases the final crucial parameter. Thus even without highly accurate temperature sensors the evolution of the measured wall temperatures provided a sufficient base for many prediction models formulated in the past. In this study indeed it could be confirmed that in most cases, independent of the phenomenological pressure variations, good heat transfer properties are maintained (see Figure 9.19) and only in a few cases at very small flow rates the flow induced instabilities affect the heat transfer (see Figure 9.22).

However for applications in HEP experiments a good prediction is needed of both, heat transfer coefficient and pressure drop, not only to dimension the pumped system in a correct way but also to calculate the heat transfer coefficient across the evaporator correctly, which relies on a correct prediction of the pressure drop. In addition a good forecast of the pressure across long transfer lines and large evaporators is needed.

Resume As motivated in chapter 6 and 7 an extensive new data base on CO_2 boiling flows in small-scale evaporators could be created with the described experimental studies, emphasizing on the effects of saturation temperature and thus filling a crucial knowledge gap for the safe operation of particle detectors which are thermally managed with CO_2 evaporators. New experimental insights for CO_2 boiling flows in small-scale evaporators in terms of pressure drop, heat transfer and bubble dynamics were gathered and could be related further to the performance of existing prediction methods, whilst basic guidelines and recommendations could be developed for future design procedures.

CHAPTER 10

Future implications for detector cooling

The major consequences which arise from the results and findings gathered for the detailed R&D project with mini- and micro-scale carbon dioxide evaporators shall be summarized here shortly for the detector cooling community. Those implications can be divided into issues concerning the performance, the resulting modelling and design and the most optimal integration of future CO_2 evaporators into the overall detector layout.

Performance The introduced detector cooling methods profit from the use of small evaporator channels due to the reduced material budget and the elevated heat transfer efficiency compared to conventional tubes. The nature of evaporative cooling allows for the dissipation of large amounts of heat which may vary over time for sensor and read-out electronics. Furthermore large temperature gradients can be avoided across the detector module and the difference between heat sink and source can be further minimized. As presented in the section on experimental results the different thermo-physical properties of carbon dioxide compared to other refrigerants are highly appropriate for the application in small channels and allow for an excellent heat transfer performance and small pressure drops. In general the high pressure of CO_2 poses no other disadvantage than the necessity of leak tight fluidic inter-connections. The most interesting effects on the heat transfer performance and the pressure drop obtained with this study may be summarized as follows:

- For tubes with an inner diameter $\geq$ 1 mm the heat transfer coefficient deteriorates for decreasing T_{sat}. This has to be taken into account during dimensioning.
- For tubes with an inner diameter of $\sim$ 0.5 mm the heat transfer coefficient stays more or less constant for decreasing T_{sat}.
- Based on the same phenomenological effect, the same is true for the multi-micro-channels.
- The latter two result in an optimal constant cooling performance across the entire temperature range encountered during the life-time of a detector.
- For tubes with an inner diameter $\geq$ 2 mm the pressure drop caused by a change in T_{sat} is negligible.
- For tubes with an inner diameter $\leq$ 1 mm the pressure drop caused by a change in T_{sat} is non-negligible and increases with decreasing inner diameter.

In general those items have to be considered during the design phase of new CO_2 detector cooling systems. The effects of T_{sat} on the pressure drop and the heat transfer inside different tube dimensions have to be understood since they influence the final amount of material and the space occupied by the chosen cooling method.

Prediction & design New and innovative Silicon Pixel Detector systems need to be designed today or in the very near future with carbon dioxide selected as the principal refrigerant for their thermal management. Nevertheless, in the future new prediction models will be formulated based on the large data set gathered for this study and based on the still remaining experimental work anticipated with the new experimental setup for detector cooling R&D with small-scale carbon dioxide evaporators. However, while waiting for new comprehensive prediction models for the pressure drop and the heat transfer of boiling flows of CO_2 in tubular small-scale evaporators, some order could be brought into the large amount of flow boiling prediction models developed so far. Due to the changing thermo-physical properties of CO_2 across the large range in saturation temperatures employed for detector cooling, instead of using only one overall applicable model, depending on the saturation temperature various models shall be used for both pressure drop and heat transfer. This is important to cope with the large range of temperatures which stands in contrast to standard refrigeration applications where in most cases a fixed cold temperature is targeted. Whilst designing a new detector cooling system with similar overall design parameters to those which have been investigated, engineers can make use of the guidelines and recommendations given in this study (Table 9.3 to 9.10). Note that the direct prediction of the pressure drop and heat transfer inside the multi-micro-channels requires further studies and lies out of the scope of this thesis.

Integration The final choice and integration of either small-scale tubular evaporators or of multi-micro-channel cold plates has to be evaluated case by case. Whilst for the latter the thermal performance, the homogeneity of the resulting temperature distribution across the sensor module and the low material budget involved are highly advantageous for the application in HEP experiments, there are still some open issues which have to be resolved before a grand-scale implementation is possible. The limitations of micro-channel-cooling as of today lie in a feasible inter-connection of multiple cold plates necessary for the cooling of numerous detector modules. Such solution exits for end-caps or similar detector geometries (e.g. LHCb VELO [44]), however for barrel configurations which are more restricted in terms of available space a large-scale technical solution is still sought after. In general compared to simple single tubes the costs of individually manufactured multi-micro-channel cold plates are naturally much higher and ways of making this technique less cost-intensive are also investigated. A field of research which is however even more financially demanding is the recent development of the direct implementation of multi-micro-channel fluidic circuits into the same silicon bulk as the actual sensor. This method induces an even better thermal performance and an almost negligible material budget. More information on the efforts undertaken at CERN and other research institutes to resolve remaining issues encountered with multi-micro-channel cold plates and further developments can be found in [159] and [160]. In general whilst all mechanical and thermo-physical properties of all involved components allow for a highly-integrated solution, tubular evaporators can also provide an efficient thermal management, whilst polyimide tubes which are theoretically fully qualified for high pressures will be characterized with CO_2 in the future. Table 10.1 shall summarize the main concerns for the integration of small-scale CO_2 evaporators into the overall detector layout.

	tubular evaporators	**multi-micro-channels**
location	barrels and end-caps	where technically possible, only end-caps (so far)
method	embedded cooling pipes	substrate with micro-channels
TFM	$\sim 12\ \mathrm{m^2K/W}$ [11]	$\sim 3\ \mathrm{m^2K/W}$ (from this study)
material budget	~ 1 % X_0 per layer for metal tubes [11]	< 0.5 % X_0 per layer [29]
	< 0.5 % X_0 per layer for polyimide tubes [161]	< 0.15 % X_0 per layer for silicon substrates [29]
		~ 0 % X_0 per layer for fully integrated multi-micro-channels [159]
open issues		- fluidic distribution
		- hydraulic inter-connection of multiple cold-plates
		- high costs

Table 10.1: General concerns for the integration of small-scale CO_2 evaporators into HEP detectors

CHAPTER 11

Conclusion

CO_2 flow boiling in small channels is a very efficient and compact cooling method for confined places such as HEP experiments, where surface power densities in the order of 1 W/cm^2 have to be dissipated from detector modules arranged in a very convoluted fashion. The efficient thermal management of Silicon Pixel Detectors with forced convective liquid flow inside tubes is necessary for systems with high demands on sensor life time and signal quality. With effective detector cooling extensive radiation damage on the sensor can be averted and the heat dissipated by the front-end electronics can be removed effectively. Whilst the use of small channels is not only advantageous in terms of the reduced material introduced into the sensitive detector area, it also has been found that thermodynamically the minimization of heat exchanger channels bears an increase of the heat transfer efficiency compared to conventional tubes. Many efforts have been undertaken in the past to understand flow boiling in micro-channels however a lot of research is still needed to fully understand the topic. In addition CO_2 has been proven to be an environmentally friendly and otherwise thermo-physically superior refrigerant and its combination with highly integrated small channel detector cooling layouts was chosen for the thermal management of the present and next generations of Silicon Pixel Detectors which are necessary for the High Luminosity LHC Project. In order to optimally design and safely operate the highly sensitive particle detectors, some of the unknowns related to CO_2 flow boiling in small channels must be resolved and new predictive methods have to be developed both for pressure drop and for the heat transfer coefficient. Hence to extend the rather limited data base on CO_2 boiling in small channels, a new test stand, which was conceptualized and designed for this project, allows to characterize mini- and micro-channel cooling devices with evaporative CO_2 with an unprecedented accuracy level in this field of research. Small-scale CO_2 evaporators of different materials and geometries can be studied by means of a parametrical flow characterization with high-end pressure and temperature sensors and by means of flow visualization with a high-speed camera. Three dimensions of small-scale tubular evaporators in stainless steel and one multi-micro-channel cold plate embedded into silicon have been characterized for this study.

The Thermal Figure of Merit achieved with the tested multi-micro-channels lies at a constant $\sim 3\,m^2K/W$ for the entire test range (+15°C to -25°C), which is a factor 4 better than the best performing conventional detector cooling method used so far. This unchanging thermal behaviour can be explained with channel size and flow confinement effects which were further studied with the more basic single channels. Furthermore qualitative flow observations from high-speed visualizations on the multi-micro-channels provided a consistent key of interpretation for the quantitative measurements gathered for the tubular evaporators.

The pressure drop and local heat transfer coefficient of CO_2 boiling flows have been studied at low vapour quality in 200 mm-long, small-diameter stainless steel tubes with inner diameters of 2.15 mm, 1 mm and 0.5 mm. The new test setup has been used to explore with high precision measurements a wide range of saturation temperatures (+15°C to -25°C) and mass fluxes (100 to 1800 $\mathrm{kg/m^2s}$) and diabatic tests were carried out for heat fluxes from 5 to 35 $\mathrm{kW/m^2}$. Established trends for the two-phase pressure drop and heat transfer reported in literature could be confirmed. Although the effect of T_{sat} on the CO_2 boiling pressure drop and heat transfer is acknowledged by different authors in literature, the subject was not yet given the same systematic attention compared to other flow boiling effects. Consequently, the present study focused on the effects of saturation temperature which was possible due to the very flexible conception of the new test setup where a recently developed CO_2 refrigeration unit for detector cooling R&D (TRACI) delivers a wide range of stably controlled saturation temperatures (+15°C to -25°C). In result it was found that T_{sat} greatly affects the boiling properties of CO_2 in small channels which has to be taken into account during the design process of future CO_2 evaporators for detector cooling.

The known effect of increasing pressure drop with decreasing T_{sat}, was found to be a superposition of two effects: the change in physical properties of CO_2 and a parallel growing influence of flow confinement effects, which gets more and more apparent with decreasing ID. The evident drifting behaviour of the two-phase pressure drop, hence of the flow characteristics, for different T_{sat} and different tube sizes suggests a transition between macro- and micro-scale flow behaviour within the range of tested parameters. The data were compared to some transition criteria proposed in literature and the outcome of this comparison seems to validate this observation. Within the temperature range of observation, all data gathered for the 2.15 mm ID tube falls into the macro-scale regime, all data gathered for the 0.5 mm ID tube can be categorized as micro-scale, whereas for the 1 mm ID tube a transition between macro- and micro-scale flow takes place. This could be further substantiated with the results gathered for the heat transfer coefficient. In general investigations with changing T_{sat} and heat flux showed shifting trends of the heat transfer coefficient α especially for the 1 mm ID tube, confirming the transitional character of the flow inside this tube and suggesting a shift of the dominating boiling mechanism from high T_{sat} to low T_{sat}. Throughout this work even in the absence of flow visualization on tubular CO_2 evaporators, the phenomenological transition of the flow within the three tube dimensions and across the tested temperature range could be confirmed by various other means (parametrical and direct signal analysis, comparison to transition criterions, comparison to external findings). Furthermore the comparison of the new experimental data with correlations predicting the two-phase pressure drop and heat transfers coefficient could further highlight the overall change of flow phenomena with T_{sat}.

It was shown that no existing correlation can fully capture the two-phase pressure drop trends experimentally measured, thus stressing the need of a more holistic approach for the prediction of the CO_2 two-phase pressure drop in small channels. From an operational point of view, it seems advisable to discard the typically used approach of applying one single correlation to a gathered data base. This is in particular important when different saturation temperatures are investigated and to achieve a more dynamic modelling approach one should instead distinguish between different correlations in combination with varying T_{sat} and inner diameters. Devoid of an overall applicable approach to predict the heat transfer coefficient during CO_2 flow boiling in small channels, likewise the application of certain individual heat transfer prediction models which aim towards a similar differentiation of flow patterns as suggested for this study may be encouraged. Three such model categories have been defined in the past based on the isolated bubble (IB) regime, the confined bubble (CoB) regime and the annular slug flow (ASF) and in the case of this study the overall saturation temperature and the confinement level is used as delimiter between the three, not the vapour quality. For low vapour qualities the data gathered for the 2.15 mm ID is predicted well with correlations falling into the IB category with nucleate boiling as dominant heat transfer mechanism. Whereas the 1 mm ID tube indeed undergoes a transition from IB to ASF and the corresponding correlations apply in this order for decreasing T_{sat} with an assumed parallel increase of the dominance of convective boiling. In the case of the 0.5 mm ID tube such delimitation is less clear underlining the possibility of new heat transfer processes occurring for highly confined CO_2 flow boiling in small diameter tubes and channels.

The general prediction capability for the heat transfer coefficient was found to be superior compared to the pressure drop. This is due to the fact that more efforts were undertaken in the past to study the heat transfer coefficient for boiling CO_2 and because - different to detector design needs - the understanding of pressure drop is less crucial for many applications. Furthermore more second order phenomenological effects may affect the pressure drop signal which makes its prediction more demanding. For detector cooling applications in HEP experiments a good prediction is needed of both, heat transfer coefficient and pressure drop, which could be addressed with this study for the case of small-scale CO_2 evaporators.

In summary, the new data gathered with this experimental study provide novel insights on evaporative flows of CO_2 in small channels. In particular, it could be shown that any model of the CO_2 boiling pressure drop and heat transfer coefficient in channels of small diameter should consider the effects of saturation temperature and their impact on the flow confinement level in order to fully capture the unique features of CO_2 flow boiling in small channels. In the future advanced models based on those new findings can enhance the design optimization process of mini- and micro-channel evaporators drastically, especially when a large range of saturation temperatures is involved. This is true for the thermal management of Silicon Pixel Detectors inside HEP experiments and whilst new comprehensive prediction models for the boiling pressure drop and heat transfer of CO_2 are being developed the results and recommendations of this study may guide the optimized design of new Silicon Pixel Detector cooling systems.

CHAPTER 12

Outlook

The initial test matrix in terms of test specimen and the conceptualization of the new experimental setup for detector cooling R&D with mini- and micro-scale CO_2 evaporators at CERN was from the beginning planned to be part of a long-term study reaching far beyond the scope of this thesis. With the new experimental setup as an important novelty for the detector cooling R&D community, the research program was launched for first tests and the large data base created so far will function as a crucial foundation for the future. However some quite ambitious research plan still lies ahead. From the various channel dimensions described in section 7.1.2 only a small portion was tested for this study. As discussed in the main text tube size transition effects could be studied providing interesting results for the research community. Additional experiments with different stainless steel tube dimensions may be carried out in the future to refine the data base created so far (1.5 mm ID, 0.75 mm ID, 0.25 mm ID and 0.13 mm ID). In order to extend the test matrix of the tubular evaporators to such low hydraulic diameters it is necessary to equip the setup with a flow restriction device (orifice) in the upstream direction of the test section to avoid major flow instabilities. Furthermore surface roughness effects may be studied in the future with investigations on tubes with the same inner diameter but different channel materials (e.g. stainless steel vs. titanium), whilst an experimental characterization of small diameter polyimide tubes with CO_2 is also part of the remaining research plan. Interesting geometry effects may result from investigations on approximately the same tube cross-section but comparing between circular and squared channel cross-sections. An important source of information during flow boiling in small channels is the visualization of the flow. Those visual results could be obtained for the multi-micro-channels, however for the tubular evaporators such experiments are still pending. Recordings on joined steel-glass single tubes are planned, where a robust interconnection of glass and stainless steel which withstand the working pressures of evaporating CO_2 has been proven to be non-trivial. In this case the heat load is only applied to the stainless steel part whilst the visualization is achieved under adiabatic conditions. For this purpose tests were carried out with the full stainless steel tubes where only one half of the tube was submitted to a heat load. This data was not discussed in the main text but will provide validation results in the future for the tests with the joined steel-glass single tubes. As shown in 7.1.2, there are different micro-channel layouts already available for testing and especially the evaluation of the circular channel layout ("donut") will provide interesting results, after resolving the problematic of the circular dicing as described in Appendix C.

Another feature of the new experimental setup which has not been used so far is the possibility to characterize any test specimen with an infrared camera whilst subjected to boiling CO_2 flows.

Collaborating institutes may be interested in the future to characterize their micro-channel layout by means of the new experimental setup for detector cooling R&D with mini- and micro-scale CO_2 evaporators at CERN, thus collecting even more experimental data.
The combination of all available investigative methods (flow characterization with high-end sensors, high-speed camera and infrared camera recordings) and at the same time the creation of a very large and reliable data base for CO_2 pressure drops, heat transfer coefficients and flow patterns in mini- and micro-channels increases the chance to finally understand micro-channel cooling phenomena on a more profound level. Understanding the physical behaviour of evaporative flow in small channels will assist in finding a theoretical micro-channel definition and can be used for the refinement of existing prediction models or the formulation of new ones, where the focus should be laid on the creation of the more meaningful non-empirical models based on the evolution of the flow pattern during flow boiling. All of the above will help to optimize design parameters of future micro-channel evaporators towards more efficient detector cooling in the context of HEP experiments. One interesting development which is already being investigated is the direct implementation of a multi-micro-channel fluidic circuit into the same silicon bulk as the actual detector [159]. This reduces thermal resistances even further, maximizes the heat transfer efficiency and minimizes the material introduced into the detector volume in terms of on-detector cooling. It is so far considered the end goal of a fully integrated detector cooling approach whilst using evaporative cooling in very small channels.

CHAPTER 13

Epilogue

This work bridges the gap between experimental particle physics and experimental fluid flow science. Often the known and intuitive behaviour of macroscopic objects described with classical mechanics have to be abandoned when studying the realm of sub-atomic particles. In a comparable way, although the difference in length scales is less profound, well-known fluid mechanics at a macroscopic level cannot fully describe the behaviour at microscopic scales, especially when it comes to the description of the movement and the energy transfer between two phases during evaporative fluid flow in tubes and channels. Unlike in particle physics, indeed no relativistic effects and most likely no quantum-mechanical effects due to the rather big length scales are responsible for these differences, nonetheless the exploration of flow boiling in small dimensions may yield more yet unknown phenomena than meets the eye.

Bibliography

[1] D. Kotliński, *The CMS pixel detector*, Nuclear Instruments and Methods in Physics Research Section A: Accelerators, Spectrometers, Detectors and Associated Equipment **465** (2001) 46, ISSN: 0168-9002,
URL: `http://www.sciencedirect.com/science/article/pii/S016890020100345X`
(cit. on p. 1).

[2] V. Vrba, *The ATLAS pixel detector*, Nuclear Instruments and Methods in Physics Research Section A: Accelerators, Spectrometers, Detectors and Associated Equipment **465** (2001) 27, ISSN: 0168-9002,
URL: `http://www.sciencedirect.com/science/article/pii/S0168900201003424`
(cit. on p. 1).

[3] D. B. Tuckerman and R. F. W. Pease, *High-performance heat sinking for VLSI*,
IEEE Electron Device Letters **2** (1981) 126 (cit. on pp. 1, 47).

[4] L. Cheng and G. Xia, *Fundamental issues, mechanisms and models of flow boiling heat transfer in microscale channels*,
International Journal of Heat and Mass Transfer **108** (2017) 97, ISSN: 0017-9310,
URL: `http://www.sciencedirect.com/science/article/pii/S0017931016326643`
(cit. on pp. 1, 47, 52, 113).

[5] G. M. Lazarek and S. H. Black, *Evaporative heat transfer, pressure drop and critical heat flux in a small vertical tube with R-113*,
International Journal of Heat and Mass Transfer **25** (1982) 945, ISSN: 0017-9310,
URL: `http://www.sciencedirect.com/science/article/pii/0017931082900709`
(cit. on pp. 1, 52, 140, 141, 146, 148, 152–154, 192).

[6] S. G. Kandlikar, *History, Advances, and Challenges in Liquid Flow and Flow Boiling Heat Transfer in Microchannels: A Critical Review*, Journal of Heat Transfer **134** (2012),
ISSN: 0022-1481, URL: `https://doi.org/10.1115/1.4005126` (cit. on pp. 1, 47, 52, 65).

[7] J. R. Thome, *Boiling in microchannels: a review of experiment and theory*,
International Journal of Heat and Fluid Flow **25** (2004) 128, ISSN: 0142-727X,
URL: `http://www.sciencedirect.com/science/article/pii/S0142727X03001371`
(cit. on pp. 1, 51).

[8] P. Tropea et al.,
CO_2 evaporative cooling: The future for tracking detector thermal management,
824 (2016) 473, ISSN: 0168-9002,
URL: `http://www.sciencedirect.com/science/article/pii/S0168900215010165`
(cit. on pp. 2, 29).

[9] E. Hihara and C. Dang, *Boiling Heat Transfer of Carbon Dioxide in Horizontal Tubes*, vol. ASME/JSME 2007 Thermal Engineering Heat Transfer Summer Conference, Volume 3, Heat Transfer Summer Conference, 2007, URL: `https://doi.org/10.1115/HT2007-32885` (cit. on pp. 2, 59, 60, 62, 63, 122).

[10] L. Cheng and G. Xia, “Flow Boiling Heat Transfer and Two-Phase Flow of Carbon Dioxide: Fundamentals, Mechanistic Models and Applications”, *Proceedings of the 4th World Congress on Momentum, Heat and Mass Transfer*, 2019 (cit. on pp. 2, 57, 58).

[11] P. Petagna, B. Verlaat and A. Francescon, “Encyclopedia of Two-Phase Heat Transfer and Flow III”, ed. by J. R. Thome, World Scientific, 2018 335 (cit. on pp. 2, 9, 20, 25, 26, 107, 159).

[12] P. Vankov, *ATLAS Upgrade for the HL-LHC: meeting the challenges of a five-fold increase in collision rate*, tech. rep. ATL-UPGRADE-PROC-2012-003. ATL-UPGRADE-PROC-2012-003, Comments: Presented at the 2011 Hadron Collider Physics symposium (HCP-2011), Paris, France, November 14-18 2011, 3 pages, 3 figures: CERN, 2012, URL: `https://cds.cern.ch/record/1419213` (cit. on p. 4).

[13] G. Aad et al., *ATLAS pixel detector electronics and sensors*, Journal of Instrumentation **3** (2008) P07007, URL: `https://doi.org/10.1088%2F1748-0221%2F3%2F07%2Fp07007` (cit. on pp. 5, 13).

[14] T. Wittig, *Slim edge studies design and quality control of planar ATLAS IBL pixel sensors*, PhD thesis: University of Dortmund, 2013 (cit. on p. 11).

[15] G. Lutz, *Semiconductor Radiation Detectors*, Springer, 1999 (cit. on p. 12).

[16] A. Collaboration, *The ATLAS experiment at CERN*, 2020, URL: `https://atlas.cern/discover` (cit. on pp. 13, 14).

[17] M. Backhaus, *The upgraded Pixel Detector of the ATLAS Experiment for Run 2 at the Large Hadron Collider*, Nuclear Instruments and Methods in Physics Research Section A: Accelerators, Spectrometers, Detectors and Associated Equipment **831** (2016) 65, Proceedings of the 10th International “Hiroshima” Symposium on the Development and Application of Semiconductor Tracking Detectors, ISSN: 0168-9002, URL: `http://www.sciencedirect.com/science/article/pii/S0168900216303837` (cit. on p. 13).

[18] M. Garcia-Sciveres et al., *The FE-I4 pixel readout integrated circuit*, Nuclear Instruments and Methods in Physics Research Section A: Accelerators, Spectrometers, Detectors and Associated Equipment **636** (2011) S155, 7th International Hiroshima Symposium on the Development and Application of Semiconductor Tracking Detectors, ISSN: 0168-9002, URL: `http://www.sciencedirect.com/science/article/pii/S0168900210009551` (cit. on pp. 13, 99).

[19] M. Backhaus, *High bandwidth pixel detector modules for the ATLAS Insertable B-Layer*, PhD thesis: University of Bonn, 2014 (cit. on p. 13).

[20] C. Leroy and P.-G. Rancoita, *Silicon Solid State Devices and Radiation Detection*, World Scientific, 2012, URL: `https://www.worldscientific.com/doi/abs/10.1142/8383` (cit. on p. 14).

[21] J. Grosse-Knetter, *Vertex measurement at a hadron collider. The ATLAS pixel detector*, (BONN-IR–2008-04), PhD thesis: University of Bonn, 2008 (cit. on pp. 14, 16).

[22] R. Wunstorf, *Systematische Untersuchungen zur Strahlenresistenz von Silizium-Detektoren für die Verwendung in Hochenergiephysik-Experimenten*, PhD thesis: University of Hamburg, 1992, URL: `https://cds.cern.ch/record/243081` (cit. on p. 16).

[23] M. Moll, *Radiation Damage in Silicon Particle Detectors microscopic defects and macroscopic properties*, PhD thesis: University of Hamburg, 1999 (cit. on pp. 17, 18).

[24] O. Krasel, *Charge collection in irradiated sensors*, PhD thesis: University of Dortmund, 2004 (cit. on p. 17).

[25] T. Ma and P. Dressendorfer, "Ionizing radiation effects in MOS devices and circuits", 1989 (cit. on p. 17).

[26] G. R. Lynch and O. I. Dahl, *Approximations to multiple Coulomb scattering*, Nuclear Instruments and Methods in Physics Research Section B: Beam Interactions with Materials and Atoms **58** (1991) 6, ISSN: 0168-583X, URL: `http://www.sciencedirect.com/science/article/pii/0168583X9195671Y` (cit. on p. 18).

[27] V. L. Highland, *Some Practical Remarks on Multiple Scattering*, Nucl. Instrum. Meth. **129** (1975) 497 (cit. on p. 18).

[28] C. Amsler et al., *Review of Particle Physics*, Physics Letters B **667** (2008) 1, Review of Particle Physics, ISSN: 0370-2693, URL: `http://www.sciencedirect.com/science/article/pii/S0370269308008435` (cit. on p. 18).

[29] A. Mapelli, P. Petagna and P. Renaud, "Micro-channel cooling for high-energy physics particle detectors and electronics", *13th InterSociety Conference on Thermal and Thermomechanical Phenomena in Electronic Systems*, 2012 677 (cit. on pp. 18, 25, 27, 159).

[30] T. A. Collaboration, *The ATLAS Experiment at the CERN Large Hadron Collider*, Journal of Instrumentation **3** (2008) S08003, URL: `https://doi.org/10.1088%5C%2F1748-0221%5C%2F3%5C%2F08%5C%2Fs08003` (cit. on pp. 18, 19).

[31] M. Olcese, *Mechanics and cooling of pixel detectors*, Nuclear Instruments and Methods in Physics Research Section A: Accelerators, Spectrometers, Detectors and Associated Equipment **465** (2001) 51, SPD2000, ISSN: 0168-9002, URL: `http://www.sciencedirect.com/science/article/pii/S0168900201003461` (cit. on p. 19).

[32] M. Moll, *Radiation tolerant semiconductor sensors for tracking detectors*, Nuclear Instruments and Methods in Physics Research Section A: Accelerators, Spectrometers, Detectors and Associated Equipment **565** (2006) 202 (cit. on p. 20).

[33] P. Petagna, “Past Experiences and Future Trends on Vertex Detector Cooling at LHC”, 2014 037 (cit. on pp. 21, 25, 26).

[34] G. Viehhauser, *Thermal management and mechanical structures for silicon detector systems*, Journal of Instrumentation **10** (2015) P09001, URL: `https://doi.org/10.1088%5C%2F1748-0221%5C%2F10%5C%2F09%5C%2Fp09001` (cit. on p. 23).

[35] G. Contin et al., *The STAR MAPS-based PiXeL detector*, Nuclear Instruments and Methods in Physics Research Section A: Accelerators, Spectrometers, Detectors and Associated Equipment **907** (2018) 60, Advances in Instrumentation and Experimental Methods (Special Issue in Honour of Kai Siegbahn), ISSN: 0168-9002, URL: `http://www.sciencedirect.com/science/article/pii/S0168900218303206` (cit. on p. 24).

[36] N. Berger et al., *The ultra-lightweight support structure and gaseous helium cooling for the Mu3e silicon pixel tracker*, Journal of Instrumentation **9** (2014) C08023, URL: `https://doi.org/10.1088%5C%2F1748-0221%5C%2F9%5C%2F08%5C%2Fc08023` (cit. on p. 24).

[37] S. Tkaczyk et al., *The CDF silicon vertex detector*, Nuclear Instruments and Methods in Physics Research Section A: Accelerators, Spectrometers, Detectors and Associated Equipment **342** (1994) 240, ISSN: 0168-9002, URL: `http://www.sciencedirect.com/science/article/pii/0168900294914346` (cit. on p. 24).

[38] A. Oyanguren, *Air cooling for Vertex Detectors*, International Workshop on Future Linear Colliders, LCWS 2011 (2012) (cit. on p. 24).

[39] A. Francescon et al., *Application of micro-channel cooling to the local thermal management of detectors electronics for particle physics*, Microelectronics Journal **44** (2013) 612 (cit. on p. 25).

[40] ATLAS Collaboration, *Letter of Intent for the Phase-II Upgrade of the ATLAS Experiment*, (2012) (cit. on p. 25).

[41] D. Contardo et al., *Technical Proposal for the Phase-II Upgrade of the CMS Detector*, (2015) (cit. on p. 25).

[42] A. Mapelli et al., “Low Mass Integrated Cooling”, *22nd International Workshop on Vertex Detectors, 16 - 20 Sep 2013, pp. 046*, 2014 (cit. on pp. 26, 27).

[43] G. Romagnoli et al., *Silicon micro-fluidic cooling for NA62 GTK pixel detectors*, Microelectronic Engineering **145** (2015) 133, Micro/Nano Devices and Systems 2014 An open focused special thematic issue of Microelectronic Engineering, ISSN: 0167-9317, URL: `http://www.sciencedirect.com/science/article/pii/S0167931715002099` (cit. on p. 27).

[44] O. de Aguiar Francisco et al.,
Evaporative CO_2 microchannel cooling for the LHCb VELO pixel upgrade,
Journal of Instrumentation **10** (2015) C05014,
URL: `https://doi.org/10.1088%5C%2F1748-0221%5C%2F10%5C%2F05%5C%2Fc05014`
(cit. on pp. 27, 28, 41, 158).

[45] A. Francescon et al., *Development of interconnected silicon micro-evaporators for the on-detector electronics cooling of the future ITS detector in the ALICE experiment at LHC*, Applied Thermal Engineering **93** (2015) (cit. on p. 27).

[46] G. Fiorenza et al., "An innovative polyimide microchannels cooling system for the pixel sensor of the upgraded ALICE inner tracker",
5th IEEE International Workshop on Advances in Sensors and Interfaces IWASI, 2013 81
(cit. on pp. 27, 28).

[47] A. Günther and K. F. Jensen,
Multiphase microfluidics: from flow characteristics to chemical and materials synthesis,
Lab Chip **6** (12 2006) 1487, URL: `http://dx.doi.org/10.1039/B609851G`
(cit. on pp. 31, 49).

[48] R. J. D. S. Lima and J. R. Thome, "Flow Pattern-Based Boiling Heat Transfer and Frictional Pressure Drop Models for Plain Horizontal Tubes",
Encyclopedia of Two-Phase Heat Transfer and Flow II, chap. 9 355,
URL: `https://www.worldscientific.com/doi/abs/10.1142/9789814623285_0016`
(cit. on p. 32).

[49] Y. Taitel and D. Barnea, "Basic Definitions of Two-Phase Flow Parameters",
Encyclopedia of Two-Phase Heat Transfer and Flow I, chap. 2 9,
URL: `https://www.worldscientific.com/doi/abs/10.1142/9789814623216_0002`
(cit. on pp. 32, 33).

[50] S.M. Zivi, *Estimation of Steady State Steam Void Fraction by Means of the Principle of Minimum Energy Production*, Journal of Heat Transfer (1964) 247 (cit. on pp. 33, 111).

[51] J. G. Collier and J. R. Thome, *Convective boiling and condensation - Third edition*,
(1994) 596 p. : ill., 24 cm, URL: `http://infoscience.epfl.ch/record/26316`
(cit. on p. 34).

[52] S.-M. Kim and I. Mudawar, *Review of databases and predictive methods for heat transfer in condensing and boiling mini/micro-channel flows*,
International Journal of Heat and Mass Transfer **77** (2014) 627, ISSN: 0017-9310,
URL: `http://www.sciencedirect.com/science/article/pii/S0017931014004360`
(cit. on pp. 34, 35, 50–52).

[53] S. G. Kandlikar, *Development of a Flow Boiling Map for Subcooled and Saturated Flow Boiling of Different Fluids Inside Circular Tubes*, Journal of Heat Transfer **113** (1991) 190,
ISSN: 0022-1481, URL: `https://doi.org/10.1115/1.2910524`
(cit. on pp. 37, 141, 152–154, 190).

[54] J. C. Chen, *Correlation for Boiling Heat Transfer to Saturated Fluids in Convective Flow*, Industrial & Engineering Chemistry Process Design and Development **5** (1966) 322, URL: `https://doi.org/10.1021/i260019a023` (cit. on pp. 37, 141, 148–150, 153, 154, 190).

[55] M. Shah, *Chart correlation for saturated boiling heat transfer: Equations and further study*, ASHRAE Transactions **88** (1982) 185 (cit. on pp. 37, 141, 152–154, 190).

[56] D. Steiner and J. Taborek, *Flow Boiling Heat Transfer in Vertical Tubes Correlated by an Asymptotic Model*, Heat Transfer Engineering **13** (1992) 43, URL: `https://doi.org/10.1080/01457639208939774` (cit. on pp. 37, 141, 150, 190).

[57] K. Gungor and R. Winterton, *A general correlation for flow boiling in tubes and annuli*, International Journal of Heat and Mass Transfer **29** (1986) 351, ISSN: 0017-9310, URL: `http://www.sciencedirect.com/science/article/pii/001793108690205X` (cit. on pp. 38, 141, 150, 152, 153, 191).

[58] Z. Liu and R. Winterton, *A general correlation for saturated and subcooled flow boiling in tubes and annuli, based on a nucleate pool boiling equation*, International Journal of Heat and Mass Transfer **34** (1991) 2759, ISSN: 0017-9310, URL: `http://www.sciencedirect.com/science/article/pii/0017931091902346` (cit. on pp. 38, 141, 152–154, 191).

[59] M. Cooper, "Heat Flow Rates in Saturated Nucleate Pool Boiling-A Wide-Ranging Examination Using Reduced Properties", ed. by J. P. Hartnett and T. F. Irvine, vol. 16, Advances in Heat Transfer, Elsevier, 1984 157, URL: `http://www.sciencedirect.com/science/article/pii/S0065271708702053` (cit. on pp. 38, 64, 141, 146, 148, 152–154, 191).

[60] J. Wattelet et al., *Evaporative characteristics of R-12, R-134a, and a mixture at low mass fluxes*, ASHRAE Transactions **94-2-1** (1994) 603 (cit. on pp. 38, 141, 152, 153, 191).

[61] J. R. Thome and A. Cioncolini, "Chapter Four - Flow Boiling in Microchannels", ed. by E. M. Sparrow, J. P. Abraham and J. M. Gorman, vol. 49, Advances in Heat Transfer, Elsevier, 2017 157, URL: `http://www.sciencedirect.com/science/article/pii/S0065271717300011` (cit. on pp. 38, 48, 50, 51, 65).

[62] H. Blasius, *Das Ähnlichkeitsgesetz bei Reibungsvorgängen in Flüssigkeiten*, Forschg. Arb. Ing.-Wes **134** (1913) (cit. on pp. 39, 97, 98).

[63] W. H. McAdams, W. K. Woods and R. L. Bryan, *Vaporization inside horizontal tubes – II – benzene–oil mixtures*, ASME Transactions **64** (1942) (cit. on pp. 40, 129, 197).

[64] D. R. H. Beattie and P. B. Whalley, *A simple two-phase frictional pressure drop calculation method*, International Journal of Multiphase Flow **8** (1982) 83, ISSN: 0301-9322, URL: `http://www.sciencedirect.com/science/article/pii/030193228290009X` (cit. on pp. 40, 129, 197).

[65] A. Cicchitti et al.,
Two-phase cooling experiments – pressure drop, heat transfer and burnout measurement,
Energia Nuclear **7** (1960) 407 (cit. on pp. 40, 129, 197).

[66] A. E. Dukler, M. Wicks and R. G. Cleveland,
Pressure drop and hold-up in two-phase flow part A – a comparison of existing correlations and part B – an approach through similarity analysis, AIChE Journal **10** (1964) 38
(cit. on pp. 40, 55, 129).

[67] W. W. Akers, H. A. Deans and O. K. Crosser,
Condensation heat transfer within horizontal tubes,
Chemical engineering progress symposium series **55** (1959) 171 (cit. on pp. 40, 129, 197).

[68] S. Lin et al.,
Local frictional pressure drop during vaporization of R-12 through capillary tubes,
International Journal of Multiphase Flow **17** (1991) 95, ISSN: 0301-9322,
URL: `http://www.sciencedirect.com/science/article/pii/030193229190072B`
(cit. on pp. 40, 129, 197).

[69] D. Steiner, "Heat Transfer to Boiling Saturated Liquids", VDI Verlag, 1993 (cit. on p. 40).

[70] R. W. Lockhart and R. C. Martinelli,
Proposed correlation of data for isothermal two-phase, two-component flow in pipes,
Chemical Engineering Progress **45** (1949) 39 (cit. on pp. 40, 57, 129, 198).

[71] D. Chisholm, *A theoretical basis for the Lockhart-Martinelli correlation for two-phase flow*,
International Journal of Heat and Mass Transfer **10** (1967) 1767, ISSN: 0017-9310,
URL: `http://www.sciencedirect.com/science/article/pii/0017931067900476`
(cit. on pp. 40, 57, 129, 138, 198).

[72] D. Chisholm, *Pressure gradients due to friction during the flow of evaporating two-phase mixtures in smooth tubes and channels*,
International Journal of Heat and Mass Transfer **16** (1973) 347, ISSN: 0017-9310,
URL: `http://www.sciencedirect.com/science/article/pii/001793107390063X`
(cit. on pp. 40, 57, 129, 137, 138, 199).

[73] H. Müller-Steinhagen and K. Heck,
A simple friction pressure drop correlation for two-phase flow in pipes,
Chemical Engineering and Processing: Process Intensification **20** (1986) 297,
ISSN: 0255-2701,
URL: `http://www.sciencedirect.com/science/article/pii/0255270186800083`
(cit. on pp. 40, 57, 58, 129, 131, 135–139, 200).

[74] L. Friedel, "Improved Friction Pressure Drop Correlations for Horizontal and Vertical Two-Phase Pipe flow", *European Two-Phase Flow Group Meeting*, 1979
(cit. on pp. 40, 57, 58, 96, 129, 131, 134, 136–139, 200).

[75] R. Grönnerud, *Investigation of liquid hold-up, flow resistance and heat transfer in circulation type of evaporators. Part IV: two-phase flow resistance in boiling refrigerants*,
Bulletin de l'Institut International du Froid **Annexe 1972-1** (1979)
(cit. on pp. 41, 57, 129, 136–139, 200).

[76] B. Verlaat, M. van Beuzekom and A. Lysebetten, *CO_2 cooling for HEP experiments*, (2008) (cit. on pp. 41, 78).

[77] D. Attree et al., *The evaporative cooling system for the ATLAS inner detector*, Journal of Instrumentation **3** (2008) P07003, URL: `https://doi.org/10.1088%5C%2F1748-0221%5C%2F3%5C%2F07%5C%2Fp07003` (cit. on p. 41).

[78] M. Oriunno et al., *Design and prototype studies of the TOTEM Roman pot detectors*, Nuclear Instruments and Methods in Physics Research Section A: Accelerators, Spectrometers, Detectors and Associated Equipment **581** (2007) 499, VCI 2007, ISSN: 0168-9002, URL: `http://www.sciencedirect.com/science/article/pii/S0168900207017044` (cit. on p. 41).

[79] A. Francescon et al., *Performance of the ALICE SPD cooling system*, Journal of Physics: Conference Series **395** (2012) 012063, URL: `https://doi.org/10.1088%5C%2F1742-6596%5C%2F395%5C%2F1%5C%2F012063` (cit. on p. 41).

[80] A. Delil, A. Woering and B. Verlaat, *Development of a Mechanically Pumped Two-Phase CO_2 Cooling Loop for the AMS-2 Tracker Experiment*, SAE Technical Papers (2002) (cit. on p. 41).

[81] J. Daguin et al., "Evaporative CO_2 cooling system for the upgrade of the CMS pixel detector at CERN", *13th InterSociety Conference on Thermal and Thermomechanical Phenomena in Electronic Systems*, 2012 723 (cit. on p. 41).

[82] K. Abe et al., *Design and performance of the SLD vertex detector: a 307 Mpixel tracking system*, Nuclear Instruments and Methods in Physics Research Section A: Accelerators, Spectrometers, Detectors and Associated Equipment **400** (1997) 287, ISSN: 0168-9002, URL: `http://www.sciencedirect.com/science/article/pii/S0168900297010115` (cit. on p. 41).

[83] S. Kwan, *The BTeV pixel detector*, Nuclear Instruments and Methods in Physics Research Section A: Accelerators, Spectrometers, Detectors and Associated Equipment **549** (2005) 60, VERTEX 2003, ISSN: 0168-9002, URL: `http://www.sciencedirect.com/science/article/pii/S0168900205009666` (cit. on p. 41).

[84] G. Myhre et al., "Anthropogenic and Natural Radiative Forcing", *Climate Change 2013: The Physical Science Basis. Contribution of Working Group I to the Fifth Assessment Report of the Intergovernmental Panel on Climate Change*, ed. by T. Stocker et al., Cambridge University Press, 2013 659, URL: `https://www.ipcc.ch/site/assets/uploads/2018/02/WG1AR5_Chapter08_FINAL.pdf` (cit. on p. 42).

[85] Y. Zhao et al., *Flow boiling of CO_2 in microchannels*, ASHRAE Transactions **106** (2000) 437 (cit. on pp. 43, 44, 53, 55, 58).

[86] R. Yun et al.,
Boiling heat transfer and dryout phenomenon of CO_2 in a horizontal smooth tube,
International Journal of Heat and Mass Transfer **46** (2003) 2353
(cit. on pp. 43, 59–61, 64, 140).

[87] H.-K. Oh et al.,
Flow boiling heat transfer characteristics of carbon dioxide in a horizontal tube,
Applied Thermal Engineering **28** (2008) 1022, ISSN: 1359-4311,
URL: `http://www.sciencedirect.com/science/article/pii/S1359431107002244`
(cit. on pp. 43, 59, 60).

[88] K. Moriyama, A. Inoue and H. Ohira, *The Thermohydraulic Characteristics of Two-Phase Flow in Extremely Narrow Channels : The Frictional Pressure Drop and Heat Transfer of Boiling Two-Phase Flow, Analytical Model*,
Transactions of the Japan Society of Mechanical Engineers Series B **58** (1992) 393
(cit. on p. 47).

[89] P. A. Kew and K. Cornwell,
Correlations for the prediction of boiling heat transfer in small-diameter channels,
Applied Thermal Engineering **17** (1997) 705, ISSN: 1359-4311,
URL: `http://www.sciencedirect.com/science/article/pii/S1359431196000713`
(cit. on pp. 50, 52, 113, 140, 141, 146–148, 151–154, 193).

[90] A. Ullmann and N. Brauner, *The prediction of flow pattern maps in mini channels*,
Multiphase Science and Technology **19** (2007) 49 (cit. on pp. 50, 113).

[91] C. Ong and J. Thome, *Macro-to-microchannel transition in two-phase flow: Part 1 - Two-phase flow patterns and film thickness measurements*,
Experimental Thermal and Fluid Science **35** (2011) 37, ISSN: 0894-1777,
URL: `http://www.sciencedirect.com/science/article/pii/S0894177710001500`
(cit. on pp. 50, 113).

[92] S. Kandlikar and W. Grande, *Evolution of Microchannel Flow Passages–Thermohydraulic Performance and Fabrication Technology*, Heat Transfer Engineering **24** (2003)
(cit. on pp. 50, 53).

[93] K. Mishima and T. Hibiki,
Some characteristics of air-water two-phase flow in small diameter vertical tubes,
International Journal of Multiphase Flow **22** (1996) 703, ISSN: 0301-9322,
URL: `http://www.sciencedirect.com/science/article/pii/0301932296000109`
(cit. on pp. 52, 57, 129, 138, 201).

[94] T. N. Tran et al., *Two-phase pressure drop of refrigerants during flow boiling in small channels: an experimental investigation and correlation development*,
International Journal of Multiphase Flow **26** (2000) 1739, ISSN: 0301-9322,
URL: `http://www.sciencedirect.com/science/article/pii/S0301932299001196`
(cit. on pp. 52, 57, 58, 129, 136, 137, 139, 201).

[95] M. Zhang and R. L. Webb,
Correlation of two-phase friction for refrigerants in small-diameter tubes,
Experimental Thermal and Fluid Science **25** (2001) 131, ISSN: 0894-1777,
URL: `http://www.sciencedirect.com/science/article/pii/S0894177701000668`
(cit. on pp. 52, 57, 58, 129, 136–139, 201).

[96] W. Qu and I. Mudawar,
Measurement and prediction of pressure drop in two-phase micro-channel heat sinks,
International Journal of Heat and Mass Transfer **46** (2003) 2737, ISSN: 0017-9310,
URL: `http://www.sciencedirect.com/science/article/pii/S0017931003000449`
(cit. on pp. 52, 57, 129, 138, 201).

[97] P.-S. Lee and S. V. Garimella,
Saturated flow boiling heat transfer and pressure drop in silicon microchannel arrays,
International Journal of Heat and Mass Transfer **51** (2008) 789, ISSN: 0017-9310,
URL: `http://www.sciencedirect.com/science/article/pii/S0017931007003274`
(cit. on pp. 52, 57, 129, 138, 201).

[98] H. J. Lee and S. Y. Lee, *Heat transfer correlation for boiling flows in small rectangular horizontal channels with low aspect ratios*,
International Journal of Multiphase Flow **27** (2001) 2043, ISSN: 0301-9322,
URL: `http://www.sciencedirect.com/science/article/pii/S0301932201000544`
(cit. on pp. 52, 57, 129, 136–138, 201).

[99] S.-M. Kim and I. Mudawar, *Universal approach to predicting two-phase frictional pressure drop for mini/micro-channel saturated flow boiling*,
International Journal of Heat and Mass Transfer **58** (2013) 718, ISSN: 0017-9310,
URL: `http://www.sciencedirect.com/science/article/pii/S0017931012009088`
(cit. on pp. 52, 57, 129, 135, 137, 138).

[100] G. R. Warrier, V. K. Dhir and L. A. Momoda,
Heat transfer and pressure drop in narrow rectangular channels,
Experimental Thermal and Fluid Science **26** (2002) 53, ISSN: 0894-1777,
URL: `http://www.sciencedirect.com/science/article/pii/S0894177702001073`
(cit. on pp. 52, 141, 152, 192).

[101] T. Tran, M. Wambsganss and D. France,
Small circular- and rectangular-channel boiling with two refrigerants,
International Journal of Multiphase Flow **22** (1996) 485, ISSN: 0301-9322,
URL: `http://www.sciencedirect.com/science/article/pii/030193229600002X`
(cit. on pp. 52, 141, 152, 192).

[102] B. Agostini and A. Bontemps, *Vertical flow boiling of refrigerant R134a in small channels*,
International Journal of Heat and Fluid Flow **26** (2005) 296, ISSN: 0142-727X,
URL: `http://www.sciencedirect.com/science/article/pii/S0142727X04001298`
(cit. on pp. 52, 141, 152, 153, 192).

[103] W. Li and Z. Wu, *A general correlation for evaporative heat transfer in micro/mini-channels*, International Journal of Heat and Mass Transfer **53** (2010) 1778, ISSN: 0017-9310, URL: `http://www.sciencedirect.com/science/article/pii/S001793101000013X` (cit. on pp. 52, 141, 152–154, 192).

[104] S. S. Bertsch, E. A. Groll and S. V. Garimella, *A composite heat transfer correlation for saturated flow boiling in small channels*, International Journal of Heat and Mass Transfer **52** (2009) 2110, ISSN: 0017-9310, URL: `http://www.sciencedirect.com/science/article/pii/S0017931008006315` (cit. on pp. 52, 141, 152–154, 192).

[105] W. Yu et al., *Two-phase pressure drop, boiling heat transfer, and critical heat flux to water in a small-diameter horizontal tube*, International Journal of Multiphase Flow **28** (2002) 927, ISSN: 0301-9322, URL: `http://www.sciencedirect.com/science/article/pii/S0301932202000198` (cit. on pp. 52, 141, 146, 153, 154, 192).

[106] S. Kandlikar and P. Balasubramanian, *An Extension of the Flow Boiling Correlation to Transition, Laminar, and Deep Laminar Flows and Microchannels*, Heat Transfer Engineering - HEAT TRANSFER ENG **25** (2004) 86 (cit. on pp. 52, 141, 153, 154, 193).

[107] H.-K. Oh and C.-H. Son, *Flow boiling heat transfer and pressure drop characteristics of CO_2 in horizontal tube of 4.57-mm inner diameter*, Applied Thermal Engineering **31** (2011) 163, ISSN: 1359-4311, URL: `http://www.sciencedirect.com/science/article/pii/S1359431110003650` (cit. on pp. 53, 141, 193).

[108] S.-M. Kim and I. Mudawar, *Universal approach to predicting saturated flow boiling heat transfer in mini/micro-channels – Part II. Two-phase heat transfer coefficient*, International Journal of Heat and Mass Transfer **64** (2013) 1239, ISSN: 0017-9310, URL: `http://www.sciencedirect.com/science/article/pii/S0017931013003190` (cit. on pp. 53, 141, 152, 193, 202).

[109] L. Cheng et al., *New prediction methods for CO_2 evaporation inside tubes: Part I – A two-phase flow pattern map and a flow pattern based phenomenological model for two-phase flow frictional pressure drops*, International Journal of Heat and Mass Transfer **51** (2008) 111, ISSN: 0017-9310, URL: `http://www.sciencedirect.com/science/article/pii/S0017931007002839` (cit. on pp. 53, 58, 64, 129, 135–140, 147, 148, 151).

[110] L. Cheng, G. Ribatski and J. R. Thome, *New prediction methods for CO_2 evaporation inside tubes: Part II—An updated general flow boiling heat transfer model based on flow patterns*, International Journal of Heat and Mass Transfer **51** (2008) 125, ISSN: 0017-9310, URL: `http://www.sciencedirect.com/science/article/pii/S0017931007002840` (cit. on pp. 53, 64, 140, 141, 147, 148, 151–154).

[111] J. R. Thome and G. Ribatski, *State-of-the-art of two-phase flow and flow boiling heat transfer and pressure drop of CO_2 in macro- and micro-channels*, International Journal of Refrigeration **28** (2005) 1149, CO_2 as Working Fluid - Theory and Applications, ISSN: 0140-7007, URL: `http://www.sciencedirect.com/science/article/pii/S0140700705001672` (cit. on pp. 53, 57, 64, 65).

[112] J. Pettersen, *Flow vaporization of CO_2 in microchannel tubes*, Experimental Thermal and Fluid Science **28** (2004) 111, ISSN: 0894-1777, URL: `http://www.sciencedirect.com/science/article/pii/S0894177703000293` (cit. on pp. 53, 58).

[113] S. Jeong and D. Park, "Evaporating heat transfer and pressure drop of CO_2 in a multi-channel micro-tube", *Proceedings of the International Congress of Refrigeration*, 2007 (cit. on pp. 53, 55).

[114] K.-I. Choi, A. S. Pamitran and J.-T. Oh, *Two-phase flow heat transfer of CO_2 vaporization in smooth horizontal minichannels*, International Journal of Refrigeration **30** (2007) 767, ISSN: 0140-7007, URL: `http://www.sciencedirect.com/science/article/pii/S0140700706002726` (cit. on pp. 53, 59–61, 63, 64, 140, 141, 152, 153, 194).

[115] R. Yun, Y. Kim and M. S. Kim, *Convective boiling heat transfer characteristics of CO_2 in microchannels*, International Journal of Heat and Mass Transfer **48** (2005) 235, ISSN: 0017-9310, URL: `http://www.sciencedirect.com/science/article/pii/S0017931004003849` (cit. on pp. 53, 60, 64, 65, 122, 140, 146).

[116] G. Ribatski, *A Critical Overview on the Recent Literature Concerning Flow Boiling and Two-Phase Flows Inside Micro-Scale Channels*, Experimental Heat Transfer **26** (2013) 198, URL: `https://doi.org/10.1080/08916152.2012.737189` (cit. on p. 53).

[117] E. Hihara and S. Tanaka, "Boiling heat transfer of carbon dioxide in horizontal tubes", *Proceedings of the 4th IIR Gustav Lorentzen Conference on Natural Working Fluids*, 2000 (cit. on pp. 54–56, 59–64, 140, 141, 147–149, 151–154, 194).

[118] R. Yun and Y. Kim, *Two-phase pressure drop of CO_2 in mini tubes and microchannels*, Microscale Thermophysical Engineering **8** (2004) 259 (cit. on pp. 54–58, 129, 136–138, 203).

[119] T. Yamamoto et al., "Flow boiling heat transfer of carbon dioxide at high pressure in horizontal mini-channels", *Proceedings of the 6th International Conference on Multiphase Flow*, 2007 (cit. on pp. 54–57, 59–64, 129, 136–139, 203).

[120] A. S. Pamitran et al., *Two-phase pressure drop during CO_2 vaporization in horizontal smooth minichannels*, International Journal of Refrigeration **31** (2008) 1375, ISSN: 0140-7007, URL: `http://www.sciencedirect.com/science/article/pii/S014070070800073X` (cit. on pp. 54–57, 128, 195).

[121] M. Ducoulombier et al.,
Carbon dioxide flow boiling in a single microchannel – Part I: Pressure drops,
Experimental Thermal and fluid Science **35** (2011) 581, ISSN: 0894-1777,
URL: `http://www.sciencedirect.com/science/article/pii/S0894177710002487`
(cit. on pp. 54–58, 128, 129, 131, 134–139, 197, 203).

[122] J. Wu et al., *Investigation of heat transfer and pressure drop of CO_2 two-phase flow in a horizontal minichannel*, International Journal of Heat and Mass Transfer **54** (2011) 2154,
ISSN: 0017-9310,
URL: `http://www.sciencedirect.com/science/article/pii/S0017931010006897`
(cit. on pp. 54–56, 58–64).

[123] *Evaporative Heat Transfer and Pressure Drop of CO_2 in a Microchannel Tube*,
vol. ASME 3rd International Conference on Microchannels and Minichannels, Part B,
International Conference on Nanochannels, Microchannels, and Minichannels, 2005 103,
eprint: `https://asmedigitalcollection.asme.org/ICNMM/proceedings-pdf/ICMM2005/41855b/103/2624557/103\_1.pdf`,
URL: `https://doi.org/10.1115/ICMM2005-75180` (cit. on p. 55).

[124] Y. Zhao, M. Molki and M. Ohadi,
Heat transfer and pressure drop of CO_2 flow boiling in microchannels, American Society of Mechanical Engineers, Heat Transfer Division, (Publication) HTD **366** (2000) 243
(cit. on p. 58).

[125] R. Yun and Y. Kim, “Two-phase pressure drop of CO_2 in mini tubes and microchannels”,
Proceedings of the first International Conference on Microchannels and Minichannels, 2003
507 (cit. on p. 58).

[126] S. H. Yoon et al., *Characteristics of evaporative heat transfer and pressure drop of carbon dioxide and correlation development*, International Journal of Refrigeration **27** (2004) 111,
ISSN: 0140-7007,
URL: `http://www.sciencedirect.com/science/article/pii/S0140700703001324`
(cit. on pp. 59, 64, 141, 195).

[127] A. Bredesen et al., “Heat transfer and pressure drop for in-tube evaporation of CO_2”,
Proceedings of the International Conference on Heat Transfer Issues in Natural Refrigerants,
1997 (cit. on pp. 59, 61).

[128] C. Y. Park and P. S. Hrnjak,
Flow Boiling Heat Transfer of CO_2 at Low Temperatures in a Horizontal Smooth Tube,
Journal of Heat Transfer **127** (2005) 1305, ISSN: 0022-1481,
eprint: `https://asmedigitalcollection.asme.org/heattransfer/article-pdf/127/12/1305/5720017/1305\_1.pdf`,
URL: `https://doi.org/10.1115/1.2098853` (cit. on pp. 59–61).

[129] R. Mastrullo et al., *Carbon dioxide local heat transfer coefficients during flow boiling in a horizontal circular smooth tube*,
International Journal of Heat and Mass Transfer **52** (2009) 4184, ISSN: 0017-9310,
URL: `http://www.sciencedirect.com/science/article/pii/S0017931009002622`
(cit. on pp. 59, 60, 64).

[130] A. Pamitran et al., *Evaporation heat transfer coefficient in single circular small tubes for flow natural refrigerants of C3H8, NH3, and CO*$_2$, International Journal of Multiphase Flow **37** (2011) 794, ISSN: 0301-9322, URL: `http://www.sciencedirect.com/science/article/pii/S0301932211000504` (cit. on pp. 59–61, 63, 64, 141, 150, 153, 154).

[131] K.-I. Choi et al., *Boiling heat transfer of R-22, R-134a, and CO*$_2$ *in horizontal smooth minichannels*, International Journal of Refrigeration **30** (2007) 1336, ISSN: 0140-7007, URL: `http://www.sciencedirect.com/science/article/pii/S014070070700076X` (cit. on p. 59).

[132] J.-T. Oh et al., *Experimental investigation on two-phase flow boiling heat transfer of five refrigerants in horizontal small tubes of 0.5, 1.5 and 3.0mm inner diameters*, International Journal of Heat and Mass Transfer **54** (2011) 2080, ISSN: 0017-9310, URL: `http://www.sciencedirect.com/science/article/pii/S0017931010007131` (cit. on pp. 59, 64, 141, 152, 153, 195).

[133] R. Yun, Y. Kim and M. [Kim], *Flow boiling heat transfer of carbon dioxide in horizontal mini tubes*, International Journal of Heat and Fluid Flow **26** (2005) 801, ISSN: 0142-727X, URL: `http://www.sciencedirect.com/science/article/pii/S0142727X05000160` (cit. on pp. 59, 62–64, 141, 151–154, 194).

[134] M. Ozawa et al., *Flow pattern and boiling heat transfer of CO*$_2$ *in horizontal small-bore tubes*, International Journal of Multiphase Flow **35** (2009) 699, ISSN: 0301-9322, URL: `http://www.sciencedirect.com/science/article/pii/S030193220900072X` (cit. on pp. 59–63, 114).

[135] M. Ducoulombier et al., *Carbon dioxide flow boiling in a single microchannel – Part II: Heat transfer*, Experimental Thermal and Fluid Science **35** (2011) 597, ISSN: 0894-1777, URL: `http://www.sciencedirect.com/science/article/pii/S0894177710002281` (cit. on pp. 59–65, 116, 140, 141, 146–149, 151, 153, 154, 194).

[136] G. Wang, P. Cheng and H. Wu, *Unstable and stable flow boiling in parallel microchannels and in a single microchannel*, International Journal of Heat and Mass Transfer **50** (2007) 4297, ISSN: 0017-9310, URL: `http://www.sciencedirect.com/science/article/pii/S0017931007001196` (cit. on pp. 64, 125, 141, 150, 154, 194).

[137] X. Huai et al., *An experimental study of flow boiling characteristics of carbon dioxide in multiport mini channels*, Applied Thermal Engineering **24** (2004) 1443, ISSN: 1359-4311, URL: `http://www.sciencedirect.com/science/article/pii/S135943110300365X` (cit. on p. 65).

[138] J. Pettersen, *Two-Phase flow Patterns in Microchannel Vaporization of CO*$_2$ *at Near-Critical Pressure*, Heat Transfer Engineering **25** (2004) 52 (cit. on pp. 65, 111).

[139] L. Tadrist, *Review on two-phase flow instabilities in narrow spaces*, International Journal of Heat and Fluid Flow **28** (2007) 54 (cit. on pp. 70, 125).

[140] B. Munneke, K. de Roo and H. Band, *CO_2 cooling blow system*, tech. rep., CERN, 2008, URL: `https://espace.cern.ch/CO2/Public$%5C%$20Documents/Presentations$%5C%$20and$%5C%$20Publications/NIKHEF/080806_CO2coolingBlowsystem.pdf` (cit. on pp. 72, 73, 76).

[141] B. Verlaat, “TRACI, a multi-purpose CO_2 cooling system for R&D”, *Proceedings of the 10th IIR Gustav Lorentzen Conference on Natural Refrigerants*, 2012 (cit. on p. 77).

[142] B. Verlaat, “Controlling a two-phase CO_2 Loop using a two-phase Accumulator”, *Proceedings of the International Conference of Refrigeration*, 2007 (cit. on p. 77).

[143] F. Dittus and L. Boelter, *Heat transfer in automobile radiators of the tubular type*, International Communications in Heat and Mass Transfer **12** (1985) 3, ISSN: 0735-1933, URL: `http://www.sciencedirect.com/science/article/pii/073519338590003X` (cit. on pp. 97, 98).

[144] V. Gnielinski, *New equations for heat and mass transfer in turbulent pipe and channel flow*, International Chemical Engineering **2** (1976) 359 (cit. on pp. 97, 98).

[145] R. Charnay, *Experimental study of flow boiling in horizontal mini-channels at high saturation temperature*, PhD thesis: INSA de Lyon, 2015 (cit. on pp. 103, 111).

[146] T. Harirchian and S. V. Garimella, *A comprehensive flow regime map for microchannel flow boiling with quantitative transition criteria*, International Journal of Heat and Mass Transfer **53** (2010) 2694, ISSN: 0017-9310, URL: `http://www.sciencedirect.com/science/article/pii/S0017931010001158` (cit. on pp. 113, 114).

[147] J. Thome and A. Cioncolini, “Two-Phase Flow Pattern Maps for Microchannels”, *Encyclopedia of Two-Phase Heat Transfer and Flow I*, ed. by J. R. Thome, World Scientific, 2015 47 (cit. on p. 113).

[148] S. Jain, P. Jayaramu and S. Gedupudi, *Modeling of pressure drop and heat transfer for flow boiling in a mini/micro-channel of rectangular cross-section*, International Journal of Heat and Mass Transfer **140** (2019) 1029, ISSN: 0017-9310, URL: `http://www.sciencedirect.com/science/article/pii/S0017931019304880` (cit. on p. 114).

[149] D. Hellenschmidt et al., *New insights on boiling carbon dioxide flow in mini- and micro-channels for optimal silicon detector cooling*, (2019) 162535, ISSN: 0168-9002, URL: `http://www.sciencedirect.com/science/article/pii/S0168900219310654` (cit. on p. 116).

[150] J. Boure, A. Bergles and L. Tong, *Review of two-phase flow instability*, Nuclear Engineering and Design **25** (1973) 165, ISSN: 0029-5493, URL: `http://www.sciencedirect.com/science/article/pii/0029549373900435` (cit. on p. 125).

[151] D. Brutin and L. Tadrist, *Pressure drop and heat transfer analysis of flow boiling in a minichannel: influence of the inlet condition on two-phase flow stability*, International Journal of Heat and Mass Transfer **47** (2004) 2365, ISSN: 0017-9310, URL: `http://www.sciencedirect.com/science/article/pii/S0017931003006331` (cit. on p. 125).

[152] J. Barber et al., *Bubble confinement in flow boiling of FC-72 in a rectangular microchannel of high aspect ratio*, Experimental Thermal and Fluid Science **34** (2010) 1375, ISSN: 0894-1777, URL: `http://www.sciencedirect.com/science/article/pii/S0894177710001238` (cit. on p. 125).

[153] L. Yin and L. Jia, *Confined bubble growth and heat transfer characteristics during flow boiling in microchannel*, International Journal of Heat and Mass Transfer **98** (2016) 114, ISSN: 0017-9310, URL: `http://www.sciencedirect.com/science/article/pii/S0017931015311571` (cit. on pp. 125–127).

[154] R. Charnay, R. Revellin and J. Bonjour, *Discussion on the validity of prediction tools for two-phase flow pressure drops from experimental data obtained at high saturation temperatures*, International Journal of Refrigeration **54** (2015) 98, ISSN: 0140-7007, URL: `http://www.sciencedirect.com/science/article/pii/S0140700715000468` (cit. on p. 131).

[155] P.B. Whalley, *Multiphase flow and pressure drop. Heat Exchanger Design Handbook*, vol. 2, Hemisphere, 1980 (cit. on pp. 131, 134).

[156] X. Fang, Q. Wu and Y. Yuan, *A general correlation for saturated flow boiling heat transfer in channels of various sizes and flow directions*, International Journal of Heat and Mass Transfer **107** (2017) 972, ISSN: 0017-9310, URL: `http://www.sciencedirect.com/science/article/pii/S0017931016313953` (cit. on pp. 141, 147, 150–154, 196).

[157] K. Cornwell and P. A. Kew, “Boiling in Small Parallel Channels”, *Energy Efficiency in Process Technology*, ed. by P. A. Pilavachi, Springer Netherlands, 1993 624, ISBN: 978-94-011-1454-7, URL: `https://doi.org/10.1007/978-94-011-1454-7_56` (cit. on pp. 146, 148–150).

[158] V. E. Schrock and L. M. Grossman, *Forced Convection Boiling in Tubes*, Nuclear Science and Engineering **12** (1962) 474, URL: `https://doi.org/10.13182/NSE62-A26094` (cit. on p. 148).

[159] A. Mapelli, P. Petagna and M. Vos, *Micro-channel cooling for collider experiments: review and recommandations*, tech. rep. AIDA-2020-NOTE-2020-003, CERN, 2020, URL: `http://cds.cern.ch/record/2712079` (cit. on pp. 158, 159, 166).

[160] A. E. I. for Detectors at Accelerators, *WP9: New support structures and micro-channel cooling*, 2020, URL: `http://aida2020.web.cern.ch/activities/wp9-new-support-structures-and-micro-channel-cooling` (cit. on p. 158).

[161] W. Poonsawat, *Material Budget Calculation of the new Inner Tracking System, ALICE*, 2017, URL: `https://cds.cern.ch/record/2274214/plots?ln=de` (cit. on p. 159).

[162] S. W. Churchill, *Friction-factor equation spans all fluid-flow regimes*, Chemical Engineering Journal **7** (1977) 91 (cit. on p. 197).

[163] J. Tavener, “Temperature Calibration; Depths of Immersion”, *Proceedings of the Test and Measurement Conference 2006*, 2006 (cit. on pp. 214, 215).

[164] J. Taylor, *An Introduction to Error Analysis – the study of uncertainties in physical measurements*, University Science Books, 1982 (cit. on p. 217).

[165] D. Hellenschmidt, *Station for tests on micro-channel test devices*, tech. rep., CERN, 2017 (cit. on p. 218).

[166] H. Preston-Thomas, *The International Temperature Scale of 1990 (ITS-90)*, Metrologia **27** (1990) 3, URL: `https://doi.org/10.1088%2F0026-1394%2F27%2F1%2F002` (cit. on p. 218).

[167] M. Industries, *Efficient Thermocouple Calibration and Measurement*, 2020, URL: `http://www.mosaic-industries.com/embedded-systems/microcontroller-projects/temperature-measurement/thermocouple/calibration-table` (cit. on p. 223).

[168] R. J. Moffat, *Describing the uncertainties in experimental results*, Experimental Thermal and Fluid Science **1** (1988) 3, ISSN: 0894-1777, URL: `http://www.sciencedirect.com/science/article/pii/089417778890043X` (cit. on p. 227).

[169] J. Kline and F. A. McClintock, *Describing uncertainties in single-sample experiments*, Mechanical Engineering **75** (1953) 3 (cit. on p. 227).

Appendix

APPENDIX A

Correlations for the prediction of the two-phase heat transfer coefficient

For further reference the single-phase heat transfer coefficient for the liquid phase flowing alone is

$$\alpha_l = 0.023 \cdot Re_l^{0.8} \cdot Pr_l^{0.4} \cdot \frac{k_l}{D_h}, \tag{A.1}$$

whilst the single phase heat transfer coefficient for the liquid at the total mass flow rate can be written as

$$\alpha_{lo} = 0.023 \cdot Re_{lo}^{0.8} \cdot Pr_l^{0.4} \cdot \frac{k_l}{D_h}. \tag{A.2}$$

with

$$Re_l = \frac{G(1-x)D_h}{\mu_l} \tag{A.3}$$

and

$$Re_{lo} = \frac{G\,D_h}{\mu}. \tag{A.4}$$

X_{tt} is the Lockhart–Martinelli variable defined here for the case that both phases are in the turbulent regime (tt), if not otherwise denoted:

$$X_{tt} = \left(\frac{\mu_l}{\mu_v}\right)^{0.1} \left(\frac{1-x}{x}\right)^{0.9} \left(\frac{\rho_v}{\rho_l}\right)^{0.5} \tag{A.5}$$

A.1 Macro-channel correlations

Chen	$\alpha_C = F \cdot \alpha_l + S \cdot \alpha_{tp}$	
[54]		$S = 1/(1 + 2.53 \cdot 10^{-6} \cdot Re_l^{1.17})$
	$\frac{1}{X_{tt}} > 0.1$	$F = 2.35 \cdot (\frac{1}{X_{tt}} + 0.213)^{0.736}$
	$\frac{1}{X_{tt}} < 0.1$	$F = 1$
		$\alpha_{tp} = 0.00122 \cdot \frac{k_l^{0.79} \cdot cp_l^{0.45} \cdot \rho_l^{0.49} \cdot g^{0.25}}{\sigma^{0.5} \cdot \mu_l^{0.29} \cdot (h_{lv})^{0.24} \cdot \rho_v^{0.24}} \Delta T_{sat}^{0.24} \Delta P_{sat}^{0.75}$
Shah	$\alpha_S = max(E, S) \cdot \alpha_l$	
[55]		$Co = ((1-x)/x)^{0.8} \cdot (\rho_v/\rho_l)^{0.5}$
		$S = 1.8/(NN^{0.8})$
	$Fr_l \geq 0.04$	$NN = Co$
	$Fr_l < 0.04$	$NN = 0.38 \cdot Fr_l^{-0.3} \cdot Co$
	$Bo \geq 11 \cdot 10^{-4}$	$F = 14.7$
	$Bo < 11 \cdot 10^{-4}$	$F = 15.43$
	$NN \leq 0.1$	$E = F \cdot Bo^{0.5} \cdot e^{(2.47 \cdot NN^{-0.15})}$
	$0.1 < NN \leq 1$	$E = F \cdot Bo^{0.5} \cdot e^{(2.47 \cdot NN^{-0.1})}$
	$NN > 1$	$Bo > 3 \cdot 10^{-5}$: $E = 230 \cdot Bo^{0.5}$, $else\ E = 1 + 46 \cdot Bo^{0.5}$
Kandlikar	$\alpha_K = max(E, S) \cdot \alpha_{lo}$	
[53]		$Co = ((1-x)/x)^{0.8} \cdot (\rho_v/\rho_l)^{0.5}$
		$F_{Fl} = 1$
	$Fr_l \geq 0.04$	$Fr_f = 1$
	$Fr_l < 0.04$	$Fr_f = (25 \cdot Fr_l)^{0.3}$
		$S = (1.136 \cdot Co^{-0.9} \cdot Fr_f) + (667.2 \cdot Bo^{0.7} \cdot F_{Fl})$
		$E = (0.6683 \cdot Co^{-0.2} \cdot Fr_f) + (1058 \cdot Bo^{0.7} \cdot F_{Fl})$
Steiner & Taborek	$\alpha_{ST} = \left[(E \cdot \alpha_{lo})^3 + (S \cdot \alpha_{tp})^3\right]^{1/3}$	
[56]		$S = F \cdot \left(\frac{q}{1.5 \cdot 10^5}\right)^{0.8-0.1exp(1.75Pred)} \left(\frac{D_h}{0.01}\right)^{-0.4} f(M_w)$
		$F = 2.816 \cdot P_{red}^{0.45} + \left(3.4 + \frac{1.7}{1-P_{red}^7}\right) \cdot P_{red}^{3.7}$
		$f(M_w) = 0.377 + 0.199 \cdot log_{10}(M_w)$ $+0.000028427 \cdot M_w^2$
		$E = \left[(1-x)^{1.5} + 1.9 \cdot x^{0.6} \cdot (\frac{\rho_l}{\rho_v})^{0.35}\right]^{1.1}$
		$\alpha_{tp} = 18890$

Table A.1: Macro-channel correlations for the prediction of the two-phase heat transfer coefficient I.

Liu & Winterton	$\alpha_{LW} = \left[(E \cdot \alpha_{lo})^2 + (S \cdot \alpha_{tp})^2\right]^{1/2}$	
[58]		$S = \left(1 + 0.055 \cdot E^{0.1} \cdot Re_{lo}^{0.16}\right)^{-1}$
		$E = \left(1 + x \cdot Pr_l \cdot \left(\frac{\rho_l}{\rho_v} - 1\right)\right)^{0.35}$
		$\alpha_{tp} = 55P_{red}^{0.12}(-log_{10}(P_{red}))^{-0.55}M_w^{-0.5}q^{0.67}$
	$Fr_l \leq 0.05$	$E' = E \cdot Fr_l^{0.1-2Fr_l}$
		$S' = S \cdot Fr_l^{0.5}$
Gungor & Winterton	$\alpha_{GW} = (E \cdot \alpha_l) + (S \cdot \alpha_{tp})$	
[57]		$S = \left(1 + 1.15 \cdot 10^{-6}E^2 Re_l^{1.17}\right)^{-1}$
		$E = 1 + 24000 \cdot Bo^{1.16} + 1.37 \cdot (1/X_{tt})^{0.86}$
		$\alpha_{tp} = 55P_{red}^{0.12}(-log_{10}(P_{red}))^{-0.55}M_w^{-0.5}q^{0.67}$
	$Fr_l \leq 0.05$	$E' = E \cdot Fr_l^{0.1-2Fr_l}$
		$S' = S \cdot Fr_l^{0.5}$
Cooper	$\alpha_{CO} = \alpha_{tp}$	
[59]		$\alpha_{tp} = 55P_{red}^{0.12}(-log_{10}(P_{red}))^{-0.55}M_w^{-0.5}q^{0.67}$
Wattelet et al.	$\alpha_{Watt} = \left(\alpha_{tp,nb}^{2.5} + \alpha_{tp,cb}^{2.5}\right)^{0.4}$	
[60]		$E = 1 + 1.925X_{tt,Watt}^{-0.83}$
		$\Omega = 0.551P_{red}^{0.492}$
		$X_{tt,Watt} = \left(\frac{1-x}{x}\right)^{0.9}\Omega$
	$Fr_l \geq 0.25$	$R = 1$
	$Fr_l < 0.25$	$R = 1.32Fr_l^{0.2}$
		$\alpha_{tp,nb} = 55P_{red}^{0.12}(-log_{10}(P_{red}))^{-0.55}M_w^{-0.5}q^{0.67}$
		$\alpha_{tp,cb} = E \cdot \alpha_l \cdot R$

Table A.2: Macro-channel correlations for the prediction of the two-phase heat transfer coefficient II.

A.2 Micro-channel correlations

Warrier et al. [100]	$\alpha_W = E \cdot \alpha_{lo}$	$E = 1 + 6Bo^{1/16} - 5.3\,(1 - 855Bo)\,x^{0.65}$
Lazarek & Black [5]	$\alpha_{LB} = \alpha_{tp}$	$\alpha_{tp} = 30Re_{lo}^{0.857}Bo^{0.714}\frac{k_l}{D_h}$
Tran et al. [101]	$\alpha_T = \alpha_{tp}$	$\alpha_{tp} = 8.4 \cdot 10^5 \left(Bo^2 We_l\right)^{0.3} \left(\frac{\rho_v}{\rho_l}\right)^{0.4}$
Agostini & Bontemps [102]	$\alpha_{AB} = \alpha_{tp}$ $x \leq 0.43$ $x > 0.43$	$\alpha_{tp} = 28q^{2/3}G^{-0.26}x^{-0.1}$ $\alpha_{tp} = 28q^{2/3}G^{-0.64}x^{-2.08}$
Li & Wu [103]	$\alpha_{LWu} = \alpha_{tp}$	$\alpha_{tp} = 334Bo^{0.3}\left(Bd \cdot Re_l^{0.36}\right)^{0.4}\frac{k_l}{D_h}$
Bertsch et al. [104]	$\alpha_B = (E \cdot \alpha_{tp,cb}) + (S \cdot \alpha_{tp,nb})$	$S = 1 - x$ $E = 1 + 80\left(x^2 - x^6\right) exp\left(-0.6N_{conf}\right)$ $N_{conf} = \sqrt{\frac{\sigma}{g\left(\frac{\rho_l}{\rho_v}\right)D_h^2}}$ $\alpha_{l,lo} = \left(3.66 + \frac{0.668\frac{D_h}{L}Re_{lo}Pr_l}{1+0.04\left(\frac{D_h}{L}Re_{lo}Pr_l\right)^{2/3}}\right)\frac{k_l}{D_h}$ $\alpha_{l,vo} = \left(3.66 + \frac{0.668\frac{D_h}{L}Re_{vo}Pr_v}{1+0.04\left(\frac{D_h}{L}Re_{vo}Pr_v\right)^{2/3}}\right)\frac{k_l}{D_h}$ $\alpha_{tp,nb} =$ $55P_{red}^{0.12-0.2log_{10}Ra}(-log_{10}(P_{red}))^{-0.55}M_w^{-0.5}q^{0.67}$ $\alpha_{tp,cb} = \alpha_{l,lo}\,(1 - x) + \alpha_{l,vo}x$
Yu et al. [105]	$\alpha_{Yu} = \alpha_{tp}$	$\alpha_{tp} = 640000\left(Bo^2 \cdot We_l\right)^{0.27}\left(\frac{\rho_l}{\rho_v}\right)^{-0.2}$

Table A.3: Micro-channel correlations for the prediction of the two-phase heat transfer coefficient I.

Kandlikar & Balasub.	$\alpha_{KB} = max(\alpha_{tp,nb}, \alpha_{tp,cb})$	
[106]		$\alpha_{tp,nb} = 0.6683 \cdot Co^{-0.2} \cdot (1-x)^{0.8}\, h_{LO}$ $+1058 \cdot Bo^{0.7}\, (1-x)^{0.8}\, F_{Fl} h_{LO}$ $\alpha_{tp,cb} = 1.136 \cdot Co^{-0.9} \cdot (1-x)^{0.8}\, h_{LO}$ $+667.2 \cdot Bo^{0.7}\, (1-x)^{0.8}\, F_{Fl} h_{LO}$ $F_{Fl} = 1$ $f = \left(1.58 \cdot log(Re_{lo}) - 3.28\right)^{-2}$
	$Re_{lo} \geq 10^4$	$h_{LO} = \frac{Re_{lo} \cdot Pr_l \cdot \frac{f}{2} \cdot \frac{k_l}{D_h}}{1+12.7(Pr_l^{2/3}-1)(\frac{f}{2})^{0.5}}$
	$Re_{lo} < 10^4$	$h_{LO} = \frac{\left(Re_{lo}-1000\right) \cdot Pr_l \cdot \frac{f}{2} \cdot \frac{k_l}{D_h}}{1+12.7(Pr_l^{2/3}-1)(\frac{f}{2})^{0.5}}$
Kew & Cornwell	$\alpha_{Kew} = \alpha_{tp}$	
[89]		$\alpha_{tp} = 30 Re_{lo}^{0.857} Bo^{0.714} (1-x)^{-0.143} \frac{k_l}{D_h}$
Oh & Son	$\alpha_{OS} = \alpha_{tp}$	
[107]		$\alpha_{tp} = 0.034 Re_l^{0.8} Pr_l^{0.3} 1.58 (\frac{1}{X_{tt}})^{0.87} \frac{k_l}{D_h}$
Kim & Mudawar	$\alpha_{KM} = \left[(\alpha_{tp,cb})^2 + (\alpha_{tp,nb})^2\right]^{0.5}$	
[108]		$\alpha_{tp,nb} = \left(2345 Bo^{0.7} Pred^{0.38} (1-x)^{-0.51}\right) \cdot \alpha_l$ $\alpha_{tp,cb} =$ $\left(5.2 Bo^{0.08} We_l^{-0.54} + 3.5 (\frac{1}{X_{tt}})^{0.94} (\frac{\rho_v}{\rho_l})^{0.25}\right) \cdot \alpha_l$

Table A.4: Micro-channel correlations for the prediction of the two-phase heat transfer coefficient II.

A.3 Carbon dioxide correlations

Ducoulombier et al. [135]	$\alpha_D = max(\alpha_{tp,nb}, \alpha_{tp,cb})$	$\alpha_{tp,nb} = 131 P_{red}^{-0.0063} (-log_{10}(P_{red}))^{-0.55} M_w^{-0.5} q^{0.58}$
	$Bo \geq 1.1 \cdot 10^{-4}$	$\alpha_{tp,cb} = \left(1.47 \left[Bo \cdot 10^4 + 0.63(\frac{1}{X_{tt}})^{2/3}\right]\right) \cdot \alpha_{lo}$
	$Bo < 1.1 \cdot 10^{-4}$	$\alpha_{tp,cb} = \left(1 + 1.8(\frac{1}{X_{tt}})^{0.986}\right) \cdot \alpha_l$
Hihara & Tanaka [117]	$\alpha_{HT} = E\alpha_{lo}$	$E = 14700 Bo + 0.93(\frac{1}{X_{tt}})^{2/3}$
Yun et al. [133]	$\alpha_{Yun} = \alpha_{tp}$	$\alpha_{tp} = 16.26 P_{red}^{0.88} q^{0.72}$
Choi et al. [114]	$\alpha_{Ch} = (E\alpha_l) + (S\alpha_{tp,nb})$	$X_{tt,Choi} = \left(\frac{1-x}{x}\right)^{7/8} \left(\frac{\rho_v}{\rho_l}\right)^{0.5} \left(\frac{\mu_l}{\mu_v}\right)^{1/8}$ C=20 $\phi^2 = 1 + \frac{C}{X_{tt,Choi}} + \frac{1}{X_{tt,Choi}^2}$ $\alpha_{tp,nb} =$ $55 P_{red}^{0.12} (-0.4343 log_{10}(P_{red}))^{-0.55} M_w^{-0.5} q^{0.67}$ $E = 0.05\phi^2 + 0.95$ $S = 7.2694 \left(\phi^2\right)^{0.0094} Bo^{0.2814}$
Wang et al. [136]	$\alpha_{Wa} = (E\alpha_l) + (S\alpha_{tp,nb})$	$d_b = 0.51 \left(\frac{2\sigma}{g(\rho_l - \rho_v)}\right)^{0.5}$ $E = 1 + K_1 \left(\frac{1}{Xtt}\right)^{K_2}$ $Re_{tp} = Re_l E^{1.25}$ $S = 1/\left[1 + K_3 \left(\frac{(Re_{tp} \cdot 10^{-4})^2}{(Bo \cdot 10^4)^{K_4} Xtt^{K_5})}\right)\right]$ $\alpha_{tp,nb} =$ $207 \frac{k_l}{d_b} \left(q \frac{D_h}{k_l (T_{sat} + 273.15)}\right)^{0.745} \left(\frac{\rho_v}{\rho_l}\right)^{0.581} Pr_l^{0.533}$
	$D_h = 0.7$	$K_1 = 1;\ K_2 = 1.2;\ K_3 = 15;\ K_4 = 4;\ K_5 = 0$
	$D_h = 1$	$K_1 = 1;\ K_2 = 1.2;\ K_3 = 0.5;\ K_4 = 0;\ K_5 = 0$
	$D_h = 2$	$K_1 = 1;\ K_2 = 1.2;\ K_3 = 0.5;\ K_4 = 0;\ K_5 = 0$

Table A.5: CO_2 correlations for the prediction of the two-phase heat transfer coefficient I.

Yoon et al.	$\alpha_{Yo} = \left[(S\alpha_{tp,nb})^2 + (E\alpha_{lo})^2\right]^{0.5}$	
[126]		$\alpha_{tp,nb} = 55P_{red}^{0.12}(-log_{10}(P_{red}))^{-0.55}M_w^{-0.5}q^{0.67}$
		$E = \left(1 + 9.36 \cdot 10^3 xPr_l(\frac{\rho_l}{\rho_v} - 1)\right)^{0.11}$
		$S = 1/(1 + 1.62 \cdot 10^{-6}E^{0.69}{Re_{lo}}^{1.11})$
Pamitran et al.	$\alpha_{Pam} = (E \cdot \alpha_l) + (S \cdot \alpha_{tp,nb})$	
[120]		$X_{tt,Pam} = \left(\frac{1-X}{X}\right)\left(\frac{\rho_v}{\rho_l}\right)^{0.5}\left(\frac{f_l}{f_v}\right)^{1/2}$
		C=20, C$_{ref}$=0.25
		$\phi^2 = 1 + \frac{C}{X_{tt,Pam}} + \frac{1}{X_{tt,Pam}^2}$
		$\alpha_{tp,nb} = 55P_{red}^{0.12}(-0.4343log_{10}(P_{red}))^{-0.55}M_w^{-0.5}q^{0.67}$
		$E = max(\left[\left(0.009\phi^2\right)^2 + 0.76\right], 1)$
		$S = C_{ref}\left(\phi^2\right)^{-0.2093}Bo^{0.7402}$
	$Re_l \geq 2000$	$f_l = 0.079Re_l^{-0.25}$
	$Re_v \geq 2000$	$f_v = 0.079Re_v^{-0.25}$
	$Re_l < 2000$	$f_l = 16Re_l^{-1}$
	$Re_v < 2000$	$f_v = 16Re_v^{-1}$
Oh et al.	$\alpha_{Oh} = (F \cdot h_f) + (S \cdot \alpha_{tp,nb})$	
[132]		$X_{tt,Oh} = \left(\frac{1-X}{X}\right)\left(\frac{\rho_v}{\rho_l}\right)^{0.5}\left(\frac{f_l}{f_v}\right)^{1/2}$
		$\phi^2 = 1 + \frac{C}{X_{tt,Oh}} + \frac{1}{X_{tt,Oh}^2}$
	$Re_l < 2000,\ Re_v < 2000,$	C=5
	$Re_l \geq 2000,\ Re_v < 2000,$	C=10
	$Re_l < 2000,\ Re_v \geq 2000,$	C=12
	$Re_l \geq 2000,\ Re_v \geq 2000,$	C=20
	$Re_l \geq 2000$	$f_l = 0.079Re_l^{-0.25}$
	$Re_v \geq 2000$	$f_v = 0.079Re_v^{-0.25}$
	$Re_l < 2000$	$f_l = 16Re_l^{-1}$
	$Re_v < 2000$	$f_v = 16Re_v^{-1}$
		$\alpha_{tp,nb} = 55P_{red}^{0.12}(-0.4343log_{10}(P_{red}))^{-0.55}M_w^{-0.5}q^{0.67}$
		$F = max(\left[0.023\phi^{2.2} + 0.76\right], 1)$
		$S = 0.279\left(\phi^2\right)^{-0.029}Bo^{-0.098}$
	$Re_l < 2000$	$h_f = 4.36\frac{k_l}{D_i}$
	$2000 \leq Re_l \leq 10^4$	$h_f = \frac{(Re_l - 1000)Pr_l\frac{f_l}{2}\frac{k_l}{D_i}}{1+12.7({Pr_l}^{2/3}-1)(\frac{f_l}{2})^{0.5}}$
	$10^4 \leq Re_l \leq 10^6$	$h_f = \frac{Re_l Pr_l\frac{f_l}{2}\frac{k_l}{D_i}}{1+12.7({Pr_l}^{2/3}-1)(\frac{f_l}{2})^{0.5}}$
	$Re_l \geq 10^6$	$h_f = \alpha_l$

Table A.6: CO$_2$ correlations for the prediction of the two-phase heat transfer coefficient II.

A.4 Others

Fang et al.	$\alpha_{Fang} = Nu_{Fang}\frac{k_l}{D_h}$	
[156]		$Nu_{Fang} = F_f M_w^{-0.18} Bo^{0.98} Fr_l^{0.48} Bd^{0.72} \left(\frac{\rho_l}{\rho_v}\right)^{0.29} \left(log\left(\frac{\mu_{l,fluid}}{\mu_{l,wall}}\right)\right)^{-1} Y_{Fang}$
		$F_f = 2260$
	$P_{red} \leq 0.43$	$Y_{Fang} = 1$
	$P_{red} > 0.43$	$Y_{Fang} = 1.38 - P_{red}^{1.15}$

Table A.7: Correlation for the prediction of the two-phase heat transfer coefficient by Fang et al. [156].

APPENDIX B

Correlations for the prediction of the two-phase frictional pressure drop

B.1 Homogeneous models

homogeneous model	$\mu_{tp} = \mu_l$ $\frac{1}{\rho_m} = \frac{x}{\rho_v} + \frac{1-x}{\rho_l}$
McAdams et al. [63]	$\frac{1}{\mu_{tp}} = \frac{x}{\mu_v} + \frac{1-x}{\mu_l}$
Beattie & Whalley [64]	$\mu_{tp} = \beta\mu_v + (1-\beta)(1+2.5\beta)\mu_l$ $\beta = \left(1 + \left(\frac{\rho_v}{\rho_l}\right)\left(\frac{1-x}{x}\right)\right)^{-1}$
Cicchitti et al. [65]	$\mu_{tp} = x\mu_v + (1-x)\mu_l$
Dukler et al.	$\mu_{tp} = \rho_m\left(\frac{x\mu_v}{\rho_v} + \frac{(1-x)\mu_l}{\rho_l}\right)$
Akers et al. [67]	$\mu_{tp} = \frac{\mu_l}{\left((1-x)+x\left(\frac{\rho_l}{\rho_v}\right)^{0.5}\right)}$
Lin et al. [68]	$\mu_{tp} = \frac{\mu_l\mu_v}{\mu_v+x^{1.4}(\mu_l-\mu_v)}$
Ducoulombier et al. [121]	$\mu_{tp} = x\mu_v + C_\mu(1-x)\mu_l$ $C_\mu = 6.195 - 9.178P_{red}$

Table B.1: Homogeneous models for the prediction of the two-phase frictional pressure drop.

For the homogeneous models the friction factor was calculated with the Churchill expression [162] as suggested by Ducoulombier et al. [121].

B.2 Separated flow models

B.2.1 Macro-channel correlations

Lockhart-Martinelli [70]	$Re_l < 2000$, $Re_v < 2000$	C=5 $f_l = 16Re_l^{-1}$ $f_v = 16Re_v^{-1}$ $X_{ll} = \left(\frac{1-X}{X}\right)^{0.5} \left(\frac{\rho_v}{\rho_l}\right)^{0.5} \left(\frac{\mu_l}{\mu_v}\right)^{0.5}$
	$Re_l \geq 2000$, $Re_v < 2000$	C=10 $f_l = 0.079Re_l^{-0.25}$ $f_v = 16Re_v^{-1}$ $C_l = 0.046$ $C_v = 16$ $X_{tl} = Re_l^{0.4} \left(\frac{C_l}{C_v}\right)^{0.5} \left(\frac{1-X}{X}\right)^{0.5} \left(\frac{\rho_v}{\rho_l}\right)^{0.5} \left(\frac{\mu_l}{\mu_v}\right)^{0.5}$
	$Re_l < 2000$, $Re_v \geq 2000$	C=12 $f_l = 16Re_l^{-1}$ $f_v = 0.079Re_v^{-0.25}$ $C_l = 16$ $C_v = 0.046$ $X_{lt} = Re_l^{-0.4} \left(\frac{C_l}{C_v}\right)^{0.5} \left(\frac{1-X}{X}\right)^{0.5} \left(\frac{\rho_v}{\rho_l}\right)^{0.5} \left(\frac{\mu_l}{\mu_v}\right)^{0.5}$
	$Re_l \geq 2000$, $Re_v \geq 2000$	C=20 $f_l = 0.079Re_l^{-0.25}$ $f_v = 0.079Re_v^{-0.25}$ $X_{tt} = \left(\frac{1-X}{X}\right)^{0.9} \left(\frac{\rho_v}{\rho_l}\right)^{0.5} \left(\frac{\mu_l}{\mu_v}\right)^{0.1}$
Lockhart-Martinelli: C-method [71]		$\left(\frac{dP}{dz}\right)_{tp,frict} = \left(\frac{dP}{dz}\right) \phi^2$ $\left(\frac{dP}{dz}\right)_l = \frac{2f_l(1-x)^2G^2}{\rho_l D_h}$ $\left(\frac{dP}{dz}\right)_v = \frac{2f_v x^2 G^2}{\rho_v D_h}$
	$Re_l \geq 4000$	$\phi_l^2 = 1 + \frac{C}{X_{tt}} + \frac{1}{X_{tt}^2}$ $\left(\frac{dP}{dz}\right)_{tp} = \left(\frac{dP}{dz}\right)_l \phi_l^2$
	$Re_l < 4000$	$\phi_v^2 = 1 + CX_{tt} + X_{tt}^2$ $\left(\frac{dP}{dz}\right)_{tp,frict} = \left(\frac{dP}{dz}\right)_v \phi_v^2$

Table B.2: Separated flow models: Macro-channel correlations for the prediction of the two-phase frictional pressure drop I.

Lockhart-Martinelli:	$Re_{lo} < 2000$	$f_{lo} = 16Re_{lo}^{-1}$
B-method	$Re_{lo} \geq 2000$	$f_{lo} = 0.079Re_{lo}^{-0.25}$
[72]	$Re_{vo} < 2000$	$f_{vo} = 16Re_{vo}^{-1}$
	$Re_{vo} \geq 2000$	$f_{vo} = 0.079Re_{vo}^{-0.25}$
		$\left(\frac{dP}{dz}\right)_{lo} = \frac{2f_{lo}G^2}{\rho_l D_h}$
		$\left(\frac{dP}{dz}\right)_{vo} = \frac{2f_{vo}G^2}{\rho_v D}$
		$Y = \sqrt{\left(\frac{dP}{dz}\right)_{vo} / \left(\frac{dP}{dz}\right)_{lo}}$
$0 < Y \leq 9.5$	$G \geq 1900$	$B = 55/\sqrt{G}$
	$500 < G < 1900$	$B = 2400/G$
	$G \leq 500$	$B = 4.8$
$9.5 < Y < 28$	$G \leq 600$	$B = 520/\left(Y\sqrt{G}\right)$
	$G > 600$	$B = 21/Y$
$Y \geq 28$		$B = 15000/\left(Y^2\sqrt{G}\right)$
		$\phi^2 = 1 + \left(Y^2 - 1\right)\left[Bx^{0.875}\left(1-x\right)^{0.875} + x^{1.75}\right]$
		$\left(\frac{dP}{dz}\right)_{tp,frict} = \left(\frac{dP}{dz}\right)_{lo}\phi^2$

Table B.3: Separated flow models: Macro-channel correlations for the prediction of the two-phase frictional pressure drop II.

Friedel [74]		$E = (1-x)^2 + x^2 \frac{\rho_l f_{vo}}{\rho_v f_{lo}}$ $F = x^{0.78}(1-x)^{0.224}$ $H = \left(\frac{\rho_l}{\rho_v}\right)^{0.91}\left(\frac{\mu_v}{\mu_l}\right)^{0.19}\left(1-\frac{\mu_v}{\mu_l}\right)^{0.7}$ $\phi^2_{Friedel} = E + \frac{3.24 \cdot F \cdot H}{Fr_m^{0.045} We_l^{0.035}}$ $Fr_m = \frac{G^2}{g D_h \rho_m^2}$ $\left(\frac{dP}{dz}\right)_{tp,frict} = \left(\frac{dP}{dz}\right)_{lo} \phi^2_{Friedel}$
Müller-Steinhagen & Heck [73]		$A = \frac{2 f_{lo} G^2}{D_h \rho_l}$ $B = \frac{2 f_{vo} G^2}{D_h \rho_v}$ $G = A + 2(B-A)x$ $\left(\frac{dP}{dz}\right)_{tp,frict} = G(1-x)^{0.333} + Bx^3$
Grönnerud [75]		$\left(\frac{dP}{dz}\right)_{Fr} = f_{Gro}\left(x + 4\left[x^{1.8} - x^{10} f_{Gro}^{0.5}\right]\right)$ $\phi_{Gro} = 1 + \left(\frac{dP}{dz}\right)_{Fr}\left[\frac{\frac{\rho_l}{\rho_v}}{\left(\frac{\mu_l}{\mu_v}\right)^{0.25} - 1}\right]$
	$Fr_l \geq 1$	$f_{Fr} = 1$
	$Fr_l < 1$	$f_{Fr} = Fr_l^{0.3} + 0.0055\left(ln\frac{1}{Fr_l}\right)^2$
		$\left(\frac{dP}{dz}\right)_{tp,frict} = \left(\frac{dP}{dz}\right)_{lo} \phi_{Gro}$

Table B.4: Separated flow models: Macro-channel correlations for the prediction of the two-phase frictional pressure drop III.

B.2.2 Micro-channel correlations

Mishima & Hibiki [93]		$C = 21\left(1 - exp\left(-0.319 D_h\right)\right)$ $\phi_l^2 = 1 + \frac{C}{X_{tt}} + \frac{1}{X_{tt}^2}$ $\left(\frac{dP}{dz}\right)_{tp} = \left(\frac{dP}{dz}\right)_l \phi_l^2$
Tran et al. [94]		$N_{conf} = \frac{\left[\frac{\sigma}{g(\rho_l - \rho_v)}\right]^2}{D_h}$ $\Gamma = \left(\frac{dP}{dz}\right)_{vo} / \left(\frac{dP}{dz}\right)_{lo}$ $\phi_l^2 = 1 + \left(4.3\Gamma^2 - 1\right)\left(N_{conf} \cdot x^{0.875}\left(1 - x\right)^{0.875} + x^{1.75}\right)$ $\left(\frac{dP}{dz}\right)_{tp} = \left(\frac{dP}{dz}\right)_l \phi_l^2$
Zhang & Webb [95]		$\phi_l^2 = (1 - x)^2 + 2.87 x^2 P_{red}^{-1} + 1.68 x^{0.8} (1 - x)^{0.25} P_{red}^{-1.64}$ $\left(\frac{dP}{dz}\right)_{tp} = \left(\frac{dP}{dz}\right)_l \phi_l^2$
Qu & Mudawar [96]		$C = 21\left(1 - exp\left(-0.319 D_h\right)\right)\left(0.00418 G + 0.0613\right)$ $\phi_l^2 = 1 + \frac{C}{X_{tt}} + \frac{1}{X_{tt}^2}$ $\left(\frac{dP}{dz}\right)_{tp} = \left(\frac{dP}{dz}\right)_l \phi_l^2$
Lee & Garimella [97]		$C = 2566 G^{0.5466} D_h^{0.8819}\left(1 - exp\left(-0.319 D_h\right)\right)$ $\phi_l^2 = 1 + \frac{C}{X_{tt}} + \frac{1}{X_{tt}^2}$ $\left(\frac{dP}{dz}\right)_{tp} = \left(\frac{dP}{dz}\right)_l \phi_l^2$
Lee & Lee [98]	$Re_l < 2000$, $Re_v \geq 2000$	$C = 6.185 \cdot 10^{-2} Re_{lo}^{0.726}$ $\phi_l^2 = 1 + \frac{C}{X_{tt}} + \frac{1}{X_{tt}^2}$ $\left(\frac{dP}{dz}\right)_{tp} = \left(\frac{dP}{dz}\right)_l \phi_l^2$

Table B.5: Separated flow models: Micro-channel correlations for the prediction of the two-phase frictional pressure drop I.

Kim & Mudawar [108]		$Su = \frac{\rho_v \sigma D_h}{\mu_v^2}$
	$Re_l < 2000,\ Re_v < 2000,$	$C_{non-boiling} = 3.5 \cdot 10^{-5} Re_{lo}^{0.44} Su^{0.5} (\frac{\rho_l}{\rho_v})^{0.48}$
	$Re_l \geq 2000,\ Re_v < 2000,$	$C_{non-boiling} = 8.7 \cdot 10^{-4} Re_{lo}^{0.17} Su^{0.5} (\frac{\rho_l}{\rho_v})^{0.14}$
	$Re_l < 2000,\ Re_v \geq 2000,$	$C_{non-boiling} = 0.0015 Re_{lo}^{0.59} Su^{0.19} (\frac{\rho_l}{\rho_v})^{0.36}$
	$Re_l \geq 2000,\ Re_v \geq 2000,$	$C_{non-boiling} = 0.39 {Re_{lo}}^{0.03} Su^{0.1} (\frac{\rho_l}{\rho_v})^{0.35}$
	$Re_l \geq 2000$	$C = C_{non-boiling} \left(1 + 60 We_l^{0.32} Bo^{0.78}\right)$
	$Re_l < 2000$	$C = C_{non-boiling} \left(1 + 530 We_l^{0.52} Bo^{1.09}\right)$
		$\phi_l^2 = 1 + \frac{C}{X_{tt}} + \frac{1}{X_{tt}^2}$
		$\left(\frac{dP}{dz}\right)_{tp} = \left(\frac{dP}{dz}\right)_l \phi_l^2$

Table B.6: Separated flow models: Micro-channel correlations for the prediction of the two-phase frictional pressure drop II.

B.2.3 Carbon dioxide correlations

Yamamoto et al. [119]	$G_c = -1060x + 1160$ $C = 5\left(1 - exp\left(-4x\right)\right)\left(\left(\frac{2G}{G_c} + 1\right) exp\left(\frac{-2G}{G_c}\right) - 1\right) + 5.5$ $\phi_l^2 = 1 + \frac{C}{X_{tt}} + \frac{1}{X_{tt}^2}$ $\left(\frac{dP}{dz}\right)_{tp} = \left(\frac{dP}{dz}\right)_l \phi_l^2$
Yun & Kim [118]	$C = 21\left(1 - exp\left(-0.085D_h\right)\right)$ $\phi_l^2 = 1 + \frac{C}{X} + \frac{1}{X^2}$ $\left(\frac{dP}{dz}\right)_{tp} = \left(\frac{dP}{dz}\right)_l \phi_l^2$
Ducoulombier et al. C- method [121]	$\left(\frac{dP}{dz}\right)_l = \frac{2f_l(1-x)^2G^2}{\rho_l D_h}$ $\left(\frac{dP}{dz}\right)_v = \frac{2f_v x^2 G^2}{\rho_v D_h}$ $X = \sqrt{\left(\frac{dP}{dz}\right)_l / \left(\frac{dP}{dz}\right)_v}$ $C = 0.6891P_{red}^{-2.393}$ $\phi_l^2 = 1 + \frac{C}{X_{tt}} + \frac{1}{X_{tt}^2}$ $\left(\frac{dP}{dz}\right)_{tp} = \left(\frac{dP}{dz}\right)_l \phi_l^2$

Table B.7: Separated flow models: CO_2 correlations for the prediction of the two-phase frictional pressure drop.

APPENDIX C

Multi-micro-channel preparation from compound wafer

Due to two facts the division of the compound multi-micro-channel wafer fabricated at the Fondazione Bruno Kessler (FBK) into its anticipated parts proofed to be rather difficult: Firstly the wafer was 6 inch in diameter and secondly a non-linear, circular cut was required to remove the channels along the circumference of the wafer. Access to the clean room at the Centre of Micro-Nano-Technology (Cmi) at the Ecole Polytechnique Fédérale de Lausanne (EPFL) was available for further processing of the wafer according to various micro-structuring techniques. However at the time some of the required process steps could not be carried out in a strait-forward way due to the size of the wafer. Most machines were only equipped to handle 4 inch wafers. Thus it happened that the three wafers with the multi-micro-channels from LPNHE in Paris were treated each in a different way:

Wafer 1 In order to connect the multi-micro-channels to metallic tubing the immediate surface around the channel inlets and outlets required a metal coating on the silicon side. Sputtering of a metal stack onto the silicon of Titanium, Nickel and Gold (Ti: 200 nm, Ni: 350 nm, Au: 100 nm) was anticipated. However due to the mentioned machine limitations the metal was applied by evaporation. For a defined application of those metal pads a so-called hard mask was designed according to the channel inlets which is put between the electron beam evaporator and the wafer. Figure C.1 depicts the stainless steel hard mask. The rectangular cut-outs anticipated the application of an experimental heat load by means of the resulting metal pads. However for this study the dummy heat load was supplied by a different heating solution as described in section 8.2.2. After the deposition of the metal pads the circular cut of the outer annulus was attempted. Figure C.2 shows the planned cut schematically (green outline). The wafer was shipped to a company specialized on water jet cutting (WatAJet s.r.l., Italy). A handling and transportation error occurred in this context and the result was a complete destruction of the circular micro-channel layout (see C.3(a)) and a partial destruction of the inner main wafer part (see C.3(b)). The inner part was further processed with standard linear dicing cuts resulting in intact micro-channel devices, except for the inter-connection device which was damaged during the circular cutting procedure. The multi-micro-channel devices from this batch were equipped with the standard tubing as described in section 8.2.1 and used for further testing.

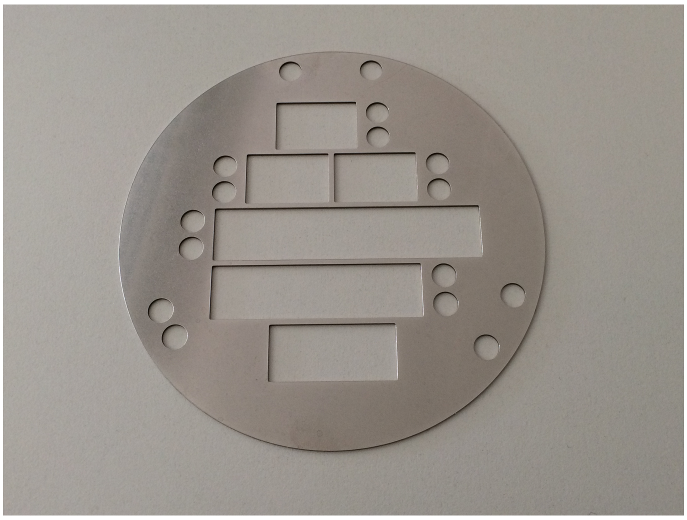

Figure C.1: 6 inch stainless steel hard mask.

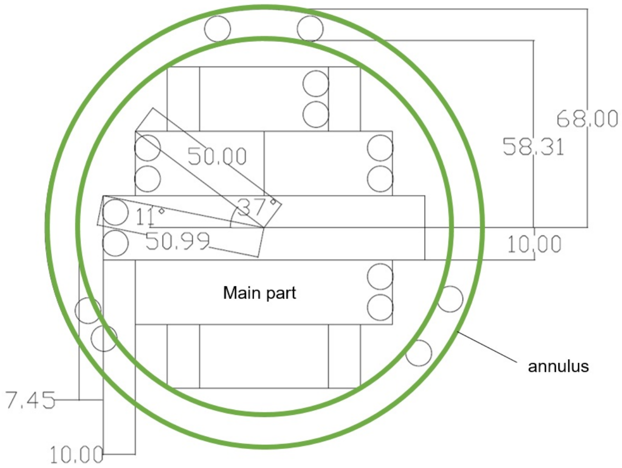

Figure C.2: Schematic of the circular cut.

Wafer 2 Due to the problematic caused by the circular cut and the mentioned machine limitations the second compound wafer was diced immediately with linear standard cuts, thus destroying the outer circular micro-channels and retrieving only the multi-micro-channel devices from the main part. Those devices were still lacking the necessary metal pads around the in and outlets. The proposed procedure was to fix those pre-cut devices on several hard masks 4 inch in diameter which then could be received by the sputtering machine at Cmi. Figure C.4 shows two different stainless steel hard masks, where the rectangular cut outs were divided in this case into several sections for a more flexible application of a dummy heat load by means of the resulting pads on the silicon substrate.

(a)

(b)

Figure C.3: Failure of the water jet dicing method I: a) damaged outer annulus ; b) damaged inner part.

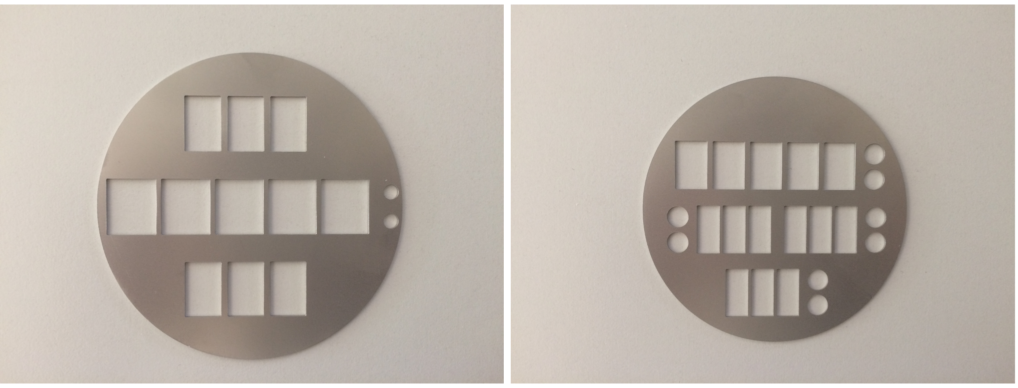

(a)

(b)

Figure C.4: 4 inch stainless steel hard mask: a) mask 1; b) mask 2.

Wafer 3 A second trial was attempted with the water jet cutting technique, whilst very clear instructions and a purpose-designed transport box were provided to the cutting company to avoid further transport and handling errors. Nevertheless the second cut also failed to produce the needed quality. A machining error occurred in this case and the absence of abrasive for 0.05 sec damaged the annulus, which is shown in Figure C.5. The channels contained in the main wafer part were again recuperated by dicing and the hard masks as described for wafer 2 can be used to apply the metal pads.

For the future further options to achieve the circular cut were inquired such as high-precision sand blasting, laser cutting and common sandblasting.

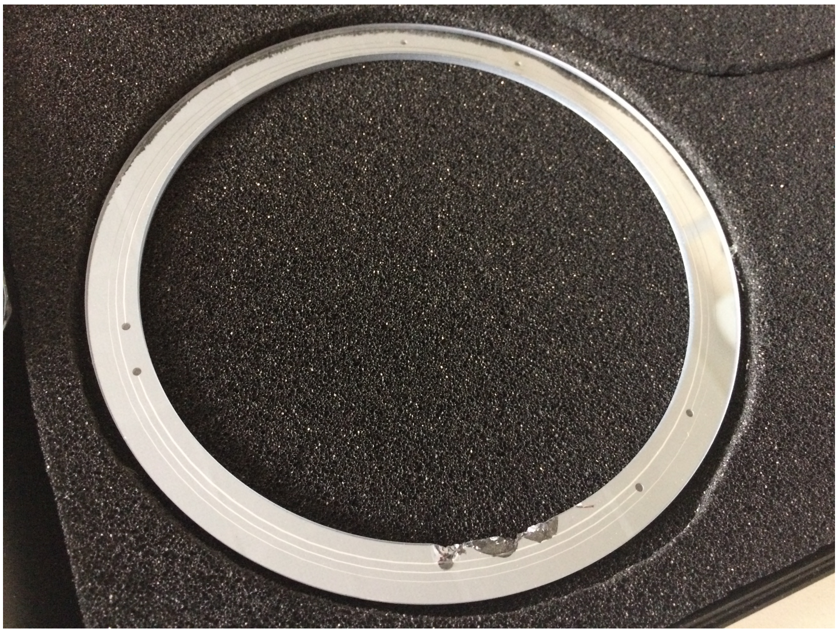

Figure C.5: Failure of the water jet dicing method II.

APPENDIX D

Setup modifications

Various adjustments to the setup layout had to be made over time. Some of the major changes and their cause will be described in the following paragraphs, which were not explicitly or only shortly mentioned in the main part of this thesis. Additional figures are included for further explanation.

Installation of a spacer flange At the very beginning of the experimental activity with the new setup for detector cooling R&D with mini- and micro-scale CO_2 evaporators at CERN inconsistencies were found in the temperature measurements. Whilst there was vacuum inside, the sensors inside the vacuum vessel closest to the back flange measured higher temperatures compared to the target temperature. One possible reason for that seemed that these sensors including the fluidic stainless steel crosses in which they were mounted were touching the back vessel flange and drawing some additional heat from it. As a solution the back flange was removed and a spacer was installed so that the vacuum vessel became longer and no metallic components could touch the vessel wall anymore. Minor deviations between the measurements could be resolved with this solution. Figure D.1 shows the spacer flange in its final position marked in blue.

However some discrepancies between target temperature and actually measured temperature still remained which triggered a long series of changes to the setup which will be described in the following. More caution was exercised and further measures towards more accurate temperature measurements were taken.

Installation of dielectric fittings When powering the joule heater whilst running experiments there were again obvious irregularities found in the temperature measurements, concluding that stray currents from the installed heater might affect the temperature of the whole system inside the vacuum vessel. The mentioned dielectric fittings were installed to eliminate this effect. Figure D.2 illustrates the used fitting as shown on the manufactures website (www.swagelok.com), which is now installed before and after the experimental section.

Relocation of the setup into an air-conditioned laboratory To eliminate daily inconsistencies in the measured data - experienced especially during the summer period - the setup was moved to a laboratory less susceptible to the daily impact of the weather. In addition this new laboratory is now

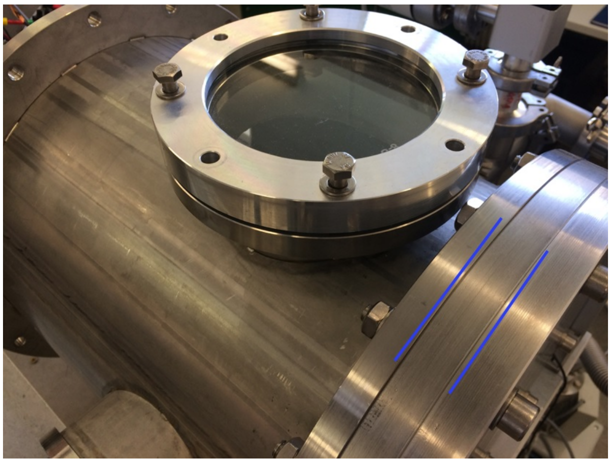

Figure D.1: Vacuum vessel with spacer flange (between blue markers).

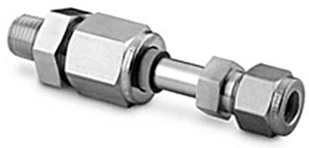

Figure D.2: Dielectric fitting from Swagelok.

equipped with an air conditioning system where the room temperature can be controlled to be at ~ 19°C.

Installation of a new heater for the cooling plant In the same context a new cartridge heater was installed in the used cooling plant (400W instead of 250 W cooling capacity). With the initial 250 W heater, despite its design operational range, the cooling plant seemed to encounter a limitation to deliver stable conditions above 18 °C saturation temperature.

Thermally insulated fluidic feed through Initially for all the fluidic feedthroughs (fluid and pressure lines) Swagelok seal fittings were used. Since the vessel flange, the seal fittings and the tubes are all made in stainless steel this posed a problem for the experiments carried out. Whilst running single-phase tests in vacuum and in the now air-conditioned lab it became obvious that some heat source influenced the heat balance of the system and was measured by the temperature sensors. One possible explanation to this was that the flange and all the stainless steel components inside the vessel are interconnected. Heat from the outside can easily find a path into the vessel and this is measureable by the sensors. The proposed solution to this problem was to disconnect all crucial inner tubing from the flange's inertia. This can be done by using special thermally insulated fluid feed throughs designed for vacuum applications, which were already mentioned in the main text. The in- and outlets for the fluid were equipped accordingly with these devices. These feed throughs were obtained from Pfeiffer Vacuum GmbH. Figure D.3 illustrates the used feed through as shown on the manufactures website (www.pfeiffer-vacuum.com). For the installation of these devices the initial vessel flange made out of aluminium had to be exchanged for a new stainless steel flange which required the dismounting of all the circuitry within and outside the vacuum vessel. The stainless steel flange was necessary for its superior results after welding compared to the trials with the aluminium flange. The welds on the aluminium flange were of poor quality and resulted in leaks in the vacuum vessel.

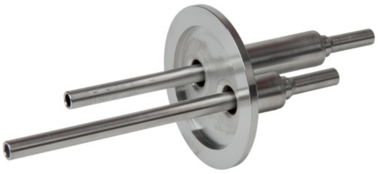

Figure D.3: Fluidic feed through from Pfeiffer Vacuum.

Optional Multi-Layer Insulation As an additional option for more accurate temperature measurements a Multi-Layer Insulation (MLI) foil can be applied to the inside of the vacuum vessel to shield the experiment further from possible radiative heat loads. MLI foil is made of multiple layers of insulation material such as metal-coated plastic layers with thin mesh-like separator layers in between. Figure D.4 shows the inside of the vessel shielded with MLI foil. For an easy application, the back flange of the vacuum vessel can be removed and the foil can be inserted.

Figure D.4: Optional MLI foil inside the vacuum vessel.

Installation of insulating PEEK inserts into the pressure lines All pressure lines inside the vacuum vessel were equipped with small PEEK inserts for insulating purposes. The pressure lines inside the vessel were cut and merged again by means of small peek tubes. These can act as electrical and thermal insulators and an example is shown in Figure D.5.

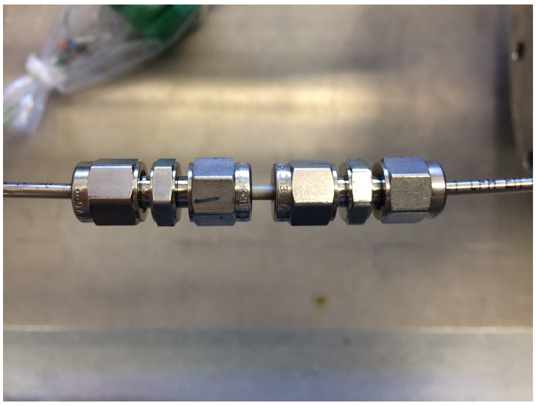

Figure D.5: Peek insert along the pressure line.

Analysis and exchange of the RTD sensors Finally the temperature sensors themselves were suspected to cause the found measurement error. In retrospect to the first measurements which were carried out in vacuum, the qualification of the used RTDs for vacuum applications was checked in more detail. Initially Pt100 sensing elements in 4-wire configuration protected by a stainless steel shaft were used which are the same sensors commonly applied in CO_2 cooling plants at CERN. The only difference being a small custom-made measurement tip in order to accommodate the micro-fluidic in-flow measurements. Both sensor types are shown in Figure D.6 (with nut and ferrule).
However, after eliminating all other possible error sources the Pt100s still measured some higher temperature in vacuum compared to tests at atmospheric conditions. Consequently, the behaviour of the RTDs in vacuum was studied more methodically. As a first step, the bare RTDs were tested in atmosphere and vacuum. They were installed inside the vacuum vessel in such a way that they were floating freely in the vessel touching no surfaces. Figure D.7 shows the installation of the RTDs for the

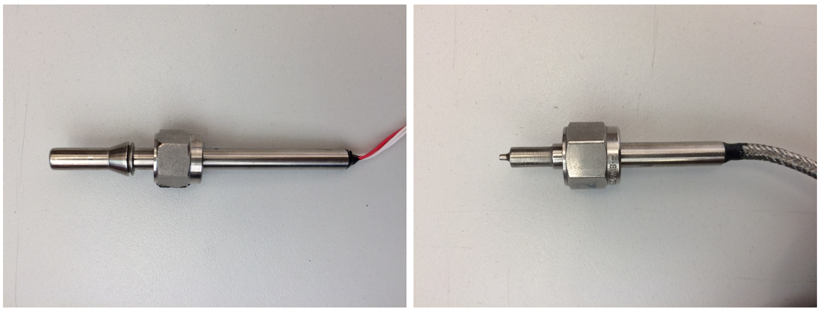

(a) (b)

Figure D.6: Pt100 sensors: a) used for CO_2 cooling plants at CERN; b) used for the new setup with custom-made measurement tip.

"floating tests". Tests were carried out in atmospheric room conditions (see Figure), with the loosely closed vessel and with vacuum inside the vessel to monitor the behaviour of the sensors. No unusual heating effect could be found for the floating sensors in all three test conditions.

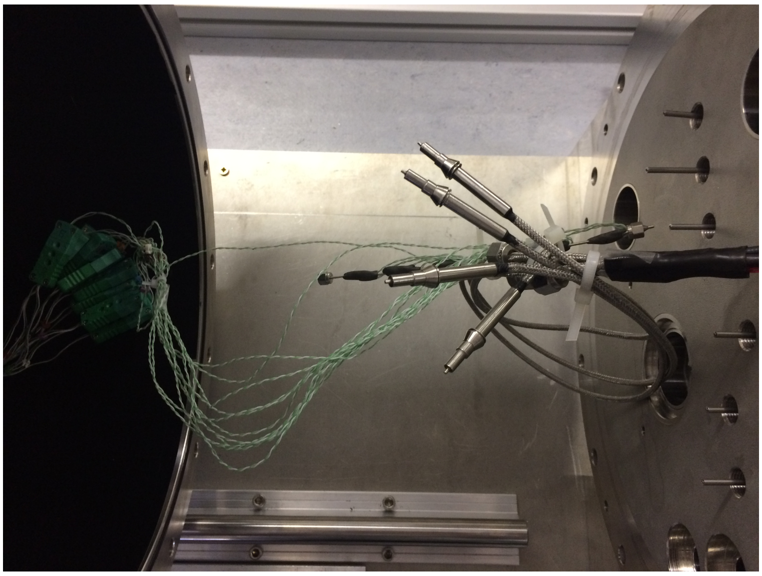

Figure D.7: "Floating" Pt100s inside vacuum vessel.

Then the RTDs were installed once more into the circuit. Similar tests were carried out to monitor the behaviour of the sensors distinguishing between empty circuit (air at 1 bar), filled circuit (CO_2 gas at 58 bar) and circuit with flow (CO_2 at various pressures) whilst in atmospheric and vacuum surroundings. To summarize these tests, it was found, that the described rise in temperature only takes place in vacuum and with CO_2 flowing in the circuit at a temperature lower than room temperature. At 19°C temperature set-point the deviation was 0.1°C, however at 15°C temperature set-point the difference was already 1°C, with an increasing trend for lower temperature set-points. After further investigation two different error sources could be distinguished:

- Self-heating effect of RTD sensors
- Insertion error of shafted sensors.

Figure D.8 illustrates the effect of both errors. The measurement of four RTD sensors within the circuit are shown in comparison with two thermocouples measuring the inlet and outlet temperature outside of the vessel. The temperature set-point of the CO_2 is 15°C starting in atmospheric conditions (vessel loosely closed). This is illustrated as green background on the plot. At some point the vacuum pump is switched on and the vacuum starts to decrease within the vessel. This is illustrated in grey. For this test the data acquisition is switched on only for a few seconds and the dashed lines demonstrate when the DAQ is off. After switching on the DAQ each time a small increase in temperature can be detected. This effect is due to the self-heating effect of RTD sensors. RTDs are passive sensors, thus they require the passage of a measurement current to produce a useful signal. This current is able to heat the sensing element and raises its temperature which may result in errors of major or minor effect depending on the excitation current level and the surroundings where the sensor is installed.

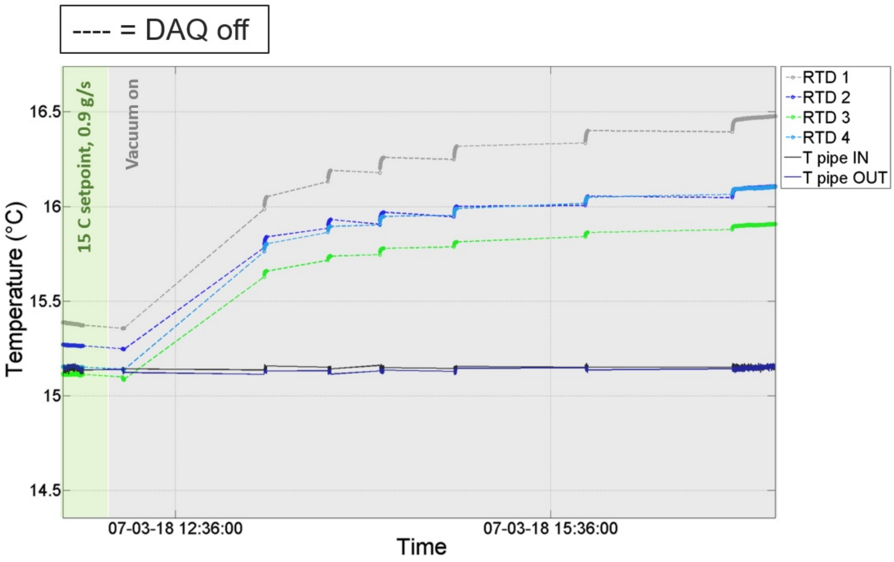

Figure D.8: RTD measurement error during vacuum operation.

Self-heating of a resistance thermometer is expressed in mW/°C. This is the power in milli-watt which raises the internal temperature of the sensor by 1°C. The higher this value the more this effect is negligible. Using very low currents can reduce the elevated temperature error for a given sensor. The consequential error is inversely proportional to the capacity of the sensor to evacuate the additional heat. This depends on the sensor material and the environment of installation, e.g. where the sensor is immersed in. The error in a non-moving gas can be multiple times higher compared to the error found for a flowing or circulating fluid. Since in vacuum the additional heat cannot be removed by convection or other means it will remain in the sensor material or spread to adjacent objects by conduction. Measuring micro-fluidic behaviour on very small scales this can cause major errors in the measurement itself but also in the very fine tuned heat load applied to the test section. The tests were carried out with the above mentioned readout chain from National Instruments using the NI 9217 (4 RTD, 0Ω to 400Ω, 24 Bit) and the standard excitation current of 1 mA per channel. To compensate further for this self-heating effect a newly developed multiplexing board could be obtained from colleagues from the EP-DT-DI group at CERN (X. Pons et al.). Here very low excitation currents can be applied to the sensors (μA) and a new powering and multiplexing scheme is possible. Instead of powering the sensors continuously they can be powered only for a specified amount of time and are then switched off again to avoid any long-term overheating. In the future the same tests as described before could be carried out with this new read-out configuration to compare with the data obtained with the old read-out system. After further analysis, the second error causing the major increase in sensed temperature was found to be due to an insertion error of shafted temperature sensors. All stem thermometers develop a temperature gradient along their shaft caused by the difference between the measured and the ambient temperature. Depending on the temperature difference between the two media, this can cause errors in the measured signal. This effect can be reduced by inserting the sensor further into the measured medium where the required insertion depth is measured in stem diameters. The effect also depends on the ambient surroundings to which the extruding part of the sensor is exposed to. This can be e.g. air flow or insulation material [163]. In vacuum this means all the heat from the ‘ambient side’ will conduct into the sensing element and if not sufficiently inserted into the medium causes large signal distortions. A combination of both – insufficient insertion depth and operation in vacuum - is believed to be the cause of the found temperature misrepresentations. For more information on temperature calibration and sensor immersion depth, please refer to [163]. The solution for this problem lies in the manufacturing of fully custom-made RTD sensors. Hence a bare Pt100 sensing element is placed directly into the flow with the help of a specially machined PEEK sensor housing. It is fixed within the housing by means of CO_2 ‘resistant’ epoxy. The sensors leak-tightness and stiffness is assured by filling the remaining housing with glue. Thus the new sensors are electrically and thermally insulated from the remaining circuit and cannot develop a temperature gradient along their stems. Figure D.9 gives an example of the custom-made RTD sensors (with nut and ferrule) which are installed now at all the experimental measurement points (MP) described in the main text.

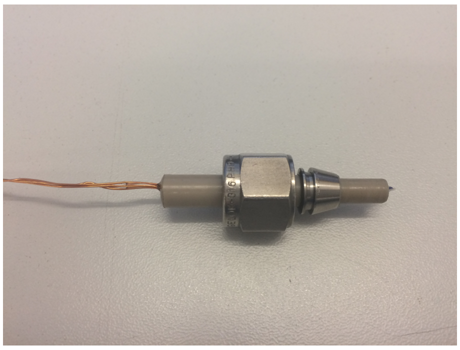

Figure D.9: Custom-made RTD sensor with PEEK housing, in 4-wire configuration.

APPENDIX E

Uncertainty analysis

E.1 Basics on measurement uncertainties

The calculation of the experimental uncertainties and their propagation is carried out based on various references dedicated to experimental error analysis which are summarized in e.g. [164]. An experimental result Y which is computed from N measured parameters $X_{1...N}$ can be written as the so-called measurement equation:

$$Y = f\,(X_1,\ X_2,\ X_{3,}...\,X_N). \tag{E.1}$$

The corresponding propagation law leads to an estimate of the measurand Y, which is denoted y. The estimate is obtained using input estimates for X_1, X_2, ... X_N, denoted x_1, x_2, ... x_N. Thus it is for the resulting estimate of Y:

$$y = f\,(x_1,\ x_2,\ x_{3,}...\,x_N). \tag{E.2}$$

The uncertainty of y arises from the uncertainty u_i of the different input estimates x_i. These components of uncertainty are called standard uncertainty and are equal to the positive square-root of the estimated variance. Linking all the standard uncertainties from the input estimates together leads to the combined standard uncertainty of the measurement result y, which is denoted $u_c(y)$. To obtain the estimated standard deviation of the result y there is the positive square root of the estimated variance $u_c^2(y)$. It can be written as

$$u_c^2(y) = \left(\frac{\partial f}{\partial_{x_1}}\right)^2 u^2(x_1) + \left(\frac{\partial f}{\partial_{x_2}}\right)^2 u^2(x_2) + ... + \left(\frac{\partial f}{\partial_{x_N}}\right)^2 u^2(x_N). \tag{E.3}$$

Equation E.3 is written on the basis of a first-order Taylor series approximation of the measurement equation E.1. It is often called the law of propagation of uncertainty, whilst the partial derivatives $\partial_f / \partial_{x_i}$ are called sensitivity coefficients and are determined algebraically or numerically.

E.2 Instrumentation accuracy

The uncertainties of all explicitly measured values are obtained through the sensor calibration data given by the manufacturer. Table E.1 lists the measurement characteristics of the used instrumentation.

Note that the uncertainty of all temperature sensors is improved after calibration (see E.3). The instrument specifications of the National Instrument modules are listed in more detail in [165].

Measurement	Device	Calibration range	Uncertainty
ΔP	Differential pressure transducer	0 ÷ 3 bar	± 0.005 % of full scale
P_1	absolute pressure transducer	0 ÷ 100 bar	±0.04 % of full scale
P_2	absolute pressure transducer	0 ÷ 100 bar	±0.04 % of full scale
P_4	absolute pressure transducer	0 ÷ 100 bar	±0.04 % of full scale
P_{vacuum}	vacuum gauge	5×10-9 ÷ 1000 mbar	±30% of reading
T_{1-6}	RTD Pt100 (before calibration)	(-200 ÷ 600 ˚C)	±(0.15 + 0.002|T|) ˚C
$T_{wallouter}$	thermocouples K-type (before calibration)	- 50 ÷ 250 ˚C	±1.5 ˚C
$\dot{m}$	Coriolis mass flow meter 1	0.03 ÷ 0.6 kg/min	±0.2 % of reading
$\dot{m}$	Coriolis mass flow meter 2	12 ÷ 600 g/h CO2	±0.2 % of reading + 0.5 g/h
$V_{Jouleheater}$	Power supply Joule heater: volt meter	0 ÷ 18 V	±0.2 % + 1 digit
$A_{Jouleheater}$	Power supply Joule heater: ampere meter	0 ÷ 20 A	±0.5 % + 1 digit
$V_{pre-heater}$	Power supply pre-heater: volt meter	0 ÷ 18 V	±0.2 % + 1 digit
$A_{pre-heater}$	Power supply pre-heater: ampere meter	0 ÷ 20 A	±0.5 % + 1 digit
$V_{post-heater}$	Power supply post-heater: volt meter	0 ÷ 35 V	±0.2 % + 1 digit
$A_{post-heater}$	Power supply post-heater: ampere meter	0 ÷ 10 A	±0.5 % + 1 digit

Table E.1: Measurement equipment.

E.3 Calibration and uncertainty of temperature sensors

E.3.1 Calibration and uncertainty of the Pt100 probes

The calibration of the six RTDs used in the experimental unit is realized by means of a water bath and a Secondary Platinum Resistance Thermometer (SPRT) as reference (Fluke SPRT 5626 with Fluke readout 1502A). The calibration is carried out in conformity with guidelines given by the International Temperature Scale of 1990 (ITS-90) [166]. The resistance of the Pt100 to be calibrated is measured whilst submerged in the water bath. The reference is also submerged in the bath at the same depth and in close proximity of the probes to be calibrated reading out the temperature. Figure E.1 shows the layout of the calibration setup. This was carried out at three different temperatures above 0°C: first an ice bath was prepared, then the room temperature was measured in the water bath after equalizing with the air temperature and a hot bath at about 60°C was prepared. For following calculations the triple point of water measured with the experiment probes is needed. However, since it was not possible to use a triple point cell, the resistance at the triple point for all four probes was extracted from the data where the reference showed 0.01°C. According to ITS-90 calibrations are parameterized in terms of the dimensionless resistance ratio W(T) as defined by

$$W(T) = \frac{R(T)}{R(T_{H_2O,TP})}, \tag{E.4}$$

where R(T) is the resistance of the probe at the measured temperature and R($T_{H_2O,TP}$) is the resistance of the probe at the water triple point (H_2O, TP). Furthermore ITS-90 specifies a reference function W_r(T) which is based on a highly accurate SPRT and used to approximate W(T) of any sensor. The

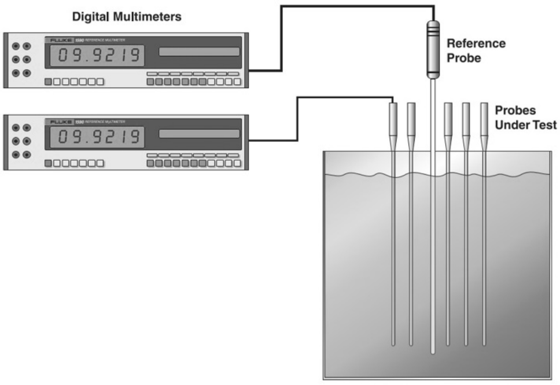

Figure E.1: Setup for the RTD temperature calibration (Fluke).

function can be written for the range from 273.15 K to 1234.93 K as follows:

$$W_r(T) = C_0 + \sum_{i=1}^{i=9} C_i \left[\frac{\left(\frac{T}{K}\right) + 754.15}{481} \right]^i . \tag{E.5}$$

The values for C_0 and C_i are predefined and are given in the ITS-90 guideline:

C_0	2.78157254
C_1	1.64650916
C_2	-0.13714390
C_3	-0.00649767
C_4	-0.00234444
C_5	0.00511868
C_6	0.00187982
C_7	-0.00204472
C_8	-0.00046122
C_9	0.00045724

However ITS-90 also accounts for the deviation of the sensor from the ideal representation of W_r(T). A deviation function is defined as the difference between the observed resistance ratio and the reference function value

$$\Delta W(T) = W(T) - W_r(T). \tag{E.6}$$

For the sub-range between 273.15 K and 429.7485 K, ΔW(T) is given by

$$\Delta W(T) = a \cdot [W(T) - 1] . \tag{E.7}$$

Plotting the two representations of ΔW(T) against each other using the measured data and applying a linear regression allows to define the calibration coefficient a as the slope of the regression line. Figure E.2 shows this relationship for one RTD in example. The equations of the linear fit can be found on the right.

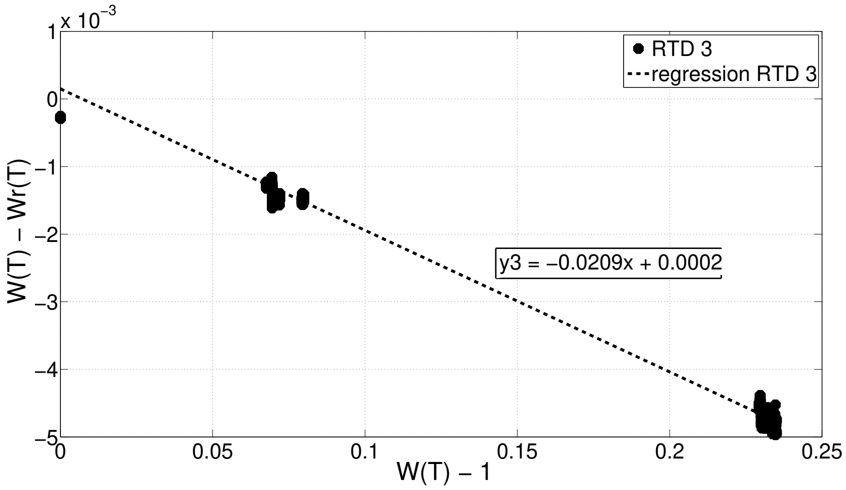

Figure E.2: Propagation of the deviation function.

With this regression the calibration coefficient can be obtained. Table E.2 shows the fitted calibration coefficients and the uncertainty of this regression which can be neglected for the following calibration.

	a	u(a_{cal})
RTD 3	-0.0209	7.85e-05

Table E.2: Uncertainty of calibration coefficient.

With the calibration coefficient the measured temperature in °C can be calculated from the inverse function of equation E.5. This is given by

$$\frac{T}{K} - 273.15 = D_0 + \sum_{i=1}^{i=9} D_i \left[\frac{W_r(T) - 2.64}{1.64}\right]^i . \qquad \text{(E.8)}$$

The values for D_0 and D_i are predefined and are given in the ITS-90 guideline:

D_0	439.932854
D_1	472.418020
D_2	37.684494
D_3	7.472018
D_4	2.920828
D_5	0.005184
D_6	-0.963864
D_7	-0.188732
D_8	0.191203
D_9	0.049025

Figure E.3 shows in which way the measured resistance can now be related to temperature. Only the case for RTD 3 is shown as example. A second regression has to be applied and the uncertainty u(T_{cal})

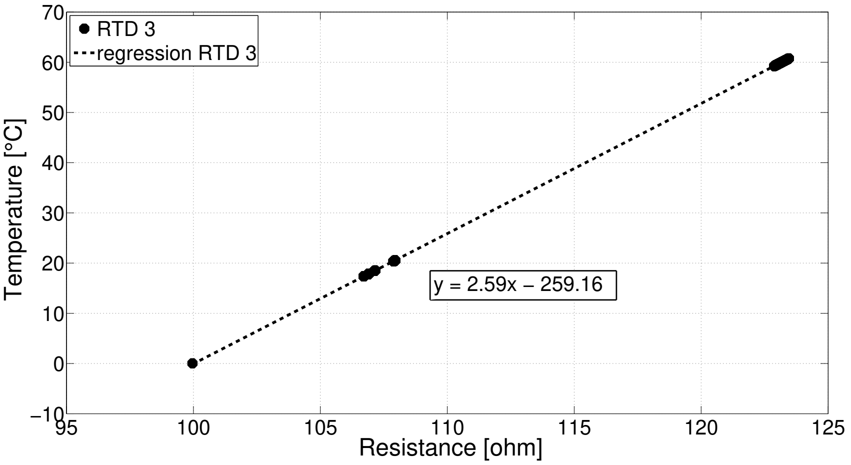

Figure E.3: Applied regression for RTD calibration.

of this regression results in 0.0134 °C for all the six sensors. This results in an overall calibration uncertainty of the sensors which is given in Table E.3. The NI module 9217 is therefore re-calibrated as well and the initial uncertainty arising from the module is included in the given uncertainty. Thus the calibration uncertainty is equal to the measurement uncertainty.

Calibration uncertainty for RTD sensors [K]	
SPRT (with factor 2)	0.004
regression uncertainty of SPRT	0.0001
readout uncertainty of SPRT	0.006
regression uncertainty of sensor temperature	0.0134
	0.0152

Table E.3: Calibration uncertainty of RTD sensors.

E.3.2 Calibration and uncertainty of the thermocouples

The calibration of the thermocouples used in the experimental section is also realized by means of a water bath and the SPRT as reference. The calibration is again carried out in conformity with guidelines given by the International Temperature Scale of 1990 (ITS-90). In this case there are different formulas given for the particular type of thermocouple. The thermocouples which are used for the experiment are K-type thermocouples and are calibrated according to this procedure. The voltage of the thermocouples to be calibrated is measured whilst submerged in the water bath (ice bath, room temperature bath and 60 °C bath). The reference is also submerged in the bath at the same depth and in close proximity of the probes to be calibrated reading out the temperature of the water. For the K-type thermocouple the ITS-90 guideline defines a reference function as follows for temperatures below 0 °C,

$$E = \sum_{i=0}^{i=n} c_i (T)^i . \tag{E.9}$$

The equation for temperatures above 0 °C can be written as

$$E = \sum_{i=0}^{i=n} c_i (T)^i + \alpha_0 \cdot e^{\alpha_1 (T - 126.9686)^2}, \tag{E.10}$$

where E the thermoelectric voltage of the sensor in millivolts and T the temperature measured by the SPRT in degree Celsius. The coefficients c_i and α are predefined and given for the temperature range between 0 and 1372 °C:

c_0	-1.7600413686E-02
c_1	3.8921204975E-02
c_2	1.8558770032E-05
c_3	-9.9457592870E-08
c_4	3.1840945719E-10
c_5	-5.6072844889E-13
c_6	5.6075059059E-16
c_7	-3.2020720003E-19
c_8	9.7151147152E-23
c_9	-1.2104721275E-26

α_0	1.185976E-01
α_1	-1.183432E-04

Comparing the reference function with the actual measurement shows an obvious offset from this function after applying two linear fits to the two data sets. Figure E.4 shows this relation in example for one thermocouple. To compensate this difference the necessary mathematical calculations are applied to adjust the raw measurement to the reference data based on the slope and the intercept of

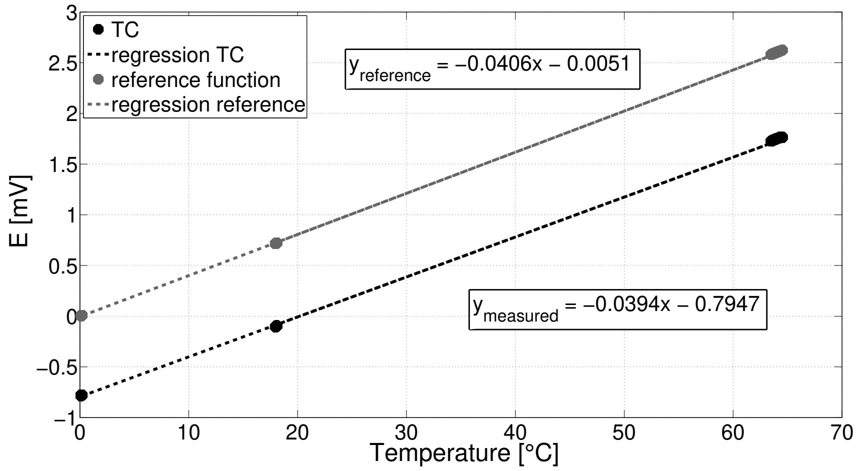

Figure E.4: Temperature vs. thermo-electric voltage: measured data and reference function.

both regression lines. After this the actual measured temperature could be deduced from an inverse function also given in the ITS-90 guidelines. However, [167] recommends a rational polynomial function instead of using the NIST polynomial equation given for K-type thermocouples. This rational polynomial can be written as follows

$$T = T_0 + \frac{(E - E_0)\left[p_1 + (E - E_0)\left[p_2 + (E - E_0)\left[p_3 + p_4(E - E_0)\right]\right]\right]}{1 + (E - E_0)\left[q_1 + (E - E_0)\left[q_2 + q_3(E - E_0)\right]\right]}, \tag{E.11}$$

where T is the measured thermocouple temperature in °C and E is the thermocouple voltage in milli-volt. The coefficients T_0, V_0, p_i and q_i were found by means of a least squares curve fit to the NIST data [167]. The coefficients are given for the temperature range between 0 and 350 °C as follows:

T_0	1.7500000E+02
V_0	7.1403100E+00
p_1	2.5040994E+01
p_2	3.8091126E+00
p_3	9.8221418E-01
p_4	6.7337382E-02
q_1	1.5021861E-01
q_2	4.0587216E-02
q_3	2.8615924E-03

With this rational polynomial equation the fluctuating errors resulting from the NIST equation can be homogenized and brought down to 0.022 °C (compare: NIST 0.05 °C) for the whole range looked at. The final calibration uncertainty in degree Celsius is the regression uncertainty when plotting the corrected thermocouple voltage versus the calculated temperature. An example is given in Figure E.5. The uncertainties arising from these regressions and calculations are summarized in Table E.4 where the final total measurement uncertainty for the thermocouples is shown. This can be found for all the individual sets of thermocouples used for the different tube dimensions. For following uncertainty analysis the uncertainty of the thermocouples measuring the outer wall temperature of the experimental tubes is averaged over all calibrated thermocouples (not shown) and 0.1 K is used.

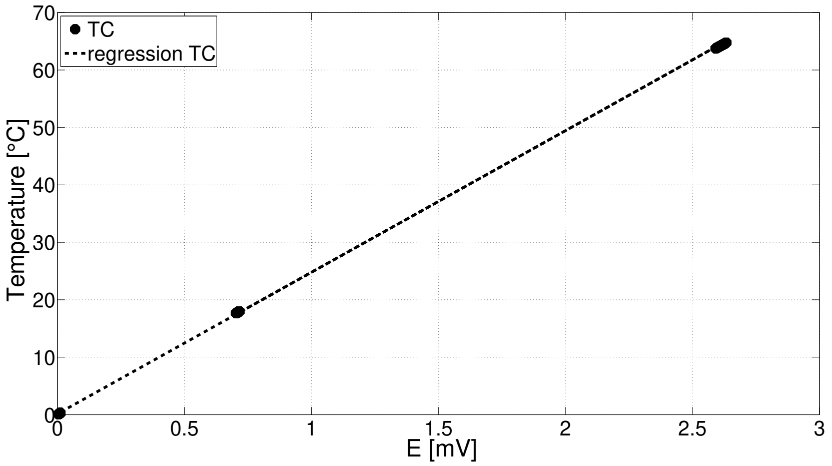

Figure E.5: Corrected thermoelectric voltage vs. calculated temperature.

ID [mm]	0.5	1.0	2.15
SPRT uncertainty (with factor 2) [K]	0.004		
regression uncertainty of SPRT [K]	0.0001		
readout uncertainty of SPRT [K]	0.006		
regression uncertainty (calibration uncertainty) [K]	0.137	0.107	0.130
rational inverse function (measurement uncertainty) [K]	0.022		
total measurement uncertainty [K]	**0.139**	**0.110**	**0.132**

Table E.4: Total measurement uncertainties for K-type thermocouples.

E.4 Measurement and uncertainty of pressure

The uncertainty of the pressure measurement (absolute and differential) arises from the sensor accuracy (analog output, 4-20 mA) and from the read-out module (analog input, +/- 20 mA, NI 9203). The evolution of the combined uncertainty with pressure for the absolute pressure sensors (GE, UNIK 5000) is given in Figure E.6. The evolution of the combined uncertainty with pressure for the differential pressure sensors (Endress+Hauser) is given in Figure E.7.

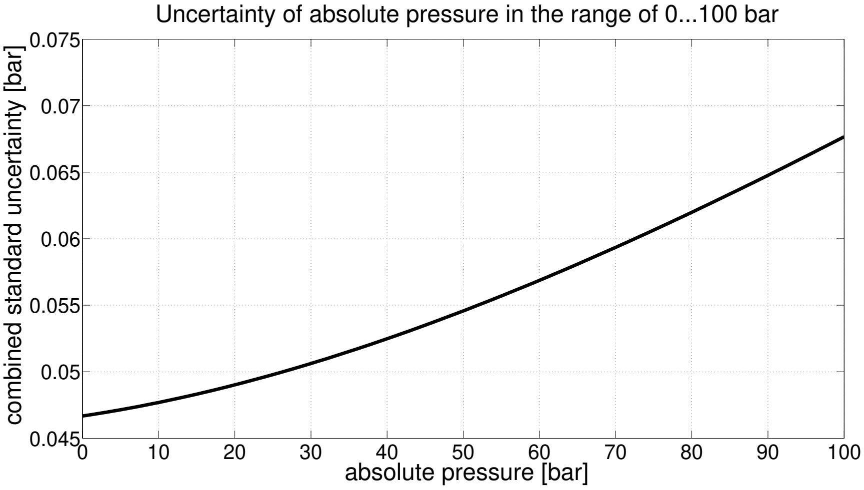

Figure E.6: Uncertainty of the absolute pressure.

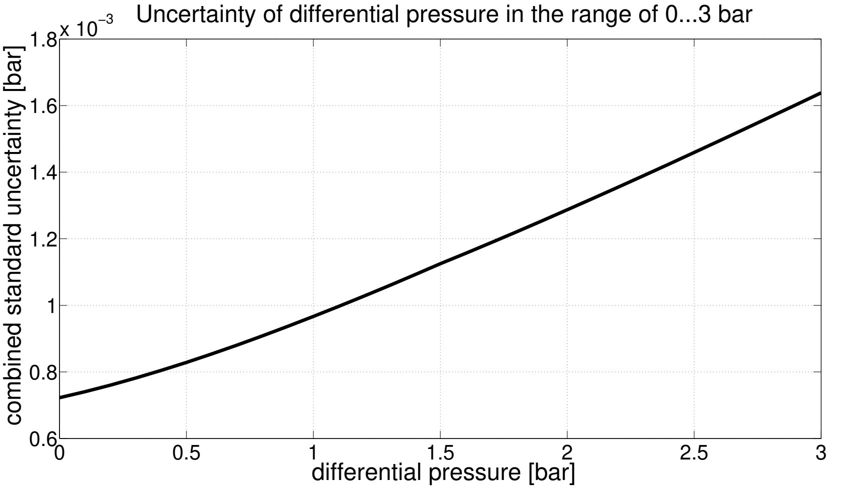

Figure E.7: Uncertainty of the differential pressure (E+H).

E.5 Measurement and uncertainty of saturation temperature

The uncertainty of the saturation temperature is determined by means of the absolute pressure measurements in the experiment. Its development for increasing saturation temperatures can be found in Figure E.8.

E.6 Measurement and uncertainty of relevant geometries and distances

The relevant test section dimensions are measured, estimated or given by the manufacturer. The tolerances of the inner and outer diameter of the stainless steel tubes are given by the manufacturer.

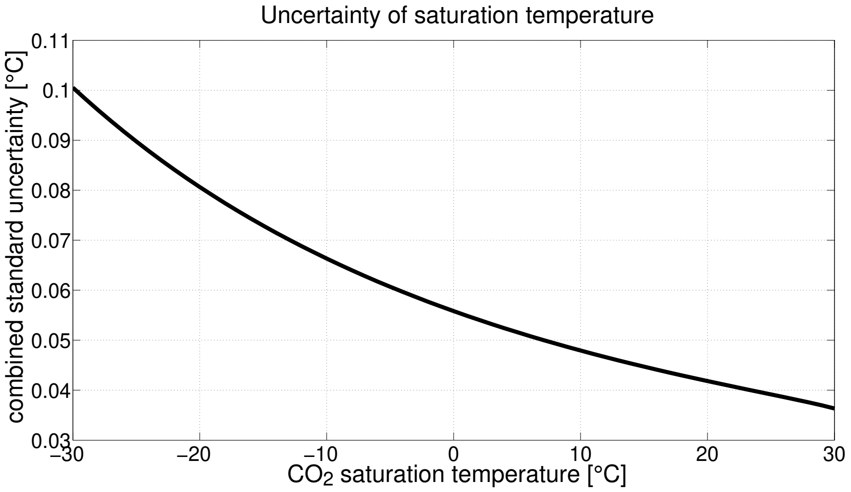

Figure E.8: Uncertainty of the CO_2 saturation temperature.

For all tube dimensions in stainless steel and titanium the same tolerances apply: ID tolerance and OD tolerance +/- 0.0254 mm. To improve the uncertainty related to the tube diameters the inner and outer diameters of the three tube dimensions were measured with an optical microscope. An overall uncertainty for the stainless steel tubes can be deduced from these results which is used for the remaining part of the error analysis and presented in Table E.5.

stainless steel			
ID [mm]	deviation [mm]	OD [mm]	deviation [mm]
0.5	0.0064	1.58	0.0060
1	0.0066	1.58	0.0057
2.15	0.0073	3.17	0.0063

Table E.5: Uncertainty of inner and outer diameter of the stainless steel test tubes.

Following remaining lengthwise dimensions are measured with a Vernier calliper (ABSOLUTE Digimatic, Mitutoyo, accuracy ± 0.02 mm) and the uncertainties are estimated accordingly:

- L_q heated tube section : 180 mm ± 1 mm; 170 mm ± 1 mm

- L_{DP} tube length: 200 mm ± 0.5 mm

E.7 Uncertainties of REFPROP software

It is assumed that the uncertainties caused by the evaluation of thermodynamic state variables by the REFPROP software does not cause relevant errors and are neglected in this error analysis.

E.8 Calculation and uncertainty of derived parameters

The uncertainties for all derived parameters are calculated according to the single-sample uncertainty analysis suggested by Moffat [168]. With this method only the precision error is taken into account whilst bias errors are neglected. Moffat refers to the error propagation equation given by Kline and McClintock [169] which was mentioned before as equation E.3. The general uncertainty with constant odds is calculated for following derived parameters:

- mass flux G [$\mathrm{kg/m^2s}$],
- heating power Q [W],
- heat flux q [$\mathrm{W/m^2}$],
- heat transfer coefficient α [$\mathrm{W/m^2K}$] and
- Nusselt number.

E.8.1 Calculation and uncertainty of the mass flux G

For the mass flux within the metal tubes following Table E.6 was developed as test matrix based on common mass flux values found in literature.

mass flux G [$\mathrm{kg/m^2s}$]		
2.15 mm ID	1 mm ID	0.5 mm ID
-	-	1800
-	-	1400
-	1200	1200
-	1000	1000
800	800	-
600	600	-
500	500	-
400	400	-
200	200	-
150	150	-
100	100	-

Table E.6: Mass flux test matrix.

According to Table E.6, Table E.7 lists the corresponding mass flow rates.
The mass flux G is calculated with following formula:

$$G = \frac{\dot{m}}{\frac{\pi}{4}D_i^2}. \tag{E.12}$$

The uncertainty of the mass flux is calculated with

$$\left(\frac{u_c(G)}{G}\right)^2 = \left(\frac{u(\dot{m})}{\dot{m}}\right)^2 + 2^2\left(\frac{u(Di)}{Di}\right)^2. \tag{E.13}$$

mass flow rate $\dot{m}$ [g/s]		
2.15 mm ID	1 mm ID	0.5 mm ID
-	-	0.342
-	-	0.266
-	0.986	0.228
-	0.822	0.190
2.983	0.658	-
2.237	0.493	-
1.864	0.411	-
1.492	0.329	-
0.746	0.164	-
0.559	0.123	-
0.373	0.082	-

Table E.7: Mass flow rate test matrix.

With the given uncertainty propagation equation, the accuracies of the two different flow meters and the deviations of the inner diameter of the stainless steel tubes this results in Table E.8 for the corresponding uncertainties of the derived mass flux.

uncertainty [%]		
2.15 mm ID	1 mm ID	0.5 mm ID
-	-	2.65
-	-	2.65
-	1.32	2.65
-	1.32	2.65
0.63	1.32	-
0.63	1.32	-
0.63	1.39	-
0.63	1.39	-
0.63	1.33	-
0.63	1.34	-
0.78	1.35	-

Table E.8: Uncertainties on mass flow rate test matrix.

E.8.2 Calculation and uncertainty of the heating power Q

The heating power Q applied to the test section is

$$Q = U \cdot I \tag{E.14}$$

and its uncertainty is calculated as

$$u_c^2(Q) = I^2 \cdot u^2(U) + U^2 \cdot u^2(I). \tag{E.15}$$

E.8.3 Calculation and uncertainty of the heat flux q

The heat flux q applied to a cylindrical tube section is calculated with following formula

$$q = \frac{Q}{\pi \cdot L_q \cdot D_i} \tag{E.16}$$

and the uncertainty of the heat flux is calculated with

$$\left(\frac{u_c(q)}{q}\right)^2 = \left(\frac{u_c(Q)}{Q}\right)^2 + \left(\frac{u(Di)}{Di}\right)^2 + \left(\frac{u(L_q)}{L_q}\right)^2. \tag{E.17}$$

For the different stainless steel tube dimensions following uncertainty situations were found for the corresponding heat flux (Figure E.9).

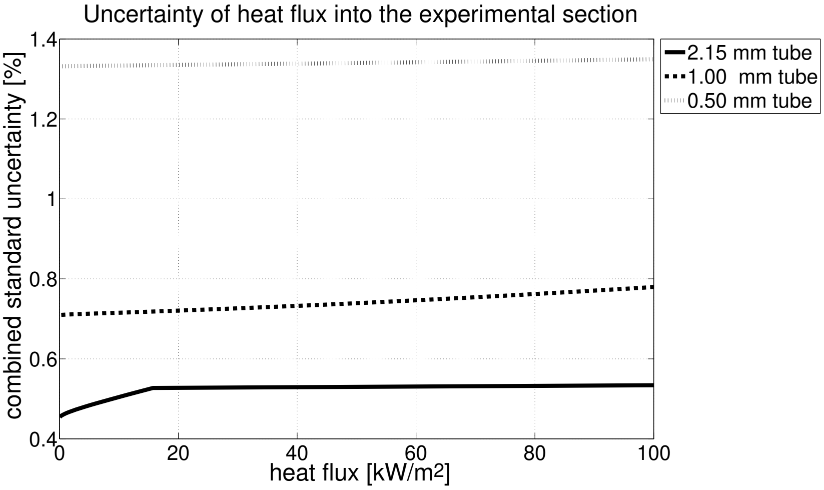

Figure E.9: Uncertainty of the heat flux in the stainless steel tubes.

E.8.4 Calculation and uncertainty of the heat transfer coefficient

The heat transfer coefficient is calculated by means of following formula

$$\alpha = \frac{q}{T_{w,o} - T_{sat} - \Delta T_w}. \tag{E.18}$$

The one-dimensional, radial, steady-state heat conduction equation for a hollow cylinder with a uniform heat flux is used to calculate ΔT_w

$$\Delta T_w = \left[\frac{q \cdot D_i}{4\lambda_{SS316}}\right]\left[\frac{\psi(1 - ln\psi) - 1}{1 - \psi}\right], \tag{E.19}$$

where

$$\psi = (D_o/D_i)^2 \tag{E.20}$$

The uncertainty of the heat transfer coefficient is composed of four major uncertainty sources: (i) the external wall temperature T$_{w,o}$, (ii) the saturation temperature T$_{sat}$, (iii) the power Q applied to the experiment and (iv) the inner and outer diameter of the measured tube. The uncertainty in the length of the heater and the uncertainty of the tabulated value of the thermal conductivity of stainless steel 316 are neglected. Thus following equation for the uncertainty propagation of the heat transfer coefficient can be used for further evaluation:

$$\begin{aligned} u_c^2(\alpha) = {} & \left[\frac{\alpha}{T_{w,o} - T_{sat} - \Delta T_w}\right]^2 u^2(T_{w,o}) + \left[\frac{\alpha}{T_{w,o} - T_{sat} - \Delta T_w}\right]^2 u^2(T_{sat}) + \\ & \left[\frac{\alpha}{T_{w,o} - T_{sat} - \Delta T_w}\frac{\partial \Delta T_w}{\partial Q} + \frac{\alpha}{T_{w,o} - T_{sat} - \Delta T_w}\frac{\partial q}{\partial Q}\right]^2 u^2(Q) + \\ & \left[\frac{\alpha}{T_{w,o} - T_{sat} - \Delta T_w}\frac{\partial \Delta T_w}{\partial D_i} + \frac{\alpha}{T_{w,o} - T_{sat} - \Delta T_w}\frac{\partial q}{\partial D_i}\right]^2 u^2(D_i) + \\ & \left[\frac{\alpha}{T_{w,o} - T_{sat} - \Delta T_w}\frac{\partial \Delta T_w}{\partial D_i}\right]^2 u^2(D_o). \end{aligned} \tag{E.21}$$

Tables E.9 to E.11 give the uncertainties for the heat transfer coefficient in % for the various tube diameters. The notation a|b|c inside the table cells stands for three different saturation temperatures in comparison. These are namely +20 °C, +5 °C and -20°C.

q [kW/m^2] α[kW/m^{2}K]	5	10	20	30	35
5	5.7 | 6.4 | 9	2.8 | 3.2 | 4.5	1.4 | 1.6 | 2.4	1.5 | 1.6 | 2.1	5 | 5 | 5.1
10	11.4 | 12.9 | 17.9	5.7 | 6.4 | 8.9	2.8 | 3.2 | 4.5	2.2 | 2.4 | 3.2	4.8 | 4.9 | 5.2
20	22.8 | 25.8 | 35.8	11.4 | 12.9 | 17.9	5.7 | 6.4 | 8.9	3.9 | 4.4 | 6	5 | 5.3 | 6.4
30	34.3 | 38.8 | 53.7	17.1 | 19.4 | 26.8	8.5 | 9.7 | 13.4	5.7 | 6.5 | 9	5.8 | 6.3 | 8.3
35	40 | 45.3 | 62.7	20 | 22.6 | 31.3	10 | 11.3 | 15.6	6.7 | 7.5 | 10.4	6.3 | 7 | 9.4

Table E.9: Uncertainties on heat transfer coefficient in the 2.15 mm ID stainless steel tubes.

q [kW/m^2] α[kW/m^{2}K]	5	10	20	30	35
5	5.7 | 6.5 | 9.2	2.9 | 3.2 | 5	1.5 | 1.7 | 3.1	1.1 | 1.2 | 2.7	1 | 1.1 | 2.6
10	11.4 | 12.9 | 18	5.7 | 6.5 | 9.1	2.9 | 3.2 | 4.9	1.9 | 2.2 | 3.5	1.7 | 1.9 | 3.2
20	22.9 | 25.9 | 35.9	11.4 | 12.9 | 17.9	5.7 | 6.4 | 9	3.8 | 4.3 | 6.1	3.3 | 3.7 | 5.3
30	34.4 | 38.9 | 53.8	17.2 | 19.4 | 26.9	8.6 | 9.7 | 13.4	5.7 | 6.4 | 9	4.9 | 5.5 | 7.7
35	40.1 | 45.4 | 62.7	20 | 22.7 | 31.4	10 | 11.3 | 15.7	6.6 | 7.5 | 10.4	5.7 | 6.4 | 8.9

Table E.10: Uncertainties on heat transfer coefficient in the 1 mm ID stainless steel tubes.

q [kW/m^2] α[kW/m^{2}K]	5	10	20	30	35
5	5.8 | 6.6 | 10.1	3.1 | 3.4 | 6.5	1.8 | 2 | 5.2	1.5 | 1.6 | 4.9	1.4 | 1.5 | 4.9
10	11.5 | 13 | 18.4	5.8 | 6.5 | 9.9	3 | 3.4 | 6.2	2.2 | 2.4 | 5.3	1.9 | 2.1 | 5
20	23 | 26 | 36.1	11.5 | 13 | 18.3	5.8 | 6.5 | 9.7	3.9 | 4.4 | 7	3.4 | 3.8 | 6.3
30	34.5 | 38.9 | 53.9	17.2 | 19.5 | 27.1	8.6 | 9.7 | 13.7	5.8 | 6.5 | 9.4	4.9 | 5.6 | 8.2
35	40.2 | 45.4 | 62.9	20.1 | 22.7 | 31.5	10 | 11.3 | 15.9	6.7 | 7.6 | 10.8	5.7 | 6.5 | 9.3

Table E.11: Uncertainties on heat transfer coefficient in the 0.5 mm ID stainless steel tubes.

E.8.5 Calculation and uncertainty of the Nusselt number

The Nusselt number Nu is calculated with following formula:

$$Nu = \frac{\alpha D_i}{k} \tag{E.22}$$

and the uncertainty of the Nusselt number is calculated with

$$\left(\frac{u_c(Nu)}{Nu}\right)^2 = \left(\frac{u_c(\alpha)}{Q}\right)^2 + \left(\frac{u(Di)}{Di}\right)^2 + \left(\frac{u(k)}{L_q}\right)^2 . \tag{E.23}$$

APPENDIX F

Additional results

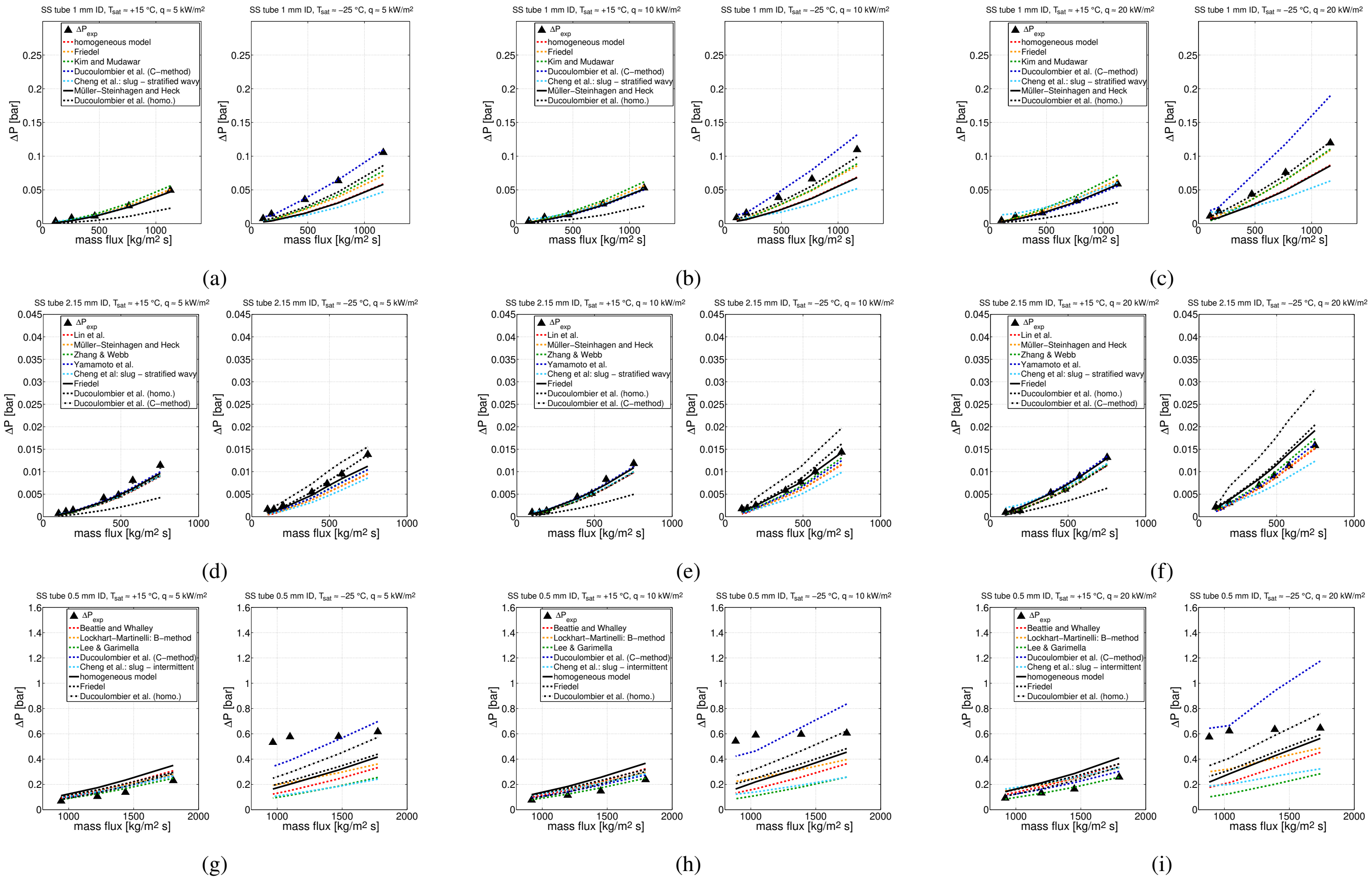

Figure F.1: Pressure drop: Effect of T_{sat} and mass flux on the applicability of different correlations at $T_{sat} \approx 15°C$ and -25°C.

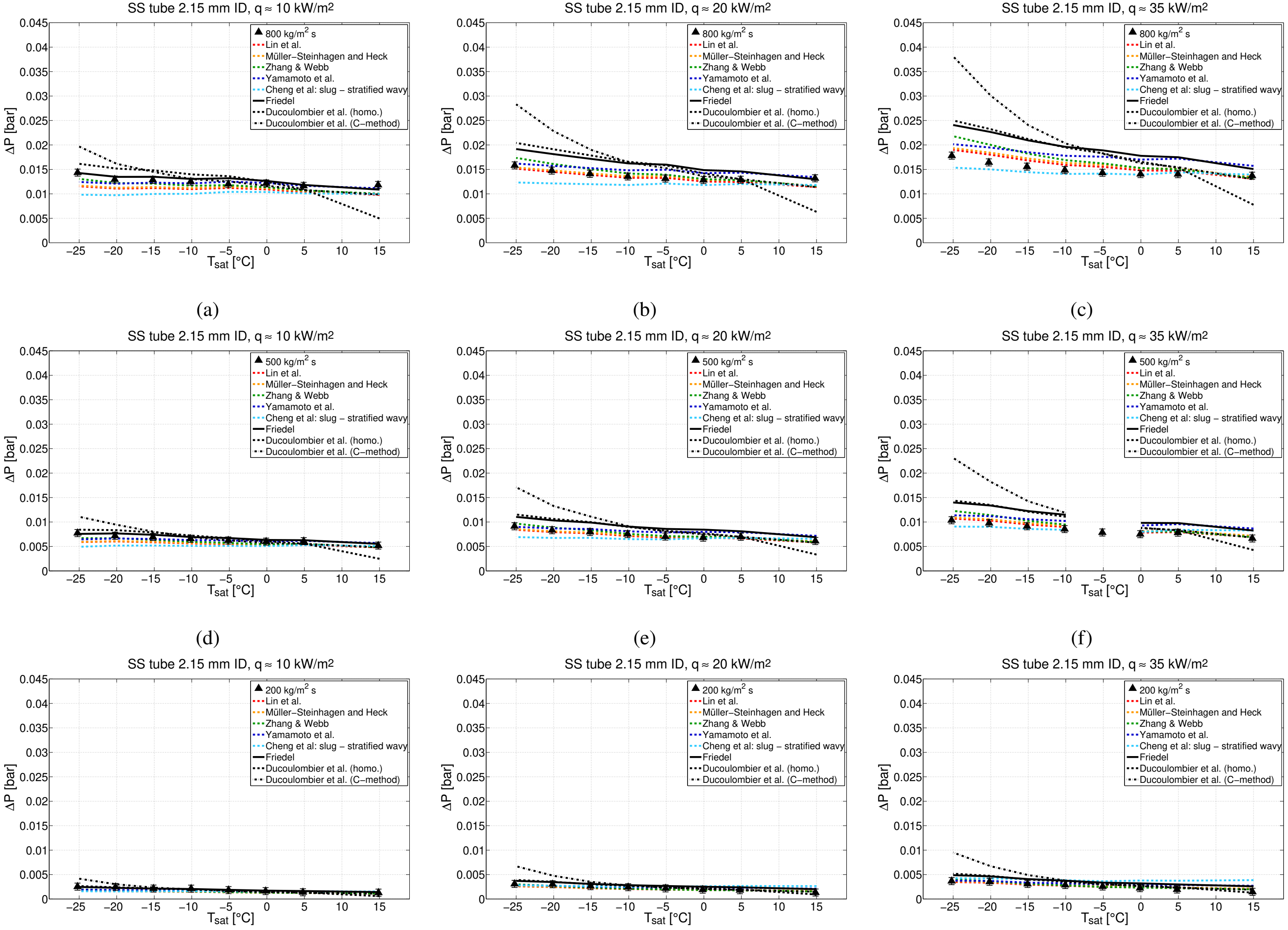

(a) (b) (c)

(d) (e) (f)

(g) (h) (i)

Figure F.2: Pressure drop: Effect of T_{sat} on the applicability of of different correlations: 2.15 mm ID tube.

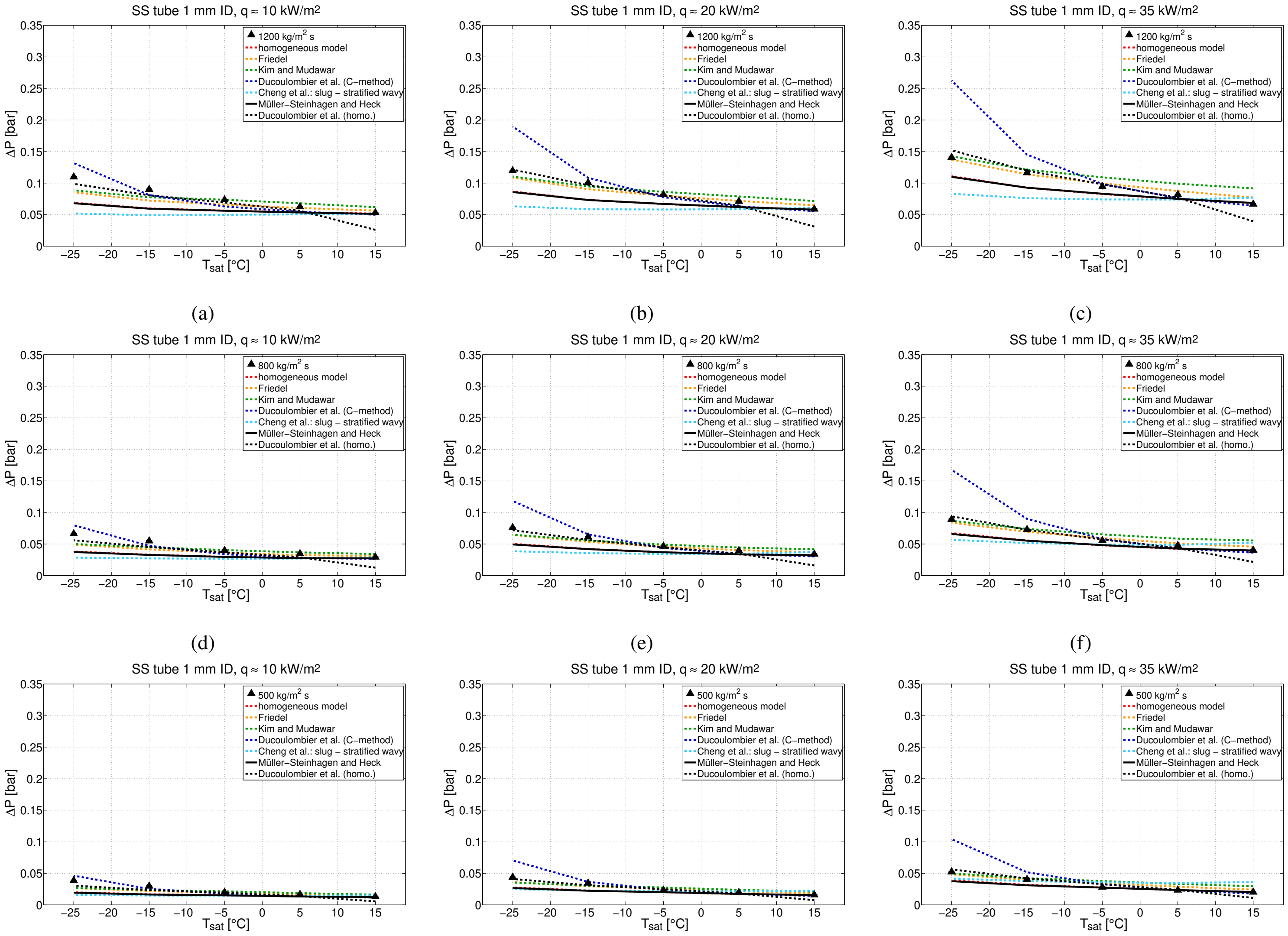

(a) (b) (c)

(d) (e) (f)

(g) (h) (i)

Figure F.3: Pressure drop: Effect of T_{sat} on the applicability of of different correlations: 1 mm ID tube.

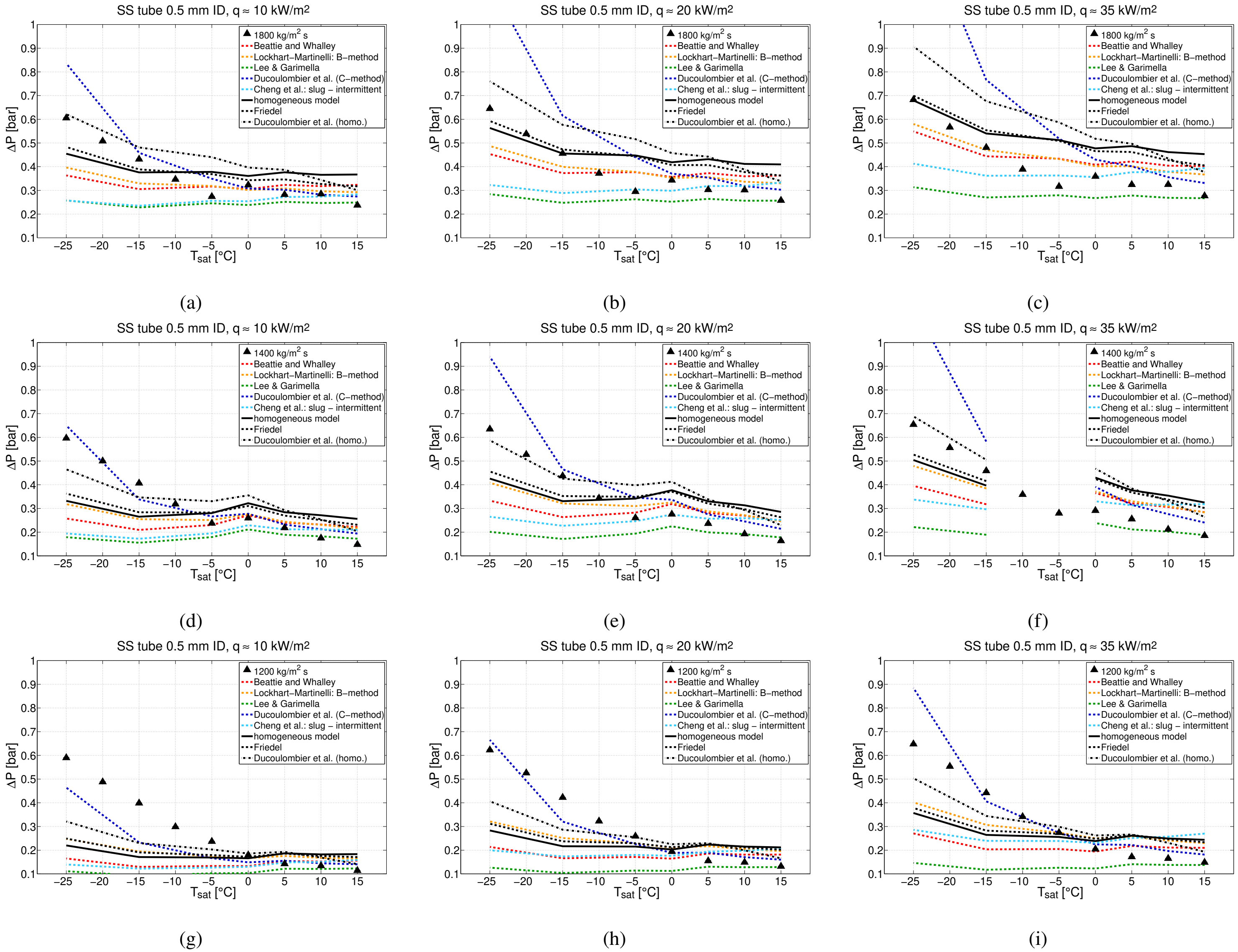

(a) (b) (c)

(d) (e) (f)

(g) (h) (i)

Figure F.4: Pressure drop: Effect of T$_{sat}$ on the applicability of of different correlations: 0.5 mm ID tube.

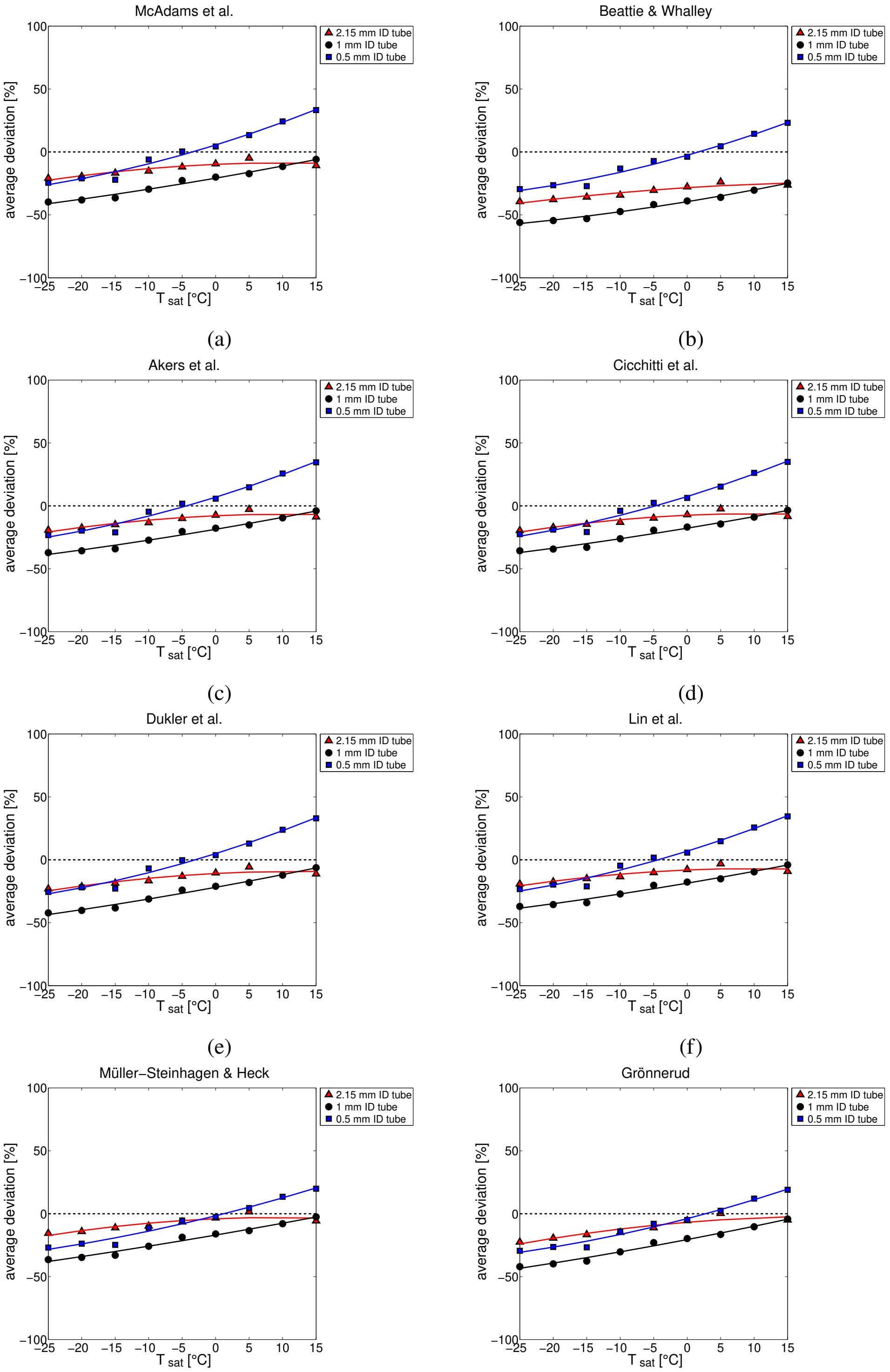

(a) (b)

(c) (d)

(e) (f)

(g) (h)

Figure F.5: Pressure drop: Average deviation of experimental values from selected prediction methods I.

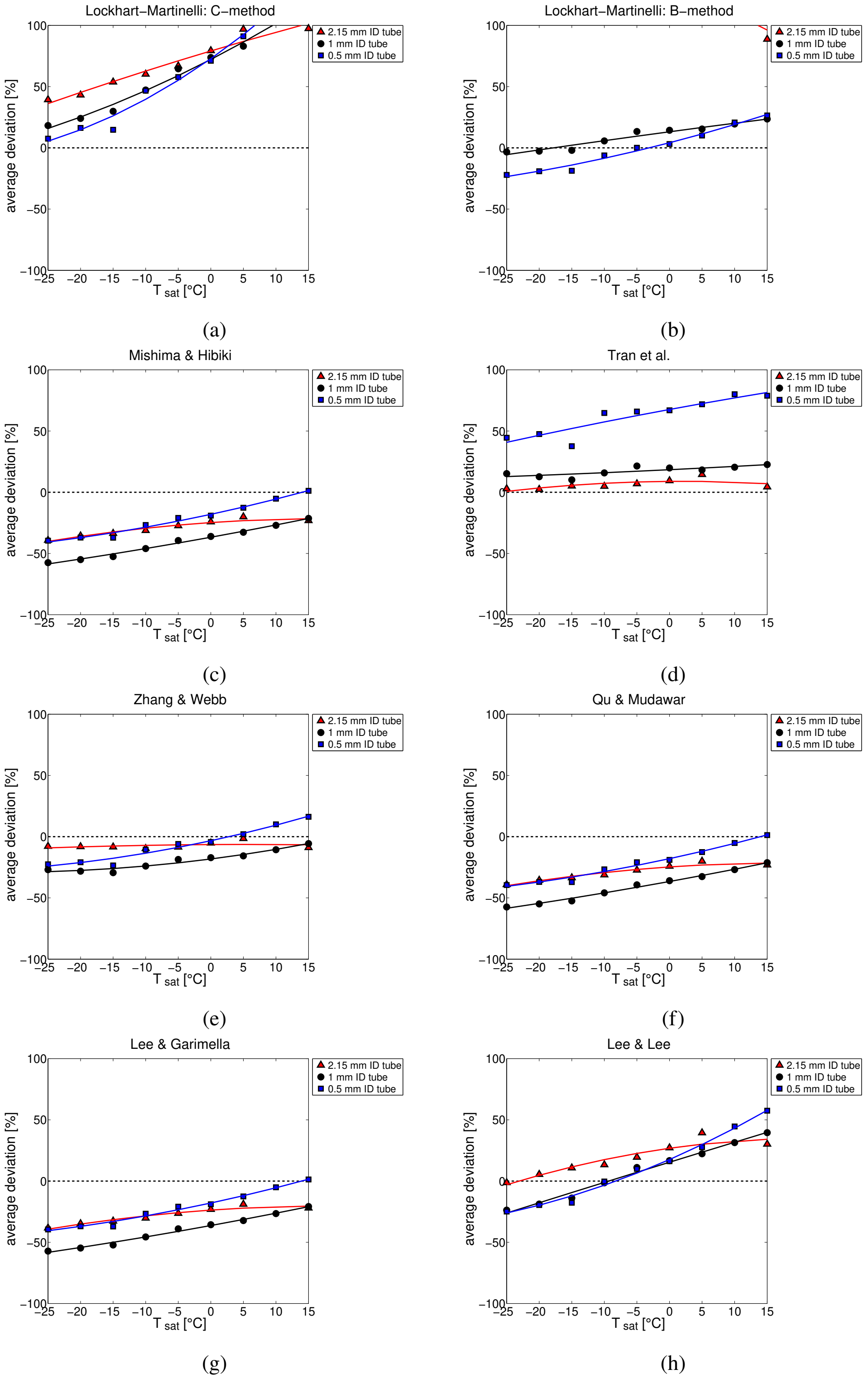

Figure F.6: Pressure drop: Average deviation of experimental values from selected prediction methods II.

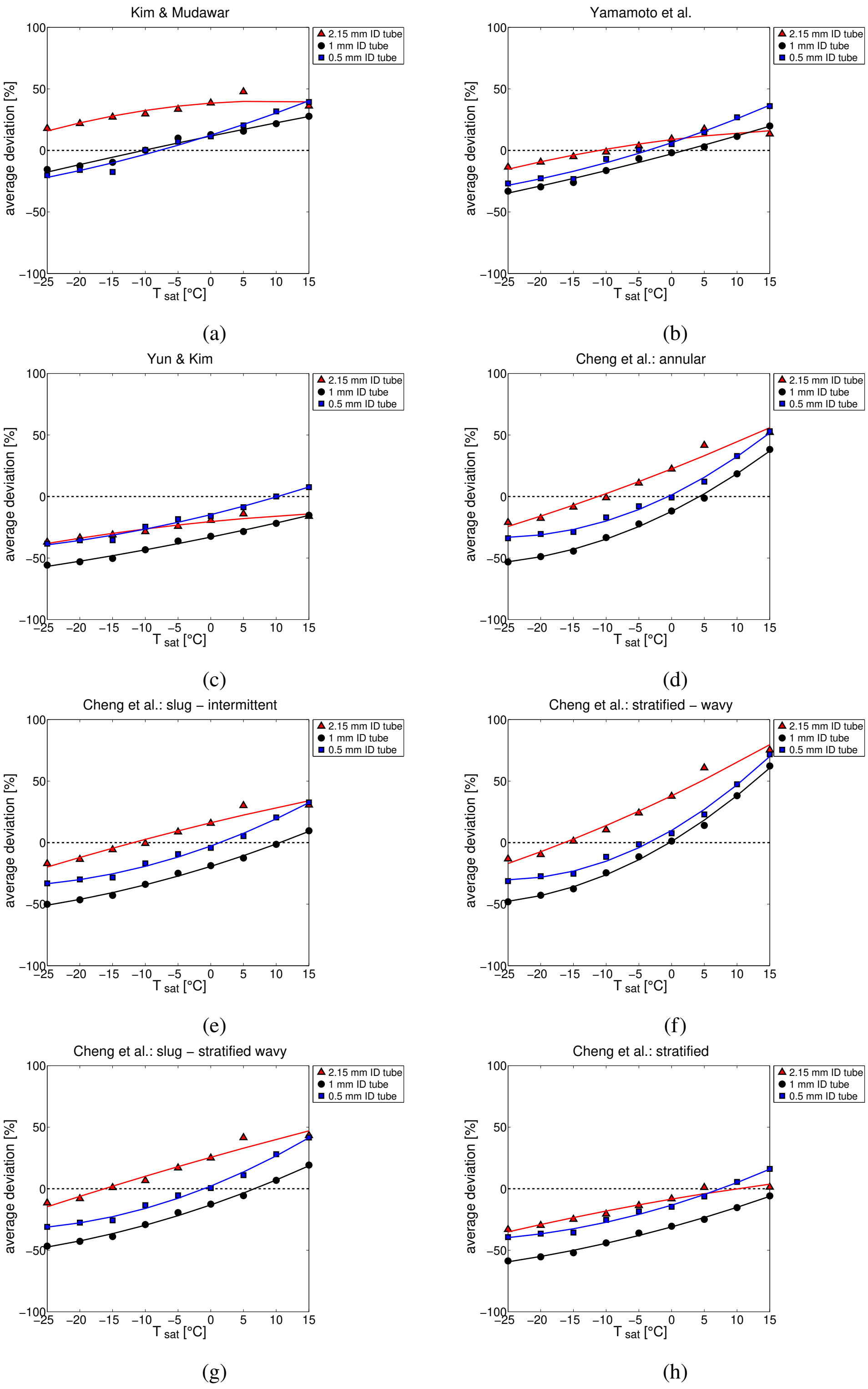

(a) (b) (c) (d) (e) (f) (g) (h)

Figure F.7: Pressure drop: Average deviation of experimental values from selected prediction methods II.

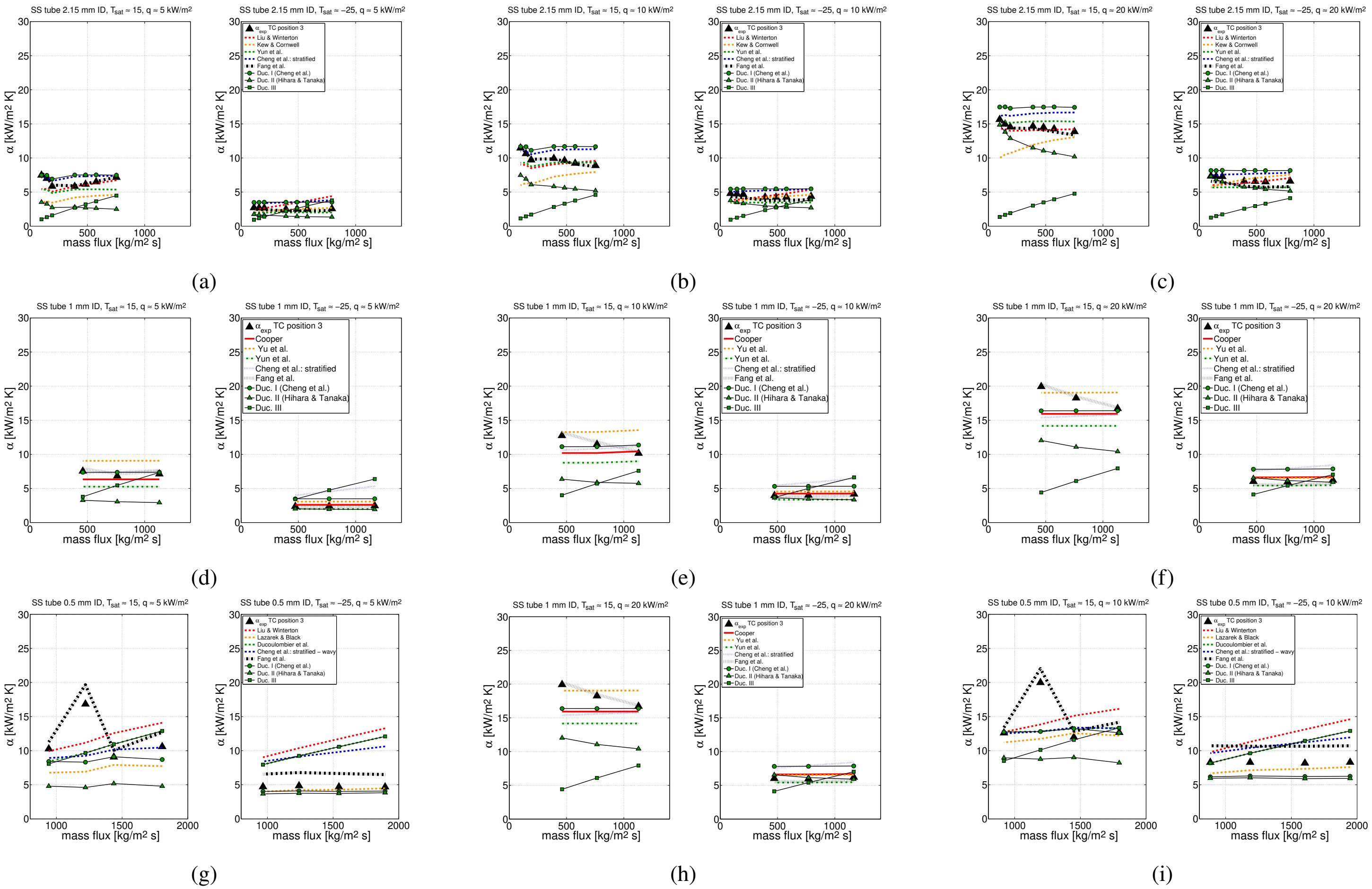

(a) (b) (c)

(d) (e) (f)

(g) (h) (i)

Figure F.8: Heat transfer coefficient: Effect of T_{sat} and mass flux on the applicability of different correlations at T_{sat} ≈ 15°C and -25°C.

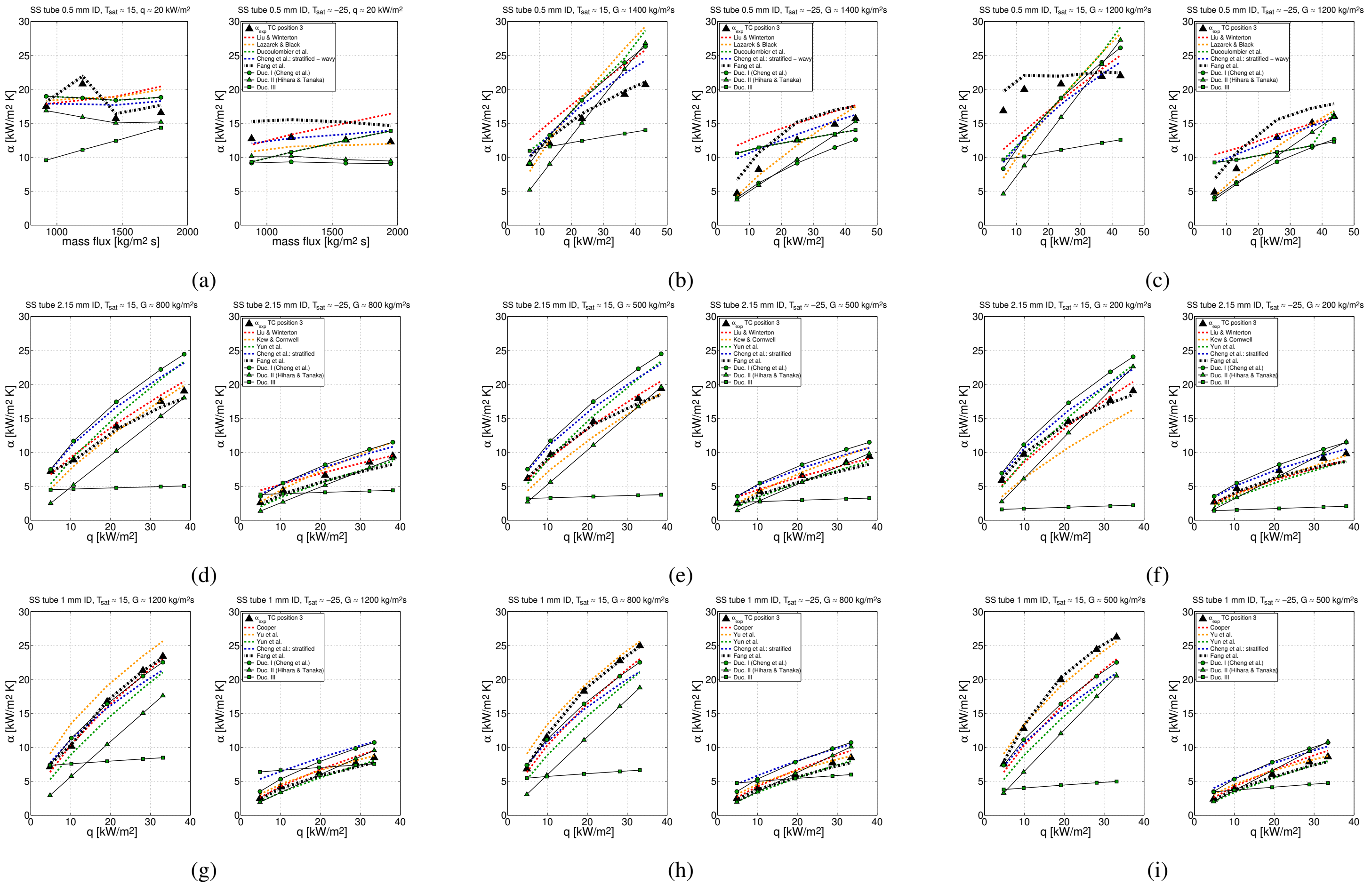

Figure F.9: Heat transfer coefficient: Effect of T$_{sat}$ and heat flux on the applicability of different correlations at T$_{sat}$ ≈ 15°C and -25°C.

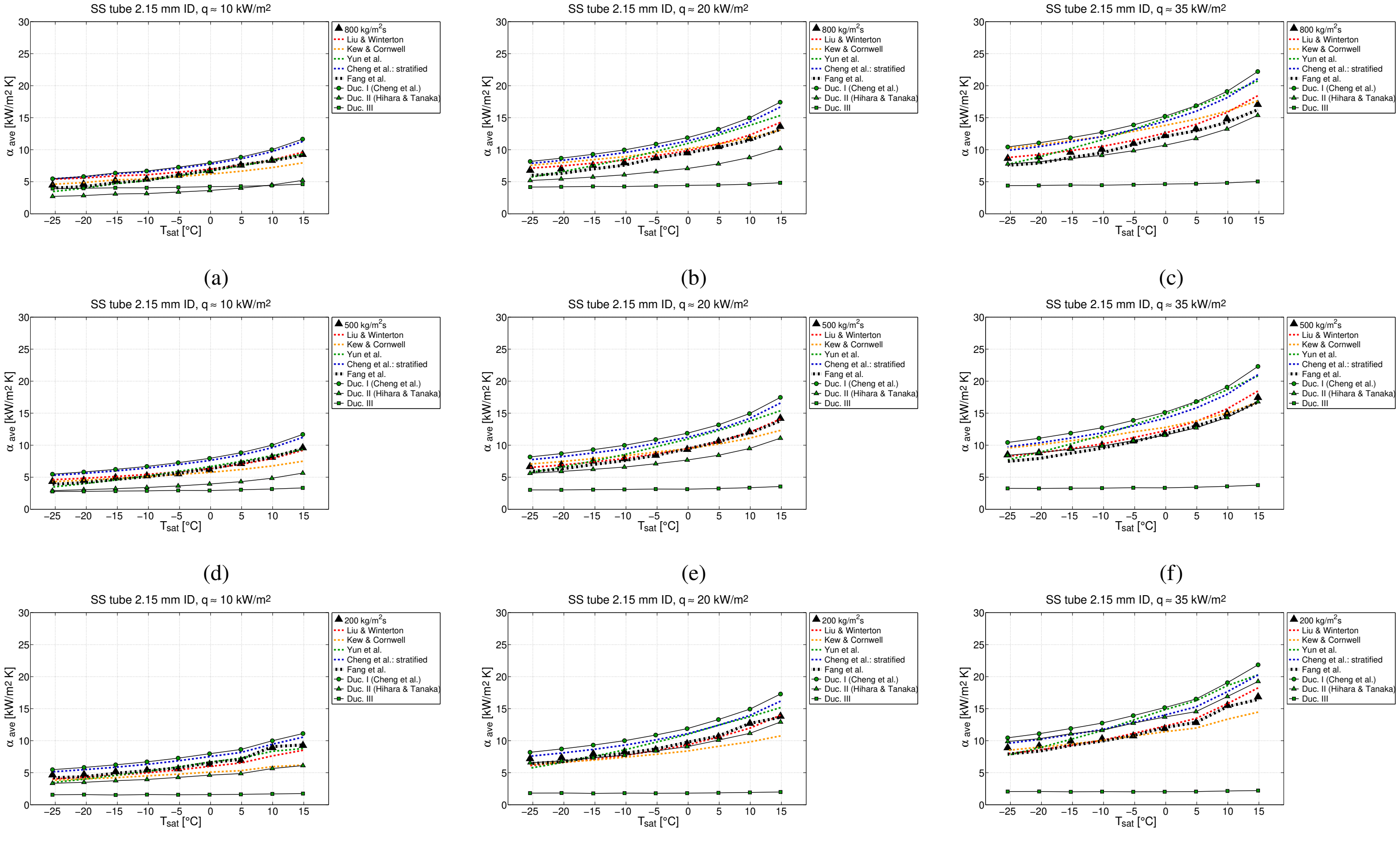

(a) (b) (c)

(d) (e) (f)

(g) (h) (i)

Figure F.10: Heat transfer coefficient: Effect of T$_{sat}$ on the applicability of different correlations: 2.15 mm ID tube.

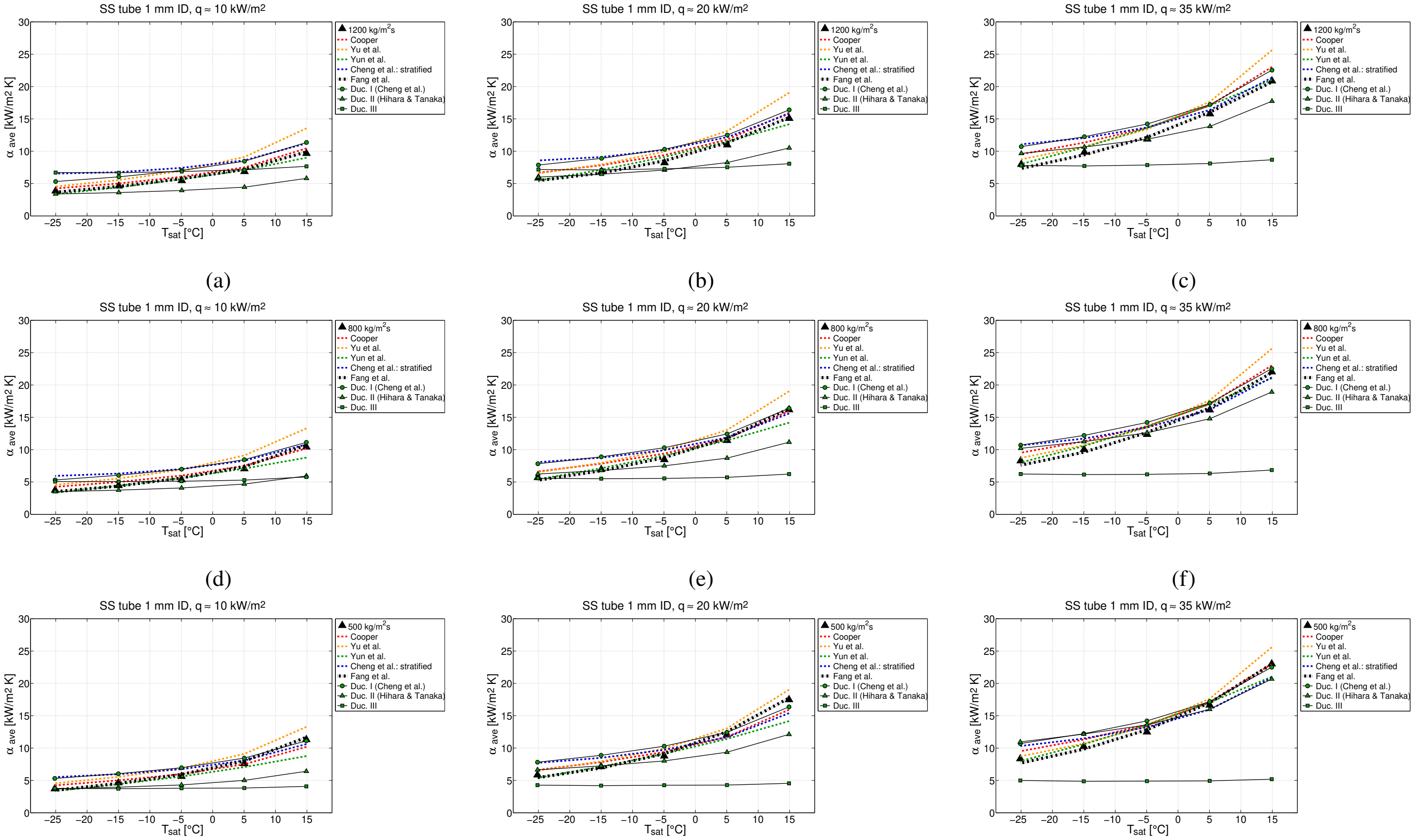

(a) (b) (c)

(d) (e) (f)

(g) (h) (i)

Figure F.11: Heat transfer coefficient: Effect of T_{sat} on the applicability of different correlations: 1 mm ID tube.

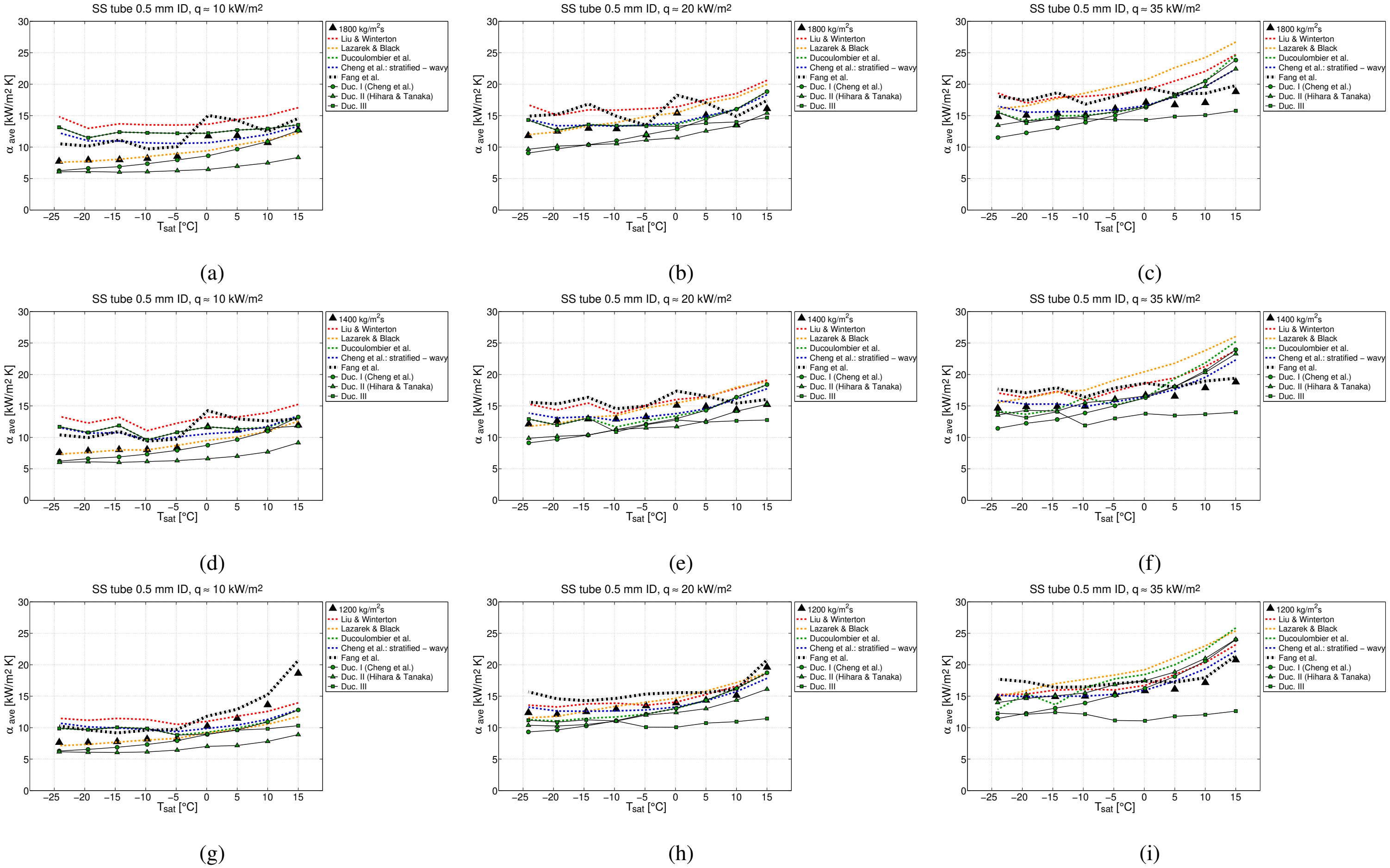

(a) (b) (c)

(d) (e) (f)

(g) (h) (i)

Figure F.12: Heat transfer coefficient: Effect of T$_{sat}$ on the applicability of different correlations: 0.5 mm ID tube.

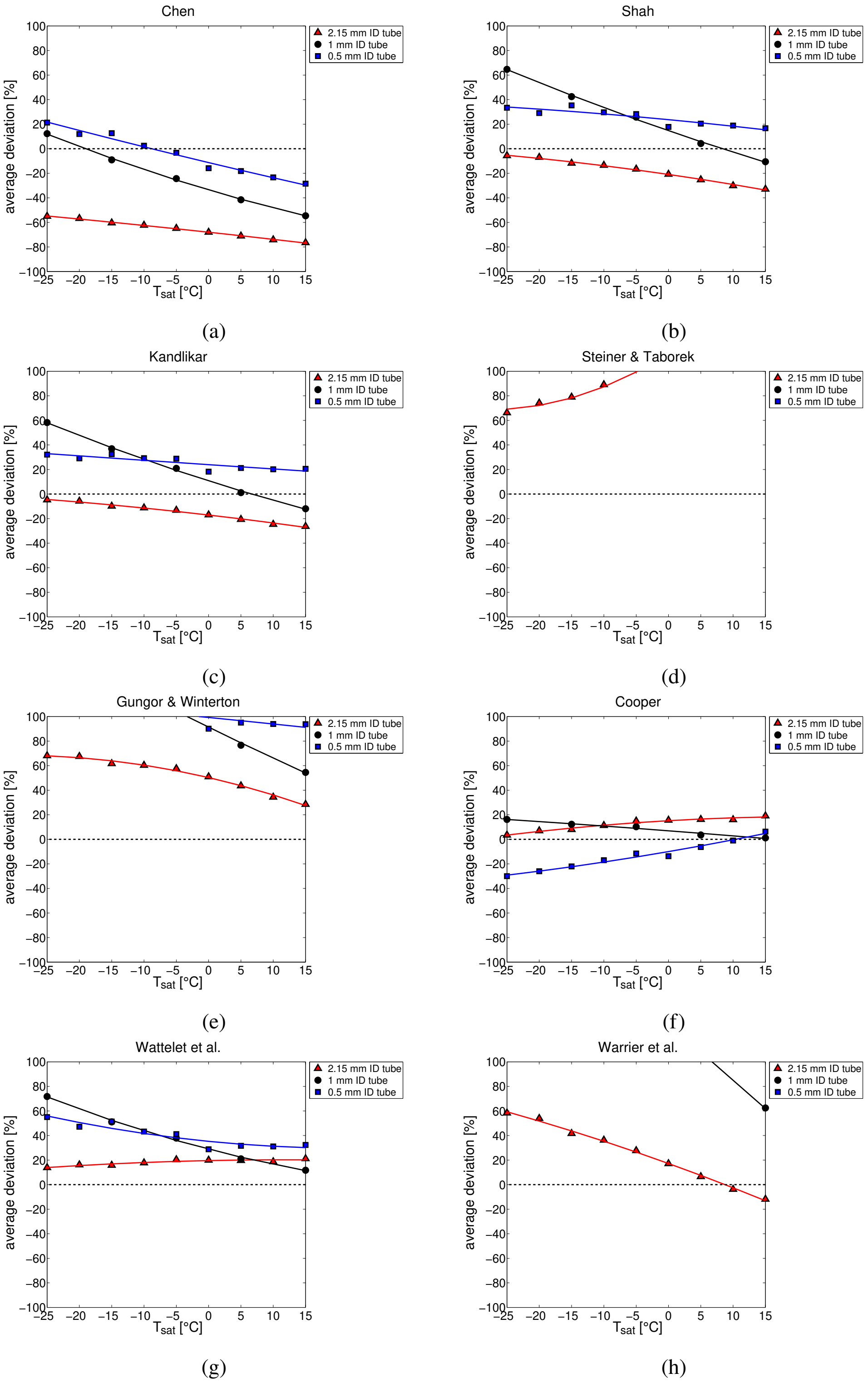

(a) (b)

(c) (d)

(e) (f)

(g) (h)

Figure F.13: Heat transfer coefficient: Average deviation of experimental values from selected prediction methods I.

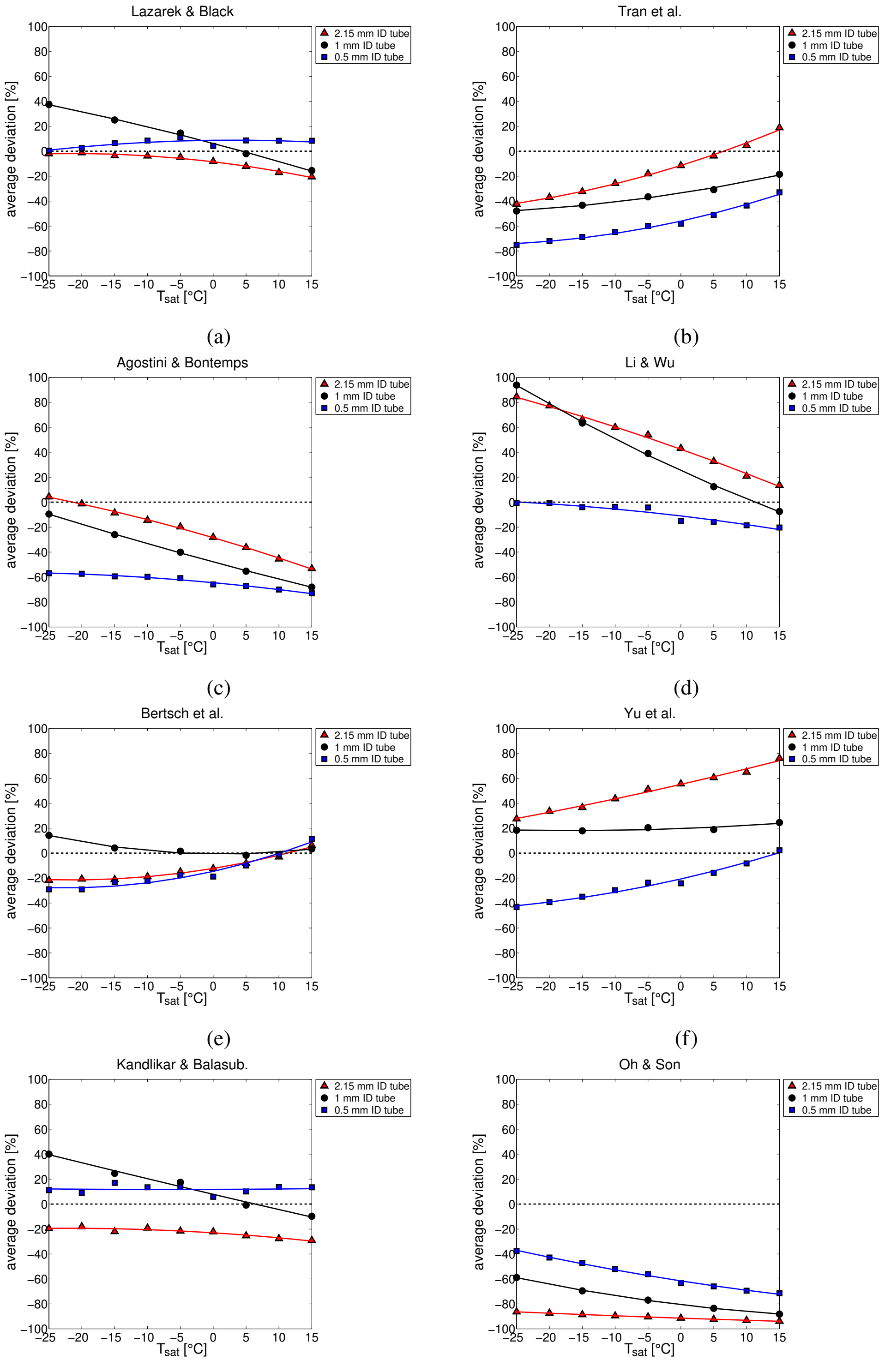

(a) (b) (c) (d) (e) (f) (g) (h)

Figure F.14: Heat transfer coefficient: Average deviation of experimental values from selected prediction methods II.

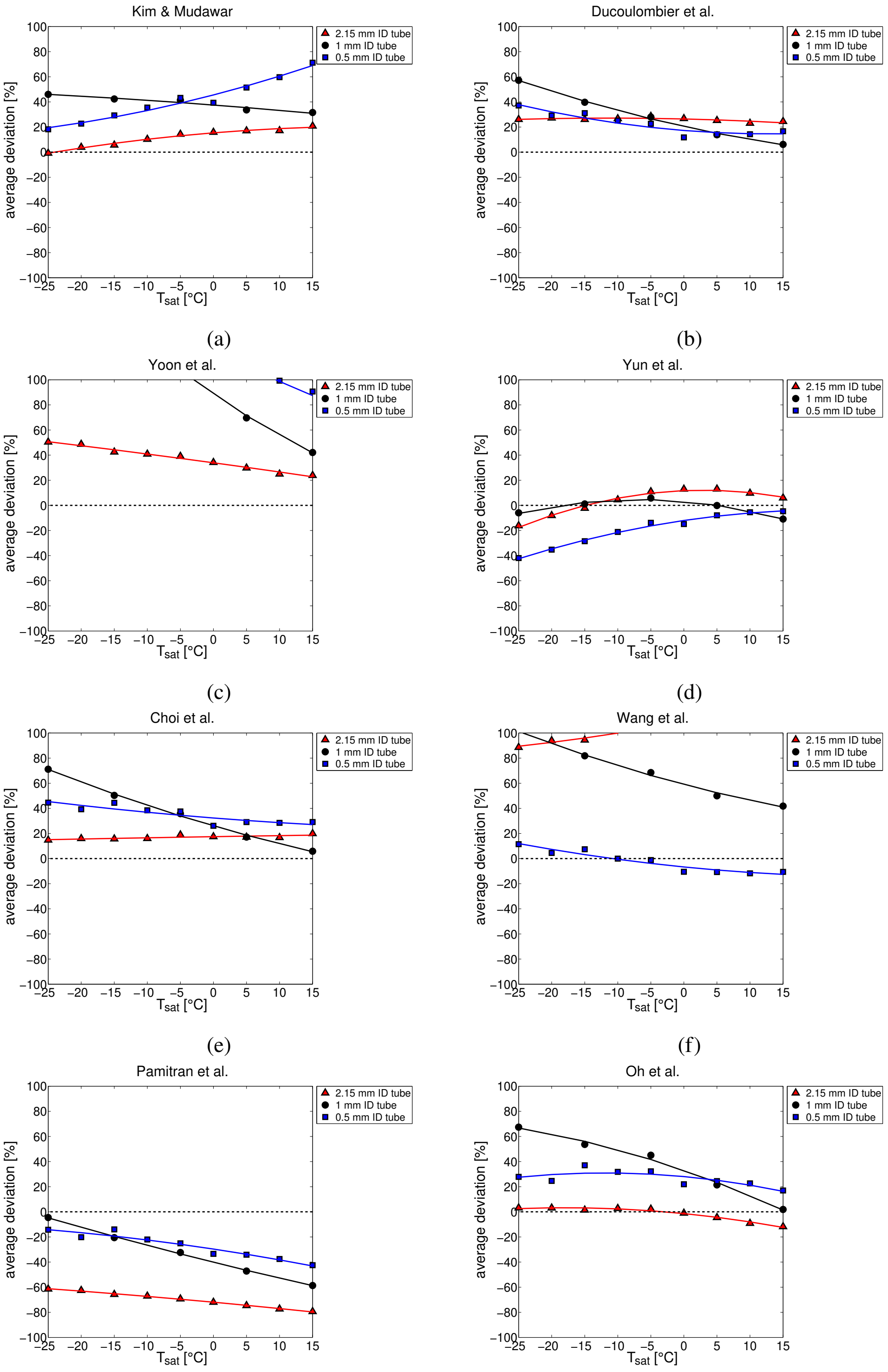

(a) (b) (c) (d) (e) (f) (g) (h)

Figure F.15: Heat transfer coefficient: Average deviation of experimental values from selected prediction methods III.

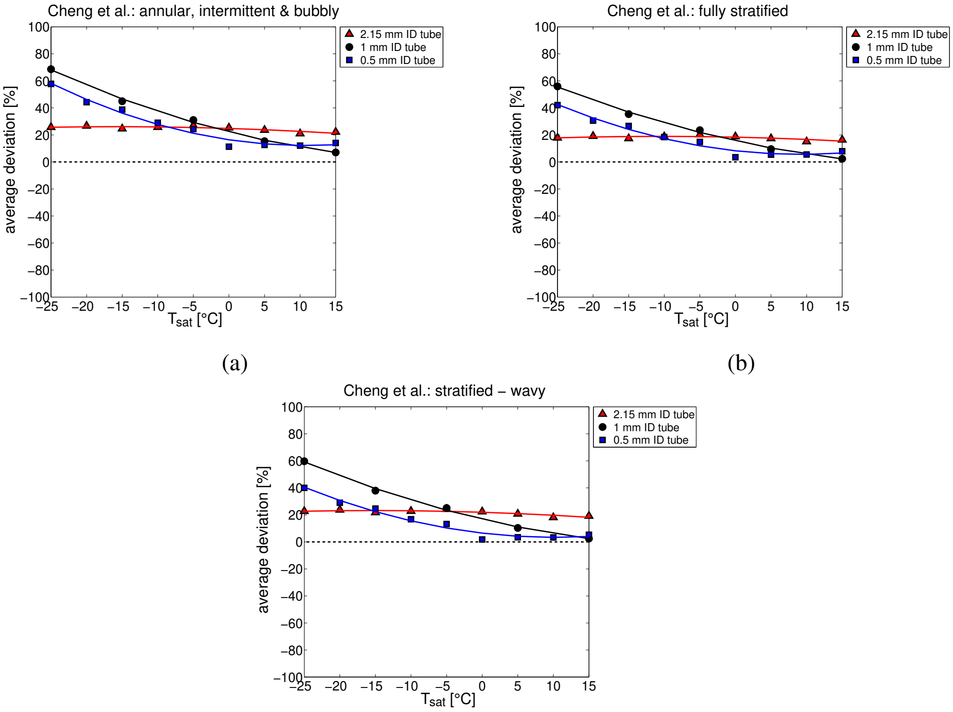

(a)

(b)

(c)

Figure F.16: Heat transfer coefficient: Average deviation of experimental values from selected prediction methods IV.

List of Figures

List of Tables

Acknowledgements

At this place I would like to say ...

Grazie to Paolo Petagna. Without him and his idea to finally bring some light and order into the so far dark and rather arbitrary matter of flow boiling at small scales, in particular with carbon dioxide as working fluid, this thesis and all the gathered results would not have been part of the scientific world. On the other hand also I would not have received the chance to be part of CERN and its Experimental Physics department, which however now - thanks to Paolo - was a great opportunity and experience to me. Paolo, thanks for your trust since the very beginning, for all your advise and help and for believing in my work when I didn't. You once mentioned to me the remark by Albert Einstein: *"A theory is something nobody believes in, except the person who made it. An experiment is something everybody believes in, except the person who made it"*. Ever since I felt a bit more at ease with my experimental work. Furthermore Grazie to Andrea Cioncolini for having him as a renowned expert on multi-phase flows on our side and for his invaluable help through many discussions. Also Grazie Paola, for your trust all along!

Danke to Professor Jochen Dingfelder. I am really grateful for his immense open-mindedness which resulted in the launch of this inter-disciplinary project and for trusting Paolo and me that this thesis in the end will be suitable for the archives in Bonn. Vielen Dank to Georg Viehhauser for his very kind offer to co-review this thesis. One thousand times Danke to my parents who always supported me, who opened up doors and opportunities for me and who taught me how to fly - to Kepler-452 and back. Also Danke, David and Daniela.

Gracias to Carlos Marinas, who at the very beginning convinced Jochen that micro-channel cooling is an interesting and relevant topic, also for the high energy physics community and that it might be worthwhile putting both of their names down for it. Also Gracias to you, Felix.

Merci to both Jeromes, J. Noel and J. Daguin, from the office next door, for their help and counsel during the construction and commissioning of the test setup and their expertise on how to navigate the vast Swagelok catalogue.

Dziękuję and **Obrigado** to Wiktor and Oscar from the LHCb micro-channel S.W.A.T. who were always there to help or otherwise turned a deaf ear when I was cursing loudly in the lab next door.

Bedankt to Bart, Tym and Kars.

Dhanyavaad to Viren. Thank you so much for the truly heroic moral support throughout all this time. Without you and your unfailing optimism I would not have made it to the end.

Thank you to all dear fellow engineers and physicists who believed in me, who taught me new things and helped me to become a better scientist and a wiser person.